Chemical Vapour Deposition Diamond

Charge Carrier Movement at Low Temperatures and Use in Time-Critical Applications

Dissertation
zur
Erlangung des Doktorgrades (Dr. rer. nat.)
der
Mathematisch-Naturwissenschaftlichen Fakultät
der
Rheinischen Friedrich-Wilhelms-Universität Bonn
angefertigt bei der
Europäischen Organisation für Kernforschung, CERN, Genf, Schweiz

von
Dipl.-Phys. Hendrik Jansen
aus
Oberhausen

Genf/Bonn, 2013

Dieser Forschungsbericht wurde als Dissertation von der Mathematisch-Naturwissenschaftlichen Fakultät der Universität Bonn angenommen und ist auf dem Hochschulschriftenserver der ULB Bonn http://hss.ulb.uni-bonn.de/diss_online elektronisch publiziert.

Neue korrigierte Version, 2015

1. Gutachter:	Prof. Dr. Norbert Wermes
2. Gutachter:	Dr. Heinz Pernegger
Tag der Promotion:	10.12.2013
Erscheinungsjahr:	2014

Preface

"Uh, diamonds!" — When people ask me about the topic of my Ph.D. thesis, my answer is usually interrupted by this exclamation after the first or second sentence. And this holds for non-physicists and physicists alike. Seemingly, people have a latent fascination with objects made of carbon atoms arranged in a certain crystalline structure, often found as octahedral-shaped specimen decorating all kinds of jewellery from rings to royal crowns. While the fascination with diamond gemstones amongst laymen, gem experts, and the wealthy is likely due to their beauty and scarcity, scientists also appreciate diamond for its outstanding physical properties, most of which stem from the strong covalent bonds between their atoms. Diamond is a metastable allotrope of carbon, but in contrast to the sp^2-forms graphite, graphene, fullerenes (buckminsterfullerene, nanotubes), and so on, where atoms are tightly bound in a plane, but less so vertically, the carbon atoms in diamond bind to four neighbouring atoms in an sp^3-form, i.e. in three dimensions and equally strong to all the four neighbours. The strong covalent bonds make diamond extremely hard, a property which has led to its wide usage in industry and medicine as part of cutting tools. Moreover, it makes diamond an extremely effective heat conductor with a five times higher heat conductivity than copper at room temperature, and thus diamond is used in silicon semiconductor manufacture as heat spreaders. Its transparency in the optical range makes it the material of choice for laser windows.

Besides the usage of "pure" diamond and its inherent properties, there is a justified interest in contaminated diamond containing certain impurities, for example nitrogen impurities. If a nitrogen impurity happens to reside close to a carbon vacancy, namely a missing carbon atom in the crystal lattice, so-called nitrogen-vacancy (N-V) centres are created. N-V centres are particularly interesting as they are optically active. The quantum state of electrons that are located at these centres can be manipulated using for instance light or electro-magnetic fields. With sufficient space between two centres, their photoluminescence can be detected individually. Therefore, N-V centres can function as a qbit, i.e. the base unit of a quantum computer. [1]

Nanodiamonds – diamonds of a few nanometres in size – may soon become crucial in human medicine. They can bind to a variety of molecules such as cancer drugs and then deliver the drug directly to the tumour cells. This increases the efficacy of a drug and reduces many potential side effects such as necrosis of healthy cells. Moreover, because they are made of carbon, nanodiamonds are non-toxic and are not seen as a threat by the immune system. [2]

These are just two examples of how science, driven by an exploratory urge, takes an object found in nature, engineers and manipulates its material properties to the most extreme, and creates a product with numerous applications. In fact, science has driven many of the important milestones in the history of human civilisation. The invention of the telescope enabled Galilei and other scientists of those days to carry out astronomical observations, confirming the earlier contrived Copernican heliocentric system. This was not only of scientific importance, but had a huge sociocultural impact as it was proven that the earth was not the centre of the solar system. It might well have been these astronomical observations that stimulated Leibniz and Newton independently to develop the

calculus allowing the prediction of planetary configurations, and remaining a key ingredient in modern physics and engineering.

Another milestone was certainly the growing understanding of the constituents of the perceptible world around us, and how these interact with each other. Anaximenes of Miletus, a Greek philosopher, thought the world was made of air; water and stone being a result of its compression, and fire a result of its dilution. This model of matter was later falsified, and replaced by others. With the discovery of the electron and Rutherford's scattering experiments using thin gold films, it became clear that the perceptible world is made of atoms; an atom in turn consists of a nuclei in the centre and electrons forming an outer shell. Maxwell described the dispersion of light in his equations, accomplishing the unification of the electric and the magnetic force into a single concept. Curie was driven by a curiosity to uncover the process behind the radioactive decay. Einstein explained the photoeffect as the quantised exchange of energy between a photon and an electron, also giving insight into wave-particle duality. Later, with the discovery of the up- and the down-quark, the gluon confining these quarks into protons and neutrons, and the bosons of the weak interaction governing the radioactive β-decay, physicists created a "Standard Model of particle physics" (SM) describing matter as quarks and leptons. The SM does not only model matter as quarks and leptons, it also describes three of the four known forces (these being the weak, the strong, and the electromagnetic force) that interact among them making use of local gauge theories. For the gravitational force, the one most perceived by humans, a quantum theory is still lacking.

It is justified to ask how much the general public cares about these findings. In the end, day-to-day life as we know it today would be impossible without the advances of science. The invention of the Internet, digital cameras and smartphones, cars, MRI machines, PET-scans, and satellite TV, among others, would have been impossible with Anaximenes' rudimentary concept of the world's constituents. And people appreciate these advances. Science is one of the important driving forces behind innovation; and encouraging and enabling young students to think and to "question the answer" is a key element in this driving force. Hence, the money spent for research and teaching facilities is money well spent.

Abbreviations

APS	—	Acoustic phonon scattering
BC	—	Bunch-crossing
BCM	—	Beam conditions monitor
BCTF	—	Fast beam current transformer
BLM	—	Beam Loss Monitor
BZ	—	Brillouin zone
CBM	—	Conduction band minimum
CERN	—	European Organisation for Nuclear Research
CCD	—	Charge collection distance
CCE	—	Charge collection efficiency
CCR	—	CERN control room
CNGS	—	CERN Neutrinos to Gran Sasso
COM	—	Centre-of-mass
CVD	—	Chemical vapour deposition
DD	—	Diamond detector
DLC	—	Diamond-like carbon
EHL	—	Electron-hole liquid
EHP	—	Electron-hole plasma
EMT	—	Effective Mass Theory
fcc	—	Face centred cubic
FWHM	—	Full-width at half-maximum
GPS	—	Global positioning system
GMT	—	General Machine Timing
hcp	—	Hexagonal close packed
IIS	—	Ionised impurity scattering
IVC	—	Inner vacuum chamber
LHC	—	Large Hadron Collider
LF	—	Likelihood function
MIP	—	Minimum ionising particle
N-V	—	Nitrogen-vacancy
NIS	—	Neutral impurity scattering
NIST	—	National Institute of Standards and Technology
pCVD	—	Polycrystalline chemical vapour deposition
PAH	—	Polycyclic aromatic hydrocarbon
pot	—	Protons on target
RT	—	Room temperature

continued

scCVD	—	Single crystal chemical vapour deposition
SCF	—	Space-charge free
SM	—	Standard model of particle physics
SNR	—	Signal-to-noise ratio
SUT	—	Sample under test
TCT	—	Transient current technique
ToF	—	Time-of-flight
TVF	—	Tube vacuum feed-through
VBM	—	Valance band minimum

Contents

1. INTRODUCTION

Progress in science leads to an ever evolving frontier of knowledge, with new, ingenious experiments testing theories and models to higher and higher precision, and in ways never thought of before. Pushing this frontier is also a goal at the largest particle accelerator ever built, the Large Hadron Collider (LHC) [3], which was constructed on the border between Switzerland and France, and is managed by the European Organisation for Nuclear Research, CERN. The LHC is a circular proton accelerator that collides two proton beams at unprecedented energy and luminosity, enabling scientists for the first time to get a glance at the elusive Higgs boson, to name just one of the important findings made since the first collisions in 2009. The protons are accelerated to a certain energy and are kept on a circular trajectory by means of magnetic fields produced by superconducting magnets, which are cooled to lower than $-270\,^{\circ}\mathrm{C}$, or 1.9 K. In order to "see" particles like the Higgs boson, that are created in collisions and decay almost immediately into other daughter-particles, one has to track these daughter-particles, namely measure their trajectory in time and space away from the collision point. As these particles are often charged, they lose a considerable part of their kinetic energy whilst traversing matter. This energy can be measured with various techniques and materials; often a semiconductor or gas is the material of choice, diamond being one example.

At room temperature, diamond is used at the LHC for a mere counting experiment in order to measure the flux of charged particles through a certain surface. [4] This measurement is needed in order to quantify the so-called beam losses. Beam losses occur when protons of the beam sheer out of their normal trajectory and hit collimators, which are installed to clean the beam from these outliers. The interaction of these outliers with a collimator produces a large amount of stray-particles which eventually leave the volume of the accelerator. Before they leave the accelerator, they traverse the cold mass of the magnet. Particle flux detectors placed within the cold mass would give the most accurate results about their flux, with diamond being one of the material candidates. As these detectors should be placed within the cold mass of the magnets, they have to be operated at the ambient temperature, i.e. at 1.9 K. These cryogenic detectors have not been realised yet, but are under investigation [5] and act as a key motivation for the research presented herein.

Diamond, a wide band gap semiconductor with exceptional electrical properties [6], has found its way in diverse fields of applications reaching from the usage as a sensor material for beam loss monitors (BLM) at particle accelerators, to laser windows [7], to UV light sensors in space applications, e.g. for space weather forecasting [8]. It is furthermore an interesting candidate for heat tolerable, radiation hard, very fast, low power transistors. Its wide band gap (5.47 eV) results in a high breakdown field ($> 10^3\,\mathrm{V/\mu m}$). Single-crystal diamond features very low leakage current of a few picoampere for field strengths $E \leq 1\,\mathrm{V/\mu m}$ rendering very precise signal current measurements possible.

Though often used at room temperature, little is known about the charge transport in diamond towards liquid helium temperatures. However, a better understanding is crucial for the operation of cryogenic BLMs, for example within the cold mass of a magnet of the Large Hadron Collider. Furthermore, for space flight applications a transistor/sensor material,

that is reliable and well understood over a huge temperature range, is desirable. In this work the method of the transient current technique is employed at temperatures between 2 K and 295 K using α-radiation. The electric field strength is varied by a factor of 30. The temperature and electric field strength dependence of the pulse shape, the charge carrier transit time, the drift velocity, the saturation velocity, and the low-field mobility is measured in detector-grade scCVD diamond. Models are presented which explain consistently the various parts of the recorded data in terms of charge creation and fundamental excitations in semiconductors on one side, and various charge transport related aspects as acoustic phonon scattering on the other.

Furthermore, the usability of diamond in time-critical applications is tested, and the main results are presented. The excellent time resolution of diamond detectors was used in order to cross-check the timing system of the CNGS facilities at CERN, providing key information in the search of the faulty system, that led to an incorrect neutrino velocity measurement above the speed of light [9] by the OPERA [10] experiment, which was later withdrawn. With the diamond detectors in place, the charge yield and the single-pulse time resolution in an high flux environment was quantified. The ATLAS experiment [11] at the LHC provides a use case for beam loss studies, and results on non-collision backgrounds are shown.

This work is structured as follows: After this introduction, diamond as a semiconductor and the physics governing them are discussed in Chap. 2. Chapter 3 gives an overview of radiation detection of charged particles and how diamond is used as a solid state ionisation chamber. Details and photographs of the set-up used, the data taking, and the data processing are described in Chap. 4, followed by the results of the cryogenic measurements presented in Chap. 5. Examples of timing applications of chemical vapour deposition diamonds and the measurement of the time resolution constitute Chaps. 6, 7, and 8, each contemplating the experimental situation of the single application.

2. CVD DIAMOND – A WIDE BAND GAP SEMICONDUCTOR

After a general overview of semiconductors (Sec. 2.1) fundamental properties, characteristic, and mechanisms are reviewed keeping a special attention to diamond (Sec. 2.2). Diamond growth is discussed in Sec. 2.3 and diamond interfaces to metal in Sec. 2.4. Amongst other sources, references [12, 13, 14, 6] were mainly used for the compilation of Chap. 2.

2.1. Introduction to Semiconductors

Ohm's law of semiconductors, namely $j = \sigma E$, allows for a categorisation of solids into metals, semiconductors, and insulators by their conductance σ, which is the constant of proportionality between an electric field strength E and its induced current density j. The conductivity of semiconductors is of electronic nature in contrast to ionic conductivity (cited after Ref. [12]). Metals, e.g. copper or gold, are solids with conductances higher than $10^4\,(\Omega\mathrm{cm})^{-1}$. Insulators like paraffin have conductances smaller than $10^{-8}\,(\Omega\mathrm{cm})^{-1}$. Semiconductors, in terms of conductances, are situated in between them; a prominent example being silicon with an intrinsic conductances of the order of $10^{-5}\,(\Omega\mathrm{cm})^{-1}$. [13] The conductivity of semiconductors depends on the temperature; the classification made above is valid at room temperature (RT). Towards lower (higher) temperatures their conductivity decreases (increases). The conductivity of intrinsic diamond at RT is effectively zero, for real diamond the conductivity depends on the quality of the diamond. Conductances of the order of $10^{-12}\,(\Omega\mathrm{cm})^{-1}$ or lower are commonly encountered values, and diamond is therefore often referred to as an insulator. However, with a closer look at the material, it becomes obvious, that diamond is best described by the term "wide band gap semiconductor". This is because (almost) all properties of diamond can be described with the same physics as encountered in silicon, just by the scaling of certain properties like the energy of the band gap. Some properties of diamond and silicon are listed in Tab. 2.1. The classification of diamond as an insulator is therefore correct in terms of conductances, but a classification as a semiconductor meets the general physical situation better.[1] Besides element semiconductors there are compound semiconductors as gallium arsenide (GaAs), indium phosphide (InP), and silicon carbide (SiC), among others. Typical applications of semiconductors range from diodes and transistors in integrated circuits, to temperature sensors, pressure sensors, photo sensors, solar cells, to light-emitting diodes and lasers.

The chemical bond in semiconductors differs from the well-known ionic bond, and is discussed here by taking the example of diamond. The electron configuration of carbon is $[1s^2 2s^2 2p^2]$, hence the valence shell is half filled. When carbon atoms are brought closely together the $[s^2p^2]$ configuration is promoted to a $[sp^3]$ configuration. The s- and p-states hybridise to four tetrahedral, directed, club-shaped functions. "The overlap of two clubs from neighbouring atoms results in an energy gain via the exchange interaction" [12, p. 10], which is larger than the energy needed for the promotion. This is the covalent bond. The

[1] Paraffin is an example of an insulator, which is not a wide band gap semiconductor.

Table 2.1.: A comparison of properties of diamond and silicon. [13] Additional values of basic properties in diamond can be found in Ref. [6], p. 30.

Element	Crystal structure	Latt. const. [Å]	Band gap [eV]	Gap type	Diel. coeff.	Density [gcm^{-3}]	Intrisic carrier conc. [cm^{-3}]	Debye Temp. [K]
C	Diamond	3.57	5.47	Ind.	5.7	3.52	10^{-27}	1860
Si	Diamond	5.43	1.12	Ind.	11.9	2.33	10^{10}	645

final outcome is a configuration with four nearest neighbours per atom resulting in the crystallisation into the "diamond structure" for e.g. diamond and silicon, only that in the silicon case the valence shell configuration is $[3s^2 3p^2]$ instead of $[2s^2 2p^2]$.

2.2. Basis of Semiconductor Physics

2.2.1. Crystal structure

An ideal three dimensional crystal lattice is described by three fundamental translation vectors $\boldsymbol{a}, \boldsymbol{b}, \boldsymbol{c}$: The *point lattice* is reproduced for every integer, linear combination of them, i.e. the set of lattice points obeys $\boldsymbol{L} = l\boldsymbol{a} + m\boldsymbol{b} + n\boldsymbol{c}$. [12, 13] A lattice structure can in general be described by more than one set of equivalent fundamental vectors. In order to represent the real lattice, on every lattice point a *basis* is situated consisting either of a single atom or of a group of atoms featuring the same composition and orientation.

A unit cell is a carefully constructed volume which reproduces the entire lattice by successively placing one unit cell next to each other in a complete and non-overlapping manner. One possibility of a unit cell is the smallest possible parallelepiped spanned by the three fundamental vectors reproducing the lattice by successive translation operations. The volume of this unit cell is $V = (\boldsymbol{a} \times \boldsymbol{b}) \cdot \boldsymbol{c}$. [13] A special type of the unit cell is the so-called Wigner-Seitz cell, which is constructed around a single lattice point. It is constructed via the perpendicular bisectors of the connecting lines between the examined lattice point and its neighbours, see Fig. 2.1 **(A)** for illustration.

In addition to the translation operation, there are other symmetry operations that can be operated on the point lattice leaving the lattice invariant, i.e. rotations, parity transformations, and their combination. The entirety of such point (point + translation) symmetry operations, that leaves the lattice invariant, forms a point group (space group). [17, 12] The number of lattice types allowing for these operations is limited: There are in total 7 (14) lattice types for the point group (space group) in the three dimensional space. These are called the Bravais lattices. One of the Bravais lattices is the face centred cubic (fcc) lattice, which is a cubic lattice with atoms at each corner and in the middle of each of the six faces, see Fig. 2.2 **(A)**. The diamond lattice is a fcc unit cell with two atoms at its basis, one at $l = m = n = 0$, or $(0, 0, 0)$ and the other at $\frac{1}{4}a \cdot (1, 1, 1)$, shown in Fig. 2.2 **(B)**. [17] The lattice constant is $a = 3.57\,\text{Å}$ in diamond, the nearest neighbour distance is $a_0 = 1.54\,\text{Å}$ resulting in an atomic concentration of $1.76 \times 10^{23}\,\text{cm}^{-3}$ and a density of $3.52\,\text{gcm}^{-3}$.

Another important aspect of a direct lattice is its reciprocal lattice, i.e. the lattice in which the Fourier transform of the original lattice is represented. Considering a plane wave with wave vector $\boldsymbol{k}$ defined by $\exp(i\boldsymbol{k} \cdot \boldsymbol{r}) = \cos(\boldsymbol{k} \cdot \boldsymbol{r}) + i \sin(\boldsymbol{k} \cdot \boldsymbol{r})$, and a set of lattice

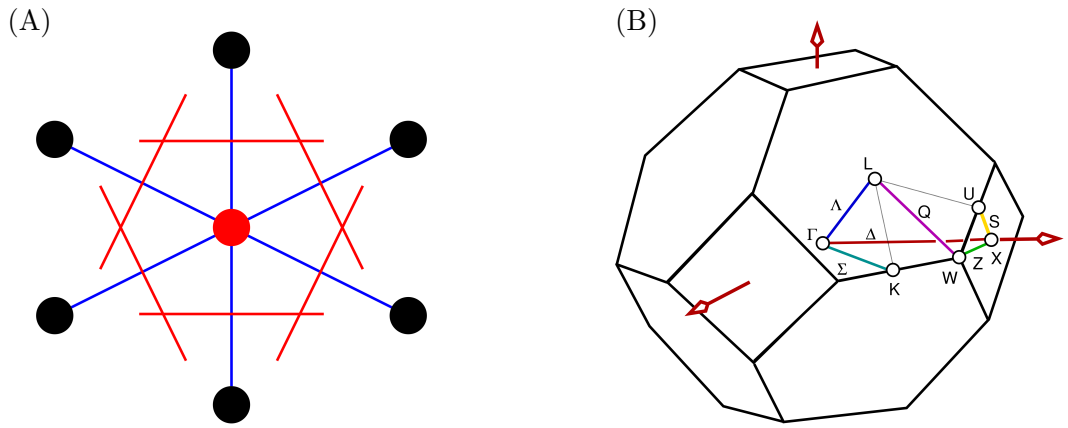

Figure 2.1.: **(A)** Construction rule of the Wigner-Seitz cell: Straight lines are drawn from the considered lattice point to the nearest neighbours. The perpendicular bisectors form the Wigner-Seitz cell. (from [15]) **(B)** The Wigner-Seitz cell of the reciprocal fcc-lattice is shown. The faces form the edge of the Brillouin zone. The indicated points are explained in the text. (from [16])

points $\boldsymbol{R}$ of the original Bravais lattice, the following holds true if this plane wave has the same periodicity as the lattice:

$$\exp\left(i\boldsymbol{k}\cdot(\boldsymbol{r}+\boldsymbol{R})\right)=\exp\left(i\boldsymbol{k}\cdot\boldsymbol{r}\right)\qquad\Rightarrow\qquad\exp\left(i\boldsymbol{k}\cdot\boldsymbol{R}\right)=1 \tag{2.1}$$

Therefore the reciprocal lattice is defined by the set of vectors $\boldsymbol{k}$ that satisfy Eq. (2.1) for all lattice points $\boldsymbol{R}$. It can be shown, e.g. using the Laue construction, cf. [12], that the following vectors satisfy this:

$$\boldsymbol{A}=2\pi\frac{\boldsymbol{b}\times\boldsymbol{c}}{(\boldsymbol{a}\times\boldsymbol{b})\cdot\boldsymbol{c}},\qquad\boldsymbol{B}=2\pi\frac{\boldsymbol{c}\times\boldsymbol{a}}{(\boldsymbol{a}\times\boldsymbol{b})\cdot\boldsymbol{c}},\qquad\boldsymbol{C}=2\pi\frac{\boldsymbol{a}\times\boldsymbol{c}}{(\boldsymbol{a}\times\boldsymbol{b})\cdot\boldsymbol{c}}. \tag{2.2}$$

The reciprocal lattice can then be represented by the form $\boldsymbol{G}=h\boldsymbol{A}+k\boldsymbol{B}+l\boldsymbol{C}$, with h,k,l integer. [13] Since this lattice is periodic, physical properties defined in $\boldsymbol{k}$-space inherit this periodicity. E.g. the electron dispersion relation, which is a representation of the electron energy in $\boldsymbol{k}$-space, is periodic. Many physical observations as reflection and diffraction of waves off crystals are readily described using the wave vector and the reciprocal lattice. It is hence a common tool in crystallography.

The construction rule of the Wigner-Seitz cell can also be used on the reciprocal lattice, the result is the so-called Brillouin zone (BZ). The first BZ of the fcc-lattice is depicted in Fig. 2.1 **(B)**. The high-symmetry point Γ is the origin of the reciprocal space, the X-, the K-, and the L-point are the edges of the first BZ in the [100], [110], and [111] direction, respectively. They are situated at $\frac{2\pi}{a}(1,0,0)$, $\frac{2\pi}{a}(3/4,3/4,0)$, and $\frac{2\pi}{a}(1/2,1/2,1/2)$, respectively.

2.2.2. Energy band model in position space

The electron energy states of single, isolated carbon atoms are discrete and equal for all carbon atoms. When the distance between single atoms is reduced to the atomic scale, hybridisation takes place, i.e. the electron states themselves change. This is a direct consequence of the Pauli principle. With decreasing distance the energy gain due to the exchange interaction rises, whereas the electrostatic repulsion increases. At the nearest neighbour

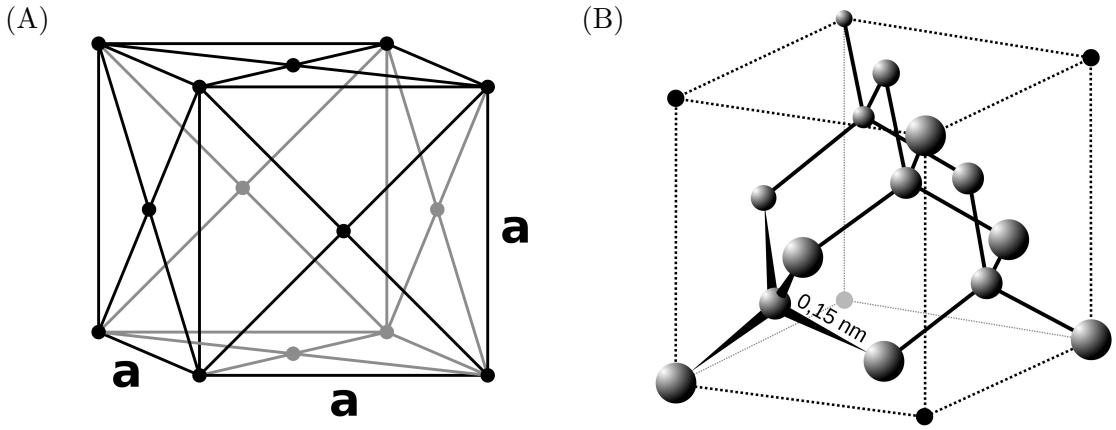

Figure 2.2.: **(A)** The fcc point lattice with a primitive basis and a lattice constant a is depicted (from [18]) next to the diamond lattice with a biatomic basis in **(B)** with a nearest neighbour distance of $a_0 = \sqrt{3} \cdot a/4 = 1.54\,\text{Å}$ (from [19]).

distance a_0 the combination of interaction and repulsion energy has a minimum, and atoms arrange themselves at this distance. The stationary atomic cores then create the periodic potential in position space for the electrons. Moreover, the former discrete states of the many atoms now arrange in "continuous bands" of energy states, i.e. bands with many states of energy differences much smaller than their absolute energy. The bands are thus a result of the coupling of the wave function of neighbouring atoms. Figure 2.3 shows this concept. Observations show a "forbidden band" in between allowed bands. In order to understand the occurrence of this forbidden energy range, or energy gap, one has to look at the energy bands in the reciprocal lattice, i.e. in $\boldsymbol{k}$-space.

2.2.3. Energy band model in k-space

The band structure, or dispersion relation of an electron in a crystal is the relationship between its energy E and momentum $\boldsymbol{k}$. $\boldsymbol{k}$ is also called crystal momentum, although it is not the momentum of a crystal atom. In order to obtain it, the time independent Schrödinger equation is solved for various approximations, one example being the one-electron approximation [13]

$$\left[-\frac{\hbar^2}{2m}\nabla^2 + V(\boldsymbol{r})\right] \phi_n(\boldsymbol{r},\boldsymbol{k}) = E_\mathrm{n}(\boldsymbol{k})\phi_\mathrm{n}(\boldsymbol{r},\boldsymbol{k}). \tag{2.3}$$

The Bloch theorem states that the solutions of this equation for periodic potentials are of the form

$$\phi_n(\boldsymbol{r},\boldsymbol{k}) = \exp\left(i\boldsymbol{k}\cdot\boldsymbol{r}\right) U_\mathrm{n}(\boldsymbol{r},\boldsymbol{k}), \tag{2.4}$$

where $U_\mathrm{n}(\boldsymbol{k},\boldsymbol{r})$ is periodic in $\boldsymbol{r}$ and n is the band index. The periodicity of U_n follows from the periodicity of the direct lattice. As discussed above, the reciprocal lattice of a periodic direct lattice is again periodic: Just as a translation by $\boldsymbol{L}$ in the direct space leaves the direct lattice invariant, the reciprocal lattice is invariant under a translation by $\boldsymbol{G}$. The energy eigenvalues $E(\boldsymbol{k})$ are thus periodic in $\boldsymbol{k}$-space and $E(\boldsymbol{k}) = E(\boldsymbol{k}+\boldsymbol{G})$. It is therefore sufficient to describe the energy-momentum relation within one Brillouin zone. As a convention, the first BZ from $k = -\pi/a$ to $k = +\pi/a$ is usually considered. The band gap E_g is then a result of the fact that there exist no eigenfunctions $\phi(\boldsymbol{r},\boldsymbol{k})$ with eigenvalues $E(\boldsymbol{k})$ that fall within

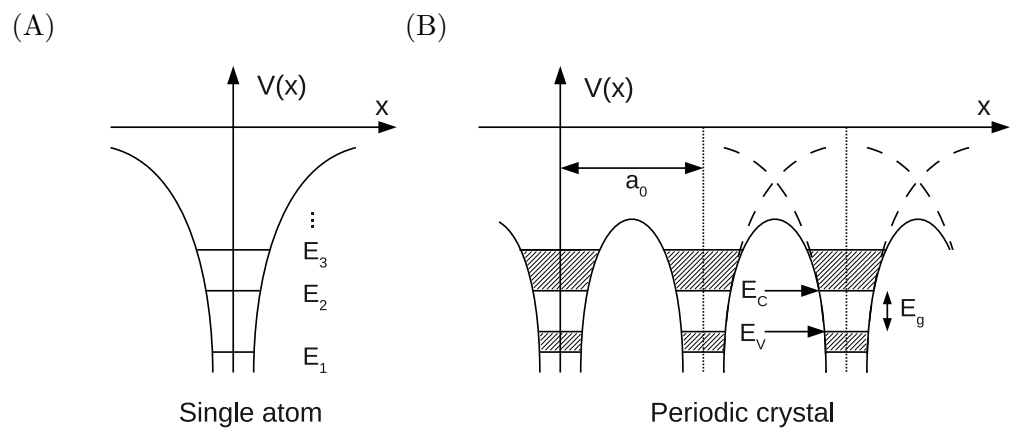

Figure 2.3.: The single atom with discrete energy states **(A)**, and the energy bands in the periodic crystal as a result of the coupling of the wave function of neighbouring atoms **(B)**. The energy gap E_g is indicated between the upper limit of the valence band (E_V) and the lower limit of the conduction band (E_C). (reproduced from [12, p. 11])

a certain energy range. The bands below the energy gap are the valence bands, which are completely filled at $T = 0\,\mathrm{K}$. The conduction bands lie above the gap; therefore the minimum of the conduction bands E_C and the maximum of the valence bands E_V define the borders of the "forbidden gap". The eigenfunctions of Eq. (2.3) are either symmetric or anti-symmetric under exchange of indistinguishable electrons. The symmetric functions have non-vanishing electron probability density between two lattice atoms and are binding, whereas the probability density of the anti-symmetric functions vanishes in the middle of two atoms, resulting in a repelling atom-electron configuration. As a result, the size of the band gap is the difference of the energy expectation values between the symmetric and the anti-symmetric eigenfunctions.

For a free electron ($V = 0$), the spacial part of the time-independent, one-dimensional Schrödinger equation is solved by $\phi_k(x) = \phi_0 \exp(ikx)$ with the eigenvalues

$$E(k) = \left(\hbar^2/2m\right) k^2 \tag{2.5}$$

corresponding to the classical expression of the kinetic energy using the quantum mechanical relation $p \equiv \hbar k$, and hence $E = p^2/2m = 1/2\, mv^2$. The dispersion relation for the non-free electron will differ from the free one, and the energy might not merely depend quadratically on k. Boundary conditions for the wave functions are imposed by the finite crystal size. For a crystal of length L, only waves with $\lambda = L, L/2, L/3, ...$ and thus $k = 0, \pm\frac{2\pi}{L}, \pm\frac{4\pi}{L}, ...$ "fit" into the crystal, with $\Delta k = \frac{2\pi}{L}$. The discrete values in k result in turn in discrete values for $E(k)$, but with macroscopic crystal sizes, a quasi-continuous k emerges and this property is inherited to $E(k)$. [12] In the non-free case, an effective, tensorial mass m^* is defined with components

$$m^*_{\mathrm{ij}} = \left(\frac{1}{\hbar^2}\frac{\partial E(\boldsymbol{k})}{\partial k_\mathrm{i} \partial k_\mathrm{j}}\right)^{-1}, \qquad i = x, y, z. \tag{2.6}$$

In other words, an electron in a periodic potential moves with an effective mass m^* rather than with m_e. Deviations from the pure quadratic dependence of $E(k)$ lead to an energy dependent effective mass.

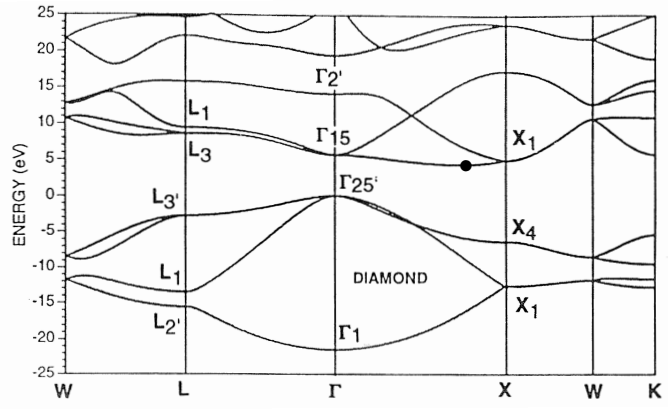

Figure 2.4.: The band structure in diamond is shown. (from [14]) The CBM is marked with a "•". The indirect band gap lies between $\Gamma_{25'}$ and "•".

Band structure calculations are commonly done within certain models making certain assumptions in order to facilitate the calculations. Important examples are the orthogonalised plane wave method, the pseudo-potential method, and the $\boldsymbol{k} \cdot \boldsymbol{p}$ method. The example shown here for diamond is, however, calculated using the linearised augmented plane wave method, see Fig. 2.4. The energetically highest point of the valence band, the valence band maximum (VBM), is marked by $\Gamma_{25'}$ and sits on the high symmetry point Γ at $\boldsymbol{k} = 0$. This point is defined to have zero energy. Above $\Gamma_{25'}$ the next allowed point is Γ_{15} with an energy $E_{\Gamma_{15}} = (7.3 \pm 0.1)\,\mathrm{eV}$, which is the lowest conduction band at $\boldsymbol{k} = 0$. This is called the direct gap in diamond. However, there are energetically lower states along e.g. the [100] direction ($\Gamma \to X$) with a minimum at a distance of $k_0 = 0.76$ in units of $\frac{\pi}{a}$. The energy of this indirect gap is $E_\mathrm{g} = 5.47\,\mathrm{eV}$ [20] and this point is the global conduction band minimum (CBM). In Fig. 2.4 the CBM is marked with a "•". Semiconductors with the CBM situated at $\boldsymbol{k} = 0$ are called direct semiconductors; indirect semiconductors like diamond have their CBM at $\boldsymbol{k} \neq 0$.

For a transition from $\Gamma_{25'}$ to the CBM, not only an energy transfer of 5.47 eV is needed in order to obey energy conservation, but also $\boldsymbol{k}$-momentum conservation has to be accounted for. This momentum is absorbed or provided by the crystal lattice in terms of phonons, i.e. vibrations of the crystal lattice. An emitted photon cannot serve to conserve $\boldsymbol{k}$-momentum: A UV-photon has a wavelength of ∼250 nm and $k = \frac{2\pi}{\lambda}$, whereas the $\boldsymbol{k}$-space is defined on the lattice constant a. The UV-photon could hence only make up for about a per mill of the $\boldsymbol{k}$-momentum.

Figure 2.4 shows the CBM along the [100] direction. However, there are six equivalent directions [100], $[\bar{1}00]$, [010], $[0\bar{1}0]$, [001], $[00\bar{1}]$ – the full set of equivalent directions denoted as $\langle 100 \rangle$ – resulting in six equivalent minima. Along one direction, the dispersion relation of the free electron is of parabolic shape. Drawn in three dimensional space spanned by k_x, k_y, and k_z, the surfaces of equal energy form ellipsoids along the $\langle 100 \rangle$ directions, as shown in Fig. 2.5 **(A)**. The ellipsoidal shape implies that the effective mass tensor does not simplify to a scalar, but that the effective mass depends on the direction. Along the symmetry axes the electron mass is the longitudinal mass $m_{e,\mathrm{l}}$, transverse to them the electron mass is the transverse mass $m_{e,\mathrm{t}}$. Holes, i.e. vacant electron states in the valence band left behind by electrons that have been excited to the conduction band, have also at least two different masses, depending on their band. The heavy (light) hole mass $m_{h,\mathrm{h}}$ ($m_{h,\mathrm{l}}$) is the mass of holes in the upper and wider (lower and narrower) valence band starting at $\Gamma_{25'}$ along the

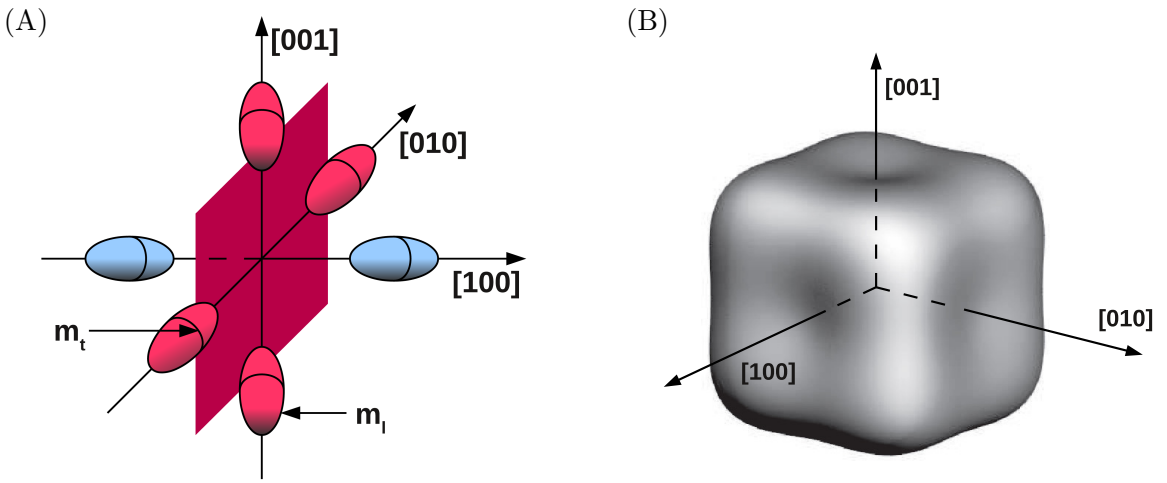

Figure 2.5.: The shape of the constant energy surfaces are shown for electrons **(A)** and heavy holes **(B)** in diamond. There are six equivalent "electron valleys" and the surfaces are ellipsoids along the $\langle 100 \rangle$ directions with their centre at $k_0 = 0.76$. The heavy hole constant energy surfaces are complicated: rather cubic with round edges and warped faces.

$\langle 111 \rangle$ directions ($\Gamma \to L$, see again Fig. 2.4 and Fig. 2.1 **(B)**). The surfaces of equal energy are shown for heavy holes in Fig. 2.5 **(B)**.

2.2.4. Phonon dispersion and thermal conductivity

At temperatures above absolute zero the atoms of a lattice move, i.e. they oscillate around their rest position. Their movement can be treated classically within the adiabatic, harmonic approximation: [14]

- Due to the Newtonian reaction principle the forces that electrons and nuclei exert upon each other are equal but directly opposed. Qualitatively, this leads to $M\ddot{R} \approx m\ddot{r}$, with the mass and position of the nucleus M and R, and those of the electron m and r. With $m \ll M$, it is obvious that the electrons accelerate much faster than the nuclei. The adiabatic approximation is then the assumption that the electrons can adapt adiabatically on the slow movement of the nuclei, in a way that the electrons remain in their ground state. Therefore, the movement of the nuclei and the electrons can be decoupled. The total energy of the system consisting of electrons and nuclei is then the simple sum of the potential energy of the electrons as a function of the nucleus position and the kinetic energy of the nuclei: $E_{\mathrm{tot}} = U_{\mathrm{el}} + T_{\mathrm{nuc}} = U_{\mathrm{el}}(\boldsymbol{R}) + \frac{\boldsymbol{P}^2}{2M}$.
- The explicit form of $U_{\mathrm{el}}(\boldsymbol{R})$ can in general be quite complicated. Within the harmonic approximation, the potential is assumed to be quadratic within a close vicinity of the rest position a_0 and depends only on the second derivative of the pair-wise interaction potential.

Within this approximation the frequency of oscillations as a function of the wave number q in a one dimensional lattice with a basis of two atoms with masses M_1 and M_2 can be calculated analytically. If additionally only the nearest-neighbour coupling is accounted for, the longitudinal oscillation frequencies are

$$\omega^2 = C \cdot \left(\frac{1}{M_1} + \frac{1}{M_2}\right) \pm C \cdot \sqrt{\left(\frac{1}{M_1} + \frac{1}{M_2}\right)^2 - \frac{4}{M_1 M_2} \sin^2\left(\frac{qa}{2}\right)} \tag{2.7}$$

with a coupling constant C. Diamond features a single element basis, i.e. $M = M_1 = M_2$, and Eq. (2.7) simplifies to

$$\omega^2 = \frac{2C}{M}\left(1 \pm \sqrt{1 - \sin^2\left(\frac{qa}{2}\right)}\right). \tag{2.8}$$

At $q = 0$, or $\lambda \to \infty$, the following two frequencies are found

$$\omega_+ = \sqrt{\frac{4C}{M}} \tag{2.9}$$

$$\omega_- = 0 \tag{2.10}$$

The dispersion relation for a one-dimensional lattice with a biatomic, single element basis is shown in Fig. 2.6 **(A)** for the longitudinal modes: longitudinal acoustic (LA) and longitudinal optical (LO). The frequency ω_- is proportional to q near $q = 0$ and the two basis atoms oscillate in phase. This branch is called the acoustic branch since the displacement of bases along the propagation direction leads to regions with denser or less dense atom density, just as in sound waves. For the upper branch the atoms oscillate in opposite phase. In ion crystals this opposite phase oscillation leads to time variable dipole moments which play an important role for the optical properties of a medium. This branch is therefore called the optical branch. For crystals with single element bases, the longitudinal modes are degenerated at the borders of the BZs ($q = \pi/a \Rightarrow \sin qa/2 = 1$), whereas different masses of the bases atoms lead to different frequencies at these points. In three dimensions transverse modes need to be added, i.e. transverse acoustic (TA) and transverse optical (TO) modes. Figure 2.6 **(B)** shows the calculated phonon spectrum for diamond within the adiabatic bond charge model (solid lines). Data points from neutron scattering experiments are shown as dots. The adiabatic bond charge model shows an excellent agreement with the data. When comparing Fig. 2.6 **(A)** and **(B)**, one can spot the LO and TO mode shown in **(A)** in the left part of **(B)**: Starting from the Γ-point on the very bottom left towards the X-point are the Δ-phonons. At the X-point the modes Δ_1 and Δ_2' meet in X_1; these are the LA and LO modes, respectively.

If the dynamics of the lattice are quantised analogous to the quantisation of the frequency spectrum of the black body radiation, the oscillation modes of the lattice with a frequency $\omega(\boldsymbol{q})$ have energies $\left(n + \frac{1}{2}\right)\hbar\omega(\boldsymbol{q})$. Here, n is the population number of the oscillation with wave vector $\boldsymbol{q}$. Phonons are the quanta of the oscillation field of a crystal, i.e. the oscillation modes of the atoms. They can be considered as quasi-particles with momentum $\boldsymbol{p} = \hbar\boldsymbol{q}$ and energy $E = \hbar\omega$, disregarding the zero-point energy.

Contrary to many other solids, the outstanding thermal conductivity of diamond is mediated almost entirely by phonons. Diamond has the highest known thermal conductivity for temperatures above ∼100 K. Pure specimen have a conductivity of $25\,\mathrm{Wcm^{-1}K^{-1}}$, ^{12}C enriched samples reach even $33\,\mathrm{Wcm^{-1}K^{-1}}$. The high thermal conductivity is rendered possible by the high phonon velocity in diamond: Longitudinal (Transversal) modes propagate with $v_{\mathrm{ph,l}} = 1.75{\times}10^6\,\mathrm{cm/s}$ ($v_{\mathrm{ph,t}} = 1.28{\times}10^6\,\mathrm{cm/s}$). $v_{\mathrm{ph,l}}$ corresponds to the velocity of sound in a medium.

(A) (B)

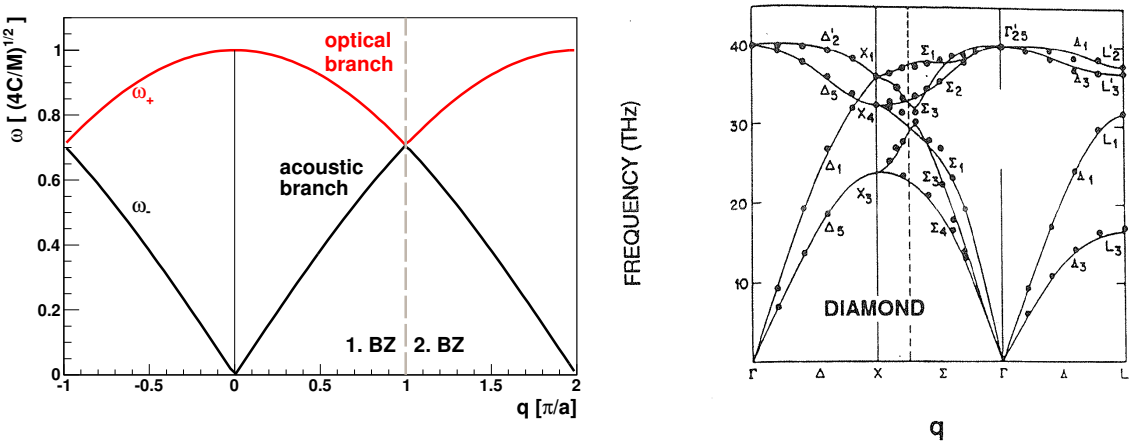

Figure 2.6.: The dispersion relation of the longitudinal lattice vibrations for a crystal lattice with a two-atomic single element basis **(A)**. On the right **(B)**, the calculated (solid lines) branches are shown along crystallographic axes. Data points from neutron scattering measurements are shown as dots. (from [14])

2.2.5. Crystal defects and impurities

The arrangement of atoms within a real crystal can differ from the ideal situation, i.e. atoms can be found displaced from their lattice site, or lattice sites remain empty. But this is not the only option for a distortion of the periodicity. During the synthesis of the crystal, the presence of foreign atoms in the deposition plasma, which can never be completely avoided, leads to the deposition of such foreign atoms in the crystal lattice.[2] Another possibility to create defects is the irradiation of diamond with energetic particles. Distortions of the periodicity of the lattice are called crystal defects. All defects distort the periodicity of the lattice and therefore the periodicity of the potential. This has an influence on the electronic and phononic transport properties of the lattice. The defects are classified in different classes: line defects, planar defects, bulk defects, and point defects:

- Line defects are defects, where e.g. a crystal plane stops within the crystal. The adjacent planes above and below the one in question then do not continue coplanar, but have to bend slightly around the line defect.
- Grain boundaries are classified as planar defects. When two crystal seeds meet during the crystal growth, the crystallographic direction of the lattice changes abruptly. These grain boundaries are abundant in polycrystalline diamond and many electrical and optical properties depend on their concentration. Another example of a planar defect are stacking faults. The hexagonal close-packed (hcp) structure differs from the fcc structure only in stacking order. If the first layer A has a second layer B above it, the atoms will not be exactly on top of each other, but the centre of the atoms from layer B are in the centre of a triangle formed of three atoms from layer A. The third layer in an hcp crystal will be exactly on top of A, and the structure evolves as ABABAB. But in the fcc configuration the third layer is in a different position with the layers being parallel to the (111) planes of the fcc unit cell and only the forth

[2]The synthesis of diamond itself will be discussed later.

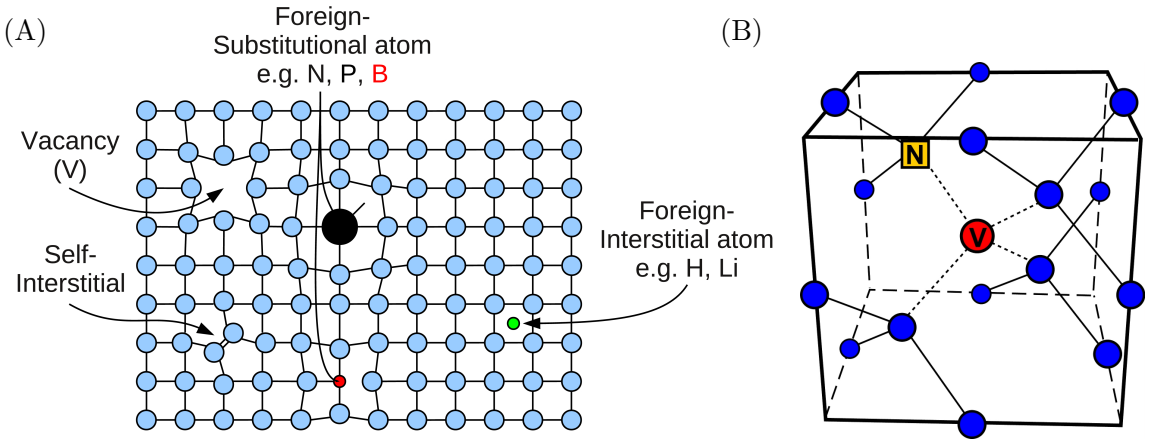

Figure 2.7.: **(A)** Different types of point defects in diamond are shown schematically. (based on [14]) **(B)** Additionally, the atomic structure of the nitrogen-vacancy centre is shown as a special type of a combined point defects. (from [21])

layer will be exactly on top of layer A again. A stacking fault in diamond could then be a stacking as ABCABCABABCABC.

- Bulk defects are regions in the bulk where many defects, e.g. vacancies, are found, or where impurities cluster. The occurrence of these bulk defects depend on the growth process on the one hand, and on the other of the mobility of defects in the bulk. In turn, the mobility of defects depends on the considered solid. A special type of bulk defects is the presence of graphite inclusions in diamond. Since the diamond configuration of the lattice is not the energetically preferred configuration, it is difficult to avoid the nucleation of carbons atoms at graphite lattice sites, and hence grown as well as natural diamond specimens always contain a certain percentage of graphite. When bulk defects extend from one surface to the other they can drastically change the electric behaviour of a certain specimen.

- Point defects, as the name suggests, are defined as zero-dimensional defects, that involve usually only one or two lattice sites. For historical reasons, they are also called *centres*, e.g. colour centres, nitrogen-vacancy centres, etc. The different types of point defects are explained below. A schematic illustration of various types of point defects is given in Fig. 2.7 **(A)**.

Many important electronic and optical properties of diamond depend on the presence, and hence concentration, of point defects. Point defects can be intrinsic – with carbon atoms misplaced from their regular lattice site –, or extrinsic involving foreign atoms, or the combination of the two. Vacancies in diamond are point defects, where a carbon lattice site is not occupied by a carbon atom. The nearest neighbours are therefore missing a binding partner and move closer towards the vacancy. A self-interstitial in diamond is an additional carbon atom within a cell. As there is no free lattice site, the additional atom leads to a distorted arrangement in its vicinity. Foreign atoms can occur on either substitutional or interstitial sites. Foreign-interstitial atoms are impurities that do not occupy a carbon lattice site. Group III elements like boron on substitutional sites create acceptor states in the band structure, since one nearest carbon neighbour will be left without an electron to form a covalent bond. Group V elements like nitrogen and phosphor have five valence

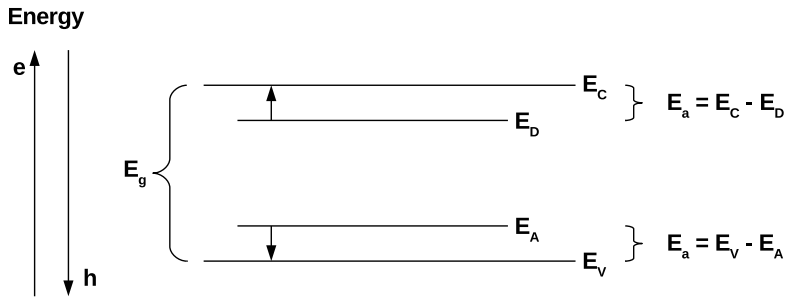

Figure 2.8.: The energy levels of donor and acceptor levels within the band gap are shown schematically. Note the that hole energy increases downwards.

electrons. On substitutional sites, four electrons are used to form covalent bonds. The fifth "dangling" electron forms a donor state. The acceptor and the donator state can be excited to the valence or the condition band, respectively, under external energy supply. This activation energy E_a is smaller than the band gap, but still of the order of at least a few hundred millielectronvolt in diamond. Prominent examples in diamond are boron (0.37 eV) [22], nitrogen (1.7 eV) [23], and phosphor with reported activation energy ranging from as low as 0.05-0.2 eV to as high as 0.84-1.16 eV [24]. Figure 2.8 schematically shows a donor and an acceptor level in the band gap, and their respective activation energies.

Of considerable interest are so called N-V centres in diamond, i.e. a substitutional nitrogen atom paired with a vacancy site, see Fig. 2.7 **(B)**. These N-V centres are electrically and optically active. Electron spins at N-V centres are well defined and sensitive to electric and magnetic fields, and light. They are therefore adjustable and can be read via lasers. Spin coherence times are approaching one second [25] making N-V centres a very interesting candidate for quantum computing using the electron spin as a qbit.

In the following, the wave function and energy levels of donor states are discussed within the Effective Mass Theory (EMT). The EMT has been developed and in detail been described by Kohn [26]. In the present work, the compilation of the basic ideas as outlined in Ref. [12] is followed. This will later on be important in order to understand the so-called inter-valley scattering of electrons. The donor atom, often a group V element, introduces an electron state in the forbidden zone between the CBM and the VBM. In order to describe the wave function of this state, the potential $\psi(\boldsymbol{r})$ of the donor is assumed to be local and of Coulomb character sufficiently far from the centre of the donor: $\psi(\boldsymbol{r}) = \psi(r) = -\frac{e}{4\pi\varepsilon_0\varepsilon_r}\frac{1}{r}$. The Schrödinger Equation is then

$$\left[-\frac{\hbar^2}{2m_e}\nabla^2 + V(\boldsymbol{r}) + e\psi(r)\right]\chi(\boldsymbol{r}) = E_\mathrm{i}\chi(\boldsymbol{r}) \tag{2.11}$$

with the lattice potential $V(\boldsymbol{r})$. The defect wave function is then expanded in terms of the known electron wave functions $\phi_\mathrm{n}(\boldsymbol{r},\boldsymbol{k})$ of the undoped crystal, see Eq. (2.3),

$$\chi(\boldsymbol{r}) = \sum_{\mathrm{n,k}} A^*_{\mathrm{n,k}}\phi_\mathrm{n}(\boldsymbol{r},\boldsymbol{k}) \tag{2.12}$$

with the band index n and the expansion coefficients $A^*_{\mathrm{n,k}}$. For an analytic calculation, only one band, the conduction band (n = 1), and a small region around the CBM in $\boldsymbol{k}$-space are considered ($\boldsymbol{k} = 0$ for direct and $\boldsymbol{k} - \boldsymbol{k}_0 = 0$ for indirect semiconductors). With almost continuous $\boldsymbol{k}$-values the spectral function $A(\boldsymbol{k})$ is defined as $A(\boldsymbol{k}) = A^*(\boldsymbol{k})/|\Delta\boldsymbol{k}|$. For its

Fourier transform $F(\boldsymbol{r}) = \int A(\boldsymbol{k}) \exp(i\boldsymbol{k}\cdot\boldsymbol{r})\,\mathrm{d}^3k$, one can show that under the assumption of a strongly localised potential the intrinsic solutions of the undoped crystal generate the conduction band with an effective dispersion relation $E(\boldsymbol{k}) = \hbar^2\boldsymbol{k}^2/2m^*$. For the Fourier transform the "Effective Mass" Schrödinger Equation remains

$$\left[-\frac{\hbar^2}{2m^*}\nabla^2 - \frac{e^2}{4\pi\varepsilon_0\varepsilon_r}\frac{1}{r}\right] F(r) = E_\mathrm{i} F(r), \tag{2.13}$$

which is identical to the Schrödinger Equation of the hydrogen atom scaled with ε_r and m^* rather than m_e. The energy E_i in Eq. (2.13) relates to the excitation from the ground state of the defect to the conduction band, just as in the case of the hydrogen atom the energy relates to the excitation from the ground state to the vacuum. The eigenvalues of Eq. (2.13) are those of the hydrogen atom scaled with the dielectric constant of the medium and the effective mass

$$E_\mathrm{i,n} = -\frac{1}{\varepsilon_r^2}\frac{m^*}{m_e}\frac{R_\mathrm{y}}{\mathrm{n}^2} \tag{2.14}$$

with $n = 1, 2, 3, ...$ and the Rydberg energy $R_\mathrm{y} = \frac{m_e e^4}{8\varepsilon_0^2 h^2} = 13.6\,\mathrm{eV}$. Assuming $\varepsilon_r = 5.7$ and $\frac{m^*}{m_e} \approx \frac{1}{2}$, an element independent defect activation energy of 0.2 eV is found. The order of magnitude of this value fits the situation for boron impurities, but e.g. the ground state of nitrogen impurities is not modelled correctly. A further correction for the "chemical shift" is needed. Important for now is the result of the spectral function $A(\boldsymbol{k})$. With the solutions for $F(r)$ being the scaled solutions of the hydrogen atom, the three-dimensional Fourier transform of the ground state becomes [12]

$$A(k) \propto \frac{1}{\left(\left(\frac{1}{a_0^*}\right)^2 + (k-k_0)^2\right)^2} \tag{2.15}$$

with the scaled Bohr radius $a_0^* = \frac{4\pi\varepsilon_0\varepsilon_r\hbar^2}{e^2 m^*}$. The energy of the ground state can then be written as $E_\mathrm{i,1} = E_\mathrm{i} = -\frac{\hbar^2}{2m^*}\frac{1}{(a_0^*)^2}$. The width of the spectral function $\Delta k = 2/a_0^*$, which is defined over the 1/4-values if the maximum, therefore depends on E_i as $\Delta k \propto \sqrt{E_\mathrm{i}}$. In other words, the deeper the ground state of the impurity the broader is the state in $\boldsymbol{k}$-space, which can have a strong effect on scattering processes. Processes that usually require a $\boldsymbol{k}$-momentum conserving phonon can occur efficiently in doped crystals, where the impurities provide the momentum conservation. [12]

2.2.6. Population statistics

For the calculation of the population statistics, i.e. the density of populated states in the conduction/valence band, two ingredients are necessary: (1) the distribution function and (2) the density of states. In order to define the distribution function easily, first the Fermi energy has to be defined. The following is based on the comprehensive descriptions given in [12] and [13].

The chemical potential μ is an intensive thermodynamic property characterising the *representative one-particle energy* within an ensemble of N particles with total energy E_tot. It is given by the fundamental thermodynamic relation of the internal energy U:

$$\mathrm{d}U = T\mathrm{d}S - p\mathrm{d}V + \sum_i \mu_i \mathrm{d}N_i \tag{2.16}$$

Here, S is the entropy and different particle types are denoted with i. At constant volume and constant entropy the chemical potential is

$$\mu_i = \frac{\partial U_i}{\partial N_i}. \tag{2.17}$$

The total derivative of the free energy $F := U - T \cdot S$ is

$$\mathrm{d}F = -S\mathrm{d}T - p\mathrm{d}V + \sum_i \mu_i \mathrm{d}N_i. \tag{2.18}$$

In thermal equilibrium ($\mathrm{d}F = 0$) and at constant temperature and volume

$$\sum_i \mu_i \mathrm{d}N_i = 0 \tag{2.19}$$

is found. Consider now the interface between a metal and a semiconductor with number of electrons N_1 and N_2. Electrons can diffuse from the semiconductor into the metal, or vice versa. In either case $\mathrm{d}N_1 = -\mathrm{d}N_2$, and the steady-state condition $\mu_1 = \mu_2$ is found. The chemical potential is called the *Fermi energy* in semiconductor physics and is constant under steady state conditions. That is, if two materials with different chemical potential (Fermi energy) are brought in close contact, the Fermi energy in both regions equalises by the net exchange of electrons until a thermal equilibrium is reached.

In a many particle system with identical particles obeying the Pauli exclusion principle, the probability to find a particle with energy E follows a Fermi-Dirac distribution. For electrons and holes with the Fermi energy E_F this respectively is

$$f_e(E) = \frac{1}{e^{(E-E_\mathrm{F})/k_\mathrm{B}T} + 1}, \tag{2.20}$$

$$f_h(E) = 1 - f_e(E) = \frac{1}{e^{(E_\mathrm{F}-E)/k_\mathrm{B}T} + 1}. \tag{2.21}$$

For the Boltzmann approximation $E - E_\mathrm{F} \gg k_\mathrm{B}T$ ($E_\mathrm{F} - E \gg k_\mathrm{B}T$) this becomes the

$$f_e(E) = e^{-(E-E_\mathrm{F})/k_\mathrm{B}T} \qquad \text{and} \qquad f_h(E) = e^{-(E_\mathrm{F}-E)/k_\mathrm{B}T}. \tag{2.22}$$

In order to calculate the population statics, a further ingredient is needed besides the distribution function. The density of states $D(\boldsymbol{k})$, or $D(E)$, is the number of states within an interval $\Delta\boldsymbol{k}$ in $\boldsymbol{k}$-space, or equivalently $\mathrm{d}E$ in energy space, at a fixed value $\boldsymbol{k}$, or E_0. Be $D(\boldsymbol{k})\mathrm{d}\boldsymbol{k} = \frac{1}{(2\pi)^3}\mathrm{d}\boldsymbol{k}$ the number of standing waves per volume in three dimensions. In E-space at a fixed energy E_0, this becomes [12, p. 105]

$$D(E_0) = \int\limits_{1.\,\mathrm{BZ}} D(\boldsymbol{k})\delta\big(E(\boldsymbol{k}) - E_0(\boldsymbol{k})\big)\,\mathrm{d}^3k \tag{2.23}$$

or written as an integral over a constant energy surface E_0

$$D(E_0) = \int\limits_{E=E_0} D(\boldsymbol{k})\frac{\mathrm{d}^3k}{|\nabla_k E(\boldsymbol{k})|}. \tag{2.24}$$

In the case of diamond with $M = 6$ equivalent valleys and with equal energy surfaces of ellipsoidal shape, the electron density of states as a function of the energy can be written as [12, p. 153]

$$D_e(E) = \frac{1}{2\pi^2}\left(M^{2/3}\frac{2m_{\mathrm{dos},e}}{\hbar^2}\right)^{3/2}\sqrt{E - E_\mathrm{C}} \tag{2.25}$$

with the electron density of state mass

$$m_{\mathrm{dos},e} = \left(m_{e,\mathrm{l}} \cdot m_{e,\mathrm{t}}^2\right)^{1/3}. \tag{2.26}$$

Analogously to the electron case, there is a hole density of states $D_h(E)$ and a hole density of states mass $m_{\mathrm{dos},h}$, which depends on the masses of holes of two different parabolic bands: (1) the light hole mass $m_{h,\mathrm{l}}$ and (2) the heavy hole mass $m_{h,\mathrm{h}}$. According to Eq. (2.6) this corresponds to two bands featuring different degrees of curvature.

Note that the density of state masses are the mass parameters that give the correct densities of states. They are to be distinguished from the moving masses of the electron/hole in the lattice potential. With expressions for both the distribution function and the density of states, the electron and hole population densities at energy E are

$$n(E) = D_e(E) f_e(E) \qquad \text{and} \qquad p(E) = D_h(E) f_h(E). \tag{2.27}$$

The free charge carrier density is then readily calculated as the integral from the CBM to infinity [13]

$$n = \int_{E_\mathrm{C}}^{\infty} D_e(E) f_e(E) \mathrm{d}E \tag{2.28}$$

$$= \frac{2}{\sqrt{\pi}} n_{\mathrm{dos,c}} \cdot F_{1/2}\left(\frac{E_\mathrm{F} - E_\mathrm{C}}{k_\mathrm{B}T}\right). \tag{2.29}$$

$F_n(\xi)$ are the so-called Fermi-Dirac integrals and are tabulated. $n_{\mathrm{dos,c}}$ ($n_{\mathrm{dos,v}}$) is the effective conduction (valence) band density of states:

$$n_{\mathrm{dos,c}} = \frac{1}{4\pi^{3/2}}\left(\frac{2m_{\mathrm{dos},e}}{\hbar^2} k_\mathrm{B}T\right)^{3/2} \qquad \text{and} \qquad n_{\mathrm{dos,v}} = \frac{1}{4\pi^{3/2}}\left(\frac{2m_{\mathrm{dos},h}}{\hbar^2} k_\mathrm{B}T\right)^{3/2}. \tag{2.30}$$

Using the Boltzmann approximation, the free charge carrier population density are

$$n = n_{\mathrm{dos,c}} \cdot \exp\left(\frac{E_\mathrm{F} - E_\mathrm{C}}{k_\mathrm{B}T}\right) \qquad \text{and} \qquad p = n_{\mathrm{dos,v}} \cdot \exp\left(\frac{E_\mathrm{V} - E_\mathrm{F}}{k_\mathrm{B}T}\right). \tag{2.31}$$

for electrons and holes, respectively. The product of n and p is the *Law of mass action*

$$n \cdot p = n_{\mathrm{dos,c}} n_{\mathrm{dos,v}} \cdot \exp\left(\frac{-E_\mathrm{g}}{k_\mathrm{B}T}\right), \tag{2.32}$$

and depends only on the temperature and the band gap E_g for a given semiconductor.

Intrinsic charge density In the case of intrinsic diamond with zero impurities ($n = n_i$ and $p = p_i$), for each thermally excited electron there is exactly one hole remaining in the valence band. Therefore neutrality yields $n_i = p_i$. Using the Law of mass action the free charge carrier density is then [13]

$$n_i = \sqrt{n_{\mathrm{dos,c}} \cdot n_{\mathrm{dos,v}}} \cdot \exp\left(-\frac{E_\mathrm{g}}{2k_\mathrm{B}T}\right). \tag{2.33}$$

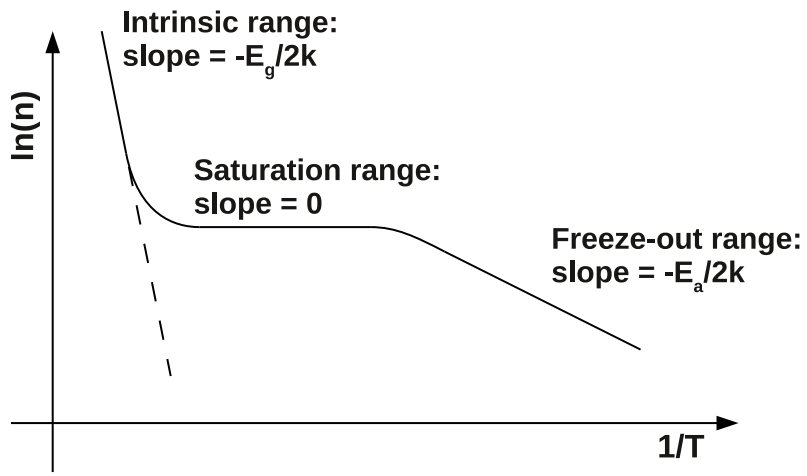

Figure 2.9.: The Arrhenius plot of the free carrier concentration is plotted over a wide temperature range. (based on [27, 12])

For intrinsic diamond with $n_{\mathrm{dos,c}} \approx 10^{20}\,\mathrm{cm}^{-3}$, $n_{\mathrm{dos,v}} \approx 10^{19}\,\mathrm{cm}^{-3}$, $E_{\mathrm{g}} = 5.47\,\mathrm{eV}$, the intrinsic charge density at 300 K is $n_i \approx 10^{-27}\,\mathrm{cm}^{-3}$. A sample of volume $V = 0.5\,\mathrm{cm} \times 0.5\,\mathrm{cm} \times 0.05\,\mathrm{cm}$ would then contain $10^{-29} \approx 0$ free electrons. In the real world intrinsic diamond does not exist. It is clear that the free charge carrier density in real diamond at RT is dominated by impurities.

Extrinsic charge density The activation energy E_{a} of donor and acceptor states was discussed within the EMT model, and was much smaller than the band gap. This has a strong effect on the free charge carrier density, as in the singly doped case (only acceptors or only donors) [13]

$$n \text{ or } p \propto \exp\left(-\frac{E_{\mathrm{a}}}{2k_{\mathrm{B}}T}\right) \tag{2.34}$$

with the activation energy E_{a} replacing E_{g} in the intrinsic case. Here, the Fermi-energy is shifted upwards and lies between E_{C} and donor level E_{D}, or between E_{V} and the acceptor energy E_{A} in the case of acceptor doping. In the mixed case, where both donors and acceptors are present in the crystal, the Fermi-energy remains around the centre of the gap if the temperature is low enough for both impurities to not be completely ionised, and [13]

$$n \text{ or } p \propto \exp\left(-\frac{E_{\mathrm{a}}}{k_{\mathrm{B}}T}\right). \tag{2.35}$$

Combining the intrinsic case with the only p-doped or the only n-doped case, the free carrier concentration over a wide temperature range is depicted in Fig. 2.9. On the abscissa the inverse temperature is plotted, on the ordinate the natural logarithm of the free charge carrier density. This is called the Arrhenius plot. Starting on the right hand side the charge density increases with increasing temperature (to the left), as more carriers from donors or acceptors are excited to the conduction or valence band. When all impurities are excited, the charge density reaches a plateau and remains constant. On the left hand side, at even higher temperatures, the intrinsic population dominates.

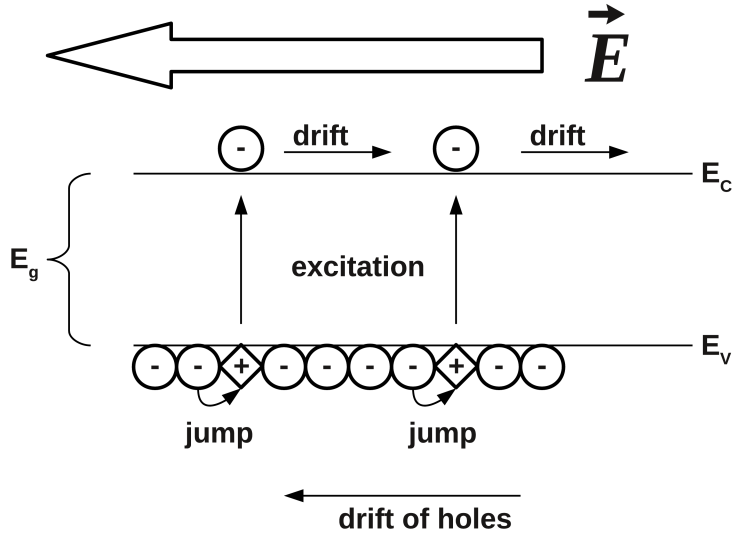

Figure 2.10.: Concept of free charge carrier drift in semiconductors. (based on [12, p. 17])

2.2.7. Electrical conductivity and transport

Electrical conductivity in intrinsic semiconductors arises only when electrons are excited from the valence band to the conduction band: At absolute zero, electrons in the fully occupied valence band cannot add to conduction as this would imply an increase in (kinetic) energy, whilst there are no free energetically higher states in this band. Additionally, an increase in kinetic energy is only possible under energy supply, which corresponds to an increase in temperature. At temperatures above absolute zero, electrons can be excited thermally to the conduction band leaving behind unoccupied states in the valence band. Without an electric field, each electron trajectory is a thermal "random walk", with no effective net velocity. Under the influence of an electrical field, the electron drifts along the electric field lines resulting in a net non-zero velocity component.

The vacant state in the valence band from an excited electron results in another type of conductivity: Electrons from neighbouring covalent bonds can "jump" into this vacant state, leading to a propagation of the vacant state in the opposite direction of the electron transport. This conduction can formally be described by formulating the entirety of the $\sim 10^{23} - 1$ electrons in the valence band. A more economic and practical way offers a single-particle representation of the vacant state, called *hole*. [12] This hole has a positive charge of $+e$. Figure 2.10 illustrates the concept of electron and hole drift.

Net charge transport in semiconductors happens in non-equilibrium situations, e.g. when free charge carriers are created locally under local energy supply with subsequent relaxation via diffusion to an quasi-equilibrium state with uniform distribution of free charge carriers over the crystal. Charge transport of free charge carriers occurs, of course, also under the influence of an externally applied electric field. In the equation of motion for the electron, external forces as electric fields as well as internal forces as e.g. the resulting force from the lattice potential, need to be accounted for. As described above, the mass of an electron within a periodic potential is replaced by an effective mass m^*, but the "lattice forces" of a perfect lattice without oscillations do not result in a resistance upon the electron. Imperfections and the presence of phonons result in scattering of the electrons. In the Drude model [28] the electron equation of motion under the influence of an externally applied electric field is

Table 2.2.: Low-field mobility values in $\mathrm{cm}^2/\mathrm{Vs}$ for various materials.

material	electron mobility	hole mobility
diamond	1800[a]	2500[a]
Si	1500[b]	450[b]
GaAs	8500[b]	320[b]

[a] measured herein [b] cf. Ref. [13]

$$m_e^* \left(\ddot{\boldsymbol{r}} + \frac{\dot{\boldsymbol{r}}}{\langle \tau_\mathrm{R} \rangle} \right) = e\boldsymbol{E}. \tag{2.36}$$

Here, different possible scattering mechanisms are combined in a single effective momentum relaxation time τ_R, or scattering time. In the steady-state ($\ddot{\boldsymbol{r}} = 0$), this leads to

$$\boldsymbol{v_e} = \frac{e \langle \tau_{\mathrm{R},e} \rangle}{m_e^*} \boldsymbol{E} = \mu_e \boldsymbol{E}, \qquad \text{with} \qquad \mu_e := \frac{e \langle \tau_{\mathrm{R},e} \rangle}{m_e^*}. \tag{2.37}$$

and equivalently $\mu_h := \frac{h \langle \tau_{\mathrm{R},h} \rangle}{m_h^*}$ for holes.[3] In this model, the mobility is independent of the electric field strength, and it is only valid for low field strengths ($E < 10^4\,\mathrm{V/cm}$ or $E < 1\,\mathrm{V/\mu m}$). The order of magnitude of the momentum relaxation time can be inferred from measured mobility values: with $\mu \approx 2000\,\mathrm{cm}^2/\mathrm{Vs}$ and $m^* \approx m_e$, it is found that $\tau_\mathrm{R} \approx 1\,\mathrm{ps}$. With electron and hole charge densities n_e and n_h, respectively, the current densities are

$$j_e = e v_e n_e \qquad \text{and} \qquad j_h = h v_h n_h \tag{2.38}$$

and the total current density is [17]

$$\boldsymbol{j} = \boldsymbol{j}_e + \boldsymbol{j}_h = (e\mu_e n_e + h\mu_h n_h)\, \boldsymbol{E} \equiv \sigma \boldsymbol{E}, \tag{2.39}$$

which is Ohm's law for semiconductors. The conductivity σ is proportional to the mobility. Common values of the low-field mobility are listed in Tab. 2.2. Drift mobility values in diamond for both carrier types, electrons and holes, in scCVD diamond samples vary significantly in the literature. Their values have been reported to be $\sim 2300\,\mathrm{cm}^2/\mathrm{Vs}$ for holes and $\sim 1700\,\mathrm{cm}^2/\mathrm{Vs}$ for electrons using α-induced currents [29], and 2000 to $2250\,\mathrm{cm}^2/\mathrm{Vs}$ for holes and 2200 to $2750\,\mathrm{cm}^2/\mathrm{Vs}$ for electrons using laser induced currents [30]. Isberg et al. reported a hole mobility value as high as $\mu_h = (3400 \pm 400)\,\mathrm{cm}^2/\mathrm{Vs}$. [31]

In Sec. 2.2.6 the intrinsic free carrier concentration n_i at room temperature was derived. It is therefore clear that the intrinsic conduction of diamond is negligible. The conductivity of real diamond crystals must therefore arise from either doping – i.e. deliberately incorporated impurities –, unintentional impurities, and/or defects. The temperature dependence of their carrier densities were also discussed in Sec. 2.2.6.

The different scattering mechanisms and their temperature dependence are now discussed. With the mobility as defined in Eq. (2.37), its temperature dependence emerges from the temperature dependence of the momentum relaxation time. The brackets denote an average

[3] e is the charge of the electron, h the charge of the hole: $\mp 1.6 \times 10^{-19}\,\mathrm{C}$.

over the energy distribution of the carriers. The relaxation time is often a polynomial function of the carrier energy with $\tau_\mathrm{R} = \tau_0 (\xi/k_\mathrm{B}T)^r$ with the kinetic energy ξ of the carrier. At low fields, and moderate temperatures, it is the acoustic phonon scattering and the ionised impurity scattering that dominates the mobility. At high fields, the emission of optical phonons becomes relevant and limits the carrier velocity. Towards low temperatures, the neutral impurity scattering can play an important role. For electrons, as well the intervalley scattering is important, as will be discussed in Chap. 5. If various independent scattering processes contribute to the total scattering, according to Matthiesson's rule their momentum relaxation time add inversely to a combined momentum relaxation time; the same holds true for the combined mobility: [32, 33]

$$\tau_\mathrm{R}^{-1} = \sum_i \tau_i^{-1}, \qquad \text{and} \qquad \mu^{-1} = \sum_i \mu_i^{-1}. \tag{2.40}$$

Acoustic phonon scattering No explicit calculation shall be given here, but can be found in Ref. [34]. Thermalised carriers have wavelengths much longer than the lattice constant and therefore scatter only with long wavelength phonons. The longitudinal long wavelength phonons are waves leading to compression or extension of the crystal lattice, which in turn affects the band edge locally. A non-constant band edge over position space introduces potential barriers off which the carriers scatter. The scattering time is inversely proportional to the temperature $\tau_\mathrm{R} \propto T^{-1}$. The temperature dependence of the mobility resulting from acoustic phonon (APS) scattering reads

$$\mu_\mathrm{APS} \propto T^{-3/2}. \tag{2.41}$$

The exponent of $-3/2$ emerges from the average over the energy distribution of the carriers. Experimental values for temperatures between 2 K and room temperature in diamond are presented in Chap. 5.

Ionised impurity scattering If impurities are thermally ionised, these impurities create stationary Coulomb-like potentials in the lattice. With increasing carrier energy, the scattering cross-section decreases. The resulting mobility of the ionised impurity scattering (IIS) can be written as [35]

$$\mu_\mathrm{IIS} \propto \frac{1}{n_\mathrm{ii}(T)}\, T^{3/2}. \tag{2.42}$$

With the exponent being $+3/2$ it can be easily distinguished experimentally from the APS. Note that the IIS is inversely proportional to the ionised impurity density n_ii. Towards lower temperatures n_ii decreases, see Fig. 2.9.

Neutral impurity scattering Neutral impurity atoms, i.e. foreign atoms that are not ionised, do not exhibit a Coulomb-like potential, but distort the lattice potential locally. Under the assumption of hydrogenic energy states of the impurity, Erginsoy [36] derived a temperature independent scattering time τ_R. Therefore $\langle\tau_\mathrm{R}\rangle = \tau_\mathrm{R}$ and the mobility is independent of the temperature, too:

$$\mu_\mathrm{NIS} \propto \frac{1}{n_\mathrm{n}}\, T^0. \tag{2.43}$$

As in the case of the IIS, the NIS is inversely proportional to the neutral impurity density n_n. With increasing temperature, neutral impurities ionise, and the neutral impurity density

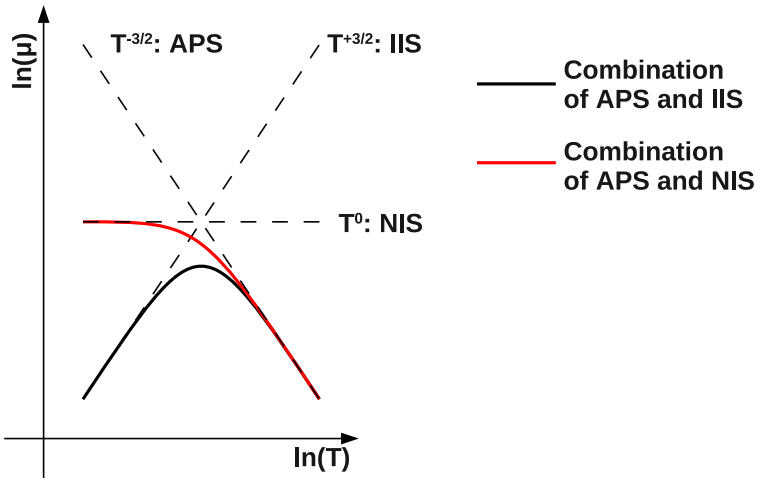

Figure 2.11.: The temperature dependence of different combinations of scattering mechanisms is shown on double-logarithmic scales, cf. as well [13, 12].

therefore decreases with increasing temperature. Other authors derived corrections to the approach followed by Erginsoy. [37, 38]

A graphical visualisation of the temperature dependence of the mobility combining the three aforementioned scattering mechanisms is shown in Fig. 2.11.

Intervalley scattering As was discussed in Sec. 2.2.3 diamond is a multivalley semiconductor with six equivalent conduction band minima. Under certain conditions electrons can scatter from one valley to another. If the valley into which the electron scatters is on the same $\boldsymbol{k}$-axis, the scattering is called *g-type*. When an electron is scattered into an orthogonal valley, it is called *f-type*, cf. illustration in Fig. 2.12. For this either a $\boldsymbol{k}$-momentum conserving phonon is required, or the momentum has to be absorbed by the impurities in the crystal [12], cf. the spectral function of impurities (Eq. (2.15)). A net flux from longitudinal valleys to orthogonal valleys, or vice versa, is called re-population. A re-population can change the average mobility – average over different valleys – and hence the drift velocity of free carriers owing to the different effective masses in the different valleys. The re-population effect can therefore be seen in the transit time of carriers, if the effect is sufficiently large.

Velocity saturation Electrons that are accelerated in an electric field gain energy. At low fields the energy gain is sufficiently small in order for the carrier energy to remain close to the thermal equilibrium value of $3/2\, k_\mathrm{B} T$. However, with increasing field strength the energy gain in between two scattering processes is large enough for the carrier to undergo inelastic scattering. In contrast to elastic scattering processes like the APS, IIS, and NIS, an inelastic process changes the energy of the carrier. First, the carrier stimulates acoustic phonon modes and the carrier temperature over the lattice temperature becomes

$$\frac{T_e}{T} = \frac{1}{2}\left(1 + \sqrt{1 + \frac{3\pi}{8}\left(\frac{\mu_0 E}{v_\mathrm{sound}}\right)^2}\right). \tag{2.44}$$

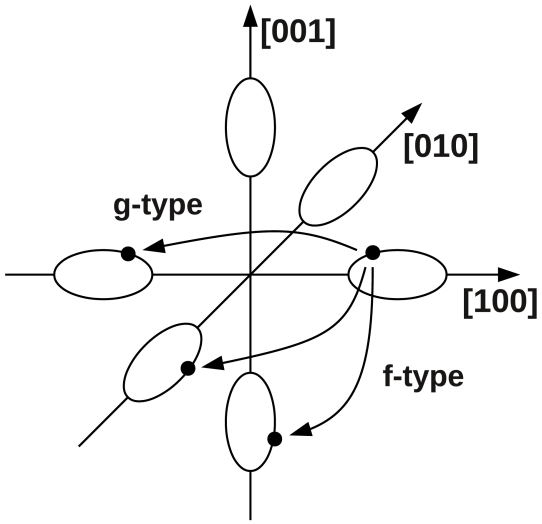

Figure 2.12.: The two different types of intervalley scattering are shown. f-type (g-type) is a scattering process into an orthogonal (parallel) valley. [39, 12]

The drift velocity scales with the square root of the ratio [40]

$$\mathrm{v}^{e}_{\mathrm{drift}} = \sqrt{\frac{T_e}{T}}\mu_0 E. \tag{2.45}$$

With further increasing fields, the carrier energy surpasses the optical phonon energy of $E_{\mathrm{opt}} = 163\,\mathrm{meV}$ in diamond leading to a velocity saturation. Within a simple model, the saturation velocity is [41]

$$\mathrm{v}_{\mathrm{sat}} = \sqrt{\frac{8E_{\mathrm{opt}}}{3\pi m_{\mathrm{dos}}}\tanh\left(\frac{E_{\mathrm{opt}}}{2kT}\right)}. \tag{2.46}$$

At temperatures tested in this work, $\tanh(...) \approx 1$. With $m_{\mathrm{dos}} \approx 0.5$ the above estimate yields $\mathrm{v}^{e}_{\mathrm{drift}} \approx 2.2{\times}10^6\,\mathrm{cm/s}$. Ferry [42] calculated a saturation velocity of $2.3{\times}10^6\,\mathrm{cm/s}$ at fields larger than $2 - 3\,\mathrm{V/\mu m}$ by solving the Boltzmann transport equations, taking into account various scattering processes. The result from Monte Carlo simulations by Osman [43] differs from Ferry's result and predicts a saturation velocity of $1.5{\times}10^6\,\mathrm{cm/s}$ at $10\,\mathrm{V/\mu m}$. In Chap. 5 the measured saturation velocity is discussed including its temperature dependence.

Effective drift velocity model According to a simple model [44], the drift velocity over a large field range is can be described as

$$\mathrm{v}_{\mathrm{drift}}(E) = \mu(E)E = \frac{\mu_0 E}{1 + \dfrac{\mu_0 E}{\mathrm{v}_{\mathrm{sat}}}}\,, \tag{2.47}$$

where μ_0 is the low-field mobility. The model reduces to the Drude model at low fields ($\mu(E) \xrightarrow{E\to 0} \mu_0$) and accounts for a saturation velocity $\mathrm{v}_{\mathrm{sat}}$ towards high fields. Details as the intervalley scattering are not accounted for therein.

2.2.8. Non-equilibrium processes

If a system is in thermal equilibrium then its carrier distribution is described by a single Fermi energy E_F. However, there are many interesting non-equilibrium cases, which deserve a closer inspection. Non-equilibrium situations in semiconductors can usually be treated making use of subsystems which themselves are in thermal equilibrium, but are not in equilibrium with each other. [12] Consider a semiconductor in thermal equilibrium, that is $n_i^2 = np$. When free charge carriers are created locally via external energy input, electrons are excited into the conduction band, though not necessarily to the band edge, but to any free state in the conduction band depending on the energy transferred to the considered electron. The electrons then thermalise via intra-band scattering processes to the band edge with a relaxation time of the order of $\tau_\mathrm{relax} \approx 10^{-13}\,\mathrm{s}$ losing their kinetic energy to phonons. The electron system is then in thermal equilibrium, but it is not with the hole system. In this situation quasi-Fermi energies E_F^e and E_F^h define the chemical potential for the two subsystems of electrons and holes, respectively. The difference $\Delta E_\mathrm{F} = E_\mathrm{F}^e - E_\mathrm{F}^h$ expresses the amount of disturbance of the equilibrium. [12] Recombination, diffusion, and other processes bring the system back to thermal equilibrium. Edge-to-edge recombination involve either $\boldsymbol{k}$-momentum conserving phonons or momentum absorbing impurities, and depending on their abundance recombination lifetimes are of the order of $\tau_\mathrm{life} \approx 10^{-9}...10^{-3}\,\mathrm{s}$. Therefore the excited carriers will first thermalise and reach an quasi-equilibrium state, and then recombine subsequently.

The generic case of charge transport in semiconductors is described by three sets of equations: (1) the Poisson equation, (2) the transport equations, and (3) the continuity equations, c.f. e.g. [13, 12]

$$\triangle\phi = -\frac{\rho}{\varepsilon_r \varepsilon_0} \tag{2.48}$$

$$\begin{aligned} \boldsymbol{j}_e &= e\mu_e n\boldsymbol{E} - e\boldsymbol{\nabla}(D_e \cdot n) \\ \boldsymbol{j}_h &= h\mu_h p\boldsymbol{E} - h\boldsymbol{\nabla}(D_h \cdot p) \end{aligned} \tag{2.49}$$

$$\begin{aligned} \frac{\partial n}{\partial t} &= G_{n_e} - R_{n_e} - \frac{1}{e}\boldsymbol{\nabla} \times \boldsymbol{j}_e \\ \frac{\partial p}{\partial t} &= G_{n_h} - R_{n_h} - \frac{1}{h}\boldsymbol{\nabla} \times \boldsymbol{j}_h \end{aligned} \tag{2.50}$$

with the electrostatic potential ϕ, the charge density ρ, the dielectric constant ε_r, the vacuum permittivity ε_0, the diffusion constants D_e and D_h for electrons and holes, respectively, and the carrier generation and recombination rate G and R. The Poisson equation follows readily from the Maxwell equations. The first term in the transport equations is the field induced current, as discussed in Sec. 2.2.7, the second one is the diffusion current induced by a non-zero concentration gradient. In the continuity equations, the last term is the spatial transport rate. Starting from these equations, the reaction of the system on a local perturbation of a previous equilibrium and its tendency to go back to an equilibrium can be expressed. Under certain conditions the equations can be solved analytically. The reduction of perturbation happens over time via e.g. recombination processes or dielectric relaxation, and over space via transport or displacement of charges including polarisation. Explicit calculations of the characteristic lengths and times of these relaxation processes shall not be given here, but only their results: [12, p. 193f]

- The dielectric relaxation time: $\tau_\mathrm{diel} = \frac{\varepsilon_0 \varepsilon_r}{e\mu n}$, about $\sim 10^{-13}\,\mathrm{s}$. It is the temporal relaxation time constant for electron (hole) density disturbance in n-doped (p-doped) semiconductors.

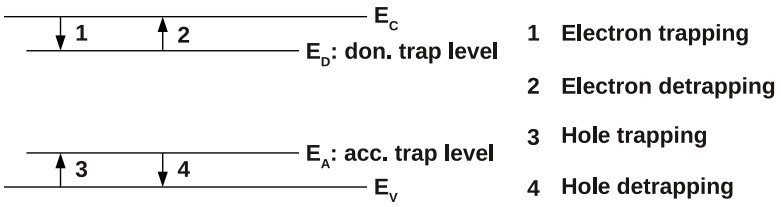

Figure 2.13.: Different types of trapping and thermal detrapping processes are shown.

- The Debye length: $\lambda_{\mathrm{Debye}} = \sqrt{\frac{\varepsilon_0 \varepsilon_r k_{\mathrm{B}} T}{e^2 n}}$. This is the spatial relaxation constant for a stationary disturbance, i.e. the screening length.
- The recombination time or lifetime: τ_{rec}, more details below.
- The diffusion length: $L = \sqrt{D\tau_{\mathrm{rec}}}$. The diffusion length describes the spatial relaxation of the disturbance via diffusion within the recombination time.
- The drift length: $L_{\mathrm{drift}} = \mu\tau_{\mathrm{rec}}|E|$. The drift length describes the spatial relaxation of the disturbance via drift within the recombination time.

Trapping and recombination processes Impurities and other imperfections of the crystal create energy levels within the band gap. Spatially seen, these levels resides at the impurity/imperfection. A free electron, or hole, approaching such sites can be "trapped" by them, resulting in a locally bound electron, or hole, at these trapping sites. They are therefore also called trapping centres. The inverse process is also allowed, i.e. after a certain time the trapped charge is excited, i.e. "detrapped" from the trap by thermal excitation. In thermal equilibrium the rates of trapping and detrapping are equal. For a system out of thermal equilibrium, i.e. $n_i^2 \neq np$, trapping processes help to restore the thermal equilibrium. Without a formal derivation, the carrier trapping times are [13]

$$\tau_{e,h} = \frac{1}{\sigma_{e,h} v_{\mathrm{th}} n_{\mathrm{trap}}} \tag{2.51}$$

with the trap density n_{trap}, the thermal velocity $v_{\mathrm{th}} \approx \sqrt{\frac{3k_{\mathrm{B}}T}{m^*}}$ and the capture cross-section for electrons or holes $\sigma_{e,h}$. The formula is plausible: (1) For higher trap densities the trapping time decreases as it is more likely that within a given time, a charge undertaking thermal movement passes close enough to a trapping centre and is trapped. (2) With higher capture cross-section the trapping is more likely. (3) With higher thermal velocity a charge covers a longer distance within a given time and is hence more likely to be trapped. Trapped electrons can either detrap or even recombine with a hole in the valence band. The detrapping time constant depends exponentially on the lattice temperature

$$\tau_{e,h}^{\mathrm{dt}} = \frac{\exp\left(E_{\mathrm{a}}/k_{\mathrm{B}}T\right)}{\sigma_{e,h} v_{\mathrm{th}} n_{\mathrm{trap}}}. \tag{2.52}$$

Detrapping time constants that are of the order of pico- or nanoseconds at RT can therefore be of the order of microseconds, or even days at cryogenic temperatures. Figure 2.13 shows two trapping and two detrapping processes.

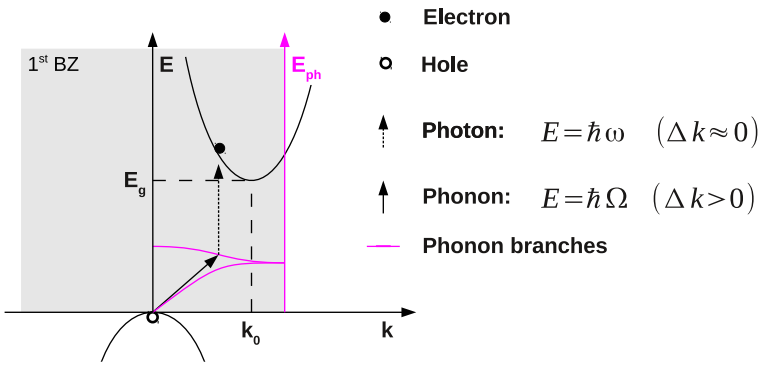

Figure 2.14.: The absorption of a photon via the excitation of an electron to the conduction band and a $\boldsymbol{k}$-momentum conserving phonon is shown. The radiative recombination is the reverse process. (from [12, p. 234])

In addition to the recombination via trapping centres radiative or non-radiative (Auger) band-to-band recombination processes are possible which involve photon emission or energy transfer to a free electron or hole, respectively. The time scale of the radiative process in diamond as a indirect semiconductor is of the order of 1 µs and is the reverse process of the photon absorption, which is shown in Fig. 2.14. The same process in direct semiconductors as e.g. GaAs are of the order of nanoseconds for equal excess carrier densities. In Auger processes a free electron recombines with a hole by transferring its energy to another free electron, or hole. The energy receiving charge therefore is excited high into the conduction/valence band. As it includes a third partner its rate is of third order: $R = C_e \cdot n^2 p + C_h \cdot p^2 n$ with the Auger coefficients C_e and C_h. [12]

2.2.9. Excitons

In 1931, Y. Frenkel proposed the existence of "excitation waves" in solids [45]. Excitons have since been observed in many semiconductors, including silicon [46] and diamond [47]. When an electron gets excited to the conduction band, it leaves behind a free electron state in the valence band, referred to as a hole. The positively charged hole and the negatively charged electron attract each other via the Coulomb force and can undergo a bonding process under the emission of a phonon into a hydrogenic state, referred to as an exciton. The energy of the two charges bound into an exciton is hence reduced by the binding energy in comparison to the free electron-hole pair, with the energy level of the electron slightly below the conduction band, as the binding energy is much smaller than the band gap. In diamond, the binding energy is $E_\mathrm{x} = (80.0 \pm 0.5)\,\mathrm{meV}$ [47] and the size is $r_x \approx 1.37\,\mathrm{nm}$, where the size is inferred from a hydrogen atom scaled with the dielectric constant and the effective mass of the exciton.

Dynamics of exitons The elementary, intrinsic excitation in semiconductors is the so-called *Wannier-Mott* exciton. Its binding energy is of the order of a few or a few tens of millielectronvolt, and its size is large compared to the nearest neighbour distance: $a_\mathrm{x} \gg a_0$. The Coulomb force between the electron and the hole constituting the exciton is screened with the dielectric constant. Under the assumption of parabolic, isotropic bands, the time independent two-particle Schrödinger equation becomes [12]

$$\left(-\frac{\hbar^2}{2m_e^*}\nabla_e^2 - \frac{\hbar^2}{2m_h^*}\nabla_h^2 - \frac{e^2}{4\pi\varepsilon_0\varepsilon_r}\frac{1}{|\boldsymbol{r}_e - \boldsymbol{r}_h|}\right)\Psi(\boldsymbol{r}_e, \boldsymbol{r}_h) = (E_{\text{tot}} - E_{\text{g}})\Psi(\boldsymbol{r}_e, \boldsymbol{r}_h). \tag{2.53}$$

The transformation into the centre-of-mass (COM) frame with the total mass $M = m_e^* + m_h^*$, the relative coordinate $\boldsymbol{r} = \boldsymbol{r}_e - \boldsymbol{r}_h$, and the COM coordinate $\boldsymbol{R} = (m_e^*\boldsymbol{r}_e + m_h^*\boldsymbol{r}_h)/M$ decouples the relative movement from the one of the centre-of-mass. The wave function factorises thus into the COM-part and the relative part: $\Psi(\boldsymbol{r}_e, \boldsymbol{r}_h) = \Psi_{\text{rel}}(\boldsymbol{r}) \cdot \Psi_{\text{COM}}(\boldsymbol{R})$. The decoupled equations stipulate hydrogenic eigenfunctions for the relative part, and standing waves for the COM part. A reduced mass m_{red} is defined as $m_{\text{red}} = (1/m_e^* + 1/m_h^*)^{-1}$. Note that the relevant effective masses of electrons and holes in all exciton formulae are the *optical* masses $m_{0,e}^*$ and $m_{0,h}^*$, which can be calculated from the density of states masses $m_{\text{dos},e}$ and $m_{\text{dos},h}$, which in turn are to be used in the actual transport problem. In diamond, the optical masses have to be carefully selected from a rather broad range of measured density of state mass values, c.f. the definitions and a discussion in Ref. [48]. The eigenvalues are

$$\begin{aligned} E_{\text{rel}} = E_{\text{x,n}} &= -\frac{1}{\varepsilon_r^2}\frac{m_{\text{red}}}{m_e}\frac{R_{\text{y}}}{\text{n}^2} \\ E_{\text{COM}} &= \frac{\hbar^2}{2M}\boldsymbol{K}^2, \end{aligned} \tag{2.54}$$

with $\boldsymbol{K} = \boldsymbol{k}_e - \boldsymbol{k}_h$. Note the similarity with Eq. (2.14). The ground state energy ($n = 1$) is the exciton binding energy $E_{\text{x},1} = E_{\text{x}} = 80\,\text{meV}$. The size of the excitons is the Bohr radius $a_0^{\text{Bohr}} = \frac{4\pi\varepsilon_0\hbar^2}{m_e e^2}$ scaled with the reduced mass and the dielectric constant: $a_{\text{x}} = \frac{m_e}{m_{\text{red}}}\varepsilon_r a_0^{\text{Bohr}} = 1.37\,\text{nm}$. [12, p. 241f]

Lifetimes The lifetime of a single, isolated exciton is governed by two competing types of processes: the thermal dissociation and the recombination. At high temperatures, the lattice provides sufficient energy to break up the exciton, i.e. excite the electron from the exciton state to the conduction band. As this is a thermodynamic effect, it is reasonable to assume, that this lifetime is directly proportional to $\exp(E_{\text{x}}/k_{\text{B}}T)$. Therefore, the thermal lifetime τ_{th} of excitons in diamond is a function of the temperature and is $\mathcal{O}(30\,\text{ps})$ at room temperature, as will be shown later. Towards lower temperatures, the thermal lifetime increases with $\exp(E_{\text{x}}/k_{\text{B}}T)$, reaching $\sim$150 µs at 50 K. The recombination lifetime of free excitons $\tau_{\text{rec}}^{\gamma}$ involving an energy-conserving UV-photon and a $\boldsymbol{k}$-conserving phonon is $\mathcal{O}(\mu\text{s})$. [49] However, photon-less recombination processes of bound excitons, e.g. bound to impurities, are considerably shorter and are $\mathcal{O}(\text{ns})$. [50] The time scale of this process is likely to be impurity density dependent. In the samples used here, the impurity density is $\mathcal{O}(\text{ppb})$ resulting in a recombination lifetime dominated by a fast photon-less recombination. Hence, the lifetime of the single, isolated exciton is dominated by the thermal lifetime at RT and by the recombination lifetime at cryogenic temperatures.

A high-density ensemble of electron-hole pairs within a confined space reaches a quasi-equilibrium with the density ratio of free e-h pairs to excitons following a Boltzmann-distribution. [51] Under these conditions, no meaningful thermal lifetime can be defined. However, if charges are dragged out of the volume via an electric field, excitons will evaporate in order to reach a new quasi-equilibrium. The evaporation lifetime τ_{evap} is not only a function of the temperature, as in the case of τ_{th}, but also of the charge flux leaving the volume. Additionally, the evaporation process is, as for τ_{th}, in competition with the recombination process. If the rate of free charges leaving the ionisation volume is larger than

Table 2.3.: The different processes involved in the decay of excitons and their order of lifetime as a function of temperature, with the dominant process for each temperature highlighted in red.

T [K]	τ_{evap} @1 V/µm	τ_{rec}	$\tau_{\text{rec}}^{\gamma}$
300	30 ps[b]	< 10 ns[a]	1 µs[c]
100	10 ns[a]	10 ns[a]	1 µs[c]
50	150 µs[b]		1 µs[c]

[a] measured [b] inferred from measurement at 100 K [c] cf. [49]

the maximal rate of evaporating excitons, the evaporation happens "freely", and hence with τ_{th} as in the case of the single, isolated exciton. Therefore, at high electric field strengths, the exciton evaporation happens with the thermal lifetime, whereas at low electric field strengths the evaporation is curbed and takes place with an evaporation lifetime $\tau_{\text{evap}} > \tau_{\text{th}}$. The evaporation lifetime dominates at high temperatures, the recombination lifetime at low temperatures. An overview of the different processes and their lifetimes is given in Tab. 2.3.

2.3. Synthesis of CVD Diamond

The growths of diamond is possible under very different conditions. Natural diamond usually forms under high pressure of 45 kbar to 60 kbar in combination with temperatures around 1300 K. These conditions can be found in two regions on earth: (1) in the lithospheric mantle and (2) below relatively stable continental plates. Volcanic activity is needed to transport diamond-bearing rock from depths about 150 km below the surface to depths in reach of human mining activities. Annually, approximately 26 000 kg of diamonds are mined. [52] Diamonds are classified in different types by concentration and type of their chemical impurities. Natural diamond are usually of type Ia (∼98 %). Type Ia diamond contains dominantly nitrogen impurities, up to 3000 ppm. Type IIa diamond contains considerably less nitrogen, often at or below the sensitivity of nitrogen detection techniques. Boron enriched type II diamonds are classified as type IIb.

Among various techniques to synthesise diamond the plasma-assisted chemical vapour deposition technique produces the highest quality diamond to date, and is the only technique discussed here. However, many details about diamond synthesis is not publicly available as many diamond growers do not publish their "recipe". The basic idea is as follows: A hot plasma is created from the source gases methane (CH_4), molecular hydrogen (H_2), and optionally an oxygen containing compound like acetone $(CH_3)_2CO$ within a reactor cavity. The plasma is created using a microwave generator usually using commercially available frequencies like 2.45 GHz, 915 MHz, or 13.56 MHz. The microwaves ionise the source gases and heat electrons to about 5000 K, whereas the neutral species remain at relatively low temperatures of about 1100 K. Hot electrons then activate the reactant gases. The plasma's centre is positioned above a substrate on which diamond is supposed to form. A schematic description of a CVD reactor is shown in Fig. 2.15 **(A)**, and a picture of a commercially available set-up in Fig. 2.15 **(B)**. Carbon atoms are produced in the hot plasma by stripping

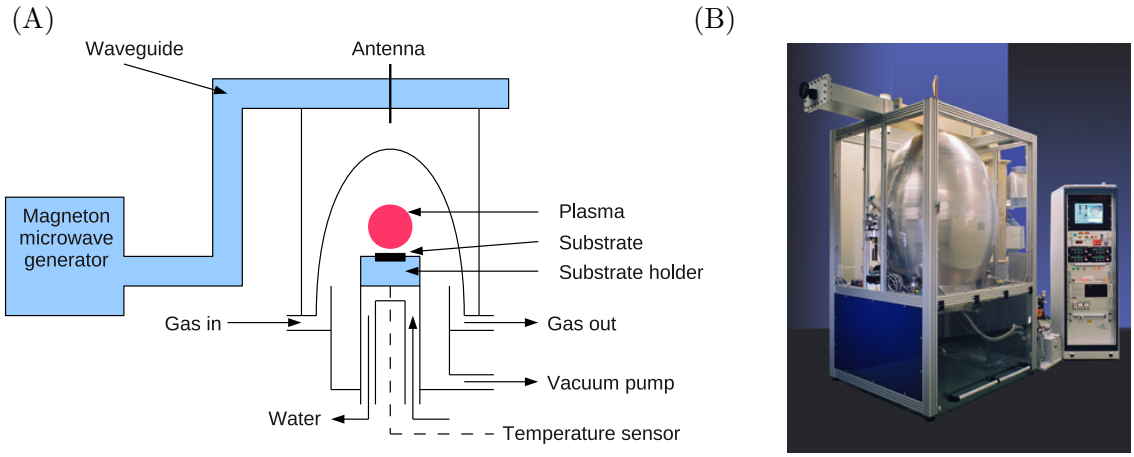

Figure 2.15.: A plasma-assisted CVD reactor is depicted schematically in **(A)**. (based on [14]) **(B)** shows a commercially available set-up. [54]

off hydrogen atoms of methane. The substrate itself is cooled and the free carbon atoms thus settle on the substrate surface. In more detail, the three main steps in chemical vapour deposition of diamond are (1) the breakup of hydrogen molecules to atomic hydrogen, (2) the diamond nucleation, and (3) the diamond growth. A detailed description of the gas phase chemistry which is important to all three steps is out of the scope of this work. Readers are referred to Ref. [53] for an overview of different chemistries and references therein for a more detailed insight.

- Atomic hydrogen plays at least three important roles in the plasma. First, it etches non-diamond-bonded material from the surface and therefore largely reduces graphite inclusions. The addition of oxygen compounds creates OH is the plasma which supports the graphite etching. Secondly, it reduces methane to CH_3, CH_3 to CH_2, ... via the reactions

$$\begin{aligned} CH_4 + H(g) &\rightarrow CH_3 + H_2(g) \\ CH_3 + H(g) &\rightarrow CH_2 + H_2(g) \\ &\vdots \end{aligned} \tag{2.55}$$

  Thirdly, it activates hydrogen-terminated carbon surface sites as it binds with the terminating hydrogen atom, see Fig. 2.16.

- Nucleation is an important step in diamond growth as it serves as the seeds of subsequent diamond deposition. However, in spite of ongoing research the nucleation process is poorly understood so far. One model discussed in Ref. [55] comprises the adsorption of polycyclic aromatic hydrocarbons (PAHs) on the substrate surface. The PAHs are formed from the source gases via chemical reactions in the plasma, but the aromatic rings consist mostly of sp^2 bonds. Hydrogen abstraction is thought to convert sp^2 bonds to sp^3 bonds.

- The growth is again a delicate issue. The temperature of the growth surface is an important property of the growth process and needs to be controlled carefully. At too high a temperature many hydrogen atoms within a small area might desorb from the surface within a short period of time (microseconds) resulting in re-arrangement of the surface into graphite. Therefore, individual hydrogen atoms have to be abstracted

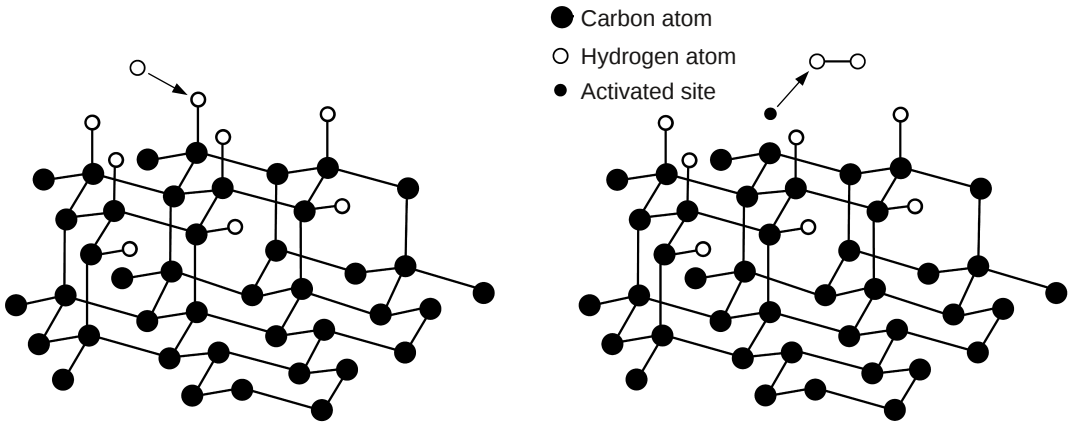

Figure 2.16.: A hydrogen terminated surface site is activated via hydrogen abstraction by atomic hydrogen. (reproduced from [57])

from the supposedly hydrogen-terminated surface, see the role of hydrogen in the first bullet. The activated site can then be filled with any reactive species. Diamond growth is thought to occur when a hydrocarbon fills the activated site with subsequent hydrogen abstraction. Note that further adsorption of PAHs is not desired after nucleation as this would increase graphitic phases in the diamond. It can thus be concluded that the conditions favouring nucleation are different from those desired for growth.

Another issue of growth is the used substrate. Homoepitaxial growth, i.e. growth of diamond on a diamond substrate, produces the highest quality results, especially when grown on a single-crystal substrate. To date, there is no economic way of producing large amounts of single-crystal chemical vapour deposition (scCVD) specimens. Drawbacks are the high costs, small size, variability in quality. When grown on a polycrystalline diamond substrate, the bulk of the diamond will contain grain boundaries. They form when diamond parts from different seeds eventually meet. The grain boundaries function as trapping and recombination centres for free charge carries, degrading the lifetime of the carriers, and hence the quality of the crystal. Polycrystalline CVD (pCVD) diamond with a CCD of the order of 250 µm in a 500 µm thick samples are grown at a rate of 1 µm/h. Grown to 1.5 mm thickness, this takes over 60 days. The quality rises during the growth process, and after growth several hundreds of micrometer of material are taken off from the nucleation side of the specimen. Single-crystal CVD diamond is likely to be grown at even lower rates in combination with smaller thicknesses and in a pure $C - H$ chemistry. [56]

In total, faster growing techniques produce diamond more economically but of (much) poorer quality. The electronic characteristics degrade rapidly with increasing impurity and defect density. The best polycrystalline CVD diamond have trapping lifetimes of the order of 1 ns, whereas scCVD diamond can be fabricated with lifetimes much larger than 30 ns. A total of about 100 000 kg [52] of diamond is synthesized annually, and are commonly used for e.g. cutting tools, laser windows, and heat spreaders.

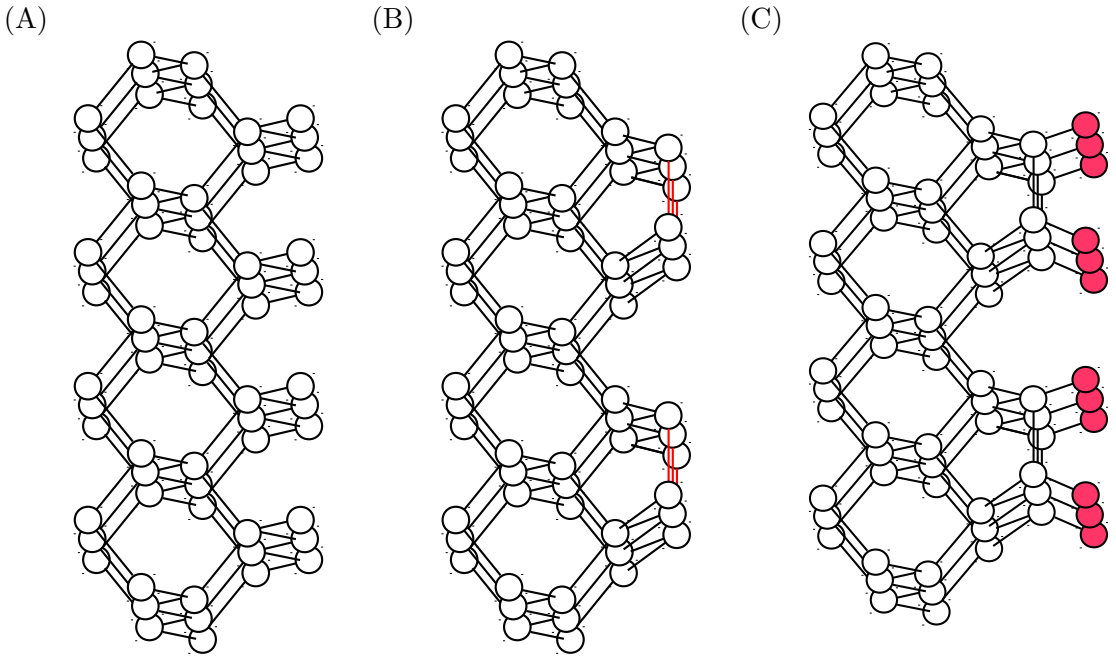

Figure 2.17.: The truncated (100) bulk **(A)**, surface energy lowering C=C dimers **(B)**, and hydrogen-terminated surface **(C)** are shown. (based on [58])

2.4. Surfaces and Contacts

For a $5 \times 5 \times 0.5\,\mathrm{mm}^3$ cuboid of diamond the number of surface atoms is small in comparison to the number of bulk atoms. However, the surface characteristics can strongly influence the characteristics of the whole specimen. Here, some surface properties of (100) faces are reviewed and is followed by a discussion about diamond-metal interfaces, i.e. what is commonly called a *contact*.

The real surface of a diamond is not just a truncated bulk. This would clearly result in at least one unsaturated, or *dangling*, bond per surface atom. This dangling bond would in turn be highly reactive and would either bind a reactant in its vicinity, or the surface would reconstruct itself. The theoretically truncated (100) surface is depicted in Fig. 2.17 **(A)**. It is thought, supported by calculations and surface analysis methods, that the surface atoms can reconstruct in a way that each two surface atoms build C=C dimers, see Fig. 2.17 **(B)**. The dimers are highlighted in red. This configuration reduces the surface energy of the electrons stemming from surface atoms considerably. A further reduction is achieved by hydrogen-termination of the dimer atoms which changes C = C bonds into a C − C ones. Figure 2.17 **(C)** shows the hydrogen-terminated surfaces.

The situation gets more sophisticated when other reactants like oxygen are allowed, or when defects emerge from the bulk to the surface. The perfect hydrogen-terminated surface is thought to be highly resistive, too. In reality, the surface currents dominate largely over bulk DC currents. This is attributed to non-perfect surfaces which are less resistive.

In order to prepare a diamond specimen for the usage as a detector, the specimen has to be coated with a metal, which in turn can be contacted via wire bonds or just by mechanical contact to e.g. a conducting spring. The contact needs to form a stable, resistant, homogeneous connection to the bulk material in order to withstand mechanical stress, facilitate handling of the detector, and to ensure a position independent detector readout. It

is desirable that the interface between the metal and the diamond surface is of *ohmic* nature, i.e. that the current flowing through the device as a function of the applied bias voltage (or electric field) is linear and symmetric in bias polarisation. If the I-V characteristics are non linear or asymmetric the contact is called a Schottky barrier contact. Measured I-V curves on scCVD diamond can often not be interpreted readily in terms of ohmic or Schottky contacts. This is due to the very small currents of below a few picoampere at RT and fields $|E| < 2\,\mathrm{V/\mu m}$. Details are discussed in Chap. 4.2.1.

Theoretically, the interface of diamond (or a semiconductor in general) with metal is interpreted in terms of Fermi levels, work functions, and electron affinities. The metal work function Φ_m is the ionisation energy of the metal into the vacuum, the electron affinity χ_s is the energy difference between the lower edge of the conduction band and the vacuum. Ψ_s is the energy difference between the Fermi level in the semiconductor and the vacuum. Considering a metal and a semiconductor surface at sufficient distance δ, the Fermi energies differ between the two. The common energy is the vacuum level. When δ is reduced until the two are in contact, i.e. δ is below the atomic distance, a net flux of electrons from either the metal to the semiconductor or vice versa takes place. This can be understood as reaching a lower energy configuration as the electrons have a lower chemical potential in one or the other medium depending on the relative positions of the Fermi levels. If the Fermi level in the semiconductor is lower, electrons flow from the metal to the semiconductor resulting in an increased Fermi level of the semiconductor in comparison to the Fermi level in the metal. Thus a thermal equilibrium is reached with equal Fermi energy in both the metal and the semiconductor.

Starting with an electrically neutral metal and an electrically neutral semiconductor, a net flow of charges results in an electric field from the net-positively charged part to the net-negatively charged part. The built-up of this field counteracts the net flow, until an equilibrium is reached. The electric field varies with distance over the semiconductor starting from the metal-semiconductor interface, and a barrier potential Φ_B is formed. Figure 2.18 shows the scenario before **(A1, B1, C1, D1)** and after **(A2, B2, C2, D2)** bringing the metal in contact with the semiconductor. Four different scenarios are shown: n- and p-type semiconductor with different metal work functions. In **(A2, B2, C2, D2)** the *band bending* effect is illustrated, i.e. the valence and the conduction band are a function of the depth, which seems to be in contradiction with the previously discussed *flat* band model. The bent bands are a result of the superposition of the flat, i.e. position independent, bands with the position dependent electrostatic energy $\Phi(x)$ building up with the net charge flow resulting in a position dependent space charge density, and in the one-dimensional case

$$\triangle\Phi(x) = -\frac{e}{\varepsilon_0\varepsilon_r}\rho(x). \tag{2.56}$$

The situation in diamond is unclear. The electronic grade scCVD diamond samples used in this work are not intentionally doped. Nitrogen and boron impurity levels are below the detection sensitivity. It is hence not known if the samples are p-type or n-type. However, the bulk resistance is much larger than the contact resistance. The barrier potential is usually of the order of a few volts, which is small compared to the applied bias voltage for the tests performed in this work. The contacts are therefore believed to not play a dominant role.

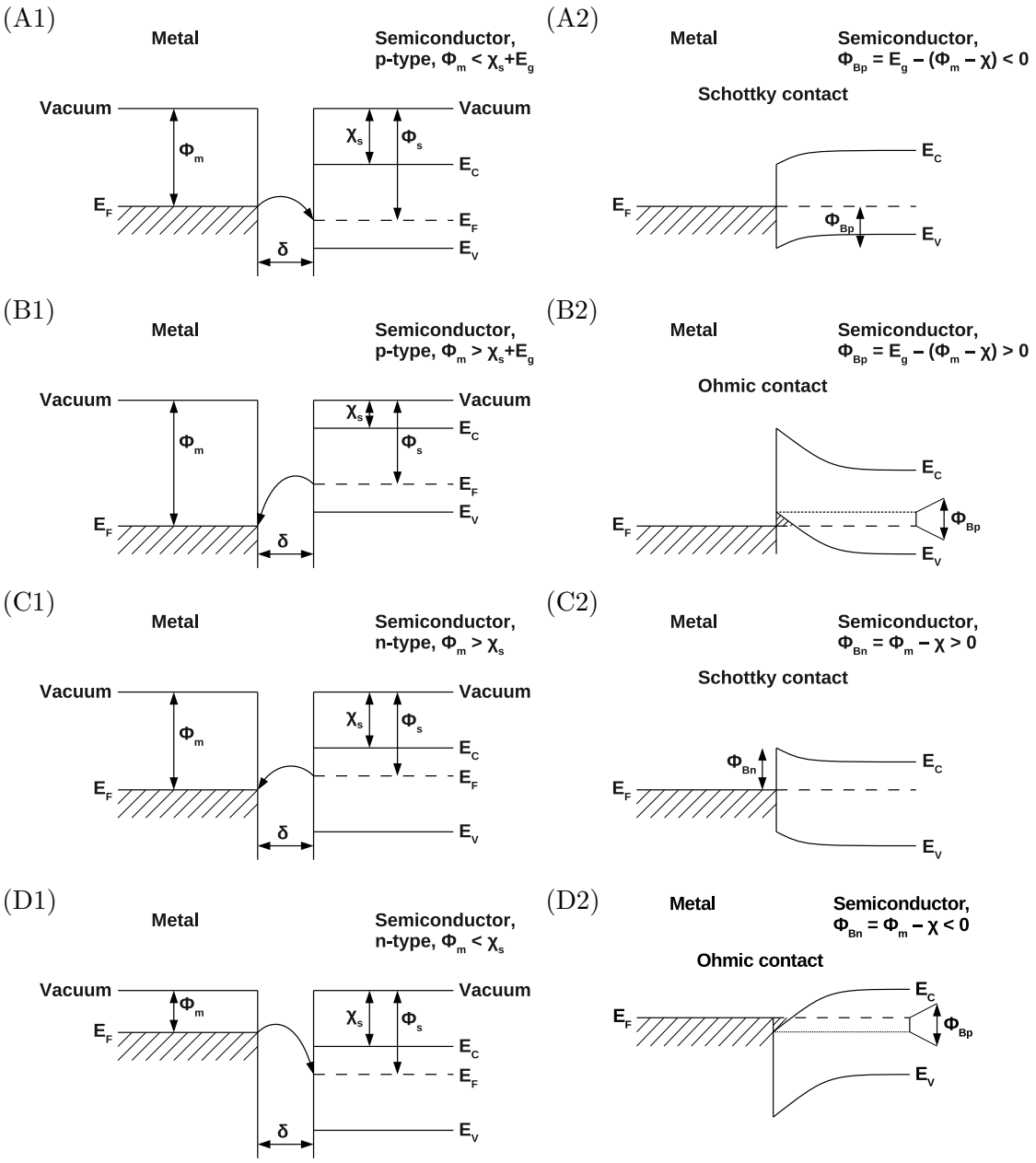

Figure 2.18.: Four different scenarios are shown: n- and p-type semiconductor with different metal work functions before (left) and after (right) bringing the metal in contact with the semiconductor. (based on [13] and [12])

3. RADIATION DETECTION

For the detection of particles traversing a piece of matter two requirements must be fulfilled: (1) the particle has to deposit, i.e. lose, energy during its transit through the detector, and (2) the deposited energy has to be convertible into a measurable quantity. The two issues are discussed in this chapter using the examples of α-particles, protons, and muons. The passage of neutral particles like photons and neutrinos through matter is not discussed here.

3.1. Energy Loss of Heavy, Charged Particles in Matter

The stopping power of heavy charged particles ($M \ll m_e$) in matter is described accurately by the Bethe equation [59] at moderately relativistic energies ($0.1 \lesssim \beta\gamma \lesssim 1000$) in units of $\mathrm{MeV cm^2 g^{-1}}$

$$-\left\langle \frac{\mathrm{d}E}{\mathrm{d}x} \right\rangle = K z^2 \frac{Z}{A} \frac{1}{\beta^2} \left[\frac{1}{2} \ln \left(\frac{2 m_e c^2 \beta^2 \gamma^2 T_{\max}}{I^2} \right) - \beta^2 - \frac{\delta(\gamma\beta)}{2} \right]. \tag{3.1}$$

The constant K is $K = 4\pi N_\mathrm{A} r_e^2 m_e c^2$ with the classical electron radius r_e, z the charge of the ionising particle in units of the elementary charge, Z the atomic number of the absorber, A the atomic mass of the absorber, β and γ are the common relativistic expressions $\beta = v/c$ and $\gamma = \frac{1}{\sqrt{1-\beta^2}} \equiv \frac{E}{M c^2}$ with the speed of light c and the projectile mass M, $T_{\max}$ is the maximum kinetic energy which can be transferred to a free electron in a single collision, I the mean excitation energy, and δ is a correction for the so-called *density effect* which is important towards relativistic energies. The function is plotted in Fig. 3.1 as a function of $\beta\gamma$ or muon momentum and its valid region is marked as "Bethe". Close inspection of Eq. (3.1) explains its qualitative behaviour as a function of β or $\beta\gamma$. For small β, the relativistic γ-factor is $\sim$1, and Eq. (3.1) is proportional to $1/\beta^2$, since $\ln(\beta^2)$ increases slowly. With v approaching c, β approaches 1, and therefore $1/\beta^2$ is constant, and $\beta\gamma$ increases. The first term inside the square brackets starts to dominate and Eq. (3.1) is proportional to $\ln(\beta\gamma)$ as can be seen from the slow increase for $\beta\gamma \gtrsim 3$ in Fig. 3.1. In the transition region the stopping power has a minimum. A particle with $\beta\gamma \gtrsim 3$ is called a minimum ionising particles (MIP).

The Bethe theory without low energy corrections is valid down to $\beta\gamma \approx 0.1$. Including various corrections the range of the Bethe formula extends down to $\beta \approx 0.05$. At even lower energies, the energy loss is not described accurately by any theory. Phenomenological fitting formulae are provided by Andersen and Ziegler. [60] Below a few 100 eV of kinetic energy, Lindhard successfully developed a theory describing the energy loss in linear dependence of β. [61]

3.1.1. α-particles

In this work, intensive use of α-radiation from an ^{241}Am source is made. The α-particles radiated by this isotope have *kinetic* energies of about 5.47 MeV. These α-particles have a $\beta = 0.054$ and a $\gamma = 1.0015$, and hence a $\beta\gamma = 0.054$ using $m_\alpha = 3.73\,\mathrm{GeV}/c^2$.

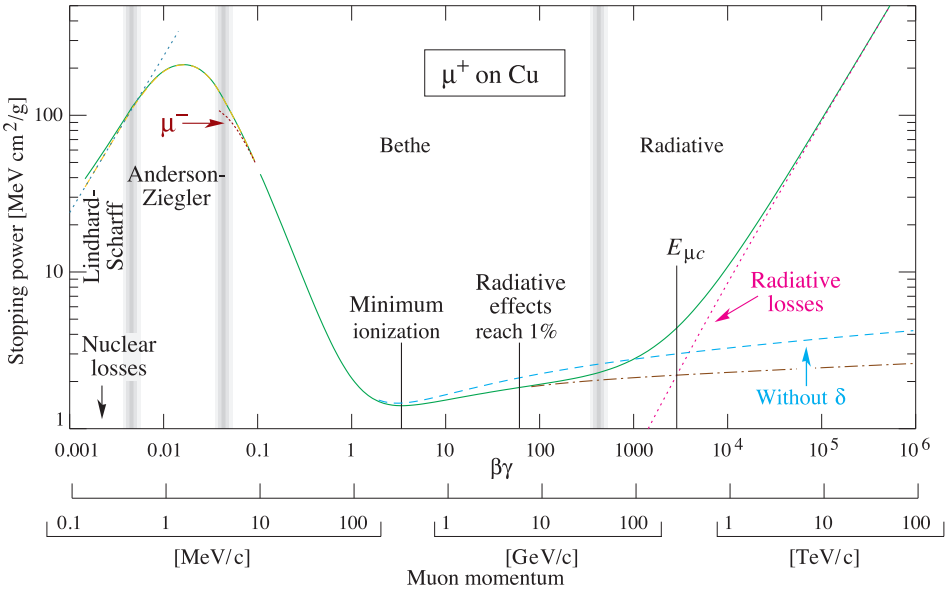

Figure 3.1.: The calculated stopping power of positive muons in copper is shown over many orders of magnitude as a function of $\beta\gamma$. The region described by the Bethe equation is marked as such. For relativistic particles radiative losses and density effects have to be accounted for. Towards lower energies several corrections to the Bethe equation need to be made. (from [62])

Following the discussion above, the lack of a satisfactory theory of the stopping power for energies in the energy regime used here necessitates experimental data to be used in order to describe the stopping process of α-particles from an ^{241}Am source. The numbers of interest are the penetration depth in matter, the distribution of deposited energy along the track, and the radial energy deposition distribution. Extensive data about the stopping power of electrons, protons, and α-particles in various materials are tabulated by the National Institute of Standards and Technology (NIST, [63]), and are listed in Appendix A. The stopping power for α-particles in amorphous carbon and water as a function of the incident particle energy is shown Fig. 3.2 **(A)**. When corrected for the absolute density of the material, the two materials, as almost all solids and liquids, have similar stopping powers over a wide energy range. The vertical line marks an incident energy of 4.6 MeV. In Fig. 3.2 **(B)** the energy loss per micrometre (black line, left scale) is shown as a function of depth along with the deposited fraction of the total particle energy (red line, right scale), which is again chosen to be 4.6 MeV. The plot is produced using the stopping power values from **(A)** and the density of diamond of 3.52 gcm^{-3}. The step size in the simulation is set to 10 nm, and for each step the energy loss over the step size is calculated. The stopping power values in between two data points are inferred using a log-log interpolation. A linear interpolation effects the stopping power by about 2 % midway between two data points. Towards the end of the particle range, at a depth of 9.65 µm the energy loss reaches a maximum, called the Bragg peak. After reaching the Bragg peak the particle is stopped within another micrometre. The simulated penetration depth is $\delta_p = 10.66\,\mu m$.

The average pair-creation E_{pair} is not the equal to the band gap, but considerably higher. This is due to the fact, that there is ionising and non-ionising energy loss. In total, an average pair creation energy of $E_{pair} \approx 12 - 14\,eV$ is found in various measurements [64]. Another reference reports values between 11 eV and 18 eV. [65] Here, a value of $E_{pair} =$

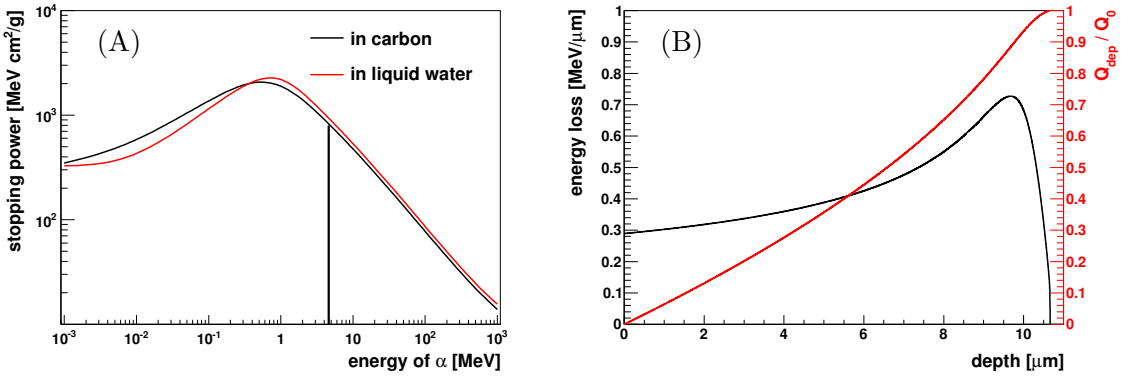

Figure 3.2.: **(A)** The stopping power of carbon and water for α-particles is plotted as a function of energy (data taken from [63]). Using values from **(A)**, the energy deposition per µm and the deposited fraction of total energy for a 4.6 MeV α-particle is shown in **(B)**.

13.25 eV is used for reference. [66] With a band gap of $E_g = 5.47$ eV for every electron-hole (eh) pair, about 7.8 eV are used to create phonons. I.e. on average ∼40 % of the total energy is used for ionisation, ∼60 % for phonon creation.

The stopping power shown in Fig. 3.2 **(A)** is the total stopping power, which consists of two parts: (1) the electronic stopping power and (2) the nuclear stopping power. In (1) the α-particle loses energy to shell electrons by exciting them from the valence band to the conduction band (not necessarily to the band-edge). The nuclear stopping power consists of the creation of phonons in the crystal and the displacement of atoms in the lattice. The electronic stopping power is four orders of magnitude higher than the nuclear stopping power down to particle energies of 1 MeV according to NIST data, and they are about equal only at 1 keV, i.e. towards the very end of the stopping process. However, the energy loss is not mostly of ionising type. The electronic energy loss of a 4 MeV α-particle produces electrons with a mean energy of 60 eV according to Ref. [67] (in water). With decreasing α-energy, the mean drops, see Fig. 3.3. The solid line in Fig. 3.3 gives the average energy of secondary electrons for He^{++}, namely α-particles. The same order of magnitude is likely to be correct as well in diamond. In turn, the low energetic electrons, called secondaries (not only δ-electrons, but all electrons, that have been excited high into the conduction band), lose their energy again by ionisation and phonon excitation. In order to sum up to 13.25 eV per e-h pair creation, the secondary electrons have to excite about four electrons to the band edge, and lose another 40 eV in phonon excitation.

Considering the kinetic energy of 60 eV of the secondaries, the radial energy distribution is considerably shorter than the penetration depth. Measurements with ^{12}C ions in water vapour at a pressure of 40 hPa showed $1/e$ radial track sizes $\mathcal{O}(150\,\text{nm})$, see Fig. 3.4 **(A)**. In order to estimate this value in diamond, it has to be scaled with the stopping power and the density under the assumption of equally energetic secondaries. Figure 3.2 **(A)** shows similar stopping powers. The density ratio diamond to the water vapour used in Fig. 3.4 **(A)** is $3.5/0.04 \approx 88$, resulting in a $1/e$ track size of about $150\,\text{nm}/88 \approx 2\,\text{nm}$ in diamond. Another measurement performed in liquid water with 3 MeV α-particles gives similar results, as is shown in Fig. 3.4 **(B)**. The steep fall-off in the first nanometres hampers the extraction of an accurate value from the plot, but confirms an $1/e$ value of a few nanometres in radial track size.

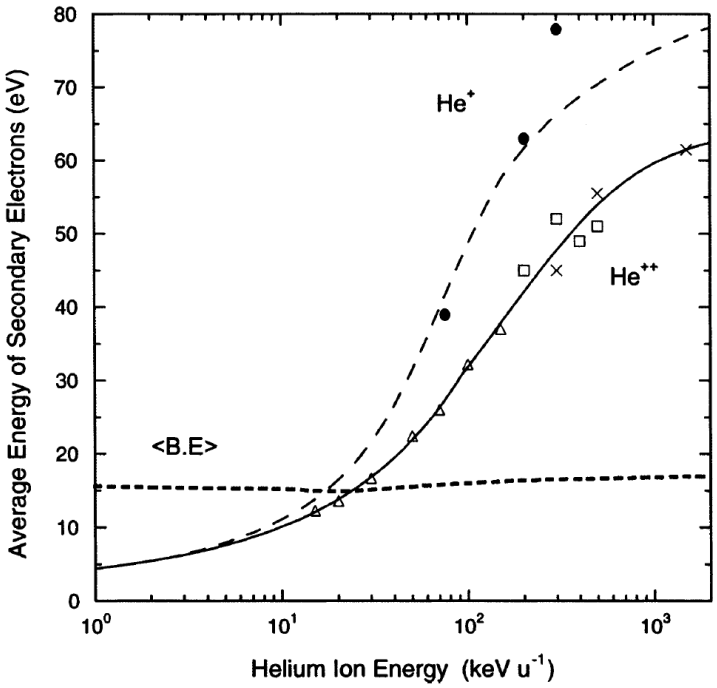

Figure 3.3.: The average energy of the secondary electrons is shown as a function of the primary energy in water. (from [67])

3.1.2. Minimum ionising particles

Cosmic rays, which consist mostly of protons, hit the earth's atmosphere and produce pions, kaons, and other particles in collisions with atmospheric molecules. The pions and kaons decay rapidly and produce muons, which are energetically enough to reach the earth's surface and even underground laboratories. Many cosmic muons that reach the surface have energies around 1 GeV and have therefore MIP character. The stopping power of diamond is about a factor of 1000 higher for α-particles at 1 MeV compared to MIPs. The α-particles used here are therefore *highly ionising* particles in comparison to MIPs.

At the CNGS experiment at CERN, 17 GeV muons are produced from pion decays and directed towards the Gran Sasso massif.[1] Muons at this energy have an energy loss slightly larger than MIPs, cf. Fig. 3.1, but due to the slow increase owing to the ln-dependence of the stopping power, the difference is small. The reasoning holds also true for 24 GeV protons.

Figure 3.5 depicts the stopping power of MIPs as a function of the absorber material. For absorbers with $Z > 6$ a linear dependence of $\ln(Z)$ is found. For carbon, the plot gives a stopping power of $1.75\,\mathrm{MeVg^{-2}cm^2} \mathrel{\widehat{=}} 616\,\mathrm{eV/\mu m}$. Note that this is the mean stopping power including large single-collision energy losses. These rare events can lead to a considerable difference in comparison to the median of the energy loss.[2] In practice, a value of 36 eh/µm is widely accepted [69, 70], which corresponds to 477 eV/µm assuming an average e-h pair creation energy in diamond of $E_{\mathrm{pair}} = 13.25\,\mathrm{eV}$.

[1] Details are given in Chap. 6.

[2] Consider 1 energy loss of 60 keV for every 1000 energy losses of 60 eV. The median is 60 eV, the mean is 120 eV.

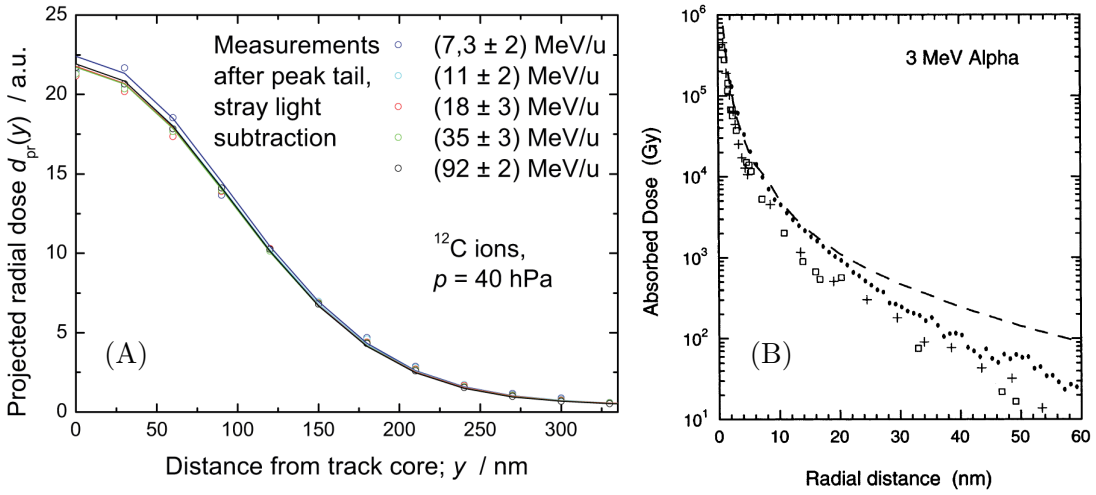

Figure 3.4.: **(A)** The radial dose distribution is shown for ^{12}C ions in water vapour at 40 hPa (from [68]). **(B)** The radial dose distribution is shown for 3 MeV α-particles in liquid water. (from [67])

3.2. Diamond as a Solid State Ionisation Chamber

The principle of operation of diamond as a charged particle detector is that of a solid state ionisation chamber. [71] In contrast to a gas-filled ionisation chamber, where ionised electrons and ions drift in an electric field between cathode and anode, a semiconductor is sandwiched between two metal electrodes, well known from a parallel plate capacitor. The incident particle then produces free eh-pairs rather than electrons and ions. They are separated by the electric field and each of the two charges drifts towards one of the contacts, which are on different potentials. The charge drift induces charges on the electrodes, and a detector current i_{det} can be read. An electrical scheme often used in particle physics is shown in Fig. 3.6. The diamond is biased over a resistor R. The biased read-out electrode is AC-coupled via a capacitor C to an amplifier, which amplifies the detector current and converts it into a voltage. Here, the detector current, or simply the "signal", is read from the high voltage side.

3.2.1. Shockley-Ramo theorem

The detector current induced by moving charges is elegantly formulated by the Shockley-Ramo theorem. [72] It makes use of a *weighting potential* Φ_{w} which describes the coupling of a charge to an electrode.[3] The weighting potential therefore depends on the electrode configuration. With the charge trajectory $\boldsymbol{r}(t)$, the induced current reads

$$i(t) = q\boldsymbol{\nabla}\Phi_{\mathrm{w}}\frac{\mathrm{d}}{\mathrm{d}t}\boldsymbol{r}(t) = -q\boldsymbol{E}_{\mathrm{w}}\boldsymbol{v}. \tag{3.2}$$

In a parallel plate configuration the weighting field is $\boldsymbol{E}_{\mathrm{w}} = -\frac{\mathrm{d}\Phi_{\mathrm{w}}}{\mathrm{d}x} = -1/d$. With the charge drift along x, the current becomes

$$i(t) = q\mathrm{v}_{\mathrm{drift}}(x,t)/d. \tag{3.3}$$

[3] N.B.: $\boldsymbol{\nabla}\Phi_{\mathrm{w}} = -\boldsymbol{E}_{\mathrm{w}} \neq -\boldsymbol{E}$, where $\boldsymbol{E}$ is the electric field.

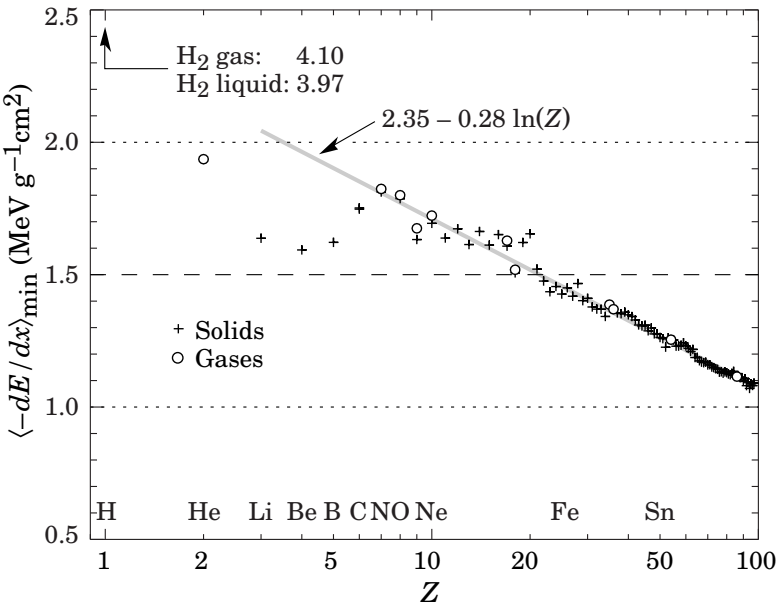

Figure 3.5.: The stopping power for MIPs is plotted as a function of the atomic number of the absorber. [62]

Assuming a time and position independent drift velocity, the time a charge needs to traverse the entire detector thickness, called the *transit time*, is

$$t_{\rm t} = \frac{d}{v_{\rm drift}}. \tag{3.4}$$

With $Q(t) = eN(t)$ and a constant drift velocity, the current reads

$$i = eN(t)/t_{\rm t}. \tag{3.5}$$

In this case the elegance of the Shockley-Ramo theorem does not show, but it greatly simplifies the derivation of induced currents on e.g. strip detectors, where a charge induces current on many electrodes. If a time-dependent amount of charge $Q(t) = eN(t)$ is considered to drift between the electrodes, and that the drift velocity is a function of the electric field and the mobility, one obtains

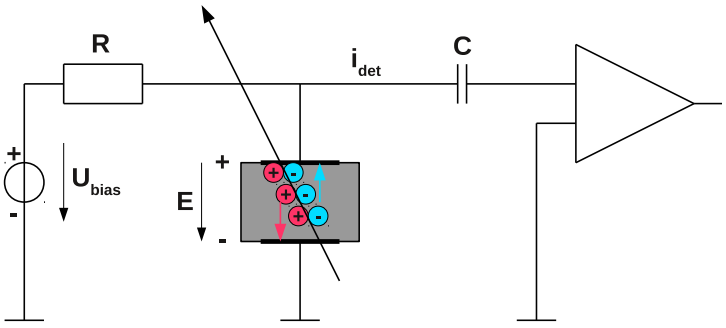

Figure 3.6.: The principle of operation of a solid state ionisation chamber is shown for a passage of a MIP particle including a simple electric read-out circuit.

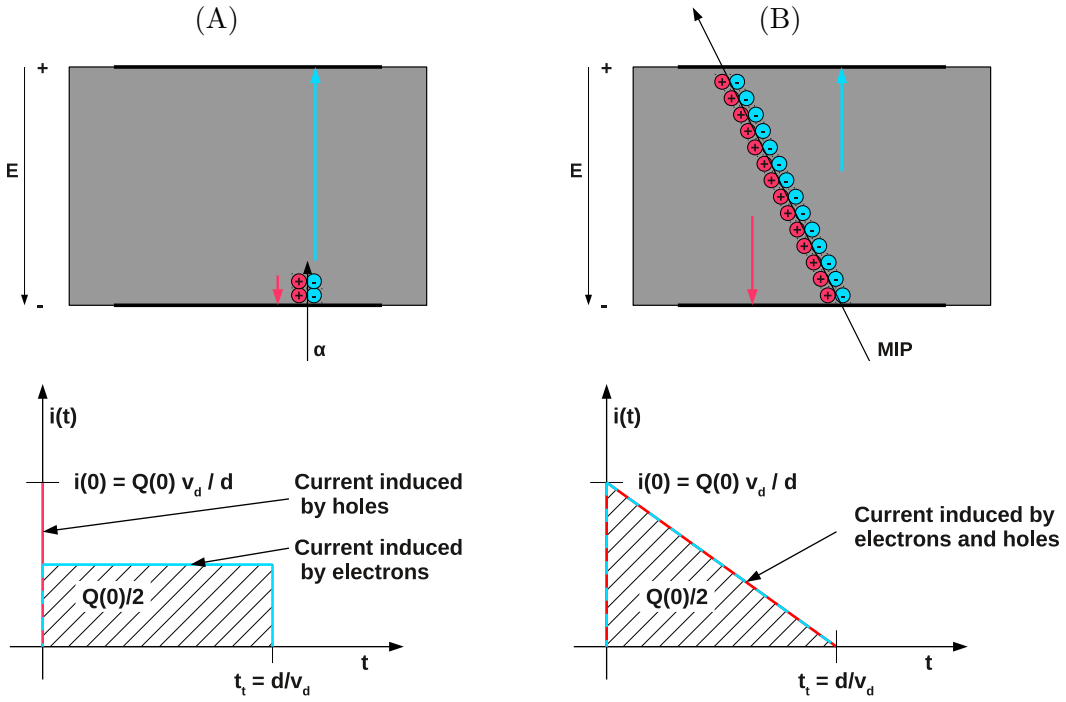

Figure 3.7.: The two modes of particle detection, calorimetric mode **(A)** and MIP mode **(B)**, are shown with their theoretical pulse shape **(bottom)** assuming a constant electric field.

$$i(t) = eN(t)\mu(E)E/d. \tag{3.6}$$

Note that in the case of position dependent electric field strengths, $v_{drift} = \mu(E)E$ is not longer valid. Instead, the differential equation $dx/dt = \mu(E)E(x)$ needs to be solved depending on $E(x)$.

3.2.2. Measured detector current and charge

In this work, diamond is used as a charged particle detector in two different "modes". The one most extensively used is the "calorimetric" mode, where the particle is stopped completely inside the sensor volume, as is the case for the highly ionising α-particle. For the second, the particle traverses the complete sensor thickness and exits the volume on the opposite site. Both situations are depicted in Fig. 3.7 **(top left/right)**. The shape of the induced current is different for the two modes. The short penetration depth of the α-particle results in a local charge package, which traverses the entire detector volume. Which charge type drifts through the bulk is a function of the chosen bias voltage. It is then collected "as a whole" at the opposite electrode. The other charge type is collected almost instantly at the incident electrode. A typical signal form is thus the rectangular form in case of highly ionising particles, if charge trapping during drift is neglected. Be Q^- the amount of produced electrons. Since electrons and holes are produced pairwise, the hole charge is $Q^+ = -Q^-$. But with one carrier type being collected immediately, the amplitude of the signal is proportional to Q^-, namely proportional to the *number* of produced pairs.

In case of MIP signals, all charges ($Q^- + Q^+$) start drifting initially, and the initial current is proportional to $Q^- + Q^+$. Those charges created close to one electrode and having the

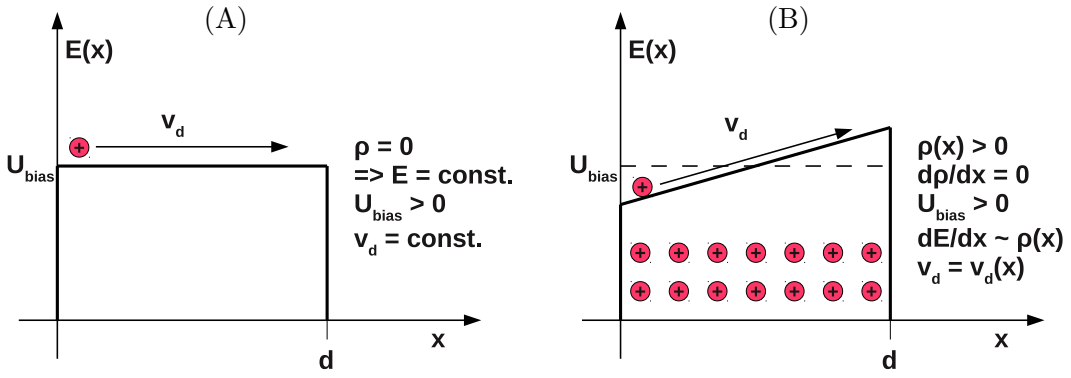

Figure 3.8.: Electric field distribution for $\rho = 0$ **(A)** and $\rho > 0$ **(B)**.

opposite sign than this electrode are collected first. The collection happens linearly for constant drift velocities resulting in a triangular-shaped signal pulse. The pulse area is then $\int (Q^- + Q^+) \cdot \mathrm{v}_{\mathrm{drift}}/d \, \mathrm{d}t = Q^-$. Figure 3.7 **(bottom)** shows the induced currents and pulse areas for both modes.

Additional issues have an impact on the signal shape. Discussed above was the case of a constant electric field over the detector thickness resulting in a constant drift velocity, cf. Fig. 3.8 **(A)**. If a non-zero net space charge is present in the detector, the electric field is altered. For a constant space charge like in silicon, i.e. $\frac{\mathrm{d}\rho}{\mathrm{d}x} = 0$, the electric field in the one-dimensional case is $\mathrm{div}(E) = \frac{\mathrm{d}E}{\mathrm{d}x} \propto \rho(x)$ and therefore evolves linearly over the detector thickness, see Fig. 3.8 **(B)**. The drift velocity is then position dependent.

The drifting charges are collected at the opposing electrode after an average transit time $t_{\mathrm{t}} = {}^{d}/_{\mathrm{v}_{\mathrm{drift}}}$. Mathematically, this "start-drift-collect" scheme can be written as follows. If a function $\dot{N}_{\mathrm{start}}(t)$ represents the distribution of the start time of drifting of charges, the total number of started charges is $N_{\mathrm{start}}(t) = \int_0^t \dot{N}_{\mathrm{start}}(t) \, \mathrm{d}t$. With the average transit time $t_{\mathrm{t}} = t_{\mathrm{coll}} - t_{\mathrm{start}}$ the distribution of the collection time of charges is $\dot{N}_{\mathrm{coll}}(t) = \dot{N}_{\mathrm{start}}(t - t_{\mathrm{t}})$, and the total number of collected charges is $N_{\mathrm{coll}}(t) = \int_0^t \dot{N}_{\mathrm{start}}(t - t_{\mathrm{t}}) \, \mathrm{d}t$. The number of drifting charges is hence

$$N_{\mathrm{drift}}(t) = N_{\mathrm{start}}(t) - N_{\mathrm{coll}}(t). \tag{3.7}$$

The scheme is depicted in Fig. 3.9 for two different start distributions assuming a local charge deposition close to the incident electrode.

Trapping processes along with the charge drift further influence the signal shape. If the trapping centres are distributed equally throughout the crystal, the trapping probability is homogeneous. With a trapping time t_{trap} the number of drifting charges is the solution of the differential equation

$$\mathrm{d}N(t) = \frac{N}{t_{\mathrm{trap}}} \mathrm{d}t. \tag{3.8}$$

The solution is

$$N(t) = N(0) \, e^{-t/t_{\mathrm{trap}}}. \tag{3.9}$$

The total measured charge Q_m is the integral over the induced current. The *charge collection efficiency* (CCE) is readily defined as the fraction of measured charge over the created charge

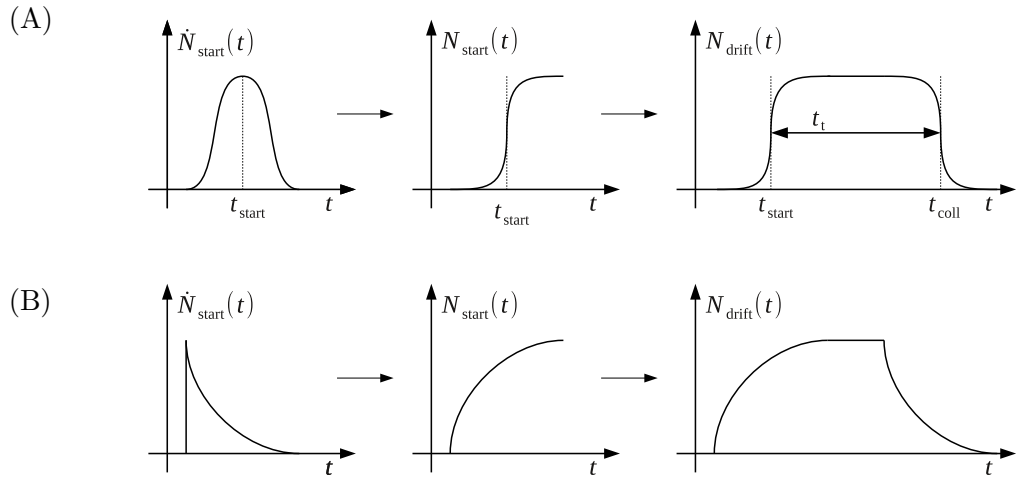

Figure 3.9.: A Gaussian **(A)** and a exponential **(B)** start time distribution function **(left column)**, their resulting number of started charges distribution **(middle column)** and the drifting charges distribution **(right column)** are shown.

$$\text{CCE} = \frac{Q_m}{Q_0}. \tag{3.10}$$

If the charge loss happens due to trapping, the charge collection distance (CCD) is

$$\text{CCD} = \frac{Q_m}{Q_0} \cdot d. \tag{3.11}$$

The CCD or CCE is often used to grade the quality of a sensor. For a scCVD diamond, the CCE is usually close to 100 %. To date, the best polycrystalline materials have CCDs of 250 to 300 µm in 500 µm thick samples.

The fluctuation in signal charge is a key characteristic of signal sensors as it determines the relative resolution $\Delta E/E$, which is important for spectroscopic measurements. In the calorimetric mode the complete energy of the incident particle is absorbed in the material. The fluctuation in signal charge is then not $\sigma_Q = \sqrt{N_i}$ with the number of ionised charges $N_i = E_0/E_{\text{pair}}$, but actually smaller than this simple statistical variance. A full discussion can be found in Ref. [73]. The incident particle energy E_0 is converted into phonons and formation of free eh-pairs

$$E_0 = E_{\text{ph}} N_{\text{ph}} + E_{\text{g}} N_i, \tag{3.12}$$

with the average phonon energy E_{ph}. Since the total energy is fixed, a fluctuation in N_i must result in a corresponding fluctuation of N_{ph}: $\Delta N_i E_{\text{g}} + \Delta N_{\text{ph}} E_{\text{ph}} = 0$, i.e. a downward fluctuation in number if ionisations results in an upward fluctuation in number of created phonons. Over many events, the energy weighted variances are therefore equal, $E_{\text{g}}\sigma_Q = E_{\text{ph}}\sigma_{\text{ph}}$, and

$$\sigma_Q = \frac{E_{\text{ph}}}{E_{\text{g}}}\sigma_{\text{ph}} = \frac{E_{\text{ph}}}{E_{\text{g}}}\sqrt{N_{\text{ph}}} \tag{3.13}$$

Using Eq. (3.12) one obtains

$$\sigma_Q = \frac{E_{\mathrm{ph}}}{E_{\mathrm{g}}}\sqrt{\frac{E_0}{E_{\mathrm{ph}}} - \frac{E_{\mathrm{g}}}{E_{\mathrm{ph}}}N_i} = \sqrt{\frac{E_{\mathrm{ph}}}{E_{\mathrm{g}}}\left(\frac{E_{\mathrm{pair}}}{E_{\mathrm{g}}} - 1\right)}\sqrt{\frac{E_0}{E_{\mathrm{pair}}}} = \sqrt{FN_i} \tag{3.14}$$

F is called the Fano factor, and $F = 0.08$ in diamond. [73] Due to the Fano factor and the smaller ionisation energies in solid state detectors compared to gas-based detectors, the energy resolution is often a factor of 25 or more better in solid state detectors.

4. EXPERIMENTAL TECHNIQUE

4.1. The Transit Current Technique

During the last 40 years, the transient current technique (TCT) has frequently been used in order to determine the charge carrier mobility and velocity in different materials. In insulators, it was used in 1970 by Lampert and Mark. [74] Later, the TCT was further developed for the measurement of the effective net charge in the space charge region of p-n junction detectors by Eremin et al. [75] Pernegger et al. carried out TCT measurements using α-particles for carrier excitation (α-TCT) in order to determine charge carrier properties in single-crystal chemical vapour deposition (scCVD) diamond at room temperature (RT). [29] This investigation was followed by Pomorski et al. [76] A study of a variety of semiconductor materials, namely CdTe, CZT, silicon p-in-n diodes, as well as two scCVDs, has been performed by Fink et al. [77] Also photon-induced TCT studies have been made with scCVD samples making use of a 5x-frequency multiplied Nd-YAG laser by Isberg et al. [31]

The α-TCT provides a direct way to measure the transit time, i.e. the time a charge needs to drift through the bulk, and hence calculate the drift velocity. This technique is usually, and also in this work, performed in a metal-semiconductor-metal structure. The semiconductor is used as a solid state ionisation chamber, see Sec. 3.2. Time-resolved currents induced on a read-out electrode by the drift of free charge carriers in an externally applied electric field are read with high bandwidth. Note that this is a current measurement, as opposed to a charge measurement. Local, free charge deposit close to the electrode on one side is realised by using highly ionising α-particles with short penetration depth from an ^{241}Am source. As the charges drift through the semiconductor bulk, the recorded signal pulse shape is sensitive to its material properties. In present scCVD diamond, trapping times larger than 30 ns have been realised. [29] If the current is read with wide bandwidth, charge carrier properties can be derived accurately from pulse characteristics. Since the charge carrier trapping time exceeds the transit time and with charge creation limited to a small depth in comparison to the bulk thickness, the transit time can readily be calculated from the time difference between the rising and the falling edge. With a known sample thickness, the drift velocity can be calculated. Measurements in a wide range of electric field strengths are used to determine the low-field mobility and the saturation velocity using Eq. (2.47).

4.2. Samples

The samples under test (SUTs), which are referred to as *S52*, *S57*, and *S79* for later reference, have been produced using the chemical vapour deposition process by Element Six Ltd (E6) [78]. The scCVD diamond samples have an area of $4.7 \times 4.7\,\mathrm{mm}^2$ and thicknesses of $d_{\mathrm{S52}} = 515\,\mu\mathrm{m}$, $d_{\mathrm{S57}} = 530\,\mu\mathrm{m}$, and $d_{\mathrm{S79}} = 529\,\mu\mathrm{m}$. A photograph of the SUTs is shown in Fig. 4.1 in the order *S52*, *S57*, and *S79* from left to right. The dislocation and impurity densities are $\lesssim 2{\times}10^{14}\,\mathrm{cm}^{-3}$. Diamond Detector Ltd. (DDL) [79] quotes a nitrogen incorporation of $< 1\,\mathrm{ppb}$. *S52* and *S57* have been metallised by DDL, *S79* at

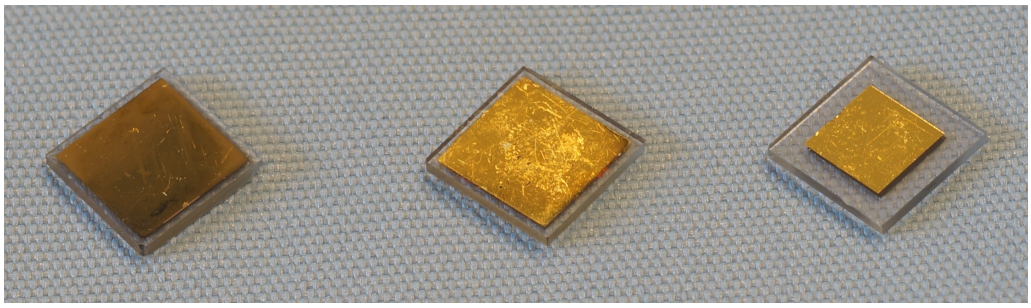

Figure 4.1.: The three SUTs are shown. The long sides are the 110 directions, the thickness evolves along the ⟨100⟩ direction.

the Physics Department of the University of Firenze, Italy. The SUTs are equipped with metal contacts on both sides. According to the specifications from the manufacturer, the DDL contacts are made from three layers: DLC[1]/Pt/Au with ∼4/10/200 nm thicknesses, respectively. The metallised area is quadratic, has a surface of $A = 4.2 \times 4.2\,\mathrm{mm}^2$, and does not include a guard ring. *S79* has a Cr-Au metallisation of ∼400 nm total thickness, spanning roughly $A = 3.2 \times 3.2\,\mathrm{mm}^2$. DDL quotes a charge collection efficiency of CCE $> 95\%$ at an electric field strength of $1\,\mathrm{V/\mu m}$. The leakage current is less than 7 pA for $E = \pm 1.1\,\mathrm{V/\mu m}$. This is about six orders of magnitude smaller than the current read with α-particles, which is $\mathcal{O}(\mu\mathrm{A})$. The capacitance of *S57* is measured to be $C_\mathrm{d} = (2.0 \pm 0.3)\,\mathrm{pF}$ with an HP Agilent 4263B. This value is in good agreement with the theoretical value of $C_\mathrm{d}^\mathrm{th} = \varepsilon_r \varepsilon_0 \frac{A}{d} \approx 1.7\,\mathrm{pF}$.

4.2.1. IV characteristics

The amount of current which flows through a sensor as a function of the applied bias voltage is an important characteristic of the sensor itself. For a resistor R, Ohm's law $U = R \cdot I$ applies, or for a semiconductor $j = \sigma \cdot E$. In a semiconductor in thermal equilibrium the bulk conductivity is mediated by free charge carriers in the bulk. The higher the free charge carrier concentration the higher is the conductivity

$$\sigma = en\mu_e + hp\mu_h \equiv 1/\rho \tag{4.1}$$

with the resistivity ρ defined as the inverse conductivity. For the moment, it is assumed that the mobility of electrons and holes is about equal $\mu = \mu_e = \mu_h = 2000\,\mathrm{cm}^2/\mathrm{Vs}$, and the sum of free electrons and holes be $\bar{n} = n + p$. This results in

$$\sigma = e\bar{n}\mu. \tag{4.2}$$

The resistivity of a cuboid with length l in between two electrodes of area A is defined via its resistance R and dimensions A and l. With increased area A more current flows through the bulk at a given field strength, and with increased distance l between the electrodes the current decreases:

$$\rho = R\frac{A}{l}. \tag{4.3}$$

In reality, when a bias is applied to a piece of semiconductor, the measured current is not only flowing through the bulk of it, but additionally currents can flow along the

[1] Diamond-Like Carbon

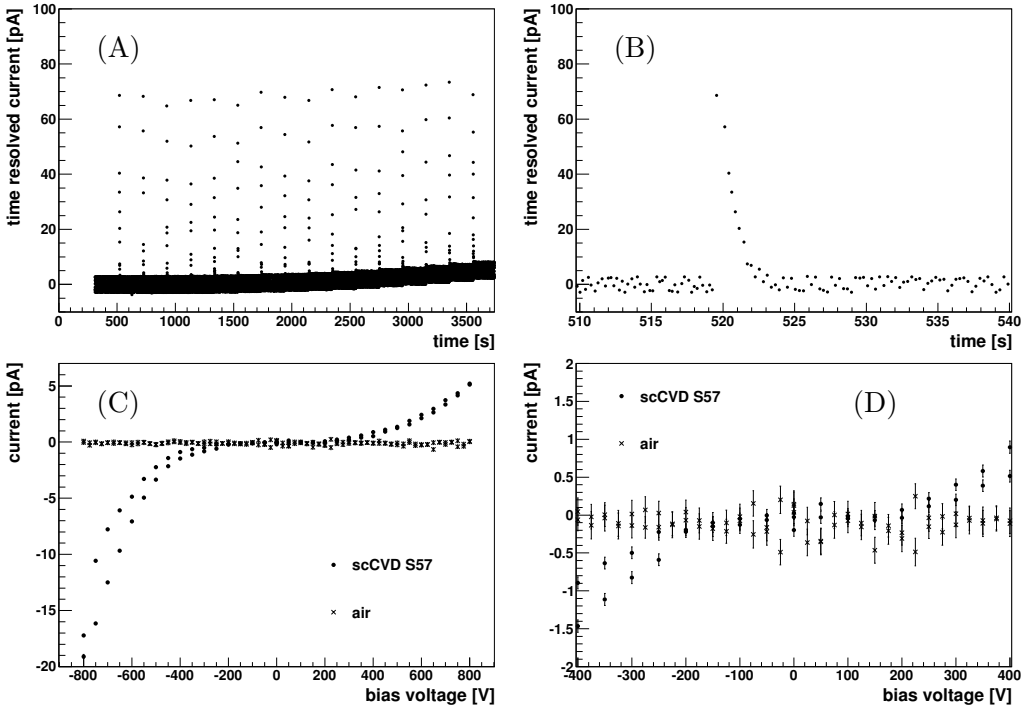

Figure 4.2.: The I-t measurement for *S57* is shown in **(A)** and a zoom into the first peak in **(B)**. **(C)** shows the derived IV characteristics with a comparison to an empty measurement. **(D)** provides a zoom of the centre region of **(C)**.

surface of the semiconductor, $j = j_{\text{bulk}} + j_{\text{surf}}$, which tampers the measurement of the bulk conductivity. The surface current is thought to flow via surface states, "cracks" in the surface induced by cutting and polishing procedures, remnants of surface treatments, etc. However, the measured current can be used as an estimate of the upper limit of the bulk conductivity assuming that all current is actually flowing through the bulk.

The measurement itself involves the repeated measurement of the current at a given bias voltage over time, over three minutes here. Then the bias is changed and the current is read again over three minutes. The current reading is repeated with ∼3 Hz. Starting at zero the bias is increased stepwise up to 800 V, then decreased down to -800 V and increased to 0 V again. The result for the diamond sample *S57* at RT is shown in Fig. 4.2. On the top left the current readings as a function of time are shown for biases between 0 V and 800 V, on the top right a zoom is shown. The spikes are the result of the bias change: With a higher bias applied to the sample, the detector capacity is charged. Hence a charging current flows which decreases exponentially within a few seconds, and a stable current of a few picoampere is reached again. The baseline reading has a noise rms of about 2 pA. After the baseline has been restored, the current readings are averaged, and the standard error of the mean is calculated. The mean is plotted with its standard error against the bias voltage in the bottom plots. A measurement without a sample is superimposed in order to check for any set-up related systematics. The "empty" measurement shows a flat IV characteristic.

The IV-characteristics of *S57* are neither symmetric nor linear. If the measured current was the bulk current, this would imply that the contacts are not ohmic, but rather of Schottky type. From the order of magnitude of the current, an upper limit of the free charge carrier density is derived. At 800 V the read current is ∼5 pA, resulting in a resistance of

$R = U/I = (1.6\pm0.1)\times10^{14}\,\Omega$ and a resistivity of $\rho = 6.7\times10^{14}\,\Omega\,\mathrm{cm}$. The conductivity is therefore $\sigma = 1.5\times10^{-15}\,(\Omega\mathrm{cm})^{-1}$. Finally, the free charge carrier concentration is

$$\bar{n} = \frac{\sigma}{e\mu} = (4.7\pm0.3)\,\mathrm{cm}^{-3}. \tag{4.4}$$

This is many orders of magnitude lower than for e.g. silicon. Note as well the impurity density, which is $\mathcal{O}(10^{14}\,\mathrm{cm}^{-3})$ according to the manufacturer specifications. This implies that almost no impurity is thermally excited. Considering the size of the diamond used here, the total number of free charge carriers is

$$N = \bar{n} \cdot V = 0.05 \approx 0. \tag{4.5}$$

This reflects the wide band gap of the diamond and supports the experimental finding that there are no known shallow (few tens of millielectronvolt) donor nor shallow acceptor levels in diamond.

4.3. Measurement Set-up

The set-up consists mainly of three parts: (1) The cryostat holding the liquid helium, (2) the inlet supplying various connections for sensors, valves, and a support for a tube which in turn provides a connection to an inner vacuum chamber situated inside and near the bottom of the cryostat, and (3) the electrical part used for the TCT measurement, temperature measurement, and temperature regulation via a heater. A schematic overview is depicted in Fig. 4.3.

The *cryostat*, shown diagonally hatched in Fig. 4.3, is a hollow cylinder, closed at the bottom, providing a volume of 40 l in its inside. For isolation, the cylinder walls are made of isolating materials. When the cryostat is e.g. about half filled with liquid helium, the helium has a temperature of 4.2 K, whereas the top of the volume is in contact with the lit of the cryostat, which remains at RT. A temperature gradient is therefore present in the cryostat volume. The ambient pressure in the cryostat is 1 bar for temperatures $T \geq 4.2\,\mathrm{K}$ and $< 1\,\mathrm{bar}$ for $T < 4.2\,\mathrm{K}$.

The *inlet* is prepared outside of the cryostat prior to the measurements. In cryogenics, the inlet describes the entirety of the cryostat's lit, cross-hatched in Fig. 4.3, providing various feed-throughs for sensors, support for the tube, the heat shields, which are connected to the lit, and possible other attachments. The inlet supported by a support structure is shown in Fig. 4.4 **(left)**. After preparation in the support structure, the inlet is hauled up with a crane and let in (respectively lowered into) the cryostat, hence the name. The support for the tube is situated in the centre of the lit. The tube vacuum feed-through (TVF), fitted with a KF50[2] vacuum flange to the tube support, is arranged around the tube and positions as well as mechanically holds the tube in the centre of the lit, see dashed box marked with "TVF" in Fig. 4.3 **(tube)**. The TVF is vacuum tight enough to support low vacua using rubber O-rings shown as blue circles. At the end of the inox steel tube, the inner vacuum chamber (IVC) is mounted, which provides room for the sensor holder. The IVC is evacuated prior to the measurements and then filled with helium gas to a pressure of $\sim5\times10^{-2}\,\mathrm{mbar}$. This provides an excellent thermal contact whilst maintaining a breakdown voltage above 1000 V. To be specific, the chosen pressure is below the position of the minimum of the Paschen curve, which describes the breakdown voltage

[2]KF XX = "Kleinflansch-Schnellverbindung" with nominal diameter of XX millimetre.

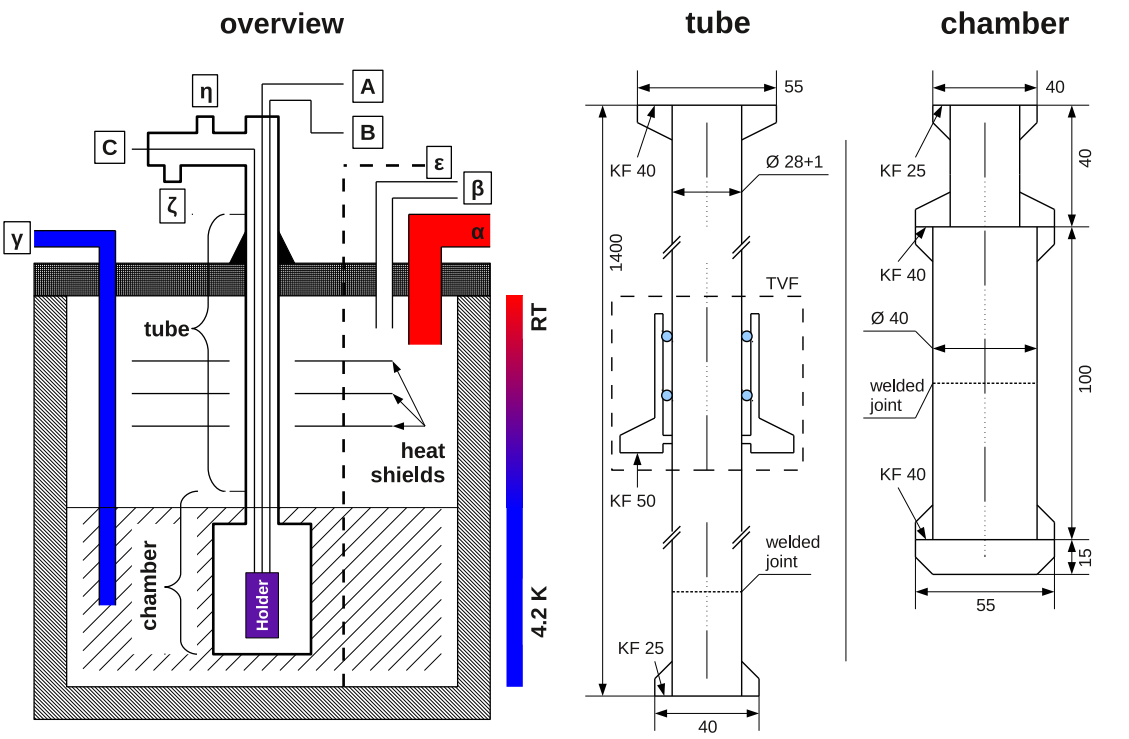

Figure 4.3.: An overview of the set-up including the cryostat with its various mechanical and electric connections is shown schematically, see text for details. On the right, the blueprints of the tube supplying the electric connections to the IVC, and of the IVC itself are illustrated.

as a function of the pressure. At $\sim 5 \times 10^{-2}$ mbar the breakdown voltage U_B increases rapidly with decreasing pressures, i.e. $dU_B/dp < 0$.

A series of photographs of the set-up is shown in Figs. 4.4, 4.5, 4.6. Different mechanical parts are denoted with Arabic numerals 1, 2, ..., electric connections are denoted with Latin capital letters A, B, C, and cryogenic/vacuum related connections with Greek letters α, β, ... The mechanical parts are: The head of the tube (1), the tube itself spanning from top to bottom in the left most picture of Fig. 4.4, the inlet (2) with its heat shields (3), the inner vacuum chamber (4), and the connection between tube and chamber (5). The connections of the inlet are: Vaporized helium out (α), pressure measurement for the cryostat volume (β), connection for the syphon used for liquid helium filling (γ), the support for the tube and its custom-made TVF (tube and TVF mounted, δ), and the connection for the level gauge (ε), which measures the liquid helium level in the cryostat. At the head of the tube, ζ marks the connection to the vacuum pump for the tube/IVC system, and η marks the connection for the pressure sensor of the tube/IVC system, cf. Fig. 4.5 **(middle)**. Besides the vacuum related parts, the head also provides the electrical feed-throughs for signal and temperature measurement as well as for the heater. The head has a plate providing four SMA feed-throughs on the top. The inside of the tube, i.e. the signal cable, heater cables, and temperature sensor cables, plus the cable support, are shown in Fig. 4.5 (top right, bottom right without tube, bottom left with tube). The SMA connection of the signal read-out is marked with A on the head side, and with A' on the IVC side of the set-up.

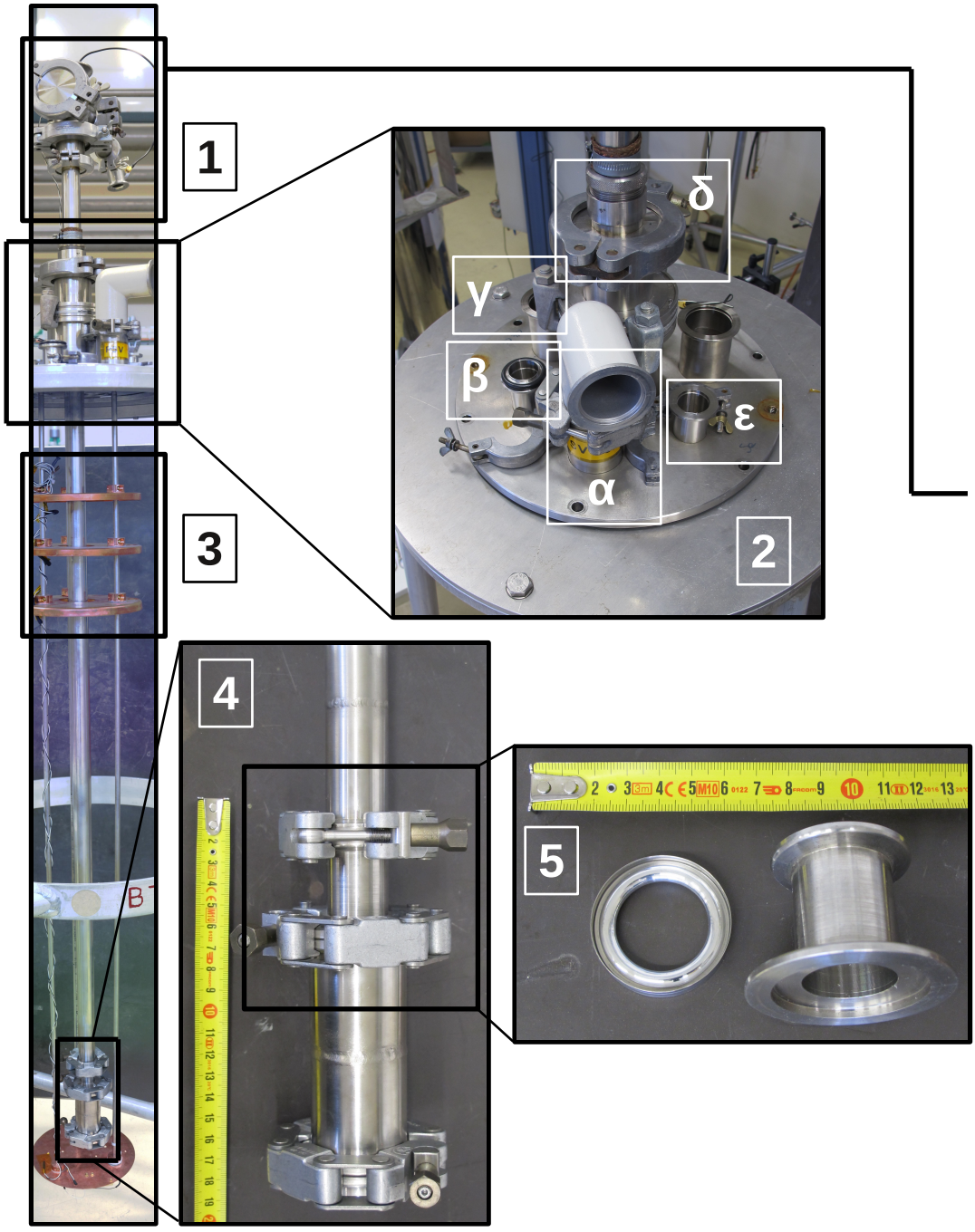

Figure 4.4.: Photographs of the set-up: The inlet with the tube, the head, and the IVC seen sideways **(left)**, the inlet in topview **(top)**, the IVC **(bottom middle)**, and the tube-IVC connection **(bottom right)**.

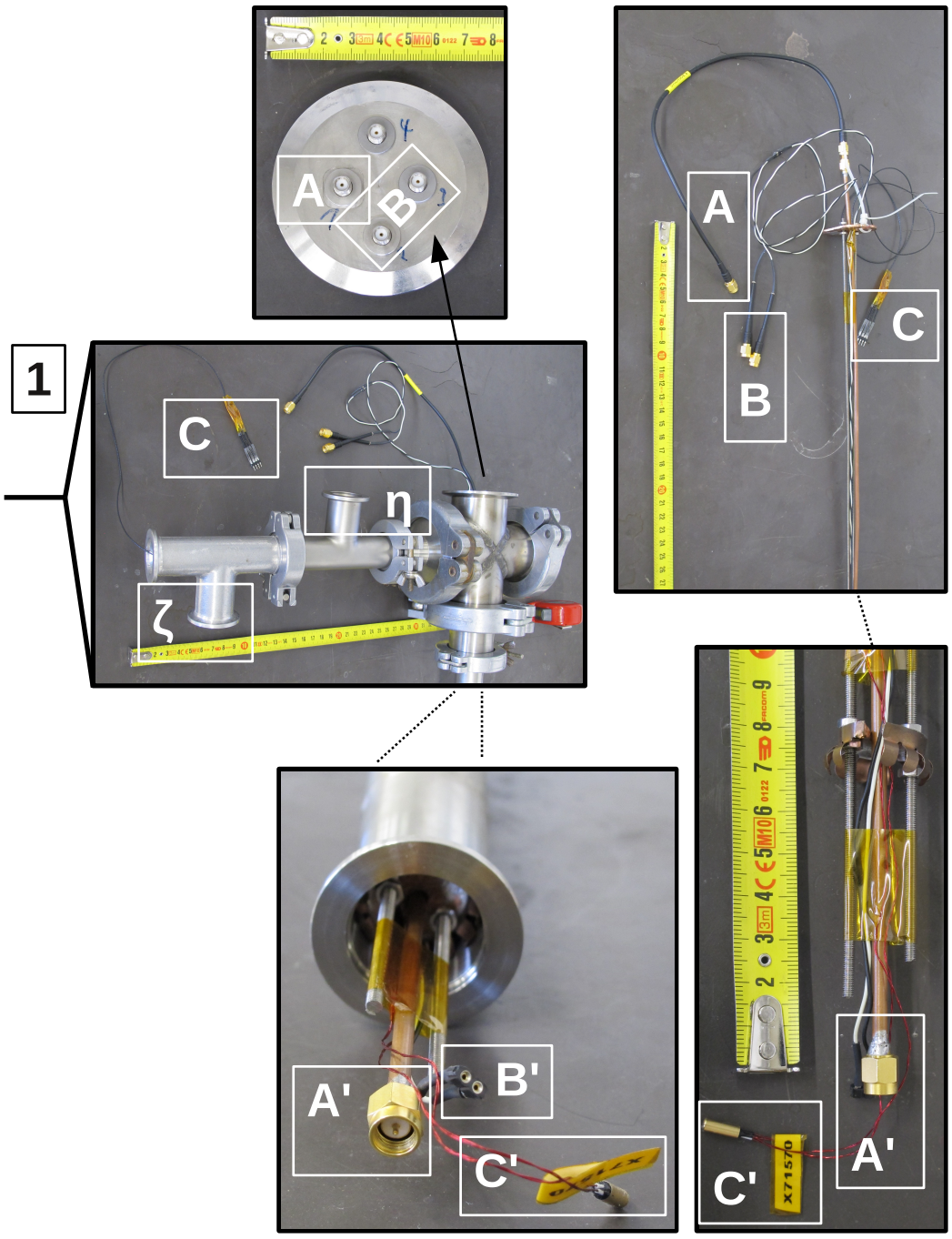

Figure 4.5.: Photographs of the set-up: The tube head together with the electrical connections for signal and temperature measurements and the heater connection **(left)**. Details of the signal line without tube **(right)**.

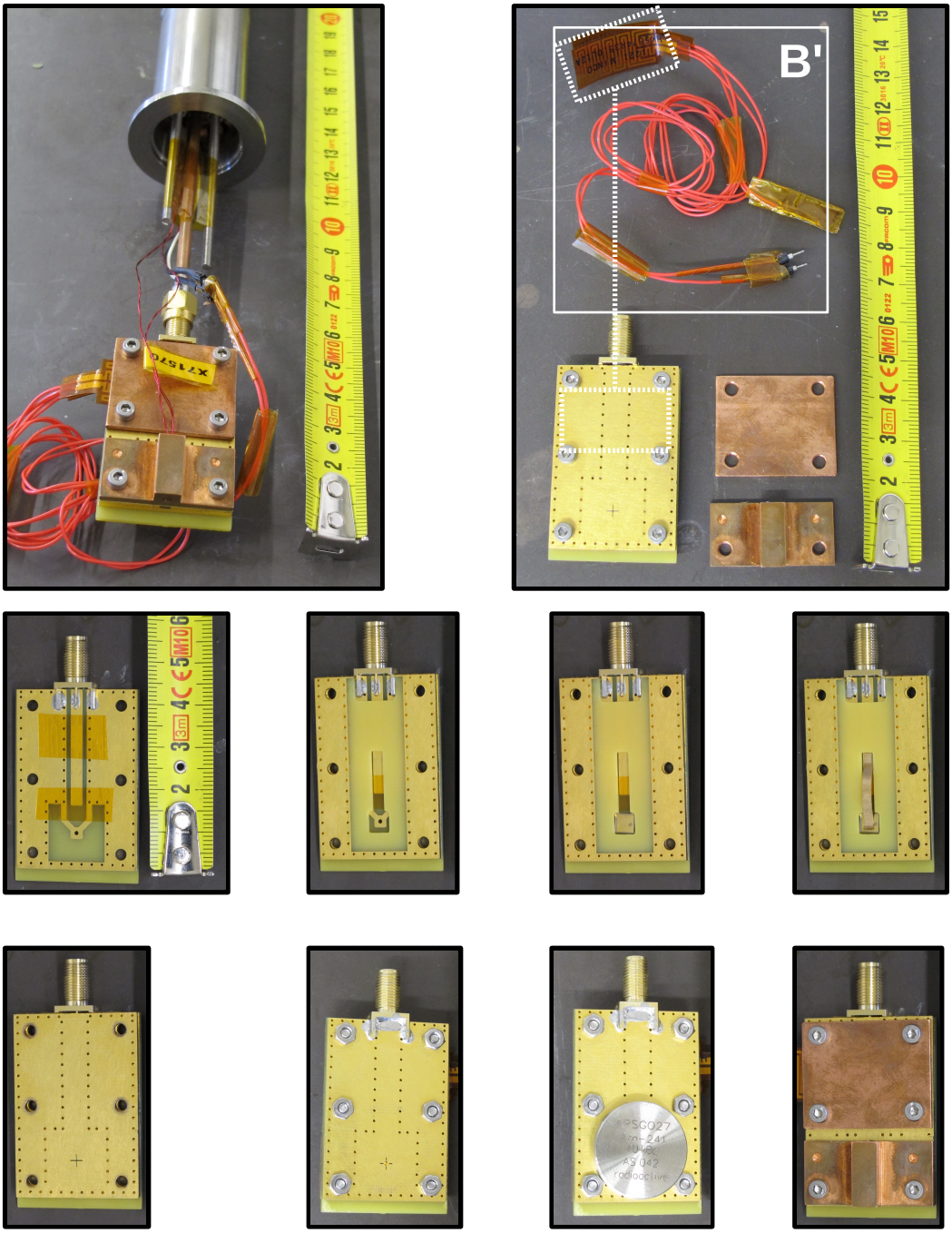

Figure 4.6.: Photographs of the set-up: The assembled detector holder **(top left)**, its various parts **(top right)**, and the step-by-step assembly **(middle and bottom row)**. (design patented by CIVIDEC Instrumentation GmbH)

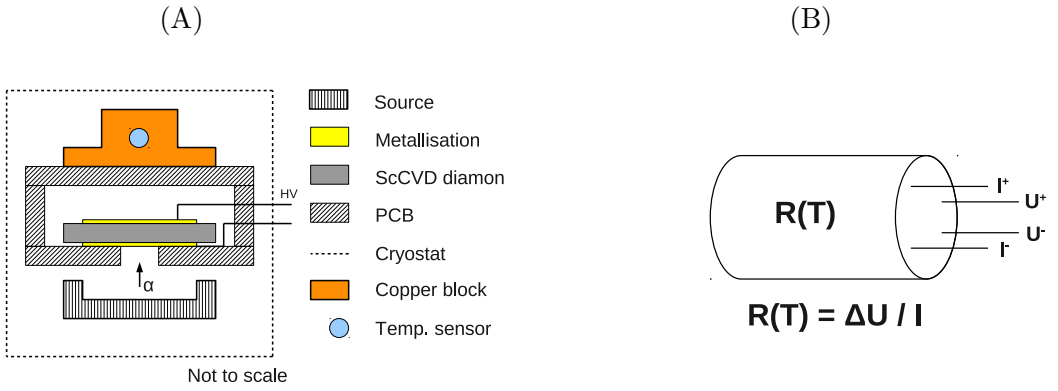

Figure 4.7.: A schematic cross-section view of the detector holder **(A)** are shown next to the principle of operation of the 4-point temperature measurement **(B)**.

B and B' denote the connections for the heater and C and C' those for the temperature measurement, head side and IVC side respectively.

The electrical part of the set-up used for the presented measurements consists of a PCB sensor holder providing 50 Ω read-out lines, a thermal heater, and a CERNOX temperature sensor. A hole of Ø = 1 mm at the bottom of the sensor holder collimates the α-particles from the ^{241}Am source and ensures that they impinge the detector only within the metallised area. The ^{241}Am source is located at a distance of 1.5 mm from the diamond's bottom electrode and the high voltage is applied to the top contact. The sensor holder is vertically inserted into the cryostat. An accurate temperature measurement (∼1 %) is ensured by placing a T-shaped copper brick on the outside of the sensor holder, which has been mechanically fixed to the holder for good thermal contact. The T-brick has a hole in which the temperature sensor is placed (C'). The electrical connection of the 50 Ω read-out lines to the amplifier, which is located outside of the cryostat, is realised via a vacuum-tight SMA feed-through.

A sketch of the cross-section view of the sensor holder is shown in Fig. 4.7 **(A)**. Figure 4.6 (second and third row) illustrates a step-by-step assembly of the holder. From left to right: The bottom PCB with the SMA jack, placement of the second PCB, insertion of the diamond, and insertion of the copper-plated beryllium spring for the realisation of the top contact. Then, placement of the top PCB, fixing with screws, placing of the ^{241}Am source on the bottom PCB, and placing of the copper plate for the heater fixation and of T-brick for temperature sensor on the top PCB.

The temperature measurement is realised via a 4-point measurement of a resistor, which has a temperature dependent resistance. Figure 4.7 **(B)** illustrates the principle of operation: A current source provides a constant current through the resistor R. The voltage drop over the resistor is measured on separate cables and is read with a Keithley 6517B. The resistivity is readily obtained by $R = \Delta U/I$. A table provided by the manufacturer reads the calibrated translation from resistance to temperature. Compare also Fig. 4.7 **(B)** with C' in Fig. 4.5.

The temperature adjustment is realised via two in series connected polyimide thermofoil heater manufactured by Minco [80]. With a fixed voltage applied to the heaters, the produced heat in a resistor R is $P = U \cdot I = U^2/R$. A constant energy input heats the holder and the sample. The sample and the holder are in thermal contact with the low pressure helium gas inside of the IVC. The gas is in thermal contact with the inner wall of the IVC,

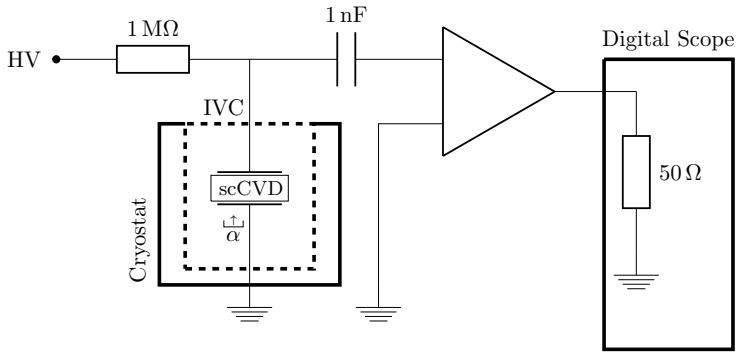

Figure 4.8.: The schematics of the α-TCT set-up.

whose outside wall is in contact with the liquid helium. Therefore the heat produced by the heaters is dissipated and a steady-state is reached between heat dissipation and heating, resulting in an adjustable, stable sample temperature.

The electrical schematics of the signal reading is shown in Fig. 4.8. The amplifier is AC-coupled to the HV line via a 1 nF capacitor. As electron-hole (e-h) pairs are created close to the bottom contact, one charge carrier type is collected there almost instantly, whilst the other drifts through the entire bulk along the [001] lattice direction to reach the top contact. Hole (electron) induced currents are read if a negative (positive) bias voltage is applied to the top contact. A Keithley 2410 is used in order to supply the bias voltage.

The α-source has an activity of roughly 40 kBq resulting in a particle flux of < 50 Hz for the chosen collimator size. Polarisation effects in the bulk of the sample due to strong radiation are thus avoided. In order to cross-check non-occurrence of polarisation effects, pulses have been compared for different radiation durations of the SUTs. The carrier transit time measured after ten minutes and after 100 minutes of radiation agree to better than $< 1\%$. Additionally, the sample was flipped over and current pulses were compared between before and after flipping. No significant differences are found.

The α-particles emitted from the ^{241}Am source have an energy of $\sim$5.5 MeV. The source is sealed with a palladium layer of $\sim$1.8 µm thickness. Taking into account the sealing and the metallisation of the SUT, the α-particles reach the bulk with $\sim$4.6 MeV, corresponding to $3.5{\times}10^5$ created e-h pairs in the bulk material under the assumption of an average e-h pair creation energy of 13.25 eV [66]. The measurements are consistent with space-charge-free (SCF) current measurements for all applied voltages.[3] At the lowest absolute applied bias voltage (30 V), the detector capacity is charged with $6{\times}10^{-11}$ C on the electrodes, or $0.37{\times}10^9\,e$, which is much larger than the number of induced e-h pairs per α-particle. Hence, the induced charge does not change significantly the electric field in the bulk region.

A 2 GHz, two-staged, bipolar transistor amplifier with an amplification factor of $A^{\mathrm{Q}}_{\mathrm{amp}} = (138{\pm}7)$ at 3.3 pF input capacitance, an rms noise at the output of $\sigma_{\mathrm{noise}} = 2.8$ mV at 3 GHz bandwidth, and an input resistance of $R_{\mathrm{in}} = 55\,\Omega$ amplifies the signal before it is read via an oscilloscope. The amplifier, built for diamond applications by CIVIDEC [81], has been tested and characterised prior to the measurements with test pulses of known amplitude and width. It shows a linear behaviour in the tested range from 10 µV to 1000 µV input amplitude. The minimum resolvable rise time with a 2 GHz amplifier is 180 ps. The cut-off frequency at -3 dB within a RC-circuit is $f_{\mathrm{cut}} = 1/(2\pi R_{\mathrm{in}}\,(C_{\mathrm{d}} + C_{\mathrm{stray}}))$. Including stray

[3] The electric field is changed only locally by the created free charges.

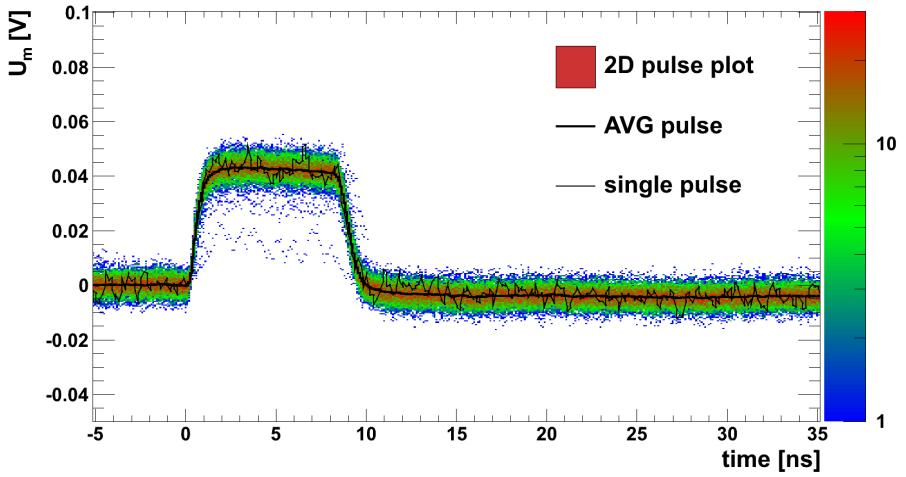

Figure 4.9.: A visualisation of the data taken at one temperature-voltage pair: The 300 recorded pulses are shown as a two-dimensional histogram, a single pulse and the average pulse are superimposed.

capacitances $f_{\text{cut}} \approx 1\,\text{GHz}$, $\tau_{\text{cut}} \approx 360\,\text{ps}$ is estimated and confirmed by data, see Sec. 5. The signal is read via a 1.6 m long, semi-rigid UT-85 cable to bring the signal out of the cryostat, and a 3.15 m high quality coax-cable outside of the cryostat. Both cables have an analogue bandwidth of ∼8 GHz. The digitalisation is realised via a LeCroy WavePro 7300A with 3 GHz analogue bandwidth at a sampling rate of 10 GS/s. Note that no bandwidth limitation nor filtering has been used. Only at small signal-to-noise ratios (SNR < 9), i.e. mostly at low bias voltages where the rise times are $> 2\,\text{ns}$, the bandwidth was limited to 200 MHz. A possible effect will be discussed later. In summary, the read-out system is fast enough to resolve fast signal rise times coming from the detector.

4.4. Data Taking and Processing

The oscilloscope's trigger settings are chosen such that individual pulses are recorded, when the pulse amplitude exceeds a certain threshold of a few millivolts in coincidence with a signal width $> 2/3$ of the actual width, which has been determined prior to each data taking with loose width cuts. However, the width cut was always $> 2\,\text{ns}$. The combination of the two conditions reduces the trigger rate of noise induced triggers to effectively zero without cutting any signal whilst maintaining a short measurement duration of a few minutes per voltage-temperature pair. For an α-TCT signal with width $< 2\,\text{ns}$ a drift velocity of $25\times10^6\,\text{cm/s}$ would be required for a sample thickness of 500 µm, which is much larger than the saturation velocity, which is of the order of $15\times10^6\,\text{cm/s}$.

Three hundred pulses were recorded for every given pair of temperature and bias voltage setting. Between two voltage settings, the HV was turned off for half a minute. After a temperature change, sufficient time was allowed to pass for the temperature to stabilise.

In the offline analysis the individual signals are corrected for trigger jitter and combined to form an average pulse. Only signals with an SNR > 3 are considered in order to reject pick-up triggers induced e.g. by other equipment in the laboratory. Figure 4.9 shows the main results of the combination of the single pulses to form an average pulse. The two-dimension scatter plot is 2D-histogram filled with 300 single acquisitions. A logarithmic

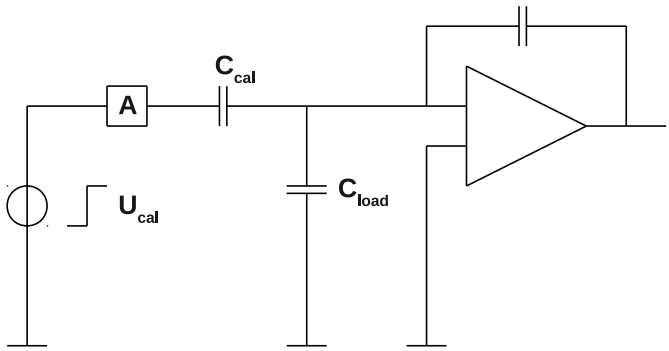

Figure 4.10.: The schematics of the charge calibration set-up is illustrated. The calibration capacity is $C_{\mathrm{cal}} = 0.9\,\mathrm{pF}$, the calibration voltage is $U_{\mathrm{cal}} = 243\,\mathrm{mV}$.

colour scheme at the side reads the number of entries per bin, with red (blue) marking the highest (lowest) counts. One example of a single pulse is superimposed. Finally, the averaged pulse (AVG) is also superimposed as a solid black line, the black line coinciding with the red region of the 2D-histogram.

To verify the set-up, published results obtained with a scCVD diamond ([29], sample *CVD2* in [77]) have been compared to results obtained with the present set-up using again the *CVD2* diamond sample. The pulse widths agree to better than 2%.

4.5. Calibration

To calibrate the set-up in an absolute manner, a *charge* sensitive amplifier, which is used for spectroscopic applications, has been used to measure the total induced charge as a function of the electric field strength at room temperature. Prior to the calibration of the measured charge with the α-source, the used charge amplifier was calibrated. The schematics of the calibration set-up are depicted in Fig. 4.10. A calibration pulse of $U_{\mathrm{cal}} = (243\pm5)\,\mathrm{mV}$ is used to create a calibration charge Q_{cal} using a capacitor C_{cal} with $C_{\mathrm{cal}} = (0.90\pm0.02)\,\mathrm{pF}$ and an attenuator A with $A = (-10.0\pm0.5)\,\mathrm{dB}$. Hence, $Q_{\mathrm{cal}} = U_{\mathrm{cal}} \cdot 10^{A/20} \cdot C_{\mathrm{cal}} = (69.2\pm4.5)\,\mathrm{fC}$, which is close enough to the actual measured charge with α-particles. The capacitive load at the amplifier input was matched to the capacitance of the detector holder later used in the experiment: $C_{\mathrm{load}} = (10.1\pm0.3)\,\mathrm{pF}$. The test charge is amplified by the charge amplifier producing a pulse with an amplitude of $a = (592\pm12)\,\mathrm{mV}$. Thus, the amplification factor is $A^{\mathrm{Q}}_{\mathrm{amp}} = \frac{a}{Q_{\mathrm{cal}}} = \frac{592\,\mathrm{mV}}{69.2\,\mathrm{fC}} = (8.6\pm0.6)\,\mathrm{mV/fC}$. Hence, the amplification factor is uncertain by $\sim$7 %.

In Fig. 4.11 the measured charge (measured voltage multiplied by $A^{\mathrm{Q}}_{\mathrm{amp}}$) using α-particles is plotted as a function of the electric field strength at RT and normal pressure. Only in the calibration set-up, the α-particles lose energy during their travel in air, and reach the bulk with less than 4.6 MeV, namely $E^{\mathrm{air}}_{\alpha} = 4.28\,\mathrm{MeV}$. At lower field strengths, less than the full charge is measured, and the measured charge increases with increasing fields, saturating at about $\sim$0.8 V/µm at a total charge yield of $Q_0 = (59.5\pm4.2)\,\mathrm{fC}$. At $\sim$0.3 V/µm, the measured charge surpasses 95 % of the total charge obtained at fields $E \geq 1\,\mathrm{V/\mu m}$. An explanation often given for the missing charge at moderate field strengths is the more probable trapping of charge carriers at these fields, as their drift is slower. During the slower drift, the charges cover a longer distance as their relative movement is dominated by the fast thermal walk, compared to the slow drift of the centre of mass. That this is not

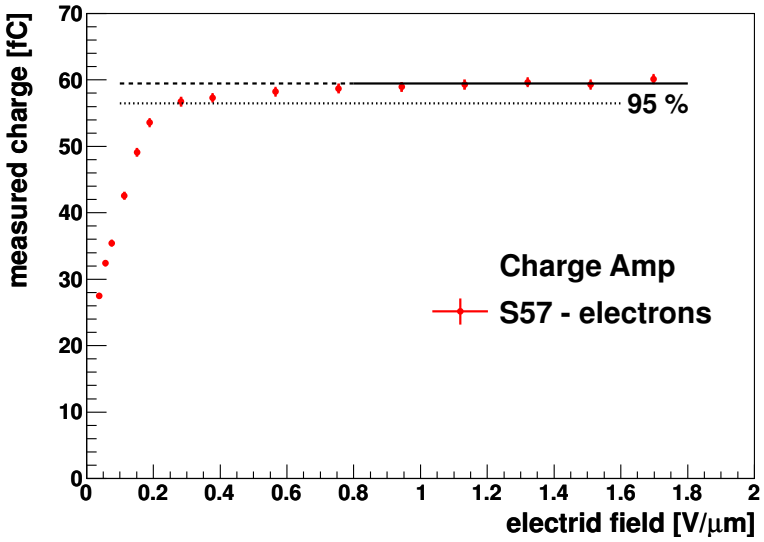

Figure 4.11.: The measured charge as measured with a *charge* sensitive amplifier is plotted as a function of the electric field. The full charge at high fields is obtained by a straight line fit (solid line) from 0.8 to 1.8 V/µm: $Q_0 = (59.5 \pm 0.3)$ fC. The error is the statistical uncertainty of the fit. At ∼0.3 V/µm the CCE surpasses 95 % (dotted line).

the case in the samples tested here is readily visible from the *flat* pulse forms presented in Chap. 5. The flatness is evidence for an negligible amount of charges being trapped during drift. It is thought that at lower biases, less charges start their drift, and hence less total charge is measured whilst maintaining a flat signal current. The full model is given in Chap. 5.

From the above measurement, also the average pair creation energy in diamond, E_{pair}, is readily derived using $N_0 = Q_0/e$

$$E_{\text{pair}} = \frac{E_\alpha^{\text{air}}}{N_0} = (11.5 \pm 0.8)\,\text{eV/pair}. \tag{4.6}$$

The measured pair creation energy lies two σ below the reference value of 13.25 eV. However, as reported in Ref. [65], the pair creation energy in diamond is sample-dependent and varies with the used radiation. It is also worth noticing, that their might be a difference between the produced and the measured charge. The produced charge is likely to be almost independent of the sample when compared between single-crystal specimen, as the momentum transfer of the ionising α-particle to the shell electrons is unlikely to depend on the quality of the crystal. But, as will be seen in Chap. 5, charges can bind rapidly into neutral excitons, and hence avoid drift, and subsequently recombine. If the recombination process is sufficiently fast, only a fraction of the produced charge actually starts drifting. It might therefore be valid to assume, that the physical pair creation energy in diamond lies below 13 eV, but that fast recombination (below 1 ns) of a fraction of the charges influence the measurement of the total charge. If the fraction of drifting, and hence measured charges of all produced charges is $\alpha = {}^{Q_m}/_{Q_0}$, a corrected form of Eq. (4.6) becomes

$$E_{\text{pair}} = \alpha \frac{E_\alpha}{N_m}, \tag{4.7}$$

where $\alpha < 1$ and might be sample-dependent, radiation dependent, temperature dependent, among others, and needs to be quantified for each case.

5. RESULTS & DISCUSSION OF TCT MEASUREMENTS

5.1. Induced Pulses from Carrier Movement

Hole and electron induced currents were recorded within a time window of 200 ns for temperatures between $T = 295\,\mathrm{K}$ and 2 K. The bias voltage was set between $30\,\mathrm{V} \leq |U_{\mathrm{bias}}| \leq 900\,\mathrm{V}$ in different step sizes. Figures 5.1, 5.2, and 5.3 show the recorded and averaged pulses for the samples *S57*, *S52*, and *S79*, respectively, at $\pm 500\,\mathrm{V}$ **(top row)** and $\pm 100\,\mathrm{V}$ **(bottom row)** for holes **(left column)** and electrons **(right column)**. The electron pulses are shown inverted. Additional pulses for *S57* are published in Ref. [82]. For temperatures $T \geq 150\,\mathrm{K}$ and $T \leq 75\,\mathrm{K}$ fast rise times ($t_{\mathrm{rise}} < 2\,\mathrm{ns}$) are observed for both hole and electron pulses at $\pm 500\,\mathrm{V}$. At lower fields both the rise time and the fall time increase. This is due to an increased diffusion with longer transit times and a mechanism explained in Sec. 5.3.

The rising edge of the signal marks the start of the charge drift. The falling edge marks the collection of charges at the opposite electrode. The time resolution for a single pulse at RT and $E = 0.94\,\mathrm{V/\mu m}$ is $\sigma_{\mathrm{t}} = \frac{\sigma_{\mathrm{noise}}}{\mathrm{slope}} \leq \frac{2.8\,\mathrm{mV}}{50\,\mathrm{mV/1\,ns}} \leq 60\,\mathrm{ps}$. Note that the initial distribution of the charge cloud also has an effect on the signal edges.

To the second half of the rising edge a fit of the form $C \cdot \left(1 - \exp\left(-t/\tau_{\mathrm{rise}}\right)\right)$ is performed to all averaged pulses at RT. At fields larger than $0.8\,\mathrm{V/\mu m}$ the time constant of the rising edge is 350 ps to 400 ps, and it increases towards lower fields. The value for the time constant found here matches the expected cut-off frequency of the measuring system, cf. Chap. 4.

At RT the signal has an almost flat top during the drift as a consequence of the field being constant over the diamond. In turn, this means that the net space-charge in the samples is small. A net space-charge of the order of $\sim 10^{11}\,e/\mathrm{cm}^3$ already leads to a significant change in pulse shape, i.e. an exponential current behaviour. [29] Such intrinsic net space-charge seems to be absent in all three samples. For $\pm 500\,\mathrm{V}$ ($E = 0.94\,\mathrm{V/\mu m}$) the pulses become shorter with decreasing temperature due to a higher carrier mobility as acoustic phonon scattering decreases with decreasing temperature, see Sec. 5.2.4.

In contrast to the temperature range $T < 75\,\mathrm{K}$ and $T > 150\,\mathrm{K}$, the observed pulse shape depends strongly on the temperature for $75\,\mathrm{K} \leq T \leq 150\,\mathrm{K}$. The rising edge develops an $1 - \exp\left(-t/\tau\right)$ behaviour while the falling edge develops a long exponentially falling tail. These features are attributed to a retaining-releasing mechanism, in which charges are retained inside the initial high density charge cloud, produced by the α-particle, due to the creation of excitons, as will be discussed in Sec. 5.3. These charges are then released with a certain temperature dependent time constant, if they have not recombined before. Note that neither polarisation nor a non-zero net-effective space charge can explain the apparent temperature dependence of the shape. The same effect on the pulse shape has been verified in all three SUTs. The decrease in area, i.e. total signal charge, with decreasing temperature for $T < 150\,\mathrm{K}$ is due to an enhanced recombination and increased release time constant from the charge cloud. A model explaining the temperature dependence of the pulse shape is presented together with a data based estimation of the involved time constants in Sec. 5.3.

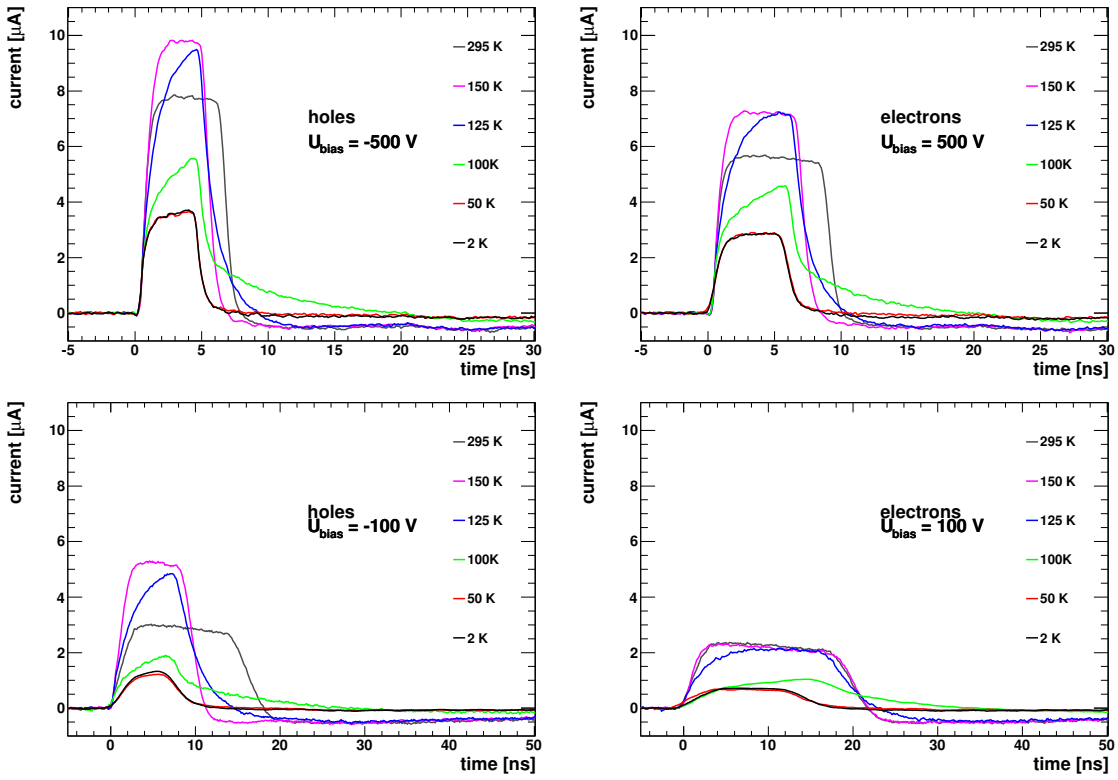

Figure 5.1.: Averaged current pulses for holes/electrons **(left/right column)** at various temperatures for $U_{\text{bias}} = \pm 500\,\text{V}$ **(top row)** and $U_{\text{bias}} = \pm 100\,\text{V}$ **(bottom row)** are shown for *S57*. The pulses for 2 K and 50 K overlap almost completely for both electron and holes. Note as well the similarity of electron pulses at 150 K and 295 K.

The recorded current does not drop to zero after all charges have been collected but rather undershoots slightly. This is likely caused by a non-perfectly optimised amplifier or due to the capacitance of the cable connecting the detector and the current amplifier. The amplitude of the undershoot correlates with the total induced signal, hence at temperatures smaller than 150 K the undershoot decreases with decreasing temperature.

5.2. Temperature Dependence of Charge Carrier Properties[1]

The temperature dependence of the low-field mobility has not been studied for temperatures below 80 K. Two studies, by Nava, Canali, et al. [66, 84, 85] and Gabrysch [86] for holes, study the drift velocities and mobilities of charge carriers in diamond at below room temperature. Here [82, 83], charge carrier properties are studied below 80 K, and for the first time down to 2 K.

5.2.1. Transit time

The transit time, t_{t}, is determined by the time difference between the end time and the start time of drift, t_{e} and t_{s}, respectively, hence $t_{\text{t}} = t_{\text{e}} - t_{\text{s}}$. A function $f(t; P)$ is fitted to each

[1] cf. Ref. [83]

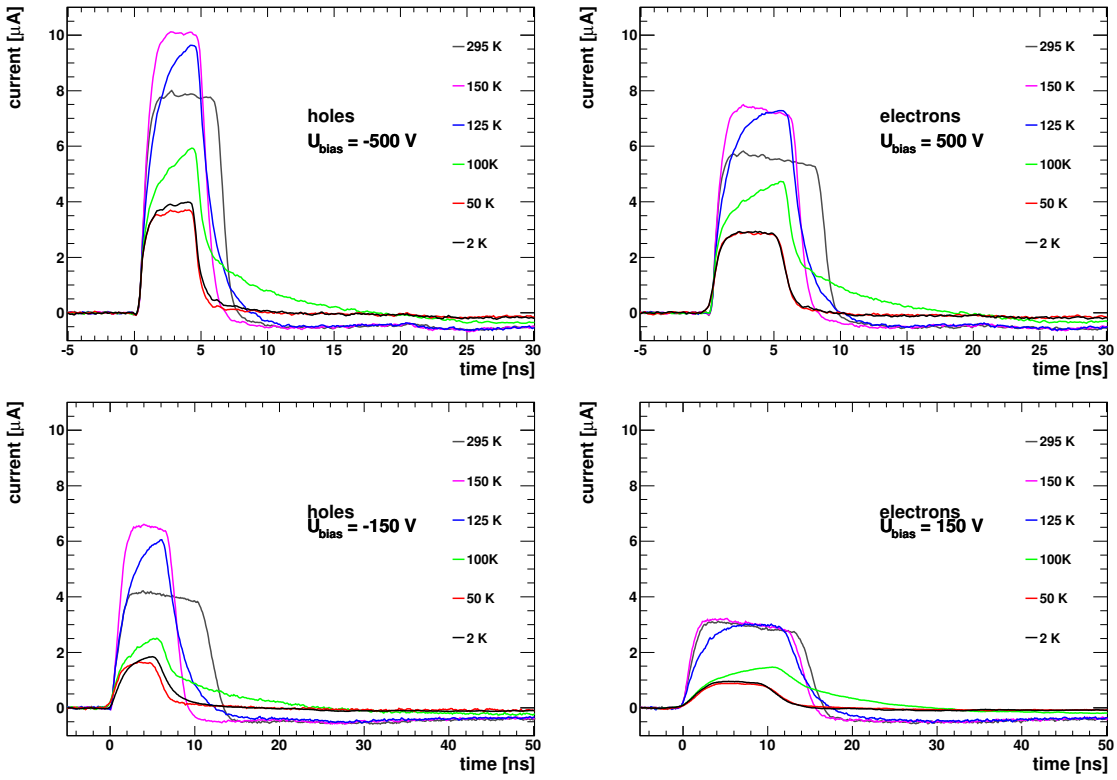

Figure 5.2.: Current pulses for *S52*, see caption of Fig. 5.1.

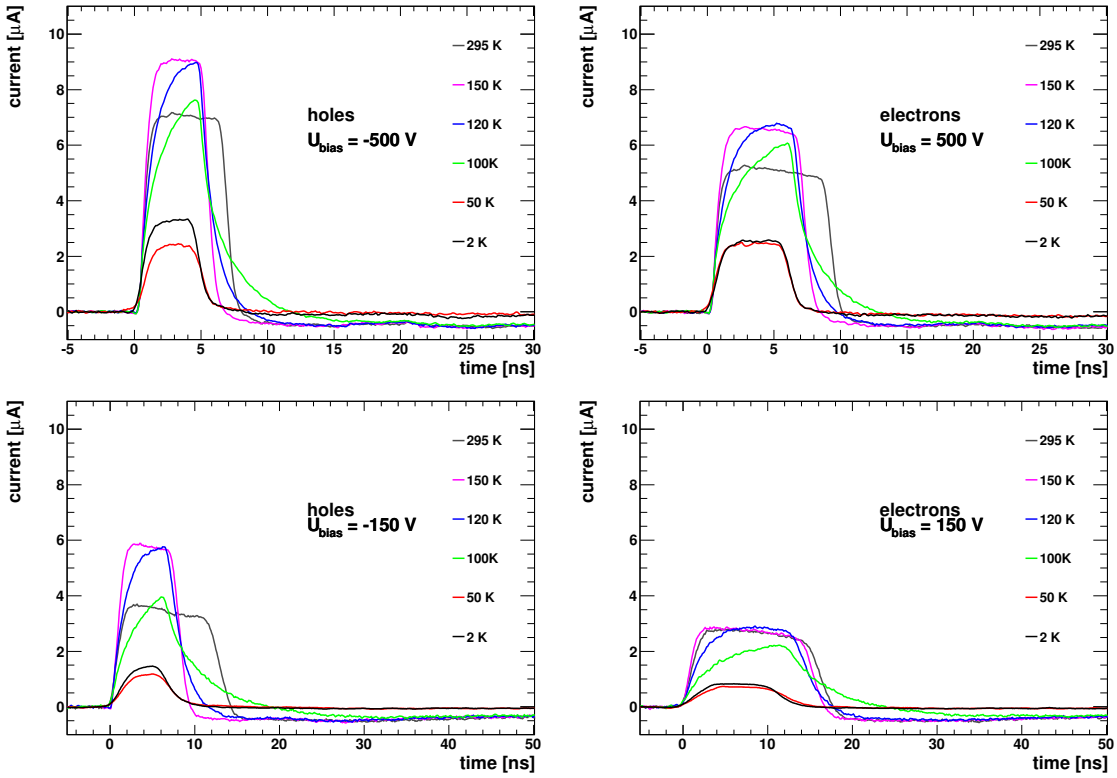

Figure 5.3.: Current pulses for *S79*, see caption of Fig. 5.1.

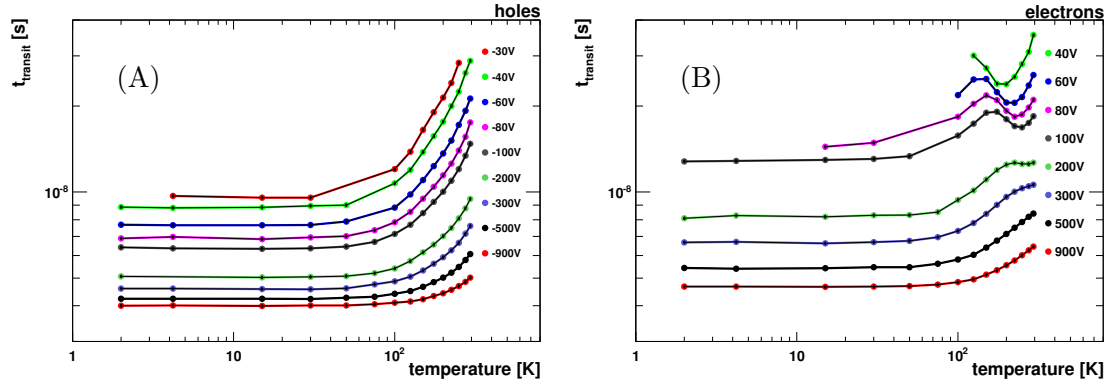

Figure 5.4.: The transit times for holes **(A)** and electrons **(B)** at various temperatures and fields are shown for *S57*. Note the double logarithmic scale. Lines are drawn for constant voltages in order to guide the eye.

current pulse in order to find t_e and t_s. $f(t;P)$ is a function of time and a set of parameters P incorporating two complementary error functions $(2-\mathrm{Erfc}(t-t_s))$ and $\mathrm{Erfc}(t-t_e)$ describing the rising and the falling edge, respectively. Additionally, an exponential component of the form $(1-\exp(-(t-t_s)/\tau)) - \Theta_{col}(t;t_e)$ with $\Theta_{col}(t;t_e) = 1-\exp(-(t-t_e)/\tau)$ for $t > t_e$ and $\Theta_{col}(t;t_e) = 0$ otherwise, is allowed, cf. Eq. (3.7). The error functions describe a Gaussian probability distribution for the start time of the drift around t_s, and respectively a collection at the opposite electrode around t_e. The 50% points mark t_s and t_e, respectively. The exponential part accounts for the charge release from the inner part of the charge cloud and its respective collection.

The influence of the integration effect of the sensor capacitance on the transit time has been evaluated. For this, measured voltage pulses $u_m(t)$ have been translated into current pulses $i_m(t)$, corrected for the integration effect using

$$i_m(t) = \frac{1}{A_{amp} R_{in}} \left[u_m(t) + R_{in} C_d \frac{\mathrm{d}u_m(t)}{\mathrm{d}t} \right] . \tag{5.1}$$

The difference in transit time between input capacitance corrected current pulses and non-corrected current pulses is negligible. The correction term has thus been omitted.

The measured transit times are shown in Fig. 5.4 for *S57* as an example. All three SUTs show the same behaviour. Transit times range from 3 ns to 40 ns for field strengths and temperatures examined in this work. Experimental sources of uncertainties affecting the measurement of the drift velocity are listed below including an estimate of their values.

(1) The uncertainty in sample thicknesses is estimated to be $< 1\%$.

(2) The error in the measurement of the transit time σ_{t_t} depends on the ability to identify the rising and the falling edge, which in turn correlates with the signal-to-noise ratio (SNR). The SNR depends on the temperature and the electric field. σ_{t_t} is estimated as $\sigma_{t_t} = \frac{\sigma_{noise}}{slope}$. At room temperature (low temperature) and $E \approx 1\,\mathrm{V/\mu m}$, this approach leads to uncertainties of the transit time measurement of approximately 1% (2%), and up to 4% at low fields.

(3) At low SNRs the bandwidth limit was used in order to extent the accessible measurement range towards lower electric fields. The bandwidth limit leads to slower rising and falling edges. The effect on the transit time at $U_{bias} = 100\,\mathrm{V}$ at RT is $\sim$1 %. At lower biases the rising/falling edges are slower, hence the effect is smaller.

(4) Errors due to a possible non-uniformity of the electric field can be neglected, as a net-space charge seems to be absent in the tested samples.

(5) The uncertainty in the electric field strength is conservatively estimated to 1%.

(6) The uncertainty of the temperature measurement is about 1%.

Figure 5.4 **(A)** shows how the transit time for holes increases with increasing temperature over the entire temperature range, and how it decreases with increasing field strength over the whole field range. For electrons, Fig. 5.4 **(B)**, the transit time decreases with increasing field but does not monotonically increase with increasing temperature for all biases. Only at high biases, down to 500 V, the transit time increases with increasing temperature over the whole temperature range. For smaller biases, a local maximum emerges, being more pronounced with decreasing bias. The position of the local maximum shifts to lower temperatures with decreasing bias. The abnormal behaviour of the electron transit time is likely to be caused by a re-population effect (see Sec. 2.2.7), a well-understood phenomenon in silicon [87]. It was recently observed in high-purity scCVD diamond [88], but at much lower temperatures and fields. A theoretical model that explains the main features of the observed electron transit times is given in Sec. 5.4.

5.2.2. Drift velocity

The recorded signal is induced by the movement of all drifting carriers. Hence the measured transit time is the average over their entirety. The measurement of the transit time t_t allows to calculate the average drift velocity as

$$\mathrm{v}_\mathrm{drift}(E) = \frac{d}{t_\mathrm{t}(E)}. \tag{5.2}$$

For holes a drift velocity of $\mathrm{v}^h_\mathrm{drift}(295\,\mathrm{K}) = (8.69\pm0.05)\times10^6\,\mathrm{cm/s}$ and for electrons of $\mathrm{v}^e_\mathrm{drift}(295\,\mathrm{K}) = (6.28\pm0.04)\times10^6\,\mathrm{cm/s}$ is measured averaged over all samples at $0.94\,\mathrm{V/\mu m}$. More values are given in Tab. 5.1.

Figure 5.5 shows the average drift velocity for holes **(left column)** and electrons **(right column)** as a function of the electric field for various temperatures. The bottom row shows the results in double logarithmic scale. The trend of the drift velocity is inverse to the trend of the transit time discussed above. For holes the drift velocity increases for a constant bias voltage with decreasing temperature. Likewise, it increases for a given temperature with increasing field strength and saturates at high fields, the asymptote yielding the saturation velocity. For electrons the deviation from the expected behaviour is again visible at low fields. Uncertainties are obtained using error propagation.

The Drude model of transport properties of electrons in materials [28] predicts a linear dependence of the drift velocity on the electric field $\mathrm{v}_\mathrm{drift} = \mu_0 E$. It is well known that this only holds true for low field strengths. With increasing fields the drift velocity saturates at a value v_sat as the carriers acquire more energy from the field in between scattering processes and hence obtain a higher effective temperature than the lattice. This results in frequent emission of optical phonons. [13] Hence, the field dependent drift velocity [44]

$$\mathrm{v}_\mathrm{drift}(E) = \mu(E)E = \frac{\mu_0 E}{1 + \dfrac{\mu_0 E}{\mathrm{v}_\mathrm{sat}}}\ , \tag{5.3}$$

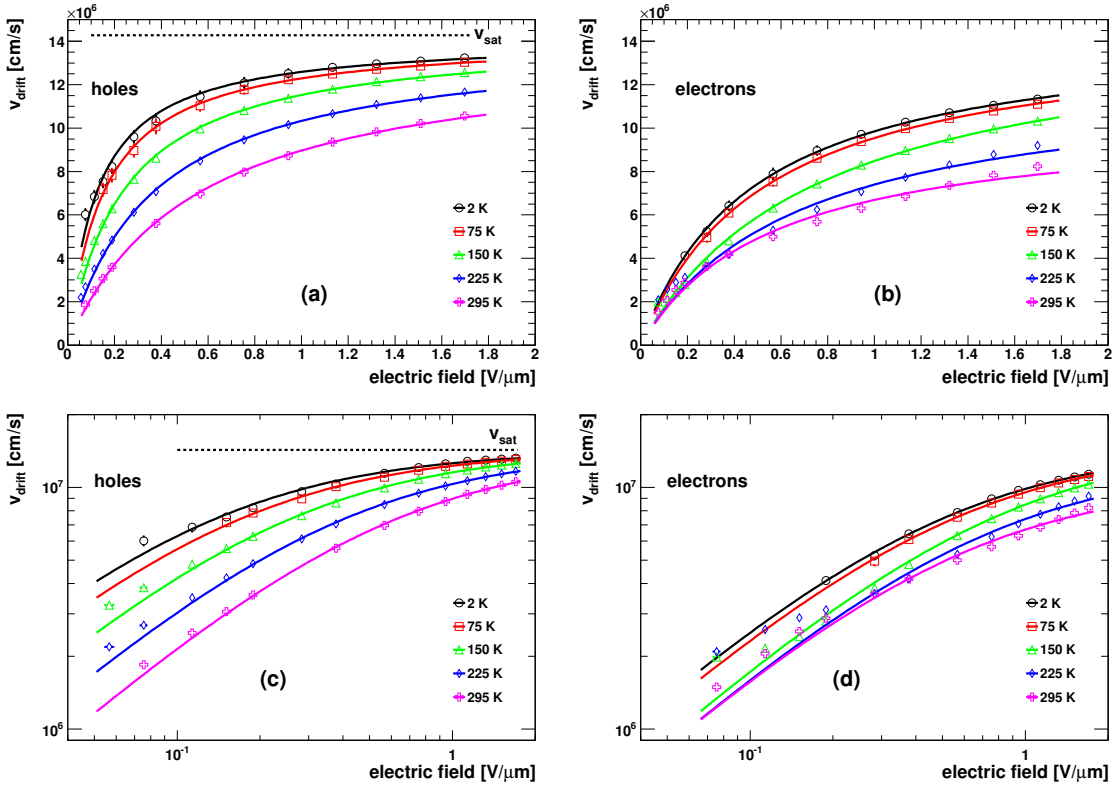

Figure 5.5.: The drift velocity is plotted against the electric field for different temperatures for *S57* in linear scale (**(a)**, **(b)**), and double logarithmic scales (**(c)**, **(d)**). The superimposed solid lines are fits according to Eq. (5.3). The dotted line shows the saturation velocity for holes, which is independent of the temperature, see Fig. 5.6. The electron saturation velocity is not constant.

is used, where μ_0 is the low-field mobility, cf. Sec. 2.2.7. The model reduces to the Drude model at low fields ($\mu(E) \xrightarrow{E \to 0} \mu_0$) and accounts for a saturation velocity v_{sat} towards high fields.

Equation (5.3) is fitted over the entire field range to both the electron and the hole data in order to check the validity of the model. The fits are superimposed in Fig. 5.5. For holes the model describes the data very well at all temperatures with a $\chi^2/\mathrm{ndf} \lesssim 1$ using the uncertainties discussed above. In order to obtain a better estimate for the uncertainties, the uncertainties are decreased until $\chi^2/\mathrm{ndf} = 1$. For electrons, a clear deviation from the model is visible, most easily spotted in the double logarithmic presentation, as Eq. (5.3) does not incorporate a possible re-population effect in the low field region. Since the model does not describe the electron data well at low fields, the procedure to adjust the uncertainties used for holes is not feasible for the electron data. Instead, the same corrections as obtained for the hole data is used, assuming the same temperature dependence of uncertainties for electrons and holes.

In order to extract the saturation velocity and its uncertainty, the fit is done once in the high field region. v_{sat} is then fixed and the fit is redone in the low field region in order to determine μ_0. Note that for electrons the drift velocity is not yet a linear function of the field at the lowest accessible biases. The performed fit can hence only serve to extract a lower limit on the electron low-field mobility.

Table 5.1.: The drift velocity (in 10^6 cm/s) for holes and electrons at various temperatures for three SUTs at ±500 V (≈ 1 V/µm). The sample average is given in the last two columns.

	S52		S57		S79		AVG	
	$v^h_{drift}(T)$	$v^e_{drift}(T)$	$v^h_{drift}(T)$	$v^e_{drift}(T)$	$v^h_{drift}(T)$	$v^e_{drift}(T)$	$v^h_{drift}(T)$	$v^e_{drift}(T)$
295 K	8.72 ± 0.08	6.33 ± 0.06	8.73 ± 0.08	6.30 ± 0.06	8.61 ± 0.07	6.20 ± 0.06	8.69 ± 0.05	6.28 ± 0.04
150 K	11.34 ± 0.12	8.36 ± 0.10	11.38 ± 0.16	8.29 ± 0.12	11.12 ± 0.12	8.06 ± 0.10	11.28 ± 0.09	8.24 ± 0.07
2 K	12.42 ± 0.15	9.79 ± 0.12	12.52 ± 0.19	9.71 ± 0.15	12.48 ± 0.20	9.60 ± 0.17	12.47 ± 0.11	9.70 ± 0.09

5.2.3. Saturation velocity

The fit results of the parameters v^h_{sat} and v^e_{sat} as a function of temperature are shown in Fig. 5.6 for holes **(left)** and electrons **(right)**. The saturation velocity for holes are $v^h_{sat}(295\,K) = (14.2\pm0.2)\times10^6$ cm/s and $v^h_{sat}(2\,K) = (14.2\pm0.2)\times10^6$ cm/s, and for electrons $v^e_{sat}(295\,K) = (13.2\pm0.3)\times10^6$ cm/s and $v^e_{sat}(2\,K) = (14.2\pm0.2)\times10^6$ cm/s averaged over all samples. The values found at room temperature are in good agreement with results reported earlier. [29]

The temperature dependence of the saturation velocity was modelled to follow [41]

$$v_{sat} = \sqrt{\frac{8E_{opt}}{3\pi m_{dos}} \tanh\left(\frac{E_{opt}}{2k_B T}\right)}, \tag{5.4}$$

predicting an almost constant saturation velocity between 2 K and RT, as $E_{opt} = 163$ meV. In this work, the hole saturation velocity v^h_{sat} is found experimentally to be almost independent of the temperature. However, this seems not to be the case for electrons. For holes, a constant fit to the saturation velocity data is done over the whole temperature range for each sample individually. The found values are $v^h_{sat}(S52) = (14.21\pm0.06)\times10^6$ cm/s, $v^h_{sat}(S57) = (14.28\pm0.07)\times10^6$ cm/s, and $v^h_{sat}(S79) = (14.20\pm0.07)\times10^6$ cm/s, with a sample average of $v^h_{sat} = (14.23\pm0.04)\times10^6$ cm/s. For electrons, v^e_{sat} seems to stabilise only below 100 K, and a constant fit is performed in this region. Regarding the three SUTs, the fits yield $v^e_{sat}(S52) = (14.23\pm0.19)\times10^6$ cm/s, $v^e_{sat}(S57) = (14.31\pm0.22)\times10^6$ cm/s, and $v^e_{sat}(S79) = (14.15\pm0.23)\times10^6$ cm/s, with a sample average of $v^e_{sat} = (14.23\pm0.12)\times10^6$ cm/s. It is interesting to see that at low temperatures the saturation velocity for electrons and holes are equal within their uncertainties.

5.2.4. Low-field mobility

The fits result in a sample averaged low-field mobility of holes (μ^h_0) and a lower limit of the low-field mobility of electrons ($\underline{\mu}^e_0$) at RT of $\mu^h_0(295\,K) = (2534\pm20)\,cm^2/Vs$ and $\underline{\mu}^e_0(295\,K) = (1850\pm23)\,cm^2/Vs$, respectively, in good agreement with Refs. [29, 30]. The obtained fit values for μ_0 for the SUTs as a function of temperature on double-logarithmic scale are shown in Fig. 5.7. The fit results for 295 K, 150 K, and 2 K are summarised in Tab. 5.2. The stated uncertainties are the statistical uncertainties resulting from the fit according to Eq. (5.3).

For holes, the low-field mobility increases with decreasing temperature over the scanned temperature range saturating towards ultra-cold temperatures. The lower limit of the electron low-field mobility found in this work stays about constant between 300 K and 150 K, and only then increases in order to saturate again at ultra-cold temperatures.

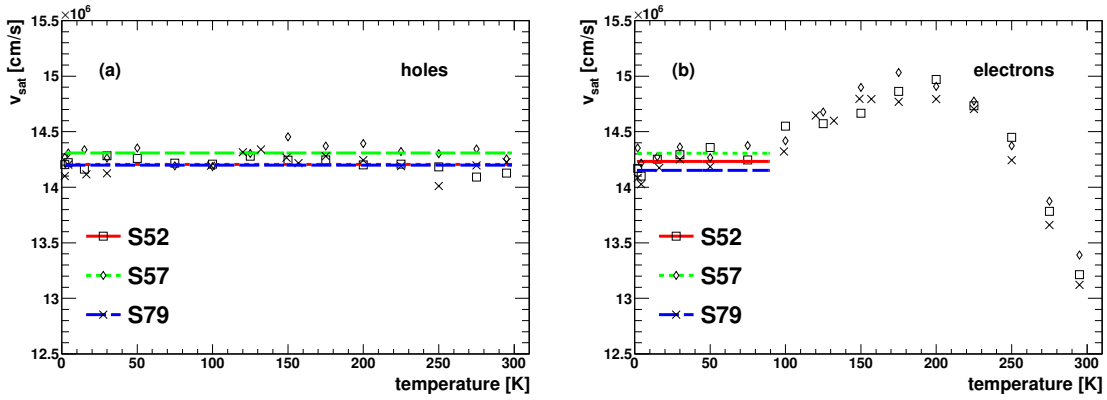

Figure 5.6.: The saturation velocity from effective mobility fits is plotted against the temperature for holes **(a)** and electrons **(b)**. Note the zero-suppression of the y-axis. The hole saturation velocity is constant over the measured temperature range, whereas the electron saturation velocity is not.

Table 5.2.: The low-field mobility in $\mathrm{cm}^2/\mathrm{Vs}$ for holes and electrons at various temperatures.

	S52		S57		S79		AVG	
	$\mu_0^h(T)$	$\mu_0^e(T)$	$\mu_0^h(T)$	$\mu_0^e(T)$	$\mu_0^h(T)$	$\mu_0^e(T)$	$\mu_0^h(T)$	$\mu_0^e(T)$
295 K	2532 ± 35	1767 ± 24	2592 ± 37	1850 ± 23	2499 ± 30	1785 ± 23	2534 ± 20	1802 ± 14
150 K	6130 ± 130	1884 ± 24	6400 ± 170	1977 ± 28	5860 ± 120	1861 ± 28	6080 ± 80	1905 ± 16
2 K	10110 ± 320	3009 ± 93	11520 ± 460	3023 ± 97	11770 ± 670	3154 ± 96	10740 ± 250	3061 ± 55

5.2.5. Modelling μ_0

Theoretically, at temperatures around 300 K the low-field mobility is limited by the acoustic phonon scattering (APS) following a behaviour like $\mu_{\mathrm{APS}} \propto T^{\alpha}$ with $\alpha = -3/2$ [34]. A fit $\mu_{\mathrm{APS}}(T) = \mu_0 \left(\frac{T}{300\,\mathrm{K}}\right)^{\alpha}$ is hence performed in the region from 200 K to 300 K to the hole data (long dashed line in Fig. 5.7 **(inset)**). The fit describes the experimental data well and the fit values are listed in Tab. 5.3. The line is continued for the reader in order to illustrate the dependence of the fit towards lower temperatures. A sample averaged value of $\alpha^h = -1.48 \pm 0.04$ is found in agreement with the theoretical predictions for acoustic phonon scattering. For electrons, the measured lower limit of the low-field mobility is about constant, $\alpha^e \approx 0$, between 150 K and 300 K. In Ref. [89] a value $\alpha^e = -0.2$ is reported, supporting as well that the mobility is not dominated by the APS in this temperature *and* field region.

Below 200 K, a clear deviation from the APS-only model is also observed for holes. For both carrier types the low-field mobility saturates towards ultra-cold temperatures. This saturation is attributed to the neutral impurity scattering (NIS), i.e. the scattering of free charge carriers off neutral impurities. For this process the scattering time is independent of the lattice temperature. This behaviour was first theoretically derived by Erginsoy[36]. With diminishing APS, the NIS becomes dominant towards ultra-cold temperatures.

Mathiessen's rule [32, 33] is used to form a new model combining the acoustic phonon scattering and the neutral impurity scattering:

$$\mu_{\mathrm{NIS+APS}}(T) = \left(\frac{1}{\mu_{\mathrm{NIS}}} + \frac{1}{\mu'_{\mathrm{APS}}(T)}\right)^{-1}. \tag{5.5}$$

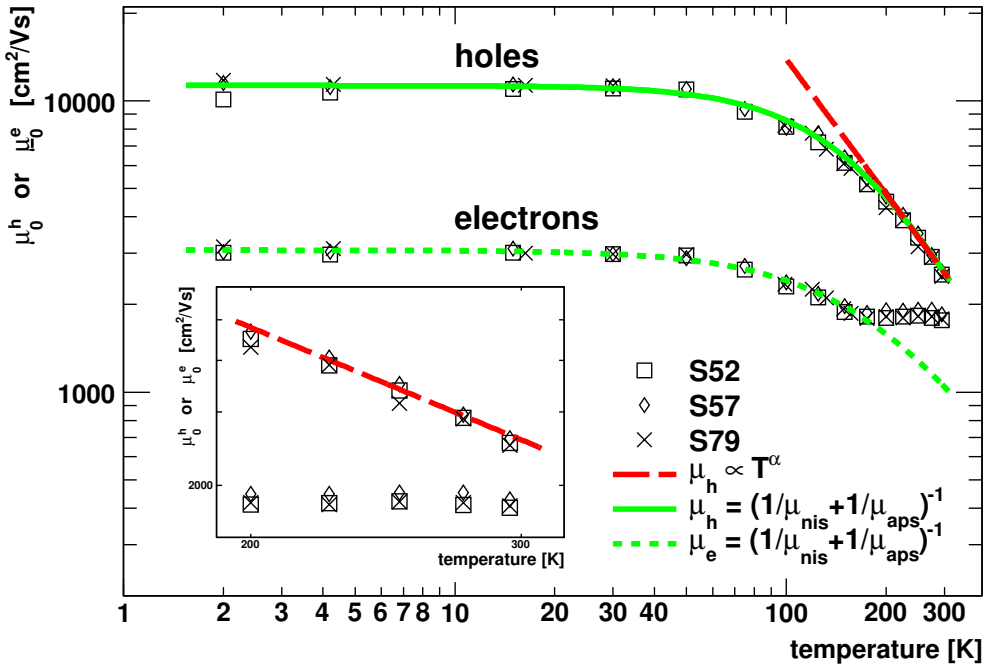

Figure 5.7.: The low-field mobility is plotted against the temperature on double-logarithmic scale. The **inset** shows the mobility for a zoomed range from 200 K to 300 K. The results for all three samples are shown: *S52* as □, *S57* as ⋄, and *S79* as ×. Superimposed are the fits (solid and short dashed line) for the APS+NIM model (see text) in the entire temperature range, and the APS-only model (long dashed line) for $T \geq 200\,\mathrm{K}$.

Equation (5.5) is fitted to the data for holes in the entire temperature range and for electrons from 2 K to 150 K. The fit results (solid and long dashed lines, respectively, in Fig. 5.7) are reported in Tab. 5.3. The model describes the hole data well over the entire temperature range with $\chi^2/\mathrm{ndf} \approx 1$ using the uncertainties obtained from fitting Eq. (5.3). For electrons, the model fits the data well for $T < 150\,\mathrm{K}$. The presented measurements allow to quote experimental values for the NIS-model. A sample averaged mobility of $\mu^h_{\mathrm{NIS}} = (11\,130 \pm 120)\,\mathrm{cm}^2/\mathrm{Vs}$ and $\underline{\mu}^e_{\mathrm{NIS}} = (3058 \pm 27)\,\mathrm{cm}^2/\mathrm{Vs}$ is measured. At 300 K, the fits yield $\mu'^{,h}_{\mathrm{APS}}(300\,\mathrm{K}) = (3218 \pm 35)\,\mathrm{cm}^2/\mathrm{Vs}$ and $\underline{\mu}'^{,e}_{\mathrm{APS}}(300\,\mathrm{K}) = (1410 \pm 140)\,\mathrm{cm}^2/\mathrm{Vs}$. Note that an inclusion of the NIS in addition to the APS leads to a higher value of the APS-mobility and a smaller value of the exponent α: $\mu'^{,h}_{\mathrm{APS}} > \mu^h_{\mathrm{APS}}$ and $\alpha'^{,h} < \alpha^h$.

For the neutral impurity scattering as derived by Erginsoy, the momentum relaxation time (or scattering time) τ_{R} depends on the conductivity effective mass m^*_{c}, the dielectric constant ε, and the neutral impurity density n_{n}:

$$\tau_{\mathrm{NIS}} = \frac{8\pi^3 m^{*2}_{\mathrm{c}} e^2}{20\varepsilon\varepsilon_0 n_{\mathrm{n}} h^3}, \tag{5.6}$$

which can be rewritten as

$$\mu_{\mathrm{NIS}} = \frac{1.44\times10^{22}\,\mathrm{cm}^{-3}}{n_{\mathrm{n}}} \frac{m^*_{\mathrm{c}}/m_0}{\varepsilon/\varepsilon_0}. \tag{5.7}$$

Table 5.3.: The fit results under the assumption of the APS-only model for holes (200 K − 300 K), the APS+NIS model for holes (2 K − 300 K), and the APS+NIS model for electrons (2 K − 150 K) are listed.

APS-only model (200 K − 300 K)		$\mu^{h}_{\mathrm{APS}}(300\,\mathrm{K})$ $\left[\mathrm{cm}^2/\mathrm{Vs}\right]$	α	χ^2/ndf
S52		2523 ± 41	-1.47 ± 0.07	1.2
S57		2574 ± 42	-1.53 ± 0.07	1.2
S79		2479 ± 38	-1.44 ± 0.07	2.9
AVG		2522 ± 24	-1.48 ± 0.04	-
APS+NIS model (2 K − 300 K)	μ^{h}_{NIS} $\left[\mathrm{cm}^2/\mathrm{Vs}\right]$	$\mu^{\prime,h}_{\mathrm{APS}}(300\,\mathrm{K})$ $\left[\mathrm{cm}^2/\mathrm{Vs}\right]$	α'	χ^2/ndf
S52	10760 ± 180	3257 ± 61	-2.14 ± 0.06	1.0
S57	11280 ± 210	3327 ± 63	-2.16 ± 0.06	1.0
S79	11550 ± 230	3104 ± 55	-2.06 ± 0.05	1.0
AVG	11130 ± 120	3218 ± 35	-2.11 ± 0.04	-
APS+NIS model (2 K − 150 K)	$\underline{\mu}^{e}_{\mathrm{NIS}}$ $\left[\mathrm{cm}^2/\mathrm{Vs}\right]$	$\underline{\mu}^{\prime,e}_{\mathrm{APS}}(300\,\mathrm{K})$ $\left[\mathrm{cm}^2/\mathrm{Vs}\right]$	α'	χ^2/ndf
S52	3027 ± 45	1370 ± 210	-1.86 ± 0.20	0.6
S57	3071 ± 48	1580 ± 270	-1.79 ± 0.23	0.4
S79	3078 ± 45	1310 ± 260	-1.98 ± 0.26	0.9
AVG	3058 ± 27	1410 ± 140	-1.87 ± 0.13	-

With the ratio $m^*_{\mathrm{c}}/m_0 \approx 0.5$, and $\mu_{\mathrm{NIS}} \approx 11\,300\,\mathrm{cm/Vs}$, a neutral impurity density of $n_{\mathrm{n}} \approx 1.2{\times}10^{17}\,\mathrm{cm}^{-3}$ is found.

Since ε and n_{n} are the same for holes and electrons, the ratio of the NIS mobilities for holes and electrons reflects an upper limit on the ratio of the conductivity effective masses. The sample averaged upper limit mass ratio $\overline{r}_m$ is found to be $\overline{r}_m = \frac{m^*_{\mathrm{c},h}}{m^*_{\mathrm{c},e}} = 3.65 \pm 0.05$. The electron conductivity effective mass is $m^*_{\mathrm{c},e} = 3\left(\frac{1}{m_l} + \frac{2}{m_t}\right)^{-1}$, and is theoretically predicted to be $m^*_{\mathrm{c},e} = 0.48\,m_0$ (Nava [84]) or $m^*_{\mathrm{c},e} = 0.40\,m_0$ (Fong [14]). The hole conductivity effective mass spreads by a factor of 3.5 in the literature: 1.60 (Rauch [90]), 0.83 (Reggiani [91]), and 0.46 (Fong [14]).

5.2.6. Conclusion

The transit time of free charge carriers in single-crystal CVD diamond is measured using the transient current technique at field strengths from −0.06 V/µm to −1.8 V/µm for holes, and 0.08 V/µm to 1.8 V/µm for electrons at temperatures between 2 K and 295 K. α-particles are used to create free charges in the sample. Three samples have been studied, all showing the same behaviour. The measured pulse shape induced by the drifting charges resembles an almost rectangular form between room temperature and 150 K reflecting an instant and continuous drift of charge carriers with constant drift velocity. A drastic change in pulse shape is observed at temperatures between $75\,\mathrm{K} < T < 150\,\mathrm{K}$.

The transit time for holes increases with increasing temperature and decreasing field. The transit time for electrons increases monotonically with increasing temperature only at high fields $E \gtrsim 1\,\mathrm{V/\mu m}$ and shows a different behaviour than the one for holes at low fields.

The drift velocity saturates at all temperatures for high fields. The hole saturation velocity is constant over the measured temperature range, whereas the electron saturation velocity stabilises only below 100 K. The saturation velocity for holes and electrons, averaged over all samples, are

- $\mathrm{v}^h_{\mathrm{sat}} = (14.23 \pm 0.04) \times 10^6\,\mathrm{cm/s}$ and
- $\mathrm{v}^e_{\mathrm{sat}} = (14.23 \pm 0.12) \times 10^6\,\mathrm{cm/s}$ for $T < 100\,\mathrm{K}$.

Electrons and holes seem to have the same saturation velocity for $T < 100\,\mathrm{K}$.

At RT the measured, sample averaged values of the low-field mobility, namely

- $\mu^h_0(295\,\mathrm{K}) = (2534 \pm 20)\,\mathrm{cm^2/Vs}$ and
- $\underline{\mu}^e_0(295\,\mathrm{K}) = (1802 \pm 14)\,\mathrm{cm^2/Vs}$,

agree well with earlier results. The low-field mobility in diamond has been measured down to 2 K for the first time:

- $\mu^h_0(2\,\mathrm{K}) = (10\,740 \pm 250)\,\mathrm{cm^2/Vs}$ and
- $\underline{\mu}^e_0(2\,\mathrm{K}) = (3061 \pm 55)\,\mathrm{cm^2/Vs}$.

The mobility values at 2 K are a crucial input for the description of damage curves in scCVD diamond. [92] There, radiation induced trapping centres degrade the quality of the crystal, and substantial charge loss is observed with increasing irradiation.

Between 200 K and 300 K, the acoustic phonon scattering describes well the temperature dependence of the hole low-field mobility. The fit $\mu_{\mathrm{APS}}(T) = \mu_0 \left(\frac{T}{300\,\mathrm{K}}\right)^{\alpha}$ is performed and $\alpha^h = -1.48 \pm 0.04$ is found as the sample average in agreement with the theoretical value of $\alpha = -3/2$.

The presented measurements show a saturation of the low-field mobility towards ultracold temperatures. Over the scanned temperature range the hole low-field mobility can be explained assuming a combination of a constant mobility term stemming from neutral impurity scattering and a temperature dependent term from acoustic phonon scattering: $\mu_{\mathrm{NIS+APS}}(T) = \left(\frac{1}{\mu_{\mathrm{NIS}}} + \frac{1}{\mu'_{\mathrm{APS}}(T)}\right)^{-1}$. A fit yields the sample averaged exponents $\alpha'^{,h} = -2.11 \pm 0.04$ and $\alpha'^{,e} = -1.87 \pm 0.13$ for holes and electrons, respectively. For the neutral impurity scattering, the following sample averaged mobility values are found

- $\mu^h_{\mathrm{NIS}} = (11\,300 \pm 120)\,\mathrm{cm^2/Vs}$ and
- $\underline{\mu}^e_{\mathrm{NIS}} = (3058 \pm 27)\,\mathrm{cm^2/Vs}$.

5.3. Temperature Dependence of the Pulse Shape

The induced current pulses for electrons and holes are shown in Fig. 5.8 for selected temperatures in the range from 2 K to 295 K, all at a bias voltage of $U_{\mathrm{bias}} = \pm 500\,\mathrm{V}$, corresponding to a field strength of $E \approx 1\,\mathrm{V/\mu m}$ for the samples *S52*, *S57*, and *S79*, respectively. In contrast to Figs. 5.1, 5.2, and 5.3, Fig. 5.8 shows the pulses for additional temperatures in order to illustrate the development of the pulse shape in more detail. Very similar results

are found in all three samples. Above 150 K and below 75 K, the measured current pulses resemble a rectangular pulse reflecting an instant and continuous drift of a constant number of charge carriers with constant drift velocity, as was discussed in the last section. A drastic change in pulse shape, and hence in the number of drifting charges as a function of time, is observed at temperatures between $75\,\mathrm{K} < T < 150\,\mathrm{K}$. The rising edge develops an $1 - \exp(-t/\tau)$ behaviour, while the falling edge develops a long exponentially falling tail. This behaviour is attributed to the creation of excitons, and especially their temperature dependent evaporation lifetime, in the ionisation volume. The evaporation lifetime of excitons, i.e. the average time needed for the thermal excitation of an electron bound in an exciton to the conduction band, features an $\exp(E_\mathrm{x}/k_\mathrm{B}T)$-dependence, see Sec. 2.2.9. It increases in the scanned temperature range from ∼30 ps (300 K), to ∼10 ns (100 K), to ∼150 µs (50 K), and even longer towards 2 K. The evaporation process is in competition with a recombination process with lifetimes of the order of nanoseconds.

The integral of the current pulses is constant between room temperature and 150 K, decreases to about one third of the RT-value towards ∼75 K, and remains at this level towards even lower temperatures. Note that the appearance of tails and decrease in area set in at the same temperature $T \approx 150\,\mathrm{K}$. Furthermore, the onset of this unexpected behaviour is observed at the same temperature for both carrier types, indicating an effect that involves both carrier types simultaneously.

Highly ionizing α-particles are used to create free charge carriers at a density of about $10^{21}\,\mathrm{cm}^{-3}$ in the bulk of the diamond. Additionally, the α-particles heat the ionisation volume. In this hot, high density charge cloud, excitons and free electron-hole pairs are in thermal quasi-equilibrium with each other. [51] Firstly, the drift of free charges out of the ionisation volume towards the opposing electrode and secondly the recombination of excitons decrease the density of charges in the volume and perturb the quasi-equilibrium. A new quasi-equilibrium state is reached by the subsequent evaporation of excitons.

The current induced by the evaporated charges drifting under the influence of the electric field is again read using the transient current technique. The TCT is often used to measure the average drift velocity of free charge carriers in, e.g., semiconductors by measuring the transit time [82, 29]. However, a constant drift velocity is reached almost instantaneously. In case of a constant electric field along the drift direction, the current induced by the drifting charges on a read-out electrode is directly proportional to their number: $i(t) \propto e \cdot N(t) \cdot \mathrm{v}_\mathrm{drift}$. In this work, the current $i(t)$, and hence $N(t)$ is measured for various temperatures between 2 K and room temperature and a field ranging from 0.08 V/µm to 1.8 V/µm. A model is presented comprising the creation and the subsequent evaporation or non-radiative recombination of excitons, which predicts the observed dependencies of the pulse shape and the pulse area.

5.3.1. The model

The impinging α-particles create free charge carriers within a small volume of the diamond bulk. The ionisation volume is described by the penetration depth of the α-particle and the radial track size. In Sec. 3.1.1, an average penetration depth of $\delta_\mathrm{p} = 10.66\,\mu\mathrm{m}$ is calculated making use of NIST data and the radial $1/e$ track size is reasonably estimated to be $r_0 \approx 2\,\mathrm{nm}$. The aspect ratio of the ionisation volume is roughly $10\,000/2 = 5000$. The short r_0 is a result of the amount of energy transferred from the primary α-particle to the electrons, which is of the order of 60 eV, cf. Sec. 3.1.1. Using the amount of charge from the calibration measurement, $Q_0 = 59.5\,\mathrm{C}$, the charge density in the first radial $1/e$ length in the instant of the impingement is

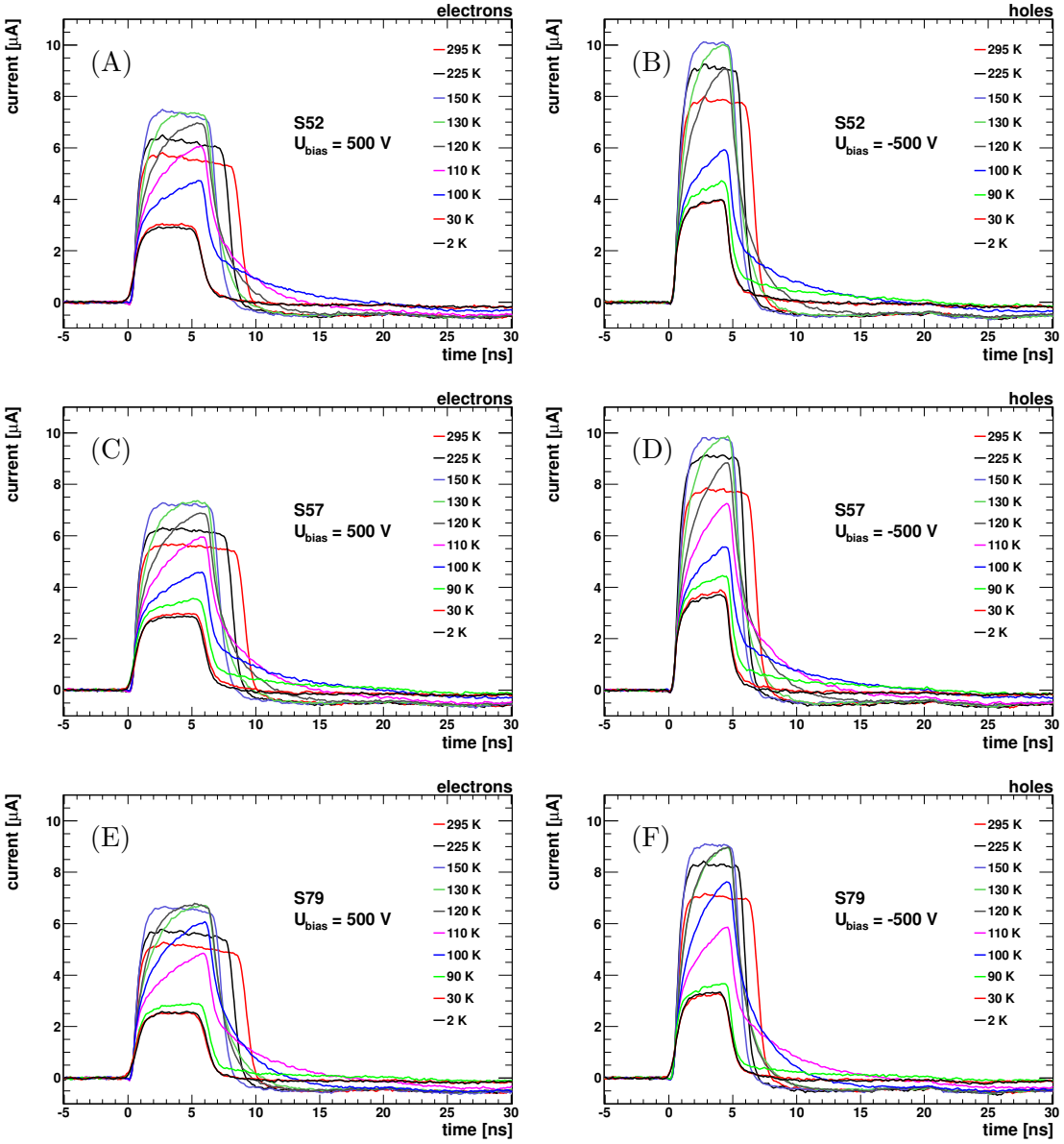

Figure 5.8.: The induced current pulses for electrons and holes at $E \approx 1\,\mathrm{V/\mu m}$ for various temperatures for the samples *S52*, *S57*, and *S79*, respectively

$$n = \frac{0.68 \cdot 59.5\,\mathrm{C}}{r_0^2 \pi \delta_\mathrm{p}} \approx 3{\times}10^{21}\,\mathrm{pairs/cm^3}. \tag{5.8}$$

As was discussed in Chap. 3, about $c_\mathrm{phon} = 60\,\%$ of the energy of the α-particle is converted into lattice vibrations, i.e. phonons. Owing to the small initial ionisation volume, a possible increase in temperature in the ionisation volume needs to be accounted for. Regarding the temperature range examined in this work, the sample temperature is always smaller than the Debye temperature, Θ_Debye, in diamond, with $\Theta = 1860\,\mathrm{K}$. Therefore, the specific heat capacity is given as

$$c_\mathrm{V}(T) = \frac{12\pi^4 R}{5}\left(\frac{T}{\Theta_\mathrm{Debye}}\right)^3. \tag{5.9}$$

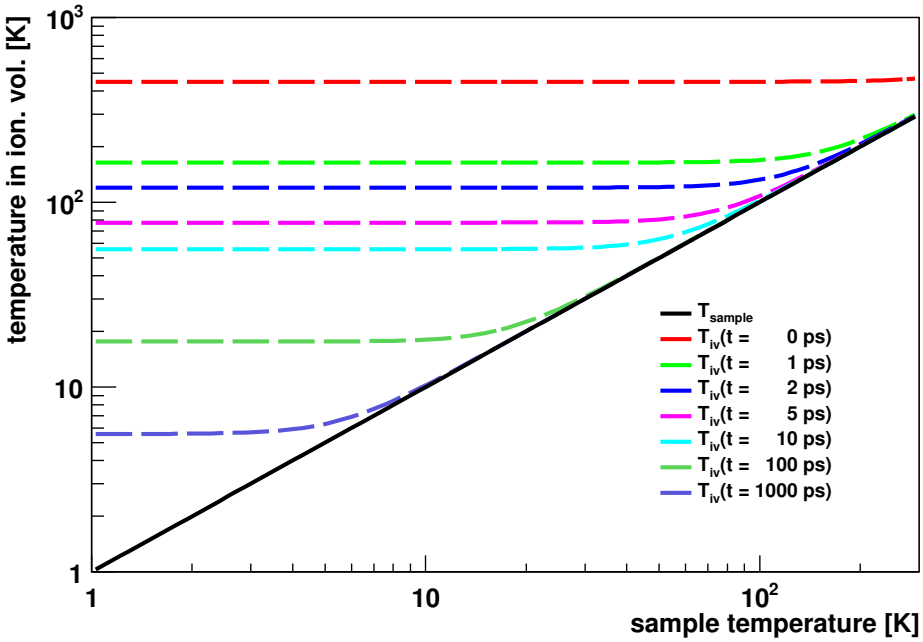

Figure 5.9.: The sample temperature before the impingement of the α-particle is shown as a black solid line. The "α-heating" ($t = 0\,\mathrm{ps}$) and the subsequent decrease in temperature via phonon transport is indicated for various time steps. The corresponding radii are $r(t = 0) \approx 2\,\mathrm{nm}$, $r(t = 1\,\mathrm{ps}) \approx 16.4\,\mathrm{nm}$, $r(t = 2\,\mathrm{ps}) \approx 30.8\,\mathrm{nm}$, etc.

Using $c_\mathrm{V} \cdot V \cdot \mathrm{d}T = c_\mathrm{phon}\mathrm{d}E$, the temperature in the initial ionisation volume T_iv as a function of the sample temperature T_0 is

$$T_\mathrm{iv} = \sqrt[4]{\frac{20\Theta_\mathrm{Debye}^3}{12\pi^4 R} \cdot \frac{c_\mathrm{phon} E}{V} + T_0^4}. \tag{5.10}$$

With the specific heat capacity depending on the temperature to the third power, the temperature of the initial ionisation volume rises almost independently of the sample temperature to about 450 K. The hot initial plasma then cools down by heat dissipation, i.e. phonon transport. The increase in heated volume happens mostly transversal to the cylindrical ionisation owing to the high aspect ratio of the ionisation volume. Averaging over the transversal modes with phonon velocities of 12.8 nm/ps and the longitudinal mode with a phonon velocity of 17.5 nm/ps, the heat dissipation occurs with roughly $v_\mathrm{phon} = 14.4\,\mathrm{nm/ps}$. The radial size of the heated volume, i.e. the *phonon front*, increases therefore roughly as

$$r(t) = r_0 + v_\mathrm{phon} \cdot t \tag{5.11}$$

with values $r(t = 0) \approx 2\,\mathrm{nm}$, $r(t = 1\,\mathrm{ps}) \approx 16\,\mathrm{nm}$, $r(t = 2\,\mathrm{ps}) \approx 31\,\mathrm{nm}$, etc. Figure 5.9 shows the temperature of the ionisation volume as a function of the initial sample temperature for different time steps, and hence radii, assuming a homogeneous temperature distribution within the heated volume. Within about 10 ps, the plasma cools to approximately 55 K at a sample temperature of 2 K, see Fig. 5.10 **(A, inset)** and Fig. 5.10 **(B, arrow)**.

The electrons inside the initially hot and dense ionisation volume thermalise to the band edge along the dispersion lines. Additionally, they undergo thermal movement and diffuse.

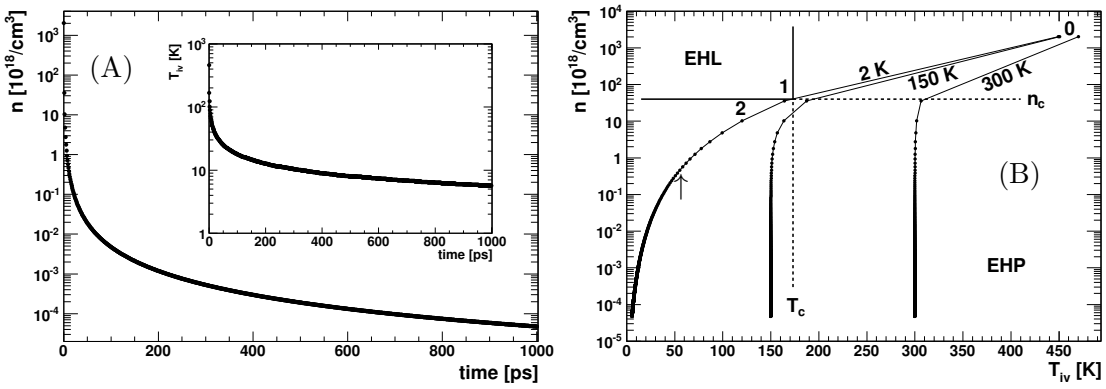

Figure 5.10.: The charge density **(A)** and the temperature **(inset)** of the ionisation volume as a function of time is shown for a sample temperature of $T = 2\,\mathrm{K}$. **(B)** The charge density is plotted against the ionisation volume temperature for different times 0, 1, 2, ... ps. The critical temperature and critical density for the formation of an EHL is added.

While the electrons have not thermalised yet, their drift cannot be characterised in terms of drift velocity/mobility, as these quantities are defined for carriers at the bottom of the conduction band. Qualitatively, the electrons remain in the volume, that is heated by the ionisation volume, for the following reason. If electrons are scattered behind the phonon front, i.e. in the cold part of the bulk, these electrons lose their energy within a few scattering processes and diffuse further with a diffusion constant given by the sample temperature, which is colder than the ionisation volume. In the extreme case of $T_0 = 2\,\mathrm{K}$, the electrons almost stop to diffuse once they are ahead of the phonon front. Therefore, the excited electrons remain approximately within the volume heated by the phonons. Making use of this assumption a rough estimation of the electron density as a function of time is then the one plotted in Fig. 5.10 **(A)**. Furthermore, with the time dependence of the density and the time dependence of the temperature at hand, the density can be plotted against the ionisation volume temperature, shown in Fig. 5.10 **(B)**. This plot shows as well the critical temperature T_c and the critical density n_c for the creation of an electron-hole-liquid (EHL), i.e. the condensed state of excitons (values taken from [12]). The estimations above lead to the conclusion that no EHL is created in the experimental situation discussed here. Hence, the charges form an electron-hole plasma (EHP).

The electrons undergoing a scattering process with an α-particle are excited into free states in the conduction band. Within $10^{-13}...10^{-12}\,\mathrm{s}$ these electrons thermalise via fast intraband scattering processes to the conduction band minima. Owing to the fast diffusion in the first picoseconds, a certain fraction of electrons and holes move to regions exhibiting a lower free charge density, "far" from the track. There, the probability of the formation of excitons is small. This creates an outer volume V_out with free electrons or holes, and an inner volume V_in, where both carrier types are present at a sufficiently high density. In this inner region, excitons form at a density n_0 leaving a density n_1 of free e-h pairs, with the density ratio n_1/n_0 tending towards a quasi-equilibrium. [51] The situation is depicted in Fig. 5.11 with **(A)** after the thermalisation but before the creation of excitons and **(B)** after the creation of excitons.

The time scale of the exciton formation process is estimated to be [93]

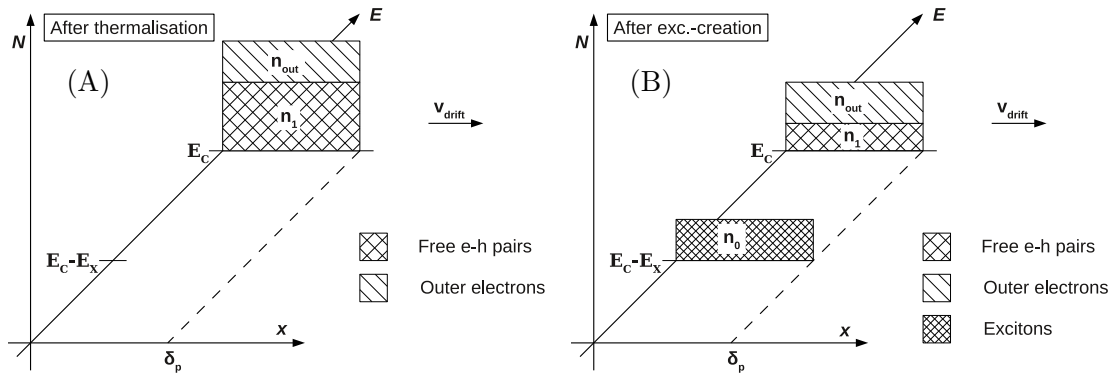

Figure 5.11.: **(A)** After the thermalisation, the charges reside at the band edge (E_C), with some fraction of the charge being "outside" (n_out), and the other part "inside" (n_1). **(B)** From n_1, a certain fraction of free e-h pairs form excitons (n_0). [51]

$$t_0 = \frac{1}{\sigma \cdot n \cdot v_\mathrm{th}}, \tag{5.12}$$

in analogy to charge trapping of free carriers in the bulk during drift. This would introduce an exciton formation time, that depends on the radial distance from the track. As an idealisation, a sharp edge is used in the calculation of the model, and it shall be seen, if this assumption is valid. Within this idealisation, assuming a cross-section $\sigma = r_x^2\,\pi$ with $r_x = 1.4\,\mathrm{nm}$ and an average thermal velocity $v_\mathrm{th} \approx 10^7\,\mathrm{cm/s}$, a reasonable density dependent exciton formation time scale of $t_0 \approx 2\,\mathrm{ps}$ is found at an assumed average density of $n = 10^{18}\,\mathrm{cm}^{-3}$, which is present after a "cooling phase". [93]

In theory, the exciton is a composite boson. However, due to the small binding energy of the exciton in comparison to the band gap, it does not behave at all like an elementary boson, i.e. the electron is almost free and keeps its fermionic nature. Additionally, the charge density in the ionisation volume is below the quantum concentration at all tested temperatures, hence the population density ratio of excitons to free e-h pairs follows a Maxwell-Boltzmann distribution if the population was unperturbed. However, the population *is* perturbed by charge drift and recombination, where the charge drift decreases the population n_1 of free e-h pairs, and recombination decreases n_0.

Non-radiative recombination processes are likely to dominate the exciton recombination process in the samples used in this work, cf. Tab. 2.3. A further decay channel of an exciton is the thermal dissociation with its associated lifetime being an exponential function of the temperature, cf. Sec. 2.2.9. At RT, the thermal energy is about one third of the binding energy (25 meV against 80 meV), which is high enough to break up excitons by exciting their electron to the conduction band. The two processes compete with each other. While the thermal dissociation process is highly temperature dependent, the recombination process is thought to be not. Within an ensemble of free e-h pairs and excitons being in thermal quasi-equilibrium, excitons will evaporate, if free electrons leave the ensemble volume in order to reach a new quasi-steady-state. This drainage of free charges is caused by the electric field.

Over time, all excitons either recombine or evaporate, and only the free electrons, including those from evaporated excitons, start to drift towards the opposing electrode and hence contribute to the measured current. The drifting charges are collected at the opposing electrode after an average transit time $t_\mathrm{t} = {}^{d}\!/_{v_\mathrm{drift}}$. The "start-drift-collect"-scheme was

discussed earlier, cf. Chap. 3. The two different start distributions in Fig. 3.9 **(top and bottom)** represent the charges that are initially in the outer volume and hence free (n_{out}), and those that evaporate from the exciton state and exit the ionisation volume (n_{exit}), respectively. In total, the pulse form is the sum of both. Combining the charges from the inner and the outer volume, the induced current density, which is the proportional to the measured quantity $i(t)$, is

$$j(t) = e\left(n_{\mathrm{out}}(t) + n_{\mathrm{exit}}(t)\right) \cdot \mathrm{v}_{\mathrm{drift}}. \tag{5.13}$$

Assuming a Gaussian shape for the start time distribution of charges stemming from the outer volume, $n_{\mathrm{out}}(t)$ is

$$n_{\mathrm{out}}(t) = n_{\mathrm{out}}(0)\left(\frac{1}{2}\big(\,\mathrm{Erfc}(t)+1\big) - \frac{1}{2}\big(\,\mathrm{Erfc}(t-t_{\mathrm{t}})+1\big)\right) \tag{5.14}$$

The first term describes the rising edge as a shifted and normalised complementary error function. The falling edge arises using Eq. (3.7).

In the following, $n_{\mathrm{exit}}(t)$ is modelled under various assumptions. [51] It is duly noted, that Prof. R. Sauer contributed the basic ideas on modelling the pulse shapes and the measured total charge with its temperature dependence, and, additonally, the impurity-assisted repopulation effect.

The free evaporation + recombination model

This model is reproduced from [94, 51]. The induced current is derived under the assumption of a free evaporation process being in competition with a recombination process. If free evaporation is assumed, the excitons start to evaporate (i.e. ionise) freely after their creation with a temperature dependent time constant $\tau_{\mathrm{th}} = t_0 \exp\left(E_{\mathrm{x}}/k_{\mathrm{B}}T\right)$, see Fig. 5.12. The rate equation of $n_0(t)$ is given by the free, i.e. thermal, evaporation and the recombination term

$$\frac{\mathrm{d}n_0}{\mathrm{d}t} = -\frac{n_0}{\tau_{\mathrm{rec}}} - \frac{n_0}{\tau_{\mathrm{th}}} = -\left(\frac{1}{\tau_{\mathrm{rec}}} + \frac{1}{\tau_{\mathrm{th}}}\right) n_0, \tag{5.15}$$

with the solution

$$n_0(t) = n_0(0)\exp\left(-t/\tau\right), \tag{5.16}$$

and

$$\frac{1}{\tau} = \frac{1}{\tau_{\mathrm{rec}}} + \frac{1}{\tau_{\mathrm{th}}}. \tag{5.17}$$

The shape of the measured pulses is described by the time constant τ, to which is referred to as the "shape constant". The density $n_1(t)$ increases by the evaporation from n_0:

$$\frac{\mathrm{d}n_1}{\mathrm{d}t} = \frac{n_0}{\tau_{\mathrm{th}}} = \frac{n_0(0)}{\tau_{\mathrm{th}}}\exp\left(-t/\tau\right). \tag{5.18}$$

with the solution

$$n_1(t) = n_1(0) + n_0(0)\frac{\tau}{\tau_{\mathrm{th}}}\big(1 - \exp\left(-t/\tau\right)\big). \tag{5.19}$$

If additionally it is assumed, that all evaporated charges exit the ionisation volume quasi-instantaneously, then $n_{\mathrm{exit}}(t) = n_1(t)$. Using Eq. (3.7), the drifting charge as a function of time coming from the inner volume is

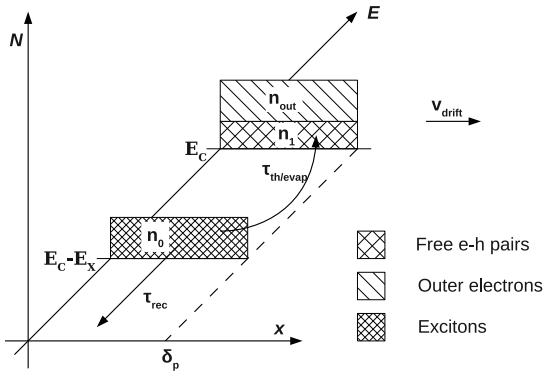

Figure 5.12.: Two processes are depicted, which drain n_0, namely the recombination with τ_{rec} and the evaporation with either τ_{th} (free evaporation) or τ_{evap} (curbed evaporation). [51]

$$n_{\mathrm{exit}}(t) = \begin{cases} n_1(0) + n_0(0)\frac{\tau}{\tau_{\mathrm{th}}}\left(1-\exp\left(-t/\tau\right)\right), & t \le t_{\mathrm{t}} \\ n_0(0)\frac{\tau}{\tau_{\mathrm{th}}}\left(1-\exp\left(-t/\tau\right)\right) - n_0(0)\frac{\tau}{\tau_{\mathrm{th}}}\left(1-\exp\left(-(t-t_{\mathrm{t}})/\tau\right)\right), & t > t_{\mathrm{t}}, \end{cases} \tag{5.20}$$

However, this model has a drawback, as the density ratio n_1/n_0 is not constant over time in this model: $\mathrm{d}(n_1/n_0)/\mathrm{d}t \neq 0$, as can be readily verified.

The curbed evaporation + recombination model

This model is a reproduction from [94]. The induced current is derived under the assumption of a curbed evaporation process being in competition with a recombination process. If the transport of the evaporating charges does not happen sufficiently fast, e.g. in the case of low electric field, the excitons do not evaporate freely, but the evaporation is curbed by the slow transport. In the above defined "inner" volume, the excitons are in quasi-equilibrium with the free e-h pairs, and it is assumed that the population density ratio for all times is

$$\frac{n_1(t)}{n_0(t)} = c \cdot \exp\left(-E_{\mathrm{x}}/k_{\mathrm{B}}T\right), \tag{5.21}$$

where c is the ratio of the densities of states $c = \frac{\Phi_1}{\Phi_0}$. The reservoir n_1 decreases only by the charge drift out of the ionisation volume, which is induced by the electric field. A fraction of the amount of charge transported away from the plasma evaporates from n_0 to n_1 reaching a new quasi-equilibrium. The described process is hence a "curbed" evaporation rather than a free one, with a time constant $\tau_{\mathrm{evap}} > \tau_{\mathrm{th}}$ replacing the thermal evaporation in Fig. 5.12. Therefore, the time constant τ_{evap}, with which carriers are excited from the bound state to the free state, depends on the temperature *and* the drift velocity:

$$\frac{\mathrm{d}n_1(t)}{\mathrm{d}t} = \frac{\mathrm{v}_{\mathrm{drift}}}{L} n_1(t) = \frac{\mathrm{v}_{\mathrm{drift}}}{L} \cdot n_0(t) \cdot c \cdot \exp\left(-E_{\mathrm{x}}/k_{\mathrm{B}}T\right) := \frac{n_0(t)}{\tau_{\mathrm{evap}}}, \tag{5.22}$$

where L is a characteristic length over which a charge needs to be transported away in order to exit n_1, and

$$\tau_{\mathrm{evap}} = \frac{L}{\mathrm{v}_{\mathrm{drift}}\, c} \exp\left(E_{\mathrm{x}}/k_{\mathrm{B}}T\right). \tag{5.23}$$

The form of τ_{evap} is particularly interesting as it incorporates two main aspects: On the one hand, it reflects the influence of the charge transport by the inverse-proportional dependence on the drift velocity. On the other hand, the Boltzmann-factor reflects the temperature dependence of the evaporation process.

The charge density in the lower state n_0 decreases owing to evaporation (τ_{evap}) and recombination (τ_{rec}):

$$\frac{\mathrm{d}n_0(t)}{\mathrm{d}t} = -\frac{n_0(t)}{\tau_{\mathrm{rec}}} - \frac{\mathrm{d}n_1(t)}{\mathrm{d}t} = -\frac{n_0(t)}{\tau_{\mathrm{rec}}} - \frac{n_0(t)}{\tau_{\mathrm{evap}}} = -\left(\frac{1}{\tau_{\mathrm{rec}}} + \frac{1}{\tau_{\mathrm{evap}}}\right) n_0(t), \tag{5.24}$$

with the solution

$$n_0(t) = n_0(0)\exp\left(-t/\tau\right), \qquad \text{and again} \qquad \frac{1}{\tau} = \frac{1}{\tau_{\mathrm{rec}}} + \frac{1}{\tau_{\mathrm{evap}}}. \tag{5.25}$$

With the solution for $n_0(t)$, Eq. (5.22) becomes

$$\frac{\mathrm{d}n_1(t)}{\mathrm{d}t} = \frac{n_0(0)}{\tau_{\mathrm{evap}}} \exp\left(-t/\tau\right). \tag{5.26}$$

Solving Eq. (5.26) and assuming again $n_{\mathrm{exit}}(t) = n_1(t)$ leads to the expression

$$n_{\mathrm{exit}}(t) = \begin{cases} n_1(0) + n_0(0)\frac{\tau}{\tau_{\mathrm{evap}}}\left(1 - \exp\left(-t/\tau\right)\right), & t \le t_{\mathrm{t}} \\ n_0(0)\frac{\tau}{\tau_{\mathrm{evap}}}\left(1 - \exp\left(-t/\tau\right)\right) - n_0(0)\frac{\tau}{\tau_{\mathrm{evap}}}\left(1 - \exp\left(-(t-t_{\mathrm{t}})/\tau\right)\right), & t > t_{\mathrm{t}}, \end{cases} \tag{5.27}$$

Here, n_{exit} has almost the same form as in Eq. (5.20), but τ_{evap} replaces τ_{th}. This model, however, has the same drawback as the free evaporation + recombination model. Additionally, n_1 cannot remain at a fixed ratio with n_0 and simultaneously increase in order to describe the amount of evaporated charges. In order to overcome this drawback, a proper relation between the densities n_1 and n_{exit} needs to be established.

The curbed evaporation + recombination + transport model

This is a modified version of a model from [94] in which a Boltzmann equilibrium is assumed to describe the physical situation, whereas this author argues for an equilibrium off the BM distribution. This could be caused by the scale of the transport time being of the order of the condensation time scale. [2]

A characteristic transport time τ_{trans} is introduced characterising the average time a charge from n_1 needs to exit the ionisation volume. Figure 5.13 illustrates the model with the exciton density n_0, the free e-h pair density n_1, and the density of charges that have left the ionisation volume n_{exit}. The initially free charges n_{out} are omitted in the figure. The excitons can either recombine with a time constant τ_{rec}, or evaporate with a time constant τ_{evap}. The transport time is thought to be inversely proportional to the drift velocity, and depends on a characteristic length L: $\tau_{\mathrm{trans}} = L/\mathrm{v}_{\mathrm{drift}}$.

[2] Note that all models discussed here do not include condensation after the cooling phase. A model that includes the condensation is currently under development.

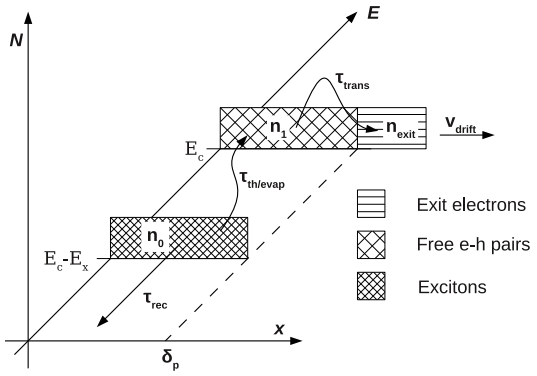

Figure 5.13.: The exciton evaporation and recombination is governed by τ_{evap} and τ_{rec}, respectively. The τ_{trans} governs the transport from n_1 to n_{exit}. n_{out} is omitted.

The reservoir n_1 is emptied via charge drifting out of the ionisation volume with the transport time τ_{trans} and thus feeds n_{exit}. Considering time slices of fixed length Δt, in every slice a fraction $\frac{v}{L}\Delta t$ of $n_1(t)$ is transferred to n_{exit}: [51]

$$n_{\text{exit}} = n_1(0)\frac{v}{L}\Delta t + n_1(1)\frac{v}{L}\Delta t + n_1(2)\frac{v}{L}\Delta t + ... = \frac{1}{\tau_{\text{trans}}}\int_0^t n_1(t')\,\mathrm{d}t'. \tag{5.28}$$

With charges leaving the ionisation volume, a new quasi-steady-state is reached by the evaporation of excitons into the free e-h pair state. A continuity equation states the equality of evaporating and exiting charges – only the amount of exiting charges can evaporate – in the thermal quasi-equilibrium:

$$\frac{n_0}{\tau_{\text{evap}}} = \frac{n_1}{\tau_{\text{trans}}} \qquad \Rightarrow \qquad \frac{n_1}{n_0} = \frac{\tau_{\text{trans}}}{\tau_{\text{evap}}} := \zeta(\tau_{\text{trans}}, T), \tag{5.29}$$

with an *a priori* unknown function $\zeta(\tau_{\text{trans}}, T)$, which defines the ratio of n_1 over n_0. Note, that if τ_{trans} is given by the drift velocity, and hence the electric field, the evaporation lifetime adapts to the present τ_{trans}, and the ratio n_1/n_0 can be assumed to be a function of the transport time and the temperature only. Equation (5.29) comes with two assumptions: (1) The condensation of free e-h pairs from n_1 to n_0 is negligible, and (2) $\tau_{\text{trans}} \ll \tau_{\text{rec}}$. In fact, the former follows from the latter. Assuming L, the characteristic length to leave the ionisation volume is $L = \delta_{\text{p}}/2$, the transport time is estimated to be of the order of $\tau_{\text{trans}} = {}^{5\times10^{-4}\,\text{cm}}/_{10\times10^{6}\,\text{cm/s}} = 50\,\text{ps}$. As will be seen later, the recombination lifetime is of the order of 10 ns, and hence indeed $\tau_{\text{trans}} \ll \tau_{\text{rec}}$. That is, the density n_1 is emptied much faster by transport than n_0 by recombination, but condensation would only take place in case n_0 was underpopulated in comparison to n_1. As this is not the case, condensation can be neglected. If one argues, that Eq. (5.29) should additionally account for recombination, one could write $\frac{n_0}{\tau_{\text{evap}}} + \frac{n_0}{\tau_{\text{rec}}} = \frac{n_1}{\tau_{\text{trans}}}$. So, only those charges evaporate that are transported away *and* that do not recombine. Solving for n_1/n_0 results in $n_1/n_0 = \tau_{\text{trans}}/\tau_{\text{evap}} + \tau_{\text{trans}}/\tau_{\text{rec}}$. But above, it was already argued that $\tau_{\text{trans}} \ll \tau_{\text{rec}}$. The error committed by neglecting the recombination in Eq. (5.29) is therefore negligible.

Again, the exciton density depends on the evaporation and the recombination lifetimes:

$$\frac{\mathrm{d}n_0}{\mathrm{d}t} = -\frac{n_0}{\tau_{\text{rec}}} - \frac{n_1}{\tau_{\text{trans}}} \overset{(5.29)}{=} -\frac{n_0}{\tau_{\text{rec}}} - \frac{n_0}{\tau_{\text{evap}}} = -\left(\frac{1}{\tau_{\text{rec}}} + \frac{1}{\tau_{\text{evap}}}\right) n_0. \tag{5.30}$$

The solution for $n_0(t)$ is the same as before

$$n_0(t) = n_0(0)\exp(-t/\tau), \qquad \frac{1}{\tau} = \frac{1}{\tau_{\text{rec}}} + \frac{1}{\tau_{\text{evap}}}. \tag{5.31}$$

n_1 follows as a direct consequence from Eq. (5.29):

$$n_1(t) = \frac{\tau_{\text{trans}}}{\tau_{\text{evap}}} n_0(0)\exp(-t/\tau). \tag{5.32}$$

Inserting Eq. (5.32) in Eq. (5.28) results in:

$$n_{\text{exit}}(t) \overset{n_{\text{exit}}(0)=0}{=} n_0(0)\frac{\tau}{\tau_{\text{evap}}}\left(1-\exp(-t/\tau)\right), \tag{5.33}$$

and again, cf. Eq. (5.20) and Eq. (5.27),

$$n_{\text{exit}}(t) = \begin{cases} n_1(0) + n_0(0)\frac{\tau}{\tau_{\text{evap}}}\left(1-\exp(-t/\tau)\right), & t \le t_{\text{t}} \\ n_0(0)\frac{\tau}{\tau_{\text{evap}}}\left(1-\exp(-t/\tau)\right) - n_0(0)\frac{\tau}{\tau_{\text{evap}}}\left(1-\exp(-(t-t_{\text{t}})/\tau)\right), & t > t_{\text{t}}, \end{cases} \tag{5.34}$$

Here, n_{exit} has the same form as in Eq. (5.27), but on the one hand the explicit form of τ_{evap} is different from the one in the "curbed evaporation + recombination"-model, and on the other the ratio n_1/n_0 is time-independent: $\mathrm{d}(n_1/n_0)/\mathrm{d}t = 0$. Therefore, with the coupling of n_1 and n_{exit}, n_1 can be in thermal quasi-equilibrium with n_0, whilst n_{exit} gives rise to the measured current.

Determination of ζ Physically reasonable appear continuous power functions in τ_{trans} and exponential functions of the inverse temperature, cf. as well Eq. (5.23). Physical boundary conditions (BQ) for the form of ζ emerge naturally from the two extreme cases of (1) no transport, i.e. infinite transport time, and (2) vanishing transport time. For the former, the ionisation volume remains unperturbed and $n_1/n_0 = \zeta$ is given by the Boltzmann distribution: $\zeta(\tau_{\text{trans}} \to \infty) = c \cdot \exp(-E_{\text{x}}/k_{\text{B}}T)$ (BQ1). For the latter, the evaporation happens freely, and the evaporation time is given by the free evaporation: $\tau_{\text{evap}} = t_0 \exp(E_{\text{x}}/k_{\text{B}}T)$, and hence $\zeta(\tau_{\text{trans}}, T) = \tau_{\text{trans}}/\tau_{\text{evap}} = \tau_{\text{trans}}/\big(t_0 \exp(E_{\text{x}}/k_{\text{B}}T)\big)$ (BQ2). A possible function for ζ is found by starting from the Boltzmann distribution $(c \cdot \exp(-E_{\text{x}}/k_{\text{B}}T))$, and allowing for a perturbation, that shifts the Boltzmann factor to smaller values, as n_1 is emptied by the drift: $1/(1+\delta)$. The perturbation δ should only be a function of the two competing processes, and therefore of $c \cdot t_0$ and τ_{trans}:

$$\zeta(\tau_{\text{trans}}, T) = \frac{1}{1+\delta}\, c \cdot \exp(-E_{\text{x}}/k_{\text{B}}T) = \frac{1}{1+\dfrac{c\cdot t_0}{\tau_{\text{trans}}}}\, c \cdot \exp(-E_{\text{x}}/k_{\text{B}}T). \tag{5.35}$$

Obviously, this choice of ζ satisfies $\zeta(\tau_{\text{trans}} \to \infty) = c \cdot \exp(-E_{\text{x}}/k_{\text{B}}T)$. Additionally, for $\tau_{\text{trans}} \to 0$, it is found that

$$\tau_{\text{evap}} = \frac{\tau_{\text{trans}}}{\zeta} = \tau_{\text{trans}} \cdot \left[\left(\frac{c\cdot t_0}{\tau_{\text{trans}}} + 1\right) c^{-1} \cdot \exp(E_{\text{x}}/k_{\text{B}}T)\right] \overset{\tau_{\text{trans}}\to 0}{=} t_0 \exp(E_{\text{x}}/k_{\text{B}}T). \tag{5.36}$$

The choice of ζ shall further be compared to the models without the incorporation of the transport time. For that purpose, the evaporation time is written under the above choice. Substituting Eq. (5.35) in Eq. (5.29) and solving for τ_{evap} leads to the expression

$$\tau_{\text{evap}} = (t_0 + \frac{\tau_{\text{trans}}}{c}) \exp{(E_{\text{x}}/k_{\text{B}}T)}. \tag{5.37}$$

For low electric field strengths, the drift velocity is low, and hence the transport time is long ($\tau_{\text{trans}} = \frac{L}{\text{v}_{\text{drift}}} \gg c \cdot t_0$). Thus,

$$\tau_{\text{evap}} \approx \frac{\tau_{\text{trans}}}{c} \exp{(E_{\text{x}}/k_{\text{B}}T)} = \frac{L}{c \cdot \text{v}_{\text{drift}}} \exp{(E_{\text{x}}/k_{\text{B}}T)}, \tag{5.38}$$

which reproduces the evaporation lifetime of the curbed model. The free evaporation at fast drift times is already fulfilled by the choice of the boundary conditions. The curbing thus results via the finite transport time. For $\tau_{\text{trans}} \to \infty$, also the evaporation time tends towards infinity. This is reasonable: Without any charges leaving the ionisation volume, no excitons can evaporate.

For the sake of completeness, the density ratio is explicitly written as

$$\frac{n_1}{n_0} = \zeta(\tau_{\text{trans}}, T) = \frac{\tau_{\text{trans}}}{c \cdot t_0 + \tau_{\text{trans}}} c \exp{(-E_{\text{x}}/k_{\text{B}}T)}. \tag{5.39}$$

For $\tau_{\text{trans}} \to \infty$, n_1/n_0 approaches the Boltzmann distribution from below, i.e. as long as the transport time is finite, n_1 is slightly smaller compared to the static case, where it is maximal. The faster the transport time, the smaller is the ratio n_1/n_0, since the charges drift faster out of the ionisation volume than they can be replaced by evaporation.

It is out of the scope of this work to proof the model discussed above. However, the model is confronted with data and thoroughly checked. It will be shown, that the model derived above is capable of describing the measured data accurately.

Total induced charge

Comparing Eqs. (5.20), (5.27), and (5.34), it is noticeable that they differ only in the evaporation time constant (τ_{th} or τ_{evap}), and in the prediction of the explicit form of τ_{evap}. But the form of n_{exit} is the same. Therefore, the density n_{exit} can be used generically in order to calculate a total induced charge, without having to specify the model itself.

Again, the general procedure to determine the total induced charge has been outlined in Refs. [93, 94], which are followed closely with minor modifications. To calculate the total induced charge, $n_{\text{exit}}(t)$ and $n_{\text{out}}(t)$ are integrated over time, modulo the appropriate factors for the conversion into charge according to the Shockley-Ramo theorem. The integral is split into two parts, i.e. (1) the *main* part from 0 to t_{t} and (2) the *tail* part from t_{t} to infinity. The main part of the current is the sum of the carriers from the initially outer charges *plus* the current induced by charges released before $t = t_{\text{t}}$, c.f. Fig. 5.14. At $t = t_{\text{t}}$, those charges that started drifting immediately are collected, and only those that started drifting after $t = 0$ form the tail. The two parts, main [93, 94] and tail, read

$$\begin{aligned} Q^{\text{main}} \propto \int_0^{t_{\text{t}}} \big(n_{\text{exit}}(t) + n_{\text{out}}(t)\big)\,\mathrm{d}t &= n_1(0)t_{\text{t}} + \frac{\tau}{\tau_{\text{evap}}} n_0(0)\big(t_{\text{t}} - \tau + \tau\, \exp{(-t_{\text{t}}/\tau)}\big) \\ &\quad + n_{\text{out}}(0)t_{\text{t}} \end{aligned} \tag{5.40}$$

$$Q^{\text{tail}} \propto \int_{t_{\text{t}}}^{\infty} n_{\text{exit}}(t)\,\mathrm{d}t \qquad = \qquad \frac{\tau}{\tau_{\text{evap}}} n_0(0)\big(\quad \tau - \tau\, \exp{(-t_{\text{t}}/\tau)}\big) \tag{5.41}$$

Geometrically, it is readily clear from Fig. 5.14 that the sum of $Q^{\text{main}} + Q^{\text{tail}}$ forms the area of a rectangle with height proportional to $n_{\text{out}} + n_1(0) + \frac{\tau}{\tau_{\text{evap}}} n_0(0)$ and width t_{t}. Therefore

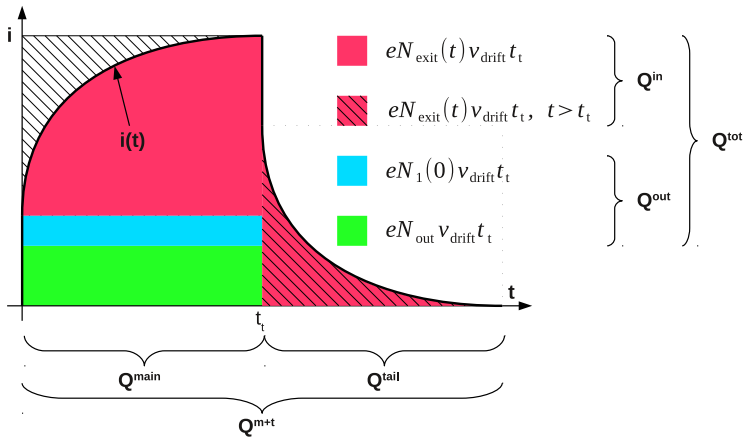

Figure 5.14.: A graphical illustration of the decomposition of the induced current is shown.

$$Q^{\text{main}} + Q^{\text{tail}} \propto \left(n_{\text{out}} + n_1(0) + \frac{\tau}{\tau_{\text{evap}}} n_0(0) \right) \cdot t_{\text{t}}. \tag{5.42}$$

The integral of the pulse, $Q = \int i(t)\,\mathrm{d}t$ using Eq. (3.5), integrated up to t_{t} is then

$$Q^{\text{main}} = Q_{\text{out}} + \frac{\tau}{\tau_{\text{evap}}} Q_{\text{in}} \cdot \frac{\tau}{t_{\text{t}}} \exp\left(-t_{\text{t}}/\tau\right), \tag{5.43}$$

and when integrated to infinity, i.e. several time constants,

$$Q^{\text{m+t}} = Q^{\text{main}} + Q^{\text{tail}} = Q_{\text{out}} + \frac{\tau}{\tau_{\text{evap}}} Q_{\text{in}}. \tag{5.44}$$

5.3.2. Comparison of the model to the data

The models described above allow for two crucial revisions against data: (1) the prediction of the total measured charge as a function of the temperature using Eqs. (5.43) and (5.44) and (2) the prediction of the temperature dependence of the shape constant. Additionally, the validity of the model is cross-checked using an n-type silicon sensor in order to compare model predictions against another semiconductor.

The measured charge as a function of temperature

At first, the measured charge is analysed as a function of temperature and compared to the model. Its predicted temperature dependence should be consistent with an exciton binding energy of $E_{\text{x}} = 80\,\text{meV}$. The measured charge as a function of temperature is shown in Fig. 5.15 for electrons **(A)** and holes **(B)** at $E \approx 1\,\text{V}/\mu\text{m}$. The statistical uncertainty on the charge is estimated to be around 1 %. The integral of the current pulses is constant at about $Q_0 = (51.0 \pm 0.5)\,\text{fC}$ between room temperature and 150 K, decreases to about one third of the RT value towards ∼75 K, and remains at this level towards even lower temperatures. This behaviour is predicted by the model under discussion. The transport time at this field strength is thought to be short enough in order for the evaporation to happen almost freely, i.e. $\tau_{\text{evap}} = t_0 \exp\left(E_{\text{x}}/k_{\text{B}}T\right)$, and therefore τ_{evap} depends exponentially on the temperature; it increases with decreasing temperature. Depending on the ratio τ/τ_{evap}, more or less excitons recombine before they thermally dissociate leading to a lower/higher measured

charge, cf. the second terms on the right hand side in Eqs. (5.43) and (5.44). Substituting $\frac{\tau}{\tau_{\text{evap}}} = \frac{1}{1+\frac{\tau_{\text{evap}}}{\tau_{\text{rec}}}}$ in Eq. (5.44) and using $\tau_{\text{evap}} = t_0 \exp(E_{\text{x}}/k_{\text{B}}T)$ gives rise to a formula $f_Q(T)$, which can be fitted to the measured charge data. The model has four parameters: (1) the total charge, (2) the outer charge, (3) the ratio $\frac{\tau_{\text{evap}}}{\tau_{\text{rec}}} = \frac{t_0}{\tau_{\text{rec}}} \exp(E_{\text{x}}/k_{\text{B}}T) := \epsilon \cdot \exp(E_{\text{x}}/k_{\text{B}}T)$ and (4) the exciton binding energy E_{x}. The total charge Q_{tot} and the outer charge Q_{out} are highly predetermined by the two plateaus before and after the charge drop at about 51 fC and 17 fC, respectively, and the inner charge is then $Q_{\text{in}} = Q_{\text{tot}} - Q_{\text{out}}$. Additionally, the exciton binding energy is set to its theoretical value $E_{\text{x}} = 80\,\text{meV}$. The fit function for the measured charge $Q^{\text{m+t}}$ becomes

$$f_{Q^{\text{m+t}}}(T) = Q_{\text{out}} + \frac{Q_{\text{in}}}{1 + \epsilon \cdot \exp(E_{\text{x}}/k_{\text{B}}T)}, \tag{5.45}$$

and only ϵ is *a priori* completely undetermined.

The fit function for Q^{main} is more complicated, as it involves the transit time t_{t} and the shape constant τ, and not only the ratio of t_0 over τ_{rec}. Therefore, it contains four free parameters (t_0 and τ_{rec} plus Q_{tot} and Q_{out}), again with Q_{tot} and Q_{out} highly predetermined. Note that t_0 and τ_{rec} are not redundant, as their absolute values form τ. t_{t} is taken from data, i.e. a simple power law fit of the transit time as a function of the temperature at $E \approx 1\,\text{V/µm}$. The fit function is then

$$f_{Q^{\text{main}}}(T) = Q_{\text{out}} + \frac{Q_{\text{in}}}{1 + \epsilon \cdot \exp(E_{\text{x}}/k_{\text{B}}T)} \cdot \frac{\tau}{t_{\text{t}}} \exp(-t_{\text{t}}/\tau), \tag{5.46}$$

and τ is again given by Eq. (5.31).

The result of the fits for Q^{main} and $Q^{\text{m+t}}$ are tabulated in Tab. 5.4 for both carrier types and the fit functions are superimposed as dotted lines in Fig 5.15. The inner charge constitutes about 2/3 of the total charge at a field of $E = 1\,\text{V/µm}$, the outer charge about 1/3, summing to a total of about 51 fC. Since t_0 and τ_{rec} are independent, though appear correlated in $f_{Q^{\text{main}}}(T)$, the fits result in estimates for both of them, but with a large uncertainties:

$$t_0 = (4\pm2)\,\text{ps} \qquad \text{and} \qquad \tau_{\text{rec}} = (20\pm10)\,\text{ns}. \tag{5.47}$$

Another estimation of t_0 is obtained by the following consideration. At around 100 K, Q_{in} has decreased to half of its RT value, see Fig. 5.15. Therefore $\frac{1}{1+\frac{\tau_{\text{evap}}}{\tau_{\text{rec}}}} = \frac{1}{2}$ and hence $\tau_{\text{evap}} = \tau_{\text{rec}}$. Both the recombination lifetime and the evaporation time at 100 K are $\sim$(14±2) K (see next subsection), and therefore $\tau_{\text{evap}} = t_0 \exp(E_{\text{x}}/k_{\text{B}}T) \approx 14\,\text{ns}$. Thus, t_0 becomes

Table 5.4.: The results of fitting, firstly, Eq. (5.46) to the charge collected until t_{t} (Q^{main}, i.e. without the tail) and secondly Eq. (5.45) to the charge including the tail ($Q^{\text{m+t}}$) are listed for electrons and holes. The exciton binding energy is fixed to 80 meV in both cases.

	Q^{main}					$Q^{\text{m+t}}$			
	Q_{tot} [fC]	Q_{out} [fC]	t_0 [ps]	τ_{rec} [ns]	χ^2/ndf	Q_{tot} [fC]	Q_{out} [fC]	$10^5\,\epsilon$	χ^2/ndf
e	50.1±0.2	16.6±0.3	4±2	20±10	1.64	51.4±0.2	17.5±0.3	9.0±0.4	0.93
h	50.2±0.2	16.0±0.3	4±2	20±10	2.00	52.0±0.2	17.1±0.3	9.6±0.4	0.82

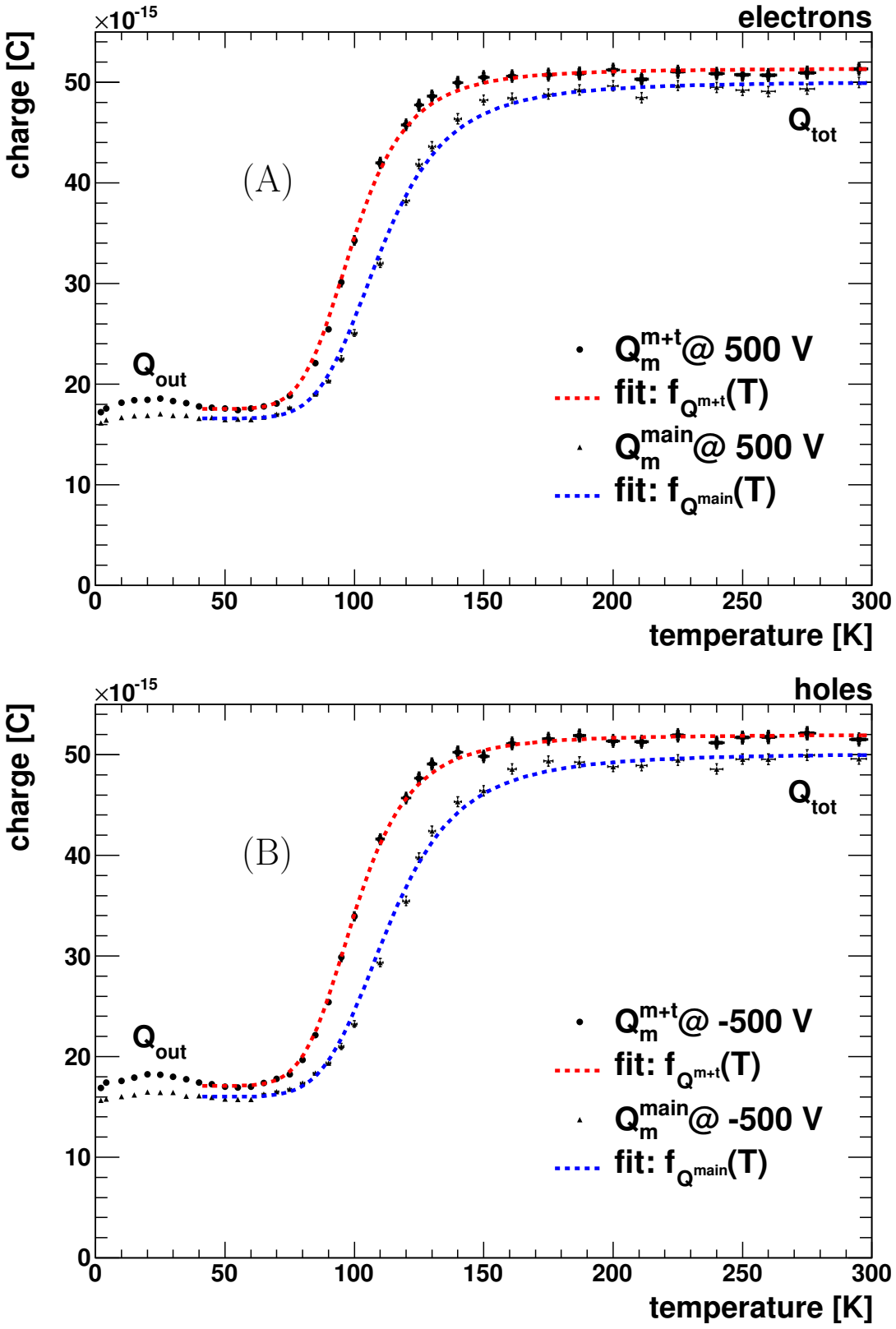

Figure 5.15.: The measured charge as a function of the temperature is shown for Q^{main} and $Q^{\mathrm{m+t}}$ for electrons **(A)** and holes **(B)**.

$$t_0 = (14\pm2)\,\mathrm{ns}/\exp\left(0.08\,\mathrm{eV}/(k_\mathrm{B}\cdot 100\,\mathrm{K})\right) = (1.3\pm0.2)\,\mathrm{ps}, \tag{5.48}$$

in reasonable accordance with the t_0-value obtained from the Q^{main}-fit. A third estimation results from the $Q^{\mathrm{m+t}}$-fit (Eq. (5.45)), where only the ratio t_0/τ_{rec} appears:

$$\epsilon = t_0/\tau_{\mathrm{rec}} = 9.3\pm0.3\times10^{-5} \tag{5.49}$$

averaging the results from electrons and holes, see Tab. 5.4. Using again the evaporation time $\tau_{\mathrm{evap}} \approx (14\pm2)\,\mathrm{K}$, it is found that

$$t_0 = (14\pm2)\,\mathrm{ns}\cdot\epsilon = (1.3\pm0.2)\,\mathrm{ps}. \tag{5.50}$$

With $t_0 \approx 1\,\mathrm{ps}$, the evaporation time at 50 K and 300 K follow to be of the order of 150 µs and 30 ps, respectively, as was reported in Tab. 2.3. It is emphasised that the experimentally found scale of t_0, namely 1 ps, is crucial for the description of the observed data. If t_0 was of the order of femtoseconds, the charge would not have decreased to half of its RT value at 100 K, but at 58 K.

The fit result from the Q^{main}-fit for the recombination lifetime, $\tau_{\mathrm{rec}} = (20\pm10)\,\mathrm{ns}$, is of the same of order of magnitude as the measured one at 100 K, with the measured one within one σ of the uncertainty of the fit result.

Additional measurements using MIPs and α-particles on silicon Equation (5.37), and thus also Eq. (5.44), predict a strong dependence of the model on the exciton binding energy. Therefore, if the model is accurate, the effects observed in diamond should also appear in other semiconductors at about the same value of $\exp\left(E_\mathrm{x}/k_\mathrm{B}T\right)$. In silicon, the exciton binding energy is $E_\mathrm{x}^{\mathrm{Si}} = 14.7\,\mathrm{meV}$, and therefore $E_\mathrm{x}/E_\mathrm{x}^{\mathrm{Si}} = 5.44$. Hence, excitons in silicon are expected to thermally evaporate down to much lower temperatures than those in diamond. This should manifest in the temperature at which the observed charge loss sets in. In diamond the charge loss starts at about 150 K, in silicon it should thus set in at about 28 K. The silicon sensor used for comparison is of n-type, float zone silicon, with a bulk doping of about $6\times10^{11}\,\mathrm{cm}^{-3}$, a thickness of 290 µm, and a full-depletion voltage of $U_{\mathrm{fd}} = 30\,\mathrm{V}$.

Figure 5.16 compares the measured, normalised charge for holes as a function of the temperature for diamond and silicon using α-particles, and for diamond using cosmic muons. The absolute charge at RT measured with the silicon sensor at a bias of $-500\,\mathrm{V}$ is $Q_{\mathrm{tot}}^{\mathrm{Si,\text{-}500\,V}} \approx 170\,\mathrm{fC}$ in accordance with the lower pair-creation energy of about 3.6 eV. The charge normalised to $Q_{\mathrm{tot}}^{\mathrm{Si,\text{-}500\,V}}$ is shown in the figure for two different bias voltages (triangles). Additionally, the normalised charge obtained with diamond is given (full black circles, normalised to 52 fC). Two important effects are visible: (1) At a bias of -60 V, i.e. $E \approx 0.2\,\mathrm{V/\mu m}$, the charge loss appears at about 30 K, in good agreement with the expectation from the exciton model (black triangles). (2) At high field strengths, no charge loss occurs, see $Q^{\alpha\text{-Si}}\,@\,-500\,V$ (red, tip-down triangles). The critical voltage, at which no charge is lost, is ∼100 V (not shown). At this critical field strength, the electric field is strong enough to tear apart the two charges bound into an exciton. The size of excitons in silicon is about $a_\mathrm{x}^{\mathrm{Si}} = 3.6\,\mathrm{nm}$. The electrostatic potential difference at both ends over the size of the exciton at the critical field strength, and its ratio over the exciton binding energy are

$$e\,\Delta\Phi_{\mathrm{crit}}^{\mathrm{Si}} = e\,\frac{U_{\mathrm{crit}}^{\mathrm{Si}}}{d}\,a_\mathrm{x}^{\mathrm{Si}} \approx e\frac{100\,\mathrm{V}}{290\,\mu\mathrm{m}}\,3.6\,\mathrm{nm} = 1.2\,\mathrm{meV}, \qquad \frac{e\,\Delta\Phi_{\mathrm{crit}}^{\mathrm{Si}}}{E_\mathrm{x}^{\mathrm{Si}}} \approx 8\,\%. \tag{5.51}$$

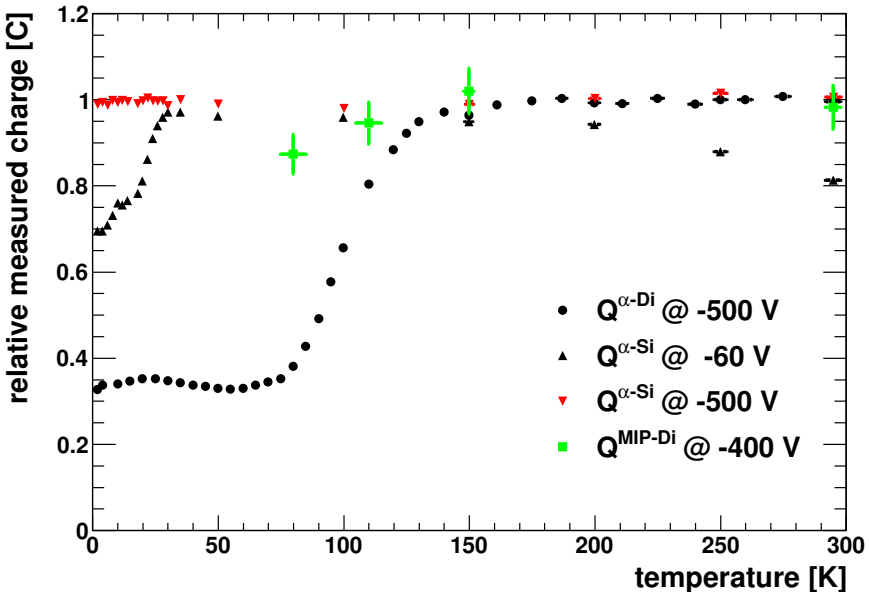

Figure 5.16.: A comparison of the total measured charge using α-particles on diamond and silicon, and MIPs on diamond. The charge loss in silicon sets in at about one fifth of the absolute temperature in comparison to diamond due to the smaller exciton binding energy. Using MIPs almost no charge loss is observed owing to the reduced charge density and thus larger exciton formation time.

In diamond, this ratio is not reached in the measurements presented here:

$$e\,\Delta\Phi^{\mathrm{Di}}_{\mathrm{max}} = e\,\frac{U^{\mathrm{Di}}_{\mathrm{max}}}{d}\,a_{\mathrm{x}} = e\frac{900\,\mathrm{V}}{530\,\mu\mathrm{m}}\,1.4\,\mathrm{nm} = 2.3\,\mathrm{meV}, \qquad \frac{e\,\Delta\Phi^{\mathrm{Di}}_{\mathrm{max}}}{E_{\mathrm{x}}} \approx 3\,\%. \tag{5.52}$$

From this estimation, it is evaluated that the full charge would be measured in diamond at a bias of 2400 V, or $E \approx 4.5\,\mathrm{V}/\mu\mathrm{m}$.

A second comparison was performed with cosmic muons, which have MIP character at the earth surface. A charge sensitive amplifier was used to collect signals induced by the passage of cosmic muons through the diamond sample. The relative charge is also shown in Fig. 5.16 (green squares). The relative charge loss at 80 K is considerably less in the case of MIPs compared to α-particles. Also this is understood qualitatively within the exciton model. Equation (5.12) reads the exciton formation time as a function of the charge density. The charge density after the phonon cooling was estimated to be about $10^{18}\,\mathrm{cm}^{-3}$ in the case of α-particles. The charge density in the track of MIPs is considerably lower, about $3{\times}10^{15}\,\mathrm{cm}^{-3}$. [95] As a consequence, the exciton formation time in the MIP tracks is reduced by a factor of roughly 300, and is therefore of the order of many hundreds of picoseconds to a few nanoseconds. Only a few excitons therefore form in the early phase of the plasma, and hence less are able to recombine at cold temperatures. The charge loss is then smaller for MIPs compared to α-particles.

The fitted τ as a function of the electric field at room temperature

The shape constant at RT as a function of the field strength is expected to increase with decreasing fields due to the increasing transport time, cf. Eq. (5.37). The transport time is inversely proportional to the drift velocity, and hence a function of the field.

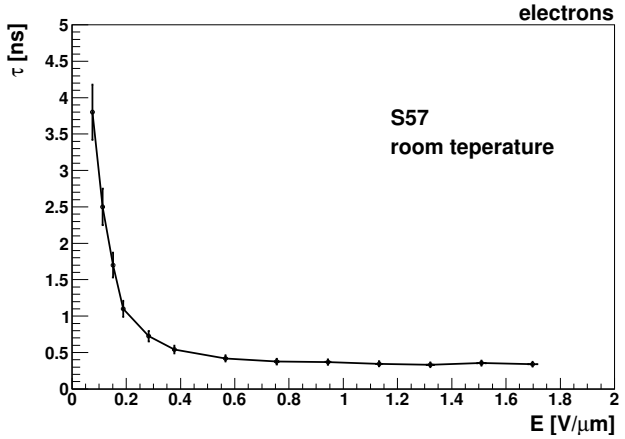

Figure 5.17.: The fitted τ at room temperature as a function of the electric field strength is shown. The solid line serves to guide the eye. The shape constant saturates at high fields towards the cut-off time constant of the measuring system.

Figure 5.17 shows the fitted shape constant as a function of the field strength. The shape constant clearly increases with decreasing fields below 0.8 V/µm and saturates at high fields towards the cut-off time constant of the measuring system. The slower rising edges are easily visible in Figs. 5.1, 5.2, and 5.3, when comparing pulses at 500 V with pulses at 100 V. The fact that the rise time is sensitive to the field strength, allows the conclusion that the recombination lifetime must be at least of the order of a few hundred picoseconds, as the shape constant is the inverse sum of the recombination lifetime and the evaporation lifetime. If τ_{rec} was considerably smaller, it would dominate τ, and hence the rise time would not increase.

As a rough estimate, the evaporation lifetime is of the order of 1 ns. With $\tau_{\mathrm{evap}} = \frac{L}{c \cdot v_{\mathrm{drift}}} \exp\left(E_{\mathrm{x}}/k_{\mathrm{B}}T\right)$, an estimate for L/c is found: $L/c = \frac{1\,\mathrm{ns} \cdot 5 \times 10^6\,\mathrm{cm/s}}{22} = 2.3\,\mu\mathrm{m}$. With $c \approx 1$, this is of the expected order of magnitude, i.e. the penetration depth.

The fitted τ as a function of the temperature

At all temperatures and fields, the modelled $i(t) \propto n_{\mathrm{exit}}(t) + n_{\mathrm{out}}(t)$ can be fitted to the measured pulse shape of $i_m(t)$; each fit resulting in a value for $\tau(T, E)$. One example of a fit of $i(t)$ to the measured pulse at 100 K and 500 V is shown in Fig. 5.18. The resulting shape constant is $\tau(100\,\mathrm{K},\, 500\,\mathrm{V}) \approx (6.8 \pm 0.1_{\mathrm{stat}} \pm 1.0_{\mathrm{sys}})\,\mathrm{ns} \approx (7 \pm 1)\,\mathrm{ns}$. The current induced from charges stemming from the outer and the inner part of the cloud are shown separately as dashed lines featuring the Erfc-shape and the exponential shape, respectively. The sum forms the solid line on top of the data. Compare as well Fig. 5.14. At this temperature, half of the inner charges recombine, thus $\frac{1}{1+\frac{\tau_{\mathrm{evap}}}{\tau_{\mathrm{rec}}}} = \frac{1}{2}$. Hence, $\tau_{\mathrm{evap}}(100\,\mathrm{K}) = \tau_{\mathrm{rec}} \approx (14 \pm 2)\,\mathrm{ns}$.

The fitted shape constant τ is shown in Fig. 5.19 as a function of temperature (closed circles) at $E \approx 1\,\mathrm{V/\mu m}$. The error bars are the statistical errors resulting from the fit. For both electrons and holes τ remains about constant at 0.4 ns between RT and 150 K. Between 150 K and 90 K, the shape constant increases steeply.[3] Due to the decrease of the amplitude of the tail in the current pulses with decreasing temperature, the signal-to-noise

[3] A comparison to measured values in the literature is difficult, or impossible, as no measurement of exciton properties in diamond using electric fields are known to the author.

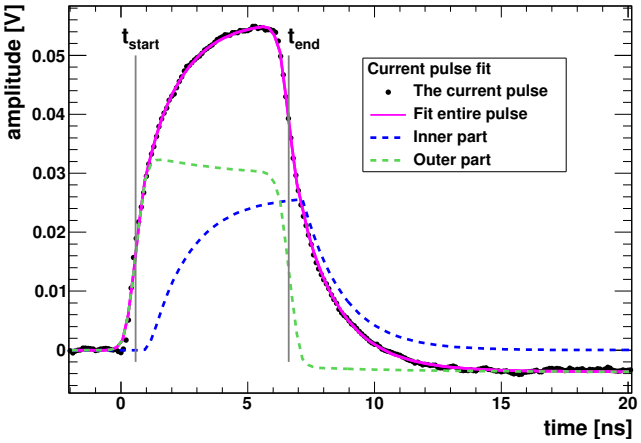

Figure 5.18.: The fit to the measured pulse at 100 K and 500 V and its components are depicted.

ratio at $T \leq 90\,\mathrm{K}$ is too small in order to accurately fit the shape constant. The fitted τ therefore decreases for $T < 90\,\mathrm{K}$. The corresponding region is marked as "insensitive".

It is now checked, if the measured temperature dependence of τ can be explained within the exciton model using the t_0-value (1 ps) extracted from charge data. Using $\frac{1}{\tau} = \frac{1}{\tau_{\mathrm{rec}}} + \frac{1}{\tau_{\mathrm{evap}}}$ and $\tau_{\mathrm{evap}} = t_0 \exp\left(E_{\mathrm{x}}/k_{\mathrm{B}}T\right)$ one finds

$$\tau(T) = \left(\frac{1}{\tau_{\mathrm{rec}}} + \frac{1}{\tau_{\mathrm{evap}}(T)}\right)^{-1} = \left(\frac{1}{\tau_{\mathrm{rec}}} + \frac{1}{t_0 \exp\left(E_{\mathrm{x}}/k_{\mathrm{B}}T\right)}\right)^{-1}. \tag{5.53}$$

A possible temperature dependence of the recombination lifetime is not allowed for. It is further important to notice that the fitted shape constant cannot be faster than the cut-off time constant, which arises from the cut-off frequency of the measuring system, cf. Chap. 4. In fact, the cut-off constant adds quadratically to the physical shape constant, resulting in the fitted shape constant. Using Eq. (5.53) and an additional such parameter τ_{cut}, a function $f_\tau(T)$ is defined as

$$f_\tau(T) = \sqrt{\left(\frac{1}{\tau_{\mathrm{rec}}} + \frac{1}{t_0 \exp\left(E_{\mathrm{x}}/k_{\mathrm{B}}T\right)}\right)^{-2} + \left(\tau_{\mathrm{cut}}\right)^2}, \tag{5.54}$$

which is to be checked against the data. Superimposed in Fig. 5.19 as dashed lines are $f_\tau(T)$ with the exciton binding energy $E_{\mathrm{x}} = 80\,\mathrm{meV}$, $t_0 = 1.3\,\mathrm{ps}$, and three different $\tau_{\mathrm{rec}} = 7, 14, 21\,\mathrm{ns}$. It is clear from Fig. 5.19 that Eq. (5.54) describes the experimental data reasonably well using the afore mentioned $E_{\mathrm{x}} = 80\,\mathrm{meV}$, $t_0 = 1.3\,\mathrm{ps}$, and $\tau_{\mathrm{rec}} = 14\,\mathrm{ns}$. Therefore, a combination of values E_{x} and t_0 exists that consistently explains two important parts of the data, i.e. the temperature dependence of both the measured charge and the fitted shape.

Additional measurements using α-particles on silicon Again silicon is used to cross-check the validity of the exciton model across another semiconductor. Similar to the effect of the exciton binding energy on the set-in temperature of the charge loss, the set-in temperature of the appearance of the tails should differ in silicon in comparison to diamond. I.e., as in the diamond case, the tails should appear in silicon at the same temperature where the charge loss sets in, so at a temperature of about 30 K, cf. Fig. 5.16.

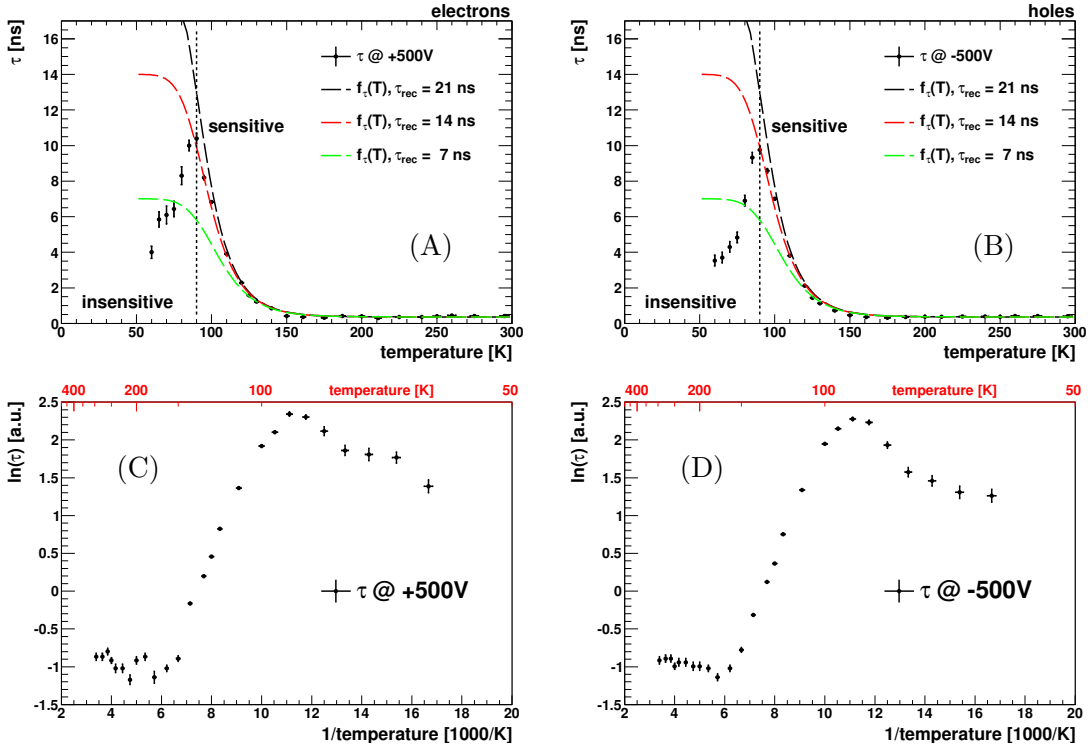

Figure 5.19.: The fitted shape constant τ is shown as a function of the temperature for electrons **(A)** and holes **(B)** at 500 V. **(C)** and **(D)** show the results in $\ln(\tau)$ vs. the inverse temperature.

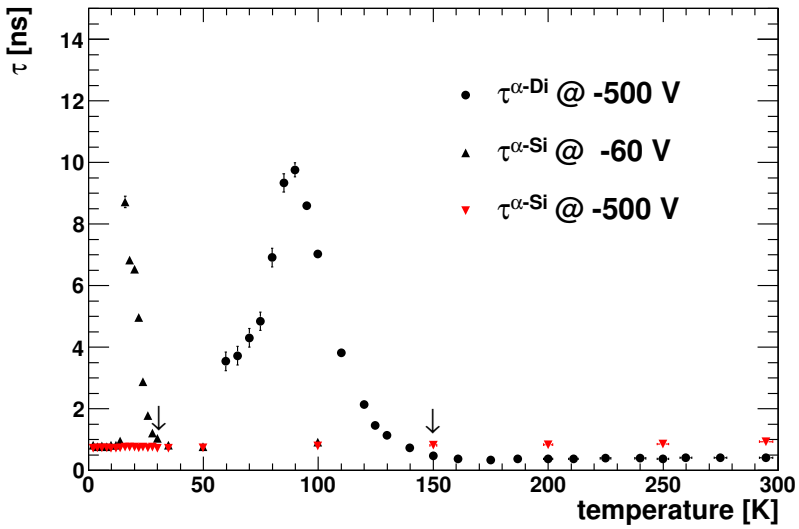

Figure 5.20.: A comparison of the fitted shape constant τ using α-particles on diamond (full circles) and silicon (triangles). The two set-in temperatures are marked with arrows. At -500 V bias, the electric field is strong enough to break up the excitons in silicon and no tails appear (red, tip-down triangles).

Shown in Fig. 5.20 are the fitted shape constants for holes in diamond at $E \approx 1\,\mathrm{V/\mu m}$ (closed circles), and in silicon at $E \approx 0.2\,\mathrm{V/\mu m}$ (black triangles) and at $E \approx 1.7\,\mathrm{V/\mu m}$ (red triangles). The tails (and exponentially rising edges) set-in at about 150 K in diamond, when the evaporation time scale reaches the order of nanoseconds. In silicon, this happens, for low field strengths, at around 30 K due to the smaller exciton binding energy. This corresponds to a similar $\exp(E_\mathrm{x}/k_\mathrm{B}T)$-value, as predicted by the exciton model. Worth noting is that at high field strengths, where no charge loss happens in silicon, neither tails do appear, as the excitons are broken up rapidly by the electric field.

The measured charge as a function of the electric field

The measured charge, Q_m, is now analysed at fixed temperatures as a function of the field strength. The difference between the initially produced charge charge and the measured is defined as [94]

$$\Delta Q = Q_\mathrm{tot} - Q_m \propto N_\mathrm{out} + N_\mathrm{in} - \left(N_\mathrm{out} + N_\mathrm{in}\,\frac{\tau}{\tau_\mathrm{evap}}\right) = N_\mathrm{in}\cdot\left(1 - \frac{\tau}{\tau_\mathrm{evap}}\right) = N_\mathrm{in}\frac{\tau_\mathrm{evap}}{\tau_\mathrm{evap}+\tau_\mathrm{rec}}. \tag{5.55}$$

If $\tau_\mathrm{rec} \to \infty$, then $\Delta Q \to 0$ and no charge is lost. In turn, if $\tau_\mathrm{evap} \to \infty$, all the inner charges recombine and $\Delta Q \propto N_\mathrm{in}$. Following this subdivision, the charge at fixed temperatures as a function of the field strength is discussed in two parts: for $T \geq 150\,\mathrm{K}$, and for $T \leq 75\,\mathrm{K}$.

At $T \geq 150$ K In this temperature range the evaporation time is considerably shorter than the recombination time, $\tau_\mathrm{evap} \ll \tau_\mathrm{rec}$. Equation (5.55) therefore simplifies to [51]

$$\Delta Q = Q_\mathrm{in}\frac{\tau_\mathrm{evap}}{\tau_\mathrm{rec}} = Q_\mathrm{in}\frac{c\cdot t_0 + \tau_\mathrm{trans}}{c\cdot\tau_\mathrm{rec}}\exp(E_\mathrm{x}/k_\mathrm{B}T) \tag{5.56}$$

$$\overset{ct_0 \ll \tau_\mathrm{trans}}{=} Q_\mathrm{in}\frac{L\exp(E_\mathrm{x}/k_\mathrm{B}T)}{c\cdot\tau_\mathrm{rec}}\frac{1}{v_\mathrm{drift}}. \tag{5.57}$$

The choice $c\cdot t_0 \ll \tau_\mathrm{trans}$ shall be motivated by data: Figure 5.21 depicts the measured charge Q_m as a function of the inverse drift velocity for T = 295, 250, 200, 150 K. It decreases from ∼52 fC at the highest field strength to ∼47 fC at $E \approx 0.2\,\mathrm{V/\mu m}$. For temperatures $\geq 150\,\mathrm{K}$, Q_m shows a linearly decreasing dependence on the inverse drift velocity over the shown range (e.g. -900 V on the left side to -100 V on the ride side for holes at RT). No saturation towards high fields is observed, and the choice $c\cdot t_0 \ll \tau_\mathrm{trans}$ is therefore justified. A saturation would be expected if the evaporation time were to saturate towards $t_0\exp(E_\mathrm{x}/k_\mathrm{B}T)$ at high fields, as is mathematically possible, compare Eq. (5.37). At least in the field strength range available in this work, no such saturation is evident promoting the choice of $c\,t_0 \ll \tau_\mathrm{trans}$.

Superimposed in Fig. 5.21 as solid lines are fits of the form

$$f_{Q_m}(1/v_\mathrm{drift}) = Q_m = Q_\mathrm{tot} - \Delta Q = Q_\mathrm{tot}\left(1 - \frac{2}{3}\,\frac{L\exp(E_\mathrm{x}/k_\mathrm{B}T)}{c\,\tau_\mathrm{rec}}\frac{1}{v_\mathrm{drift}}\right) \tag{5.58}$$

assuming $Q_\mathrm{in}/Q_\mathrm{tot} \approx 2/3$, which allows for an extraction of the slope $\beta = \frac{2}{3}\frac{L\exp(E_\mathrm{x}/k_\mathrm{B}T)}{c\,\tau_\mathrm{rec}}$. The combination of the four fits results in a slope of $\beta = (1.0\pm0.1)\,\mathrm{cm/s}$, thus

$$c\cdot\tau_\mathrm{rec} = \frac{2}{3}\frac{L\exp(E_\mathrm{x}/k_\mathrm{B}T)}{\beta} \approx 8\,\mathrm{ns}. \tag{5.59}$$

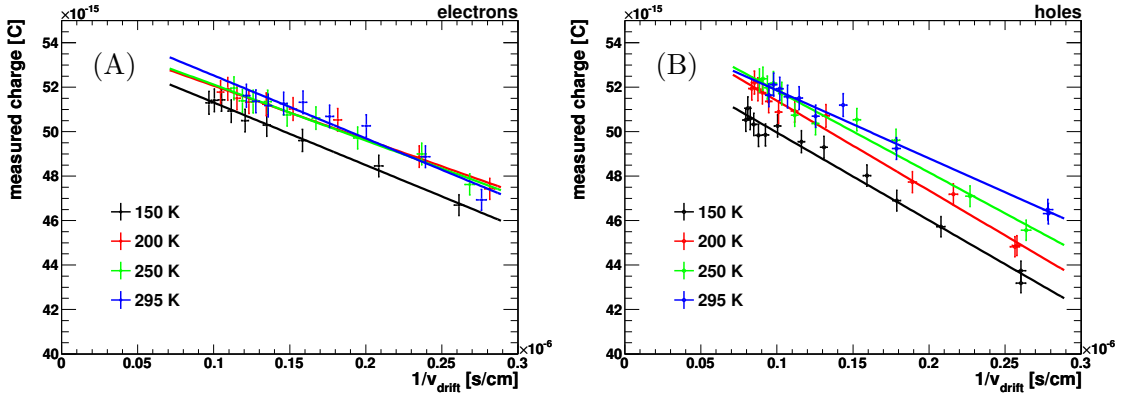

Figure 5.21.: The measured charge is shown for fixed temperatures as a function of the inverse drift velocity for electrons **(A)** and holes **(B)**. The solid line are fits according to Eq. (5.58) and are explained in the text.

This is consistent with earlier estimates, assuming that the characteristic length to leave the ionisation volume is $L = \delta_p/2 \approx 5\,\mu m = 5{\times}10^{-4}\,cm$ – that is, a simple average over the distance of all carriers to one end of the cloud for a uniform distribution of carriers. The results found agree for all three measured samples and for both carrier types. It is mentioned, that experimentally the slope does not depend strongly on the temperature, see Fig. 5.21. As the decrease in charge is proportional to τ_{evap}/τ_{rec}, and since τ_{evap} increases exponentially with decreasing temperatures, it seems evident from data that also the recombination lifetime has a temperature dependence. Further measurements are needed to clarify this aspect. Additionally, it is mentioned, that the above mechanism explains Fig. 4.11, where the measured charge is plotted against the electric field.

At $T \leq 75\,K$ In this temperature range, the evaporation lifetime has increased largely compared to the recombination lifetime. Therefore, all charges in the inner ionisation volume recombine, and the charge loss is maximal. Only the outer charges add to the measured current, and hence to the total charge. Figure 5.22 shows the measured charge for fixed temperatures as a function of the electric field strength. At temperatures $T \leq 75\,K$ the charge is a linearly increasing function of the field. As all inner charges recombine, this

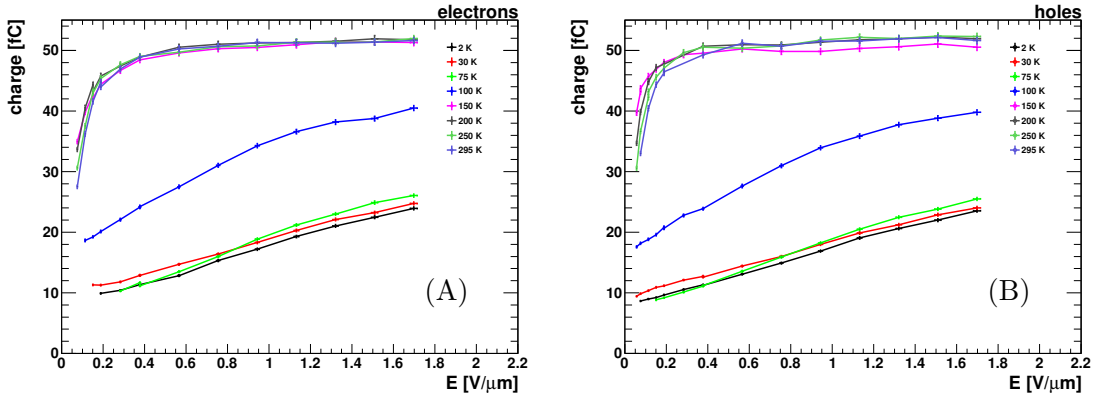

Figure 5.22.: The measured charge is shown for fixed temperatures as a function of the electric field strength for electrons **(A)** and holes **(B)**.

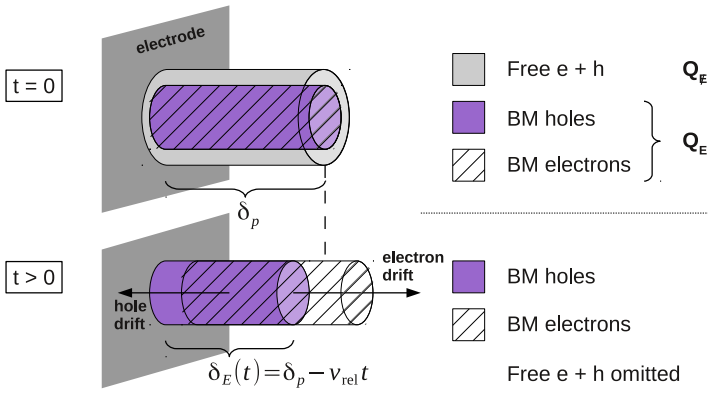

Figure 5.23.: The drift of cylindrical electrons and hole charge clouds apart from each other is illustrated.

means that the division of the total charge into outer charge and inner charge is a function of the electric field. Note that the pulses at these temperatures are *flat*. Hence, no charge is lost during drift, but with lower field strengths, less charges start drifting from the ionisation volume. Therefore, the mechanism that defines how much charge is "inside" and "outside" needs to take place within the first few hundred picoseconds. This early development of the plasma is not accessible with the measurement presented here, but only the outcome of that mechanism: the measured "outer" charge, i.e. the charge, which has not recombined in the early plasma phase.

If the linear behaviour observed in Fig. 5.22 is extrapolated towards $E = 0\,\mathrm{V/\mu m}$, the extrapolation crosses the ordinate at around 20 % of the total charge. Hence, there seems to be an amount of charge that is "outside" at all biases, and therefore free, independent of the electric field (denoted $\not E$). This might be due to the low charge density at the borders of the ionisation volume after the heat dissipation (few tens or hundreds of picoseconds). Additionally, there is a part increasing linearly with the electric field (denoted E). In this part, electrons and holes are either free or bound to excitons, and are therefore denoted Boltzmann holes (BM holes) and Boltzmann electrons in Fig. 5.23.

In total, the total charge is the sum of those charges that are not influenced by the electric field, and those, that are, hence:

$$Q_{\mathrm{tot}} = Q_{\not E} + Q_E = Q_{\not E} + Q_{\mathrm{rec}} + Q_{\mathrm{nrec}}. \tag{5.60}$$

The measured charge Q_{out} is the sum of the "at all biases outer" charge, and the not-recombined charge:

$$Q_{\mathrm{out}} = Q_{\not E} + Q_{\mathrm{nrec}}. \tag{5.61}$$

It is thought that the linear charge increase is due to a faster longitudinal drift process during the thermalisation and cooling phase. With higher field strength, the charges clouds drift apart faster, and less excitons can form after the cooling phase. [51] The scheme is depicted in Fig. 5.23. However, no quantitative model can be presented here, as there is no description of "drift" and "diffusion" of non-thermalised carriers available in the literature.

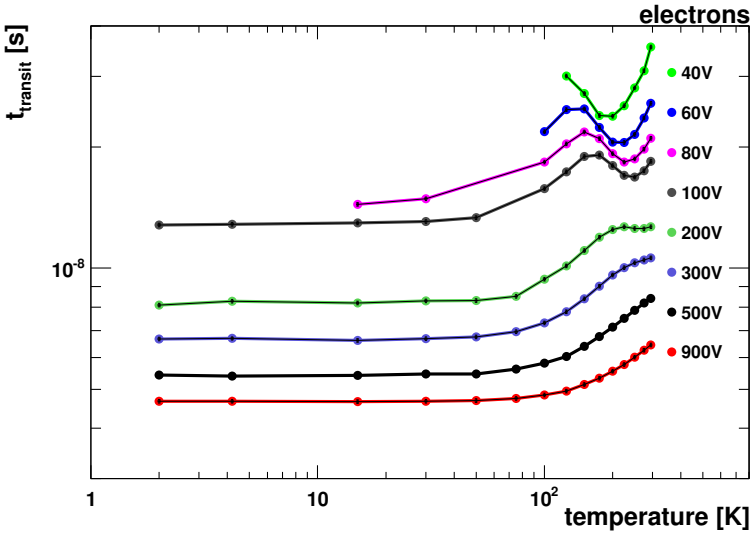

Figure 5.24.: The transit times for electrons at various temperatures and fields are shown for *S57*. Note the double logarithmic scale. Lines are drawn for constant voltages in order to guide the eye.

5.3.3. Conclusion

A model is presented in order to explain the total measured charge as well as the pulse shape as a function of the temperature. The model includes the heating and the ionisation within the ionisation volume by the α-particle and subsequent charge and phonon transport. The charges inside of the plasma form excitons, which are in a quasi-equilibrium with free e-h pairs. Recombination and drift perturb the quasi-steady-state. The recorded data are compared to model predictions, and a set of values is found, namely the exciton binding energy $E_x = 80\,\text{meV}$, a recombination lifetime of the order of a few nanoseconds, and an exciton creation time constant of the order of picoseconds, that yield an accurate description of the data. The model describes the appearance of tails and the charge losses for temperatures at and below 150 K. A further cross-check is performed with a silicon pad detector providing results that confirm the validity of the model.

5.4. The impurity-assisted repopulation effect

The transit time of electrons shows a particular behaviour, i.e. it does not monotonically increase with temperature, as would be expected from acoustic phonon scattering. Instead, see Fig. 5.24, for biases around 200 V a local maximum emerges, which is more pronounced towards lower biases, particularly visible at 60 V, 80 V, and 100 V. The position of the maximum shifts towards higher temperatures with increasing bias, until the maximum disappears at around 300 V. This behaviour is *a priori* not expected and has not been reported in the literature.

It is thought that the seen effect arises due to the different effective electron masses in different valleys [96], and a model from [94] is reproduced here and compared to data. With the transverse mass being smaller compared to the longitudinal mass, electrons drift faster (slower) in the transverse (longitudinal) valleys. This therefore results in two different drift velocities v_1 and v_2 for the different valleys. The six conduction band minima split up by an energy Δ into two different states, which are two-fold degenerated (longitudinal), and four-

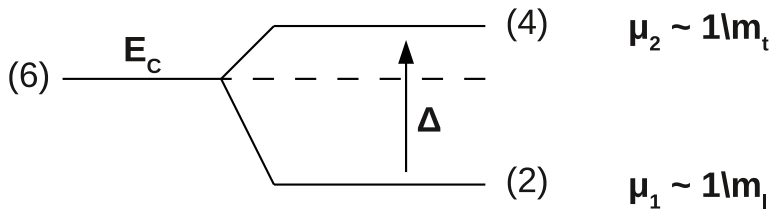

Figure 5.25.: The band splitting is illustrated. Δ is the energy difference between the two states, degeneracy is given in parentheses. [94]

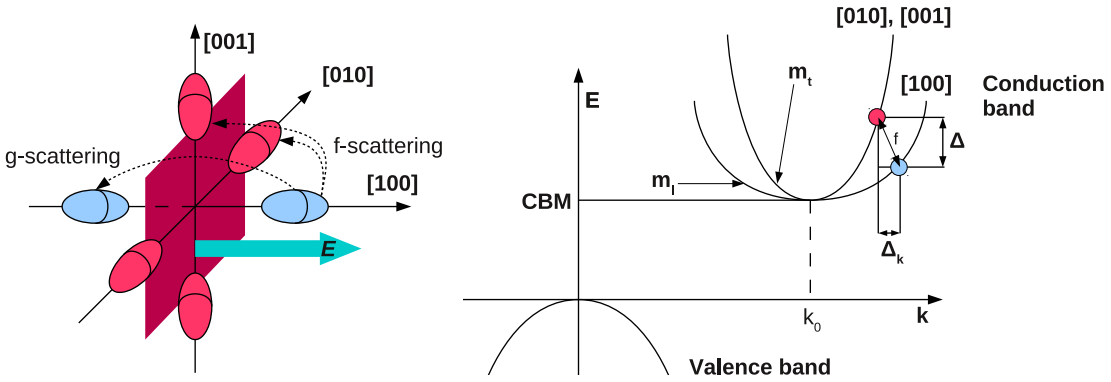

Figure 5.26.: **(A)** The f- and g-scattering processes are shown for a multivalley semiconductor and an applied electric field along the [100] direction. **(B)** The f-scattering interchanges charges from the transversal valley with the longitudinal valleys. For this, an energy difference Δ and a momentum transfer $\Delta_{\boldsymbol{k}}$ are needed. The $\Delta_{\boldsymbol{k}}$ is provided/absorbed by impurities in the lattice. [51]

fold degenerated (transversal), as is illustrated in Fig. 5.25. The presence of a sufficient amount of nitrogen impurities is thought to enable intervalley f-scattering, cf. Sec. 2.2.7 and Fig. 5.26. E.g., in order to scatter from a [100] valley to a [010] valley, a [110] phonon near the K-point, which carries a large momentum, is needed. As these are unlikely to be present in the crystal itself, nitrogen impurities with a broad spectral function might render efficient f-scattering possible.

With the degeneracy of states being 4 to 2, and assuming a Boltzmann distributed population density for the densities n_1 and n_2 – with $n_1 + n_2 = N$ –, it is found that

$$\frac{n_1}{n_2} = \frac{4}{2}\exp\left(-\Delta/k_\mathrm{B}T\right), \quad n_1 = \frac{N}{1+2\cdot\exp\left(-\Delta/k_\mathrm{B}T\right)}, \quad n_2 = \frac{N}{1+\frac{1}{2}\cdot\exp\left(\Delta/k_\mathrm{B}T\right)}. \tag{5.62}$$

The current induced by the sum of the two densities is

$$j = j_1 + j_2 = en_1v_1 + en_2v_2 = eEN\left(\frac{\mu_1}{1+2\cdot\exp\left(-\Delta/k_\mathrm{B}T\right)} + \frac{\mu_2}{1+\frac{1}{2}\cdot\exp\left(\Delta/k_\mathrm{B}T\right)}\right). \tag{5.63}$$

and the transit time becomes

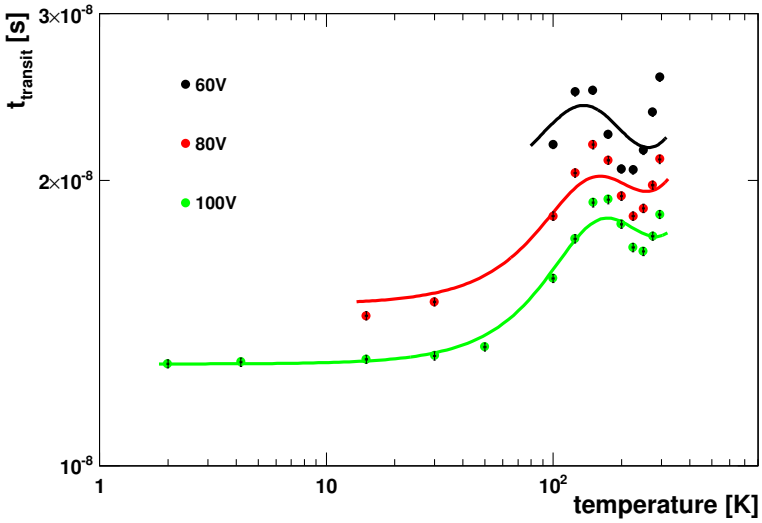

Figure 5.27.: The transit time for three selected biases is shown with their modelled t_t superimposed as solid lines. The model seems to include all features of the qualitative behaviour, but cannot serve as a precision fit.

$$t_\mathrm{t} = \frac{d}{\mu_1 E} \frac{1}{\frac{1}{1+2\cdot\exp\left(-\Delta/k_\mathrm{B}T\right)}(1-m)+m} \tag{5.64}$$

with the mobility ratio $m = \mu_2/\mu_1$. If the differing drift velocities arise only due to the mass difference, but not due to a difference in the momentum relaxation time, then m becomes independent of the temperature: $\mu_{1,2} = e\tau(T)/m^*_{1/2}$. Assuming further that the main temperature dependence of the $\mu_{1,2}$ stems from NIS and APS, the values from Tab. 5.3 can be used as a prediction of the low-field mobility: $\mu_1 = (1/\mu_\mathrm{NIS} + 1/\mu'_\mathrm{APS})^{-1}$. The actual mobility at a certain bias is, of course, lower. With these values, t_t is modelled to explain the qualitative behaviour of the measured transit time. Figure 5.27 shows modelled functions according to Eq. (5.64) for the three bias values, 60 V, 80 V, and 100 V, superimposed on the data points. The model seems to include all features of the qualitative behaviour, but cannot serve as a precision fit. The mobility ratio used for the three curves is $m = 10$ and the energy difference is $\Delta \approx 60\,\mathrm{meV}$. At the three biases, the mobility is about 78 %, 73 %, and 67 % of the low-field mobility, respectively. The mobility ratio, and therefore mass ratio if the same momentum relaxation time is assumed, was calculated to be $m = 5.2$, [97] a factor of two lower than the one used above. The difference might arise due to distinct electric field ranges used. At high fields, the electrons could have high $\boldsymbol{k}$-values, at which the bands are no longer parabolic, and therefore their effective masses are different.

The fact, that diamond might feature two different drift velocities, needs further attention. The recorded current pulses do not feature a two-step falling edge, but fall off continuously. With two drift velocities, one might naively expect two steps, as electrons in the fast valleys might arrive significantly earlier than those in the slow valleys. This was actually reported in ultra-pure scCVD diamond in a Ph.D. thesis by M. Gabrysch [64] and recently in Nature Materials [96]. The substantial difference between the results reported herein in comparison to those from Refs. [64, 96] might be that the samples used here are of worse grade. Therefore, the presence of a sufficiently large density of impurities are thought to give rise to a single, continuous falling edge via the following mechanism. The ionisation

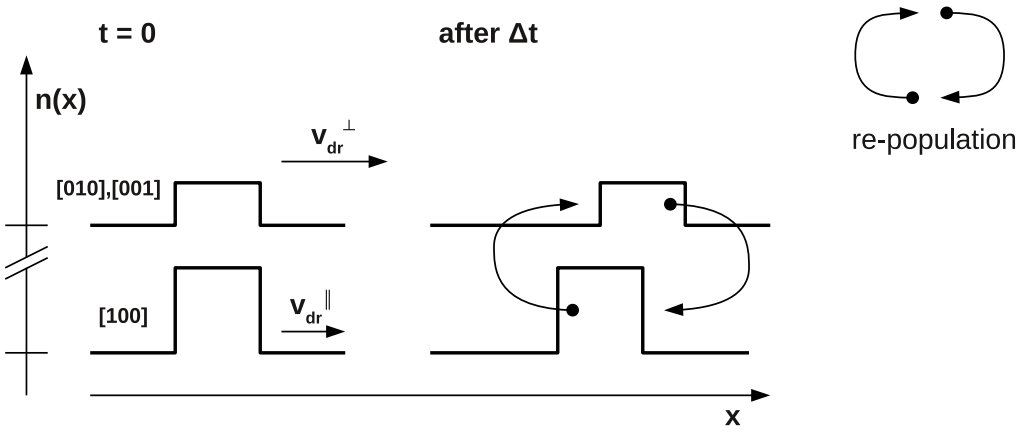

Figure 5.28.: The re-population at the fast front and the slow end of the charge package is illustrated. (from [51])

via the α-particle creates free electrons in the conduction bands over a certain depth, say a package. They thermalise and "fall" into both fast and slow valleys. When carriers in both valleys start to drift, those in the fast valleys drift faster and will reach a depth, or position, in the crystal, where no slow electrons are present. The density ratio at every position x is thought to be Boltzmann distributed. With impurities enabling f-scattering processes, electrons at the front of the package can scatter from the populated n_1 to the empty n_0, see also Fig. 5.28.
At the left end of the charge package, the opposite effect occurs. The fast electrons have already drifted further, such that there are no fast electrons in n_1 at this end. Again, f-scattering enables intervalley scattering, but now from the slow to the fast valley. This turnover process[4] happens continuously at the front and the end of the charge package. Thereby, those states that are empty, i.e. not populated, are being re-populated via the turnover process, that is, n_0 is re-populated at the fast front of the charge package, and n_1 is re-populated at the slow end of the charge package. As a result, the charge package drifts as a whole, and only one falling edge arises. [51]

Reference [96] presents the measurement of the valley quantum number of electrons, which was carried out in parallel to the work presented herein. It discusses the possibility of creating "valleytronic" devices, that make use of the valley quantum number of electrons in order to encode information, the crucial property being the different effective masses between longitudinal and transversal valleys. The work presented here shows analogue results and emphasises the importance of the use of high quality single-crystal material if valleytronic devices are to be realised.

5.5. Conclusion of the TCT Measurements

The transient current technique offers a straight forward method to measure charge carrier properties accurately in many different semiconductors, including high-impedance ones like diamond. With a temperature controlled environment, the TCT offers an even richer tool enabling the characterisation of the temperature dependence of basic charge carrier properties. Besides the low-field mobility and the saturation velocity, it is possible observe

[4]German: Umklapp-Prozess

the implications of different effective electron masses residing in different valleys. The peculiar current behaviour at temperatures between 150 K and 50 K allows for indirect observation of the evaporation of excitons. Complementarily, the amount of missing charge towards lower temperatures is the result of an increase in recombined charges, and the order of magnitude of the recombination lifetime can be extracted to be a few nanoseconds. The flat pulse form at and below 50 K readily shows the time scale of the evaporation time at cryogenic temperatures (above microseconds), and the field dependence of the measured charge below 75 K offers the conclusion, that excitons must form within the first 100 ps or so of the initial plasma. A temperature controlled TCT therefore allows for many more conclusions and observations than one may naively expect.

It was demonstrated that diamond as well as silicon can be used as a charged particle detector in the extreme environment of liquid helium temperatures. In diamond charge losses of about 2/3 are observed at temperatures below 50 K compared to the room temperature charge yield using short-ranged, highly-ionising particles. Studies with MIPs showed, however, that the charge loss is energy-loss dependent, and less charge losses are observed with MIPs in comparison to α-particles. Therefore, unirradiated diamond is fully functional for the detection of MIPs, cf. as well [92] down to at least 2 K. With no significant charge loss due to the extreme temperature environment, both CVD diamond and silicon serve as candidates for the cryogenic beam loss monitors to be installed at the LHC.

6. TIMING STUDIES FOR THE ν-ToF MEASUREMENTS AT CNGS[1]

Diamond detectors were installed as a novel, fast diagnostic tool in the CNGS facility in 2011 following the neutrino time-of-flight results published by the OPERA collaboration in September 2011. Among others, four polycrystalline CVD (pCVD) diamond detectors were placed in the so-called secondary particle beamline about 1200 m downstream of the CNGS target, where incoming protons produce kaons and pions in strong interactions. The diamond detectors measure the beam structure of the muons which are produced together with the muon neutrinos in the kaon/pion decays. Upstream of the CNGS target, a fast beam current transformer measures the proton beam structure. The sub-nanosecond single-pulse time resolution of pCVD diamond for a minimum ionising particle in combination with a GPS system allows the measurement of the GPS timing of individual muon bunches crossing the detectors with a precision of < 1 ns. The complicated structure of the CNGS muon beam in 2011 necessitates the usage of the detector response of many adjacent bunches in order to compare the proton beam structure with the muon beam structure. An analysis of the detector signals was carried out, which provides an independent timing measurement at CERN with a precision of 1.2 ns. Uncertainties from other sources as cable lengths add up to 3.4 ns, resulting in an overall precision of 3.6 ns. The distance between the beam current transformer and the diamond detectors has been measured to (1859.95±0.02) m. The nominal time-of-flight of (6205.3±1.7) ns for a 17 GeV/c muon, as present in the CNGS muon beam, falls within the uncertainties of the measured time-of-flight of (6205.2±3.6) ns. Hence, the GPS timing measurements performed at CERN are consistent.

6.1. Introduction

The CNGS facility (CERN Neutrinos to Gran Sasso) [99] aims at the direct detection of muon-neutrino to tau-neutrino oscillation by measuring the appearance of the tau-neutrino. An intense muon-neutrino beam is generated at CERN and directed over 732 km towards the Gran Sasso National Laboratory (LNGS) in Italy, where four detectors (BOREXINO [100], ICARUS [101], LVD [102], OPERA [10]) are located. In addition to the main goal of tau-neutrino measurements, the facility profits from accurate time and distance measurements between the source of the CNGS neutrino beam and the Gran Sasso experiments, allowing the determination of the neutrino velocity with high accuracy. Until 2011 the start time of the neutrinos racing towards Gran Sasso has been solely based on measurements of the fast beam current transformer that is installed in the primary proton beam line upstream the CNGS target; the time structure of the protons passing through the beam current transformer gives the Global Positioning System (GPS) time tag. After the publication from the OPERA collaboration in September 2011 on the neutrino velocity measurements [9], several polycrystalline chemical vapour deposition diamond detectors (DD) were placed in the secondary beam line about 1200 m downstream of the CNGS target in order to

[1] cf. Ref. [98]

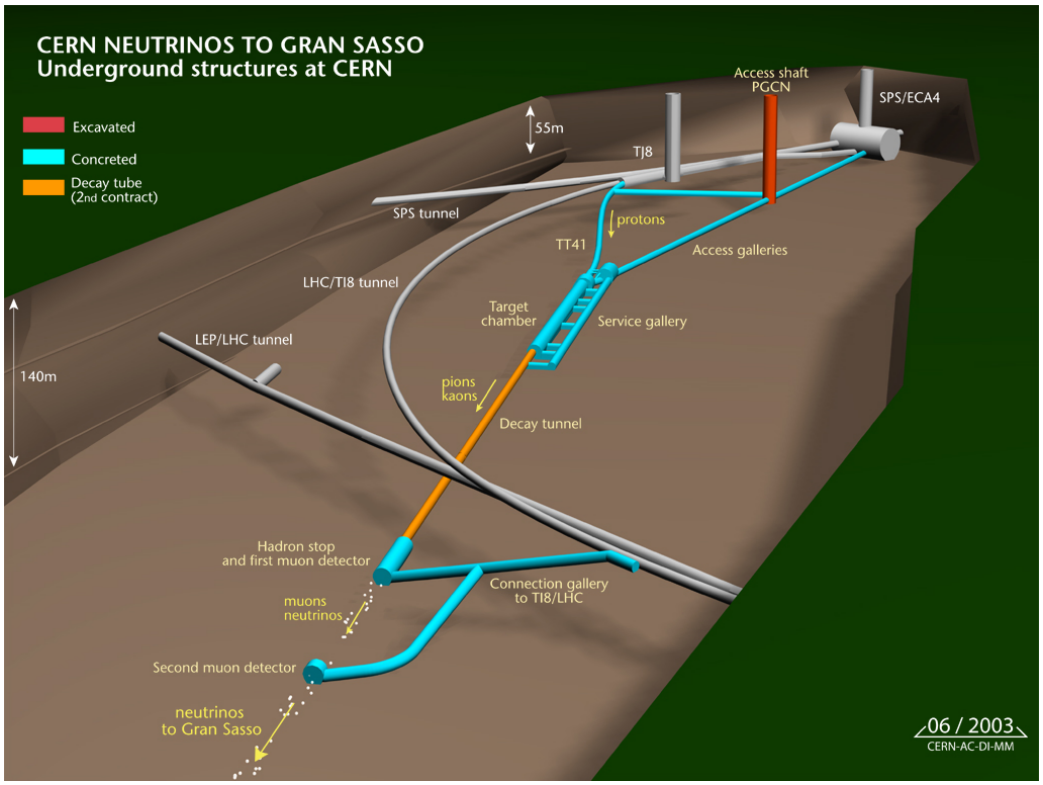

Figure 6.1.: Schematic overview of the CNGS neutrino beam facility at CERN.

measure the time structure of the muon spills independently. This allows an accurate measurement of the GPS timing of the muon bunches crossing these detectors, and provides an independent timing measurement at CERN.

6.2. The CNGS Facility

The 400 GeV/c CNGS proton beam is fast extracted from the CERN SPS accelerator; during a 6 s long cycle there are two extractions separated by 50 ms, each lasting 10.5 µs with up to 2.4×10^{13} protons/extraction. With a 5 ns bunch spacing resulting from the 200 MHz SPS RF system, the number of bunches per extraction is 2100. The beam is sent down an 840 m long proton beam line onto a carbon target producing kaons and pions. The positively charged pions and kaons are energy-selected and guided with two focusing lenses, the so-called horn and reflector, in the direction of Gran Sasso. These particles decay in a 1000 m long, 2.5 m diameter vacuum tube into muon-neutrinos and muons. All the hadrons, i.e. protons that have not interacted in the target and pions/kaons that have not decayed in flight, are absorbed in a hadron stopper, see "hadron stop" in Fig. 6.1. Only neutrinos and muons can traverse this 18 m long block of graphite and iron. The muons, which are ultimately absorbed downstream in abound 500 m of rock, are measured in two muon detector stations, each consisting of 41 ionisation chambers. The stations reside in two caverns called Pit 1 and Pit 2 which are separated by 67 m of rock. The average energy of the muon-neutrinos which are sent to Gran Sasso, is 17 GeV/c. A schematic overview of the CNGS neutrino beam facility at CERN is shown in Fig. 6.1.

The time information at CNGS for the OPERA neutrino time-of-flight (ToF) analysis was derived from a fast beam current transformer (BCTF40) [103] that is installed in the

CNGS extraction line upstream of the CNGS target. The time structure of the extracted protons is measured with this BCTF40 detector and the time information is tagged with a GPS time.

Polycrystalline CVD diamond detectors were installed in the muon pits in November 2011. Both the measurement set-up for the BCTF40 and the one for the DDs are connected to a General Machine Timing (GMT) receiver, which communicates with the GPS system. The muon beam structure is measured via the DDs and is also GPS time tagged. Using both time tags and taking into account all additional delays, the timing measurement at CERN can be verified independently.

The next section describes the experimental set-up, followed by the description of the flux simulation. Details of the trigger and timing system are explained in Sec. 6.5. The data analysis is described in Sec. 6.6.

6.3. Experimental Set-up

6.3.1. Diamond detectors

Polycrystalline CVD diamond is a suitable detector material for the measurement of the time structure of the CNGS muon beam, as the detector response to a narrow muon bunch is a signal with full width half maximum (FWHM) of approximately 2 ns. This is sufficiently smaller than the bunch spacing (5 ns) of the CNGS muon beam, and hence the signals stemming from adjacent bunches are sufficiently separated in order to identify a rising edge for each pulse. Note that the time resolution of diamond detectors is considerably shorter, i.e. it is in the sub-nanosecond regime, as will be shown in Sec. 6.6. Short signal time is realised by operating the detectors at 1 V/µm. The high free charge carrier mobility in diamond of $\sim$800 $\mathrm{cm}^2/\mathrm{Vs}$ at 1 V/µm results in a first order estimation of the FWHM of

$$t_{\mathrm{FWHM}} = \frac{\ln(2) \cdot \mathrm{CCD}}{v_{\mathrm{drift}}} = \frac{\ln(2) \cdot \mathrm{CCD}}{\mu E} \approx 1.7\,\mathrm{ns}, \tag{6.1}$$

where CCD is the charge collection distance, and a value of CCD = 200 µm is used here. Hence, the FWHM is ≤ 2 ns.

The measured signal is composed of a DC part of 10.5 µs length and is modulated by a 5 ns structure resulting from the SPS RF. The DC part is the result of the overlay of signal tails from adjacent bunches.

Three pCVD diamond detectors were installed in Pit 1, two at the centre, called Centre Top (CT) and Centre Bottom (CB) and one 135 cm left of the centre (L). A forth one is installed in Pit 2. In this work the signals from the DDs in Pit 1 are discussed. The set-up in Pit 1 is depicted in Fig. 6.2 **(left)**, and details of the Centre DDs in Fig. 6.2 **(right)**.

The sensor material was produced by Element Six [78] and metallised by Diamond Detectors Ltd [79]. DDL quotes a thickness of 500 µm and a CCD of 200 µm. Measurements have shown that the charge collection distance is rather 180 µm. All main DD parameters are listed in Tab. 6.1. The final detectors, including a sensor holder, an RF-tight housing, and a PCB with 50 Ω read-out lines, were provided by CIVIDEC Instrumentation [81].

6.3.2. Electronics, Read-out and Charge Collection

The detectors were connected to the bias voltage via a bias resistor (R1) of 1 MΩ resistance and a charging capacitor (C1), see Fig. 6.3 and Tab. 6.1. The signals were read out at the low-voltage side of the detector, which was DC-terminated to ground by a 1 MΩ resistor.

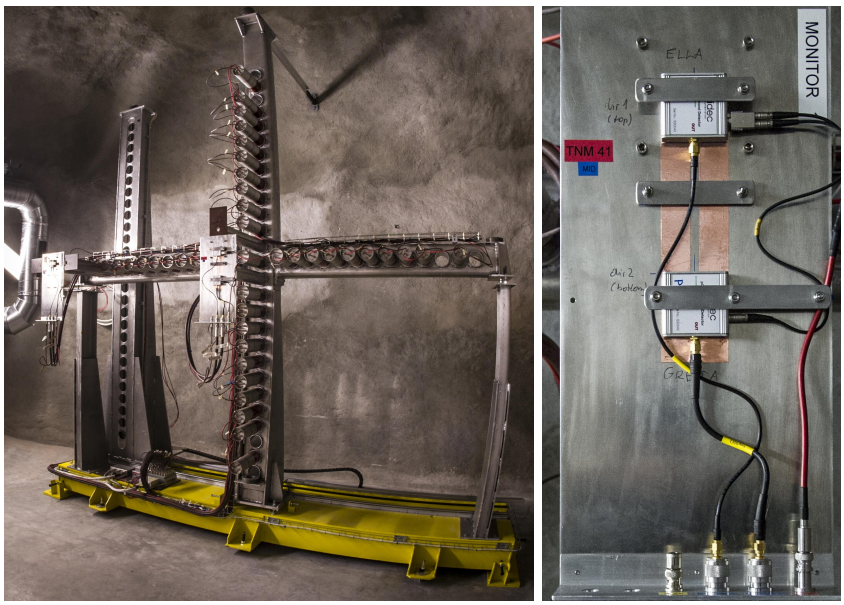

Figure 6.2.: Photo of the muon detector station **(left)** in Pit 1 with two detectors in the middle of the cross and one on the left end. Additionally, a close-up of CT and CB is shown **(right)**.

The charging capacitors were of 11 nF capacitance for CT and L, and of 2 nF capacitance for CB. All detectors were operated at 500 V, i.e. 1 V/µm. It is important to mention, that the detectors were read out directly without electronic amplification. The low detector capacitances of 10 pF and 3 pF in combination with the 50 Ω read-out impedance provide fast time constants of 500 ps and 150 ps, respectively. This allows for the resolution of the 5 ns RF structure from the extracted SPS beam, which has already been proven. [104]

Two LeCroy WaveRunner 104MXi-A oscilloscopes with an analogue bandwidth of 1 GHz and a sampling frequency of 5 GS/s were used for the data read-out. The oscilloscopes sample the incoming analogue signals with 8 bits, providing an analogue-to-digital converter range of 256. All detectors were connected to the read-out oscilloscopes via CK50 cables. [105] The 50 Ω cables have a specified attenuation per 100 m of 9.1 dB at 1 GHz and 2.7 dB at 100 MHz and a velocity factor (VF) of 78 %, VF being the speed of wave propa-

Table 6.1.: Main parameters of the diamond detectors installed in muon Pit 1.

Detector name	Centre Top (CT)	Centre Bottom (CB)	Left (L)
Specified thickness [µm] [a]	500	500	500
Electrode size [a]	∅=3 mm	8×8 mm^2	8×8 mm^2
Electrode area [mm^2] [b]	7.1	64	64
Ionisation volume [mm^3] [b]	3.53	32.0	32.0
Detector capacitance [pF] [b]	3	10	10
Time constant [ps] [b]	150	500	500
Charging capacitance [nF] [a]	11	2	11

[a] Data specified by manufacturer [b] Calculated from manufacturer data

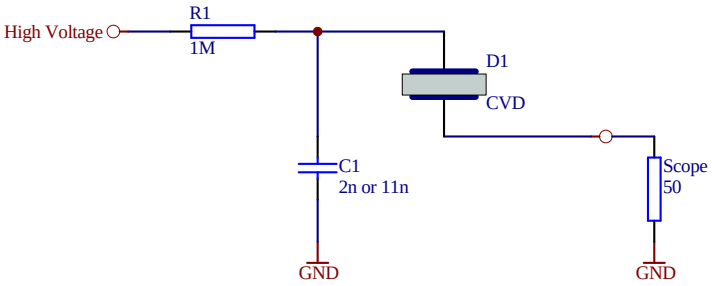

Figure 6.3.: Connection scheme of the detectors. R1 is the loading resistor for the bias voltage, C1 the charging capacitor, and D1 the detector.

gation in the cable relative to the speed of light in vacuum. The transmission time of the three CK50 cables was measured using an oscilloscope and a pulser set to output pulses of 50 ns length with a rise time of 500 ps on 50 Ω at a repetition rate of 1 kHz. The one-way transmission times are 328.1 ns, 328.3 ns and 328.1 ns for CT, CB, and L, respectively, corresponding to the actual cable length of about 77 m. The trigger signals of the oscilloscopes were calibrated within a precision of 0.5 ns.

The charge collection of all detectors were checked prior to installation in the pit at two different energies. One test was done using an ^{241}Am α-source, and the other with a ^{90}Sr β-source. The detectors showed a charge collection of (135 000±15 %) electrons/alpha, which fits the expected charge resulting from a sealed ^{241}Am α-source ($E_\alpha = 4.6$ MeV) for pCVD diamond with a CCD = 190 µm. The spread over the three detectors is due to differing CCDs. The charge tests based on the β-source showed a charge collection of (6500±20 %) electrons/MIP across the detectors, compatible with a CCD = 180 µm.

The expected collected charge per extraction from the high intensity muon beam is $Q = Q_{\mathrm{MIP}} \cdot I_\mu$, where I_μ is the muon flux integrated over the ionisation volume and over the whole extraction. The measured charge per extraction, averaged over the three detectors, agrees at a 15 % level with simulations, indicating a linear response of the diamond even at this high particle fluence. The dark current prior to the extractions is of the order of a few nanoampere, and hence negligible.

6.4. Flux Simulation

Monte Carlo simulations were exploited to assess the feasibility of the measurement and the detector working environment. Calculations were performed with the FLUKA [106] code by slightly modifying the standard set-up already used for all CNGS related simulations. [107] The reliability of this simulation framework has been verified on many observables, in particular for what concerns the response of the ionisation chambers in the muon pits. [108] No effort to describe the exact geometry of detectors and supports was performed at this stage, since the scope of the calculation was essentially to determine the time distribution of all particles that generate a signal in the diamond detectors in order to assess that this time distribution does not affect the sensitivity of the measurement. Not only muons, but also secondary electrons and photons generated by muons in the pit walls and internal materials were accounted for. The diamond detectors were modelled as a uniform layer sandwiched between two Al supporting layers of 3 mm thickness. The detectors thickness has been indicatively set at 0.1 mm (simulations were performed before the actual choice

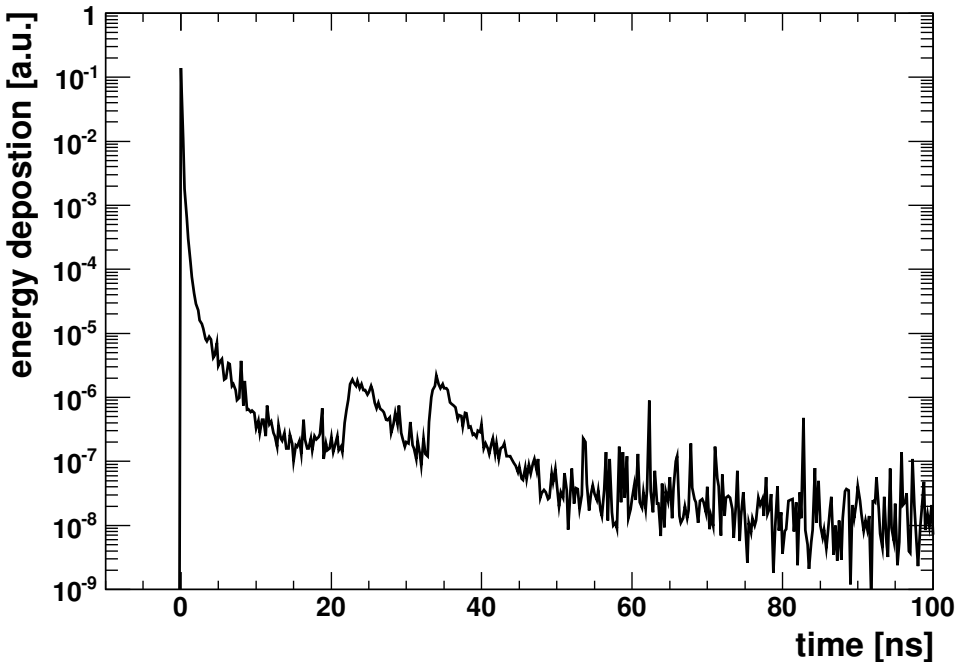

Figure 6.4.: The simulated time distribution of the energy deposition for a diamond detector in Pit 1 is shown.

of the detectors), with a density of $3.52\,\mathrm{g/cm^3}$. In the simulation, two such sandwiches were inserted in each of the muon pits, one near to the entrance wall and one in front of the ionisation chambers, oriented perpendicularly to the beam and spanning the whole transverse dimension of the pit. The energy deposition in the detectors were simulated as a function of the arrival time of particles and as a function of radial distance with respect to the beam axis. The intrinsic resolution and timing response of the detectors have not been included in the simulations. For both positions in each pit, the distribution of deposited energy versus arrival time peaks at the arrival of the muon bunch. The falling edge of the simulated signal drops two orders of magnitudes in about 2 ns. Very small secondary peaks are present, with amplitudes five orders of magnitude lower than the prompt peak, as shown in Fig. 6.4 for a single zero-width muon bunch. The time delay of these secondary peaks is consistent with the travel time of particles reaching the detectors after being reflected by the downstream pit walls. Convolution of the response to a single bunch with the time structure of a beam consisting of 2100 bunches shows that the original beam time structure is only minimally affected.

Simulated particle fluences and simulated deposited energy at the actual diamond detectors positions are reported in Tab. 6.2 per 10^{13} protons on target (pot). The contribution from charged hadrons and neutrons is negligible. Energy deposition values have been rescaled linearly to the finally used detector thickness in order to get a first order estimate of the needed dynamic range of the oscilloscope for data taking. For a single extraction with 2.4×10^{13} protons, an energy of 12 TeV are deposited in CB. With an average electron-hole-pair creation energy of 13.25 eV and a CCD of 200 µm the amount of the total measured charge per extraction is about 58 nC. An average bunch creates therefore 27 pC. If it is assumed that these charges drift for 1 ns, they induce a current of 28 mA, and hence a voltage difference of 1.35 V appears at the input of the oscilloscope. With a gain set

Table 6.2.: Particle fluencies and deposited energy at the diamond detectors positions for 10^{13} pot.

Position	Flux [particle/cm^2/10^{13} pot]			Dep. energy [GeV/cm^2/10^{13} pot]
	μ	e^+e^-	γ	sum
Pit 1, centre	$2.4 \cdot 10^7$	$2.7 \cdot 10^6$	$1.5 \cdot 10^7$	7750
Pit 1, left	$2.3 \cdot 10^6$	$8.6 \cdot 10^5$	$5.5 \cdot 10^6$	1250

to 500 mV/division, the oscilloscope translates the 1.35 V to about 80 ADC units (ADC), which can also be seen in Fig. 6.10, Sec. 6.6.

6.5. Trigger and Timing

To confirm the accuracy of the CNGS timing system it is necessary to relate the timing signals from the DDs with those from the BCTF40 detector previously used. This is achieved by finding the ToF between the two detector points using the measured timestamps and relative offsets, and ensuring that they agree with the nominal ToF over the same distance. In order for the ToF to be measured on the nanosecond scale it is necessary to know precisely all the delays introduced between the detection of a particle in the detector and the signal being registered by the system in addition to the distance travelled by the particle. The transmission times of all data-carrying cables were measured using a variety of methods, including reflectometry and using a transportable CS4000 caesium clock. [109] The distance travelled was measured by an independent survey group.

6.5.1. Survey

Initially, the survey group has aligned all the components of the CNGS line, including the BCTF40, with respect to a network of geodetic points which was determined by topographical methods linked to the SPS geodetic network. Neither GPS measurements at the surface level nor link between surface to tunnel were realised. The relative accuracy of this underground network, measured with high precision instruments such as the Electronic Distance Measurer Mekometer ME5000, the total station TDA5005 and the Gyro-theodolite GYROMAT2000, could be estimated to be in the range of a few millimetres. Then, additional measurements were carried out, with less accurate measuring techniques, to localise the DDs and the BCTF40 position with respect to the same network. These measurements yield a distance $d_{\text{BCT-DD}}$ between the BCTF40 and the DDs in Pit 1 of:

$$d_{\text{BCT-DD}} = (1859.95 \pm 0.02)\,\text{m}. \tag{6.2}$$

6.5.2. Set-up at CERN

There are two timing measurements made on the CNGS beam line; one for the primary (proton) beam as it leaves the SPS ring and passes BCTF40 and one for the secondary (muon and neutrino) beam from the DDs located in Pit 1, see Fig. 6.5. The delays examined here are those between the start time of an event window as measured by a reference GMT

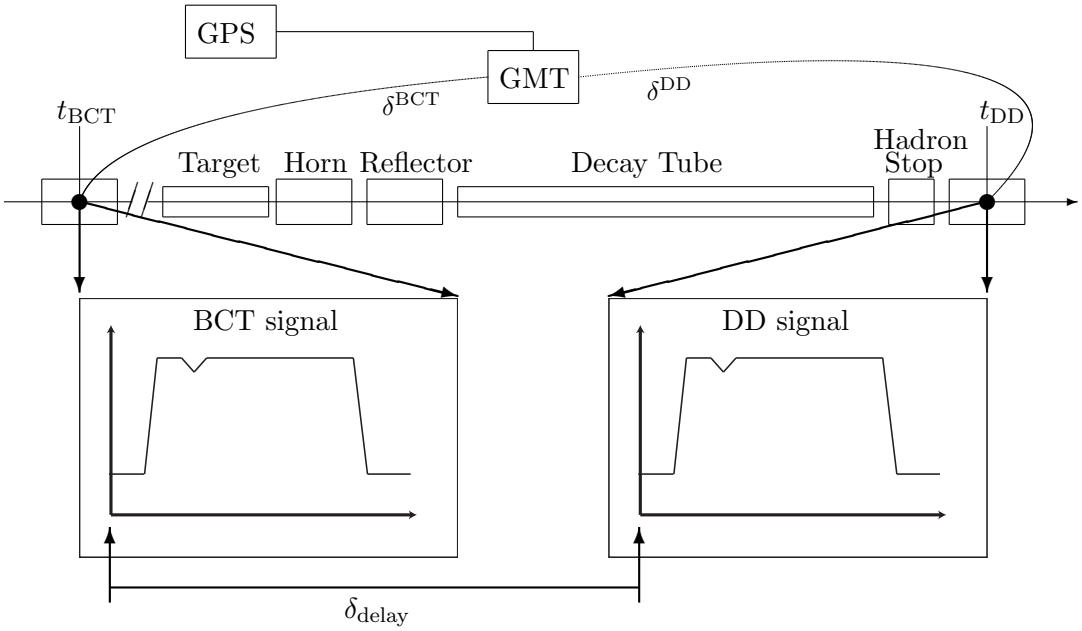

Figure 6.5.: An overview of the timing offsets at the CNGS facility is shown. The distance between the BCTF40 and the DDs is about 1860 m.

receiver located in the CERN control room (CCR) and the same time measured at the oscilloscopes reading the detector signals. Hence, this is done for the BCTF40 and for the DDs individually, with a common "clock" provided by the GMT. Additionally, the cable length for the signal transmission from the detectors to the oscilloscopes is taken into account. The different delays for the primary and the secondary beam are explained subsequently.

Primary Beam

There are four individual values which sum to create the delay δ^{BCT} for the primary beam time stamp: (1) the time taken to traverse the hardware between the BCTF40 and the oscilloscope in room HCA442, (2) between the oscilloscope and the a so-called Control Timing Receiver (CTR1) in HCA442, (3) between the CTR1 in HCA442 and the reference CTR in the CCR, and (4) a value of 99 216.0 ns subtracted, via software, from the database time stamp as a correction between the CTR time and the GPS time. These values sum to

$$\delta^{\mathrm{BCT}} = (-581.0\pm0.9 + 26.6\pm1.0 + 10\,077.8\pm2.0 - 99216.0)\,\mathrm{ns} = (-89\,692.6\pm2.4)\,\mathrm{ns}. \quad (6.3)$$

All stated corrections include propagation delays and signal encoding/decoding latencies. The stated value of 99 216.0 ns is a software delay and has no uncertainty. Figure 6.6 shows the delay chain. In order to measure the delay between the reference CTR and the CTR1, the CS4000 was transported between them, connecting it to the External Clock Input at one end and the External Start Input at the other. The accuracy of the CS4000 in the time between the two measurements is estimated to be better than 2.0 ns. [110] This delay was also calibrated by means of the two-way calibration technique with a reversible fibre path. [9, 109, 110] There is evidence for variations in the cabling delays according to the ambient temperature which can change from day to day. [109] These variations are monitored for the delay between the CTRs by a fibre running in parallel to the cable by

comparison with the original calculated value of 10 077.8 ns. The estimated yearly variation is less than 2 ns and is negligible within the time period of data taking of the data discussed in this work. However, the systematic uncertainty is taken conservatively to be 2 ns.

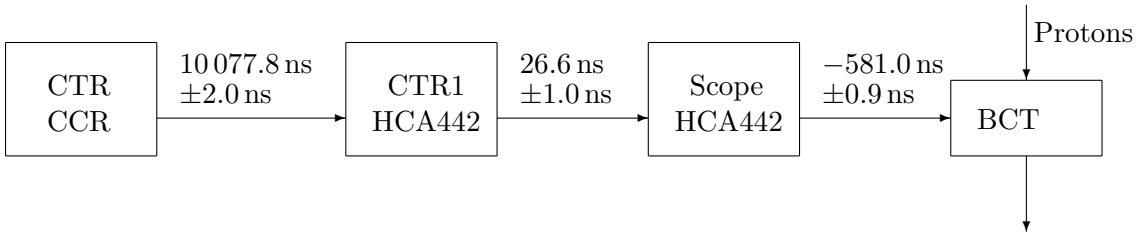

Figure 6.6.: The time delays for the primary beam time stamp are shown.

Secondary Beam

A similar process applies to the timing of the secondary beam (Fig. 6.7). It is characterised by four separate delays: (1) the time taken to traverse the hardware between the DDs and the oscilloscope in cavern TZ80, (2) between the oscilloscope trigger and the Control Timing Receiver (CTR2) in cavern TZ80 providing the trigger time stamps (3) the position of the trigger signal within the read-out window, (4) and finally between the CTR2 timebase and the timebase of reference CTR installed in the CCR. The rising edge of the trigger signal triggering the oscilloscope in TZ80, which is time-related to the onset of the SPS kicker magnet, can be placed *somewhere* around or within the read-out window of the oscilloscope. As the time difference between the *start* of the read-out window of the BCTF40 and that of the DDs is derived in this section, the relative position of the rising edge of the trigger to the start of the read-out window has to be accounted for. Note, that a different position of the trigger edge would have let to an equivalently differing choice of the software delay explained in Sec. 6.5.3. The trigger is placed at 2500 ns after the start of the read-out window, hence the window starts 2500 ns earlier. It should be noted that point (4) above was measured only with the help of the two-way technique, due to the impossibility of transporting the CS4000 to the TZ80 cavern. The sum of the delays yield the value

$$\delta^{\mathrm{DD}} = (-328.2\pm0.5 + 31.1\pm1.0 - 2500.0 + 29\,082.9\pm2.0)\,\mathrm{ns} = (26\,285.8\pm2.3)\,\mathrm{ns}. \quad (6.4)$$

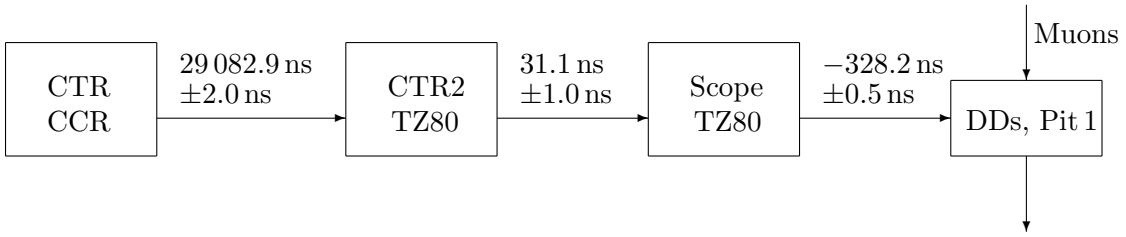

Figure 6.7.: The time delays for the secondary beam time stamp are shown.

6.5.3. Calculation of $\delta_{\mathbf{delay}}$

The time stamps $t^{\mathrm{BCT}}_{\mathrm{GPS}}$ and $t^{\mathrm{DD}}_{\mathrm{GPS}}$ as logged on the TIMBER database [111] for the primary and the secondary beams, respectively, are adjusted by the above offsets to yield:

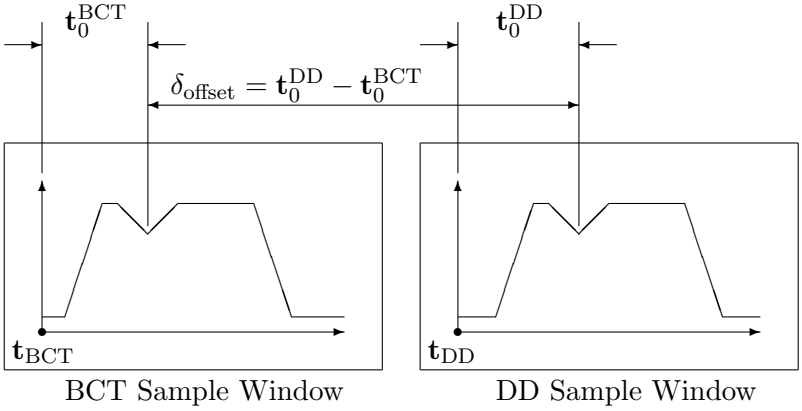

Figure 6.8.: Illustration of the timeline offset between the two read-out windows.

$$t_{\mathrm{BCT}} = t_{\mathrm{GPS}}^{\mathrm{BCT}} + \delta^{\mathrm{BCT}} \tag{6.5}$$

and

$$t_{\mathrm{DD}} = t_{\mathrm{GPS}}^{\mathrm{DD}} + \delta^{\mathrm{DD}} - 30\,000.0\,\mathrm{ns} \tag{6.6}$$

for the start times of the measurement windows. The $-30\,000.0$ ns is a software delay with no uncertainty and stems from fact that the TIMBER database provides only a certain time window (12 µs) out of the total read-out time span. The GPS time stamps logged in the TIMBER database hold a difference of

$$t_{\mathrm{GPS}}^{\mathrm{BCT}} - t_{\mathrm{GPS}}^{\mathrm{DD}} = (79\,911.3 \pm 0.5)\,\mathrm{ns}. \tag{6.7}$$

The time difference between the start of the read-out window of the BCTF40 and the start of the read-out window of the DDs is hence:

$$\begin{aligned}
\delta_{\mathrm{delay}} &= t_{\mathrm{DD}} - t_{\mathrm{BCT}} \\
&= t_{\mathrm{GPS}}^{\mathrm{DD}} + \delta^{\mathrm{DD}} - 30\,000.0\,\mathrm{ns} - \left(t_{\mathrm{GPS}}^{\mathrm{BCT}} + \delta^{\mathrm{BCT}}\right) \\
&= (-79\,911.3 \pm 0.5 + 26\,285.8 \pm 2.3 + 89\,692.6 \pm 2.4 - 30000)\,\mathrm{ns} \\
&= (6067.1 \pm 3.4)\,\mathrm{ns}.
\end{aligned} \tag{6.8}$$

6.6. Data Analysis

The timeline offset δ_{offset} of the data within the read-out windows is derived in this section. This is needed, since the windows from BCTF40 and the DDs might not be equally fitted around the signals as depicted in Fig. 6.8. Using δ_{offset} and δ_{delay} from Sec. 6.5, it is possible to measure the ToF from the BCTF40 to the DDs. This serves as a cross-check of the timing of the BCTF40 detector, which was used for the ToF_ν measurements [9].

The recorded data from the DDs and from the BCTF40 is analysed offline with a custom-made analysis making use of the ROOT analysis framework [112]. As described in Sec. 6.2 the SPS delivers two extractions per cycle. The second extraction has a different shape compared to the first extraction as a result from the SPS filling scheme. Hence, averaging both extractions to form *a single* pulse is counterproductive, as pulse characteristics like

troughs and peaks used later in the analysis would be less pronounced. The analysis presented here focuses on the data obtained from the first extraction to extract a value for δ_{offset}. After the analysis of the first extraction, the possible improvement of the final results including a full analysis of the second extraction is given.

The sample rate of the presented data is 1 GS/s. Hence, only every fifth data point from the original data taking at 5 GS/s is used. This reduces the amount of data to be processed by 80 % while keeping the time resolution high enough for the purpose of this analysis. In total 151 spills recorded on 15.11.2011 between 10 a.m. and 11 a.m. (UTC) are taken into account for the presented analysis, of which 119 resulted from non-empty extractions.

First, the detector response from single extractions is shown, then the data treatment is explained, followed by the discussion of the treated data from the three DDs and the BCTF40 individually. The DD and the BCTF40 data is then used to calculate δ_{offset}.

6.6.1. Detector Response

The bare detector response as measured with the oscilloscope within a time window of 12 µs from a *single extraction* for the three DDs and the BCTF40 is shown in Fig. 6.9. As these plots hold 12000 data points each, the signals appear as a broad band at the given plot resolution. A simple 5 ns average is added in red to guide the eye. The four detector responses in Fig. 6.9 originate from the *same* extraction. With a sufficiently fast muon detector system, it is reasonable to compare the topology of the signal from the BCTF40 with those from the DDs. A comparison by eye reveals, that certain features of the signal present in all four signals, e.g. the dip flanked by two peaks from 6600 ns to 8500 ns, as indicated by the arrows. This is the first time that the proton beam structure could be compared to the muon beam structure due to the fact that before the installation of the DDs drift chambers had been used as muon detectors, which have orders of magnitudes larger rise times. Also the shape of the Left detector is similar to those from the Centre detectors, but with reduced intensity and adapted oscilloscope gain. The fact that both technologies, the beam current transformer and the solid state diamond-based ionisation chamber, show similar signals allow the conclusion that the diamond detector system works as expected with an analogue bandwidth of at least as high as the one from the BCTF40 (∼200 MHz). The similarity in shape of the signals then renders a timing analysis possible that utilises the topology of the signals. Note that the BCTF40 is a beam current transformer and detects the SPS proton beam current, whereas the DDs detect muons originating from pions and kaons produced by SPS protons in the target. However, the DD signals are very similar to the BCTF40 signal.

A zoom from 2800 ns to 2900 ns for CT is shown in Fig. 6.10 **(A)**. The 5 ns (200 MHz) SPS beam structure is evident. It is worth mentioning that the signal does not return to its baseline at the end of a bunch; each bunch has a tail of the order of a few nanoseconds. This leads to a certain pile-up of signals from neighbouring bunches. Therefore, the timing analysis needs to be carried out in such a way that it is not dependent on pile-up.

6.6.2. Signal to Noise Ratio

The baseline and the baseline noise of the i-th extraction, b_i and σ_i^{noise}, measured in ADC counts, are calculated for every non-empty extraction. The mean $\overline{\sigma}^{\text{noise}}$ characterises the mean baseline noise, $\overline{b}$ the mean baseline. Then for each DD as well as for the BCTF40 the average signal amplitude $\langle y \rangle_i$ is calculated in the range from 5000 ns to 6000 ns , where the signal reaches a "flat top". Again, the mean $\overline{\langle y \rangle}$ represents the mean signal amplitude

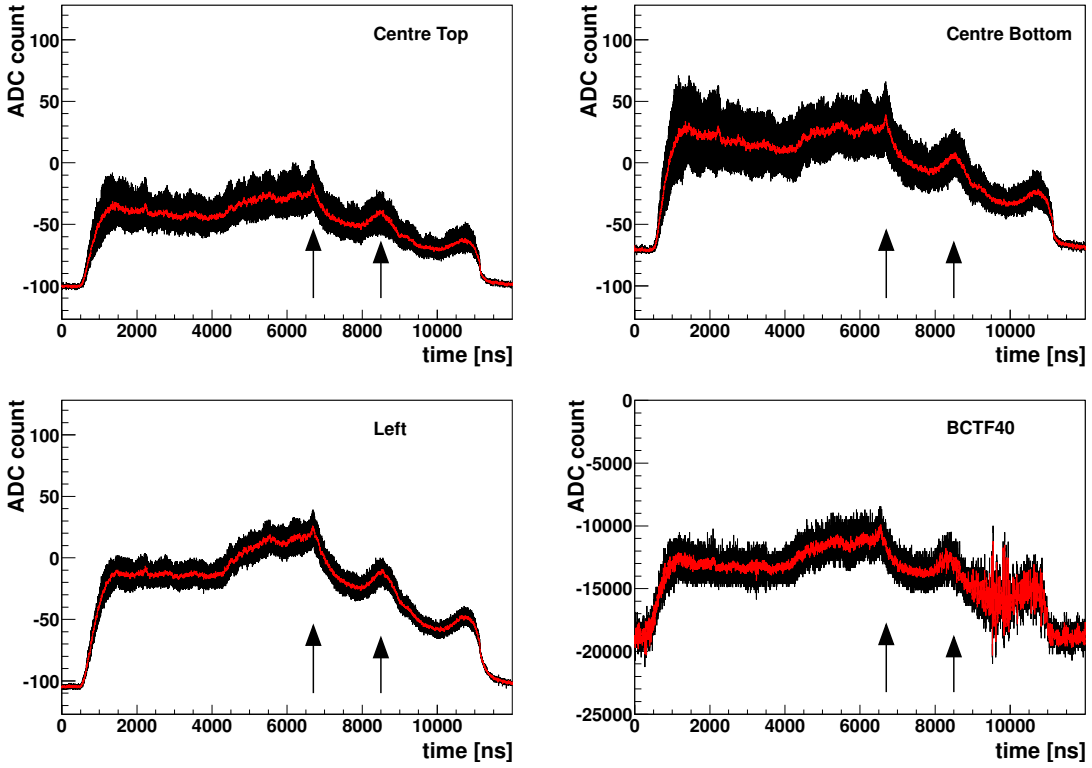

Figure 6.9.: Detector response of a single extraction. In red, a 5 ns arithmetic average is displayed to guide the eye. The arrows show the same two position in time for all detectors; a very similar structure is observed in all four.

in this region. The two values are used to quantify a signal-to-noise ratio (SNR) for every detector; all numbers are shown in Tab. 6.3.

The SNR values in Tab. 6.3 illustrate the difference in signal quality between the DDs and the BCTF40. The DDs deliver an SNR of above 64, in comparison to an SNR of 11 for the BCTF40. The signal quality of the BCTF40 also suffers from oscillations or pick-up noise in the regions from 0 ns to 2000 ns, and from 8000 ns to 12 000 ns. A frequency analysis of these parts revealed a major contribution at 25 MHz. This pick-up is common to all recorded extractions for the BCTF40. These parts of the signal are therefore disregarded in the timing analysis. CB and L have better SNRs than the CT for two reasons: (1) the electrode areas of CB and L are larger than that of CT leading to a larger signal and

Table 6.3.: Characteristic noise and signal values for the DDs and the BCTF40.

	BCT	CT	CB	L
$\overline{\sigma}^{\text{noise}}$/ADC counts	650	1.09	1.17	1.43
$\overline{\langle y \rangle}$/ADC counts	-11570	- 30.35	23.72	8.16
$\overline{b}$/ADC counts	-18791	-100.45	-71.0	-104.90
SNR	11.1	64.3	81.0	79.1

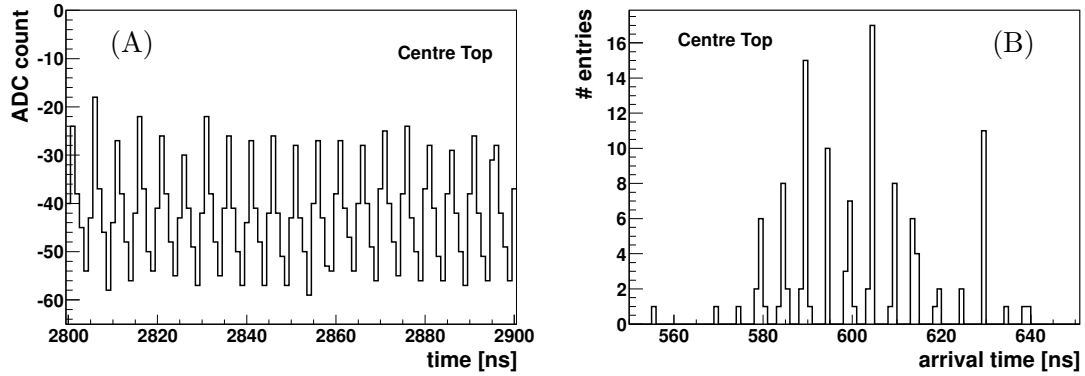

Figure 6.10.: **(A)** A zoom in the detector response for CT for a single spill is shown. **(B)** The corrected arrival time (see text) is shown as a histogram for the 119 non-empty spills.

(2) the fact that the noise is not dominated by the detectors capacity but rather by the least-significant-bit noise of the oscilloscope.

6.6.3. Time Resolution and Phase Shift

The single-pulse time resolution of DDs in combination with fast electronics has often been proven to be better than 1 ns for MIPs, cf. e.g. Ref. [113]. This holds true as well for the DDs used in this analysis and has been tested in the laboratory before installation. For a higher signal charge than the charge produced by a MIP, a better time resolution is expected. From Fig. 6.10 **(A)**, partial rise times for every bunch of $t_{\text{rise}} \leq 2\,\text{ns}$ over 30 ADC can be concluded, and hence a slope s of $s > 15\,\text{ADC/ns}$. Therefore, the time resolution $\sigma_{\text{t}} = \frac{\overline{\sigma}^{\text{noise}}}{s} < 0.1\,\text{ns}$.

The difficulty in this analysis is the complexity of the signal; the uncertainty of the point in time of the arrival of the first bunch at the DDs is not dominated by the time resolution of the DDs themselves, but by the long rise time (1 µs) of the kicker magnet resulting in a steadily increasing muon intensity per bunch arriving at the DDs during the rising edge. However, the jitter of the trigger signal is small, hence it is sufficient to find the *modulo 5 ns* shift for each extraction. This shift can then be applied to each extraction. Thereby, the phases of the extractions are aligned such that an equivalent point in time is found. The *modulo 5 ns* shift is found by analysing the signal within the global rising edge – as opposed to a local one for a single bunch – from 800 ns to 1000 ns. The SPS beam structure can easily be found by comparing five different sums $\sum^{(n)}$, where each sum represents a sum over signal amplitude values $y_{\text{DD}}(t)$ separated by 5 ns with an offset of $n = 0, 1, 2, 3, 4$ ns: $\sum^{(n)} = \sum_i y_{\text{DD}}(5i + n)$. The largest sum finds the phase φ_{i} of the maximum within the 5 ns SPS beam structure. The resulting histogram of the φ_{i}-corrected arrival time is shown in Fig. 6.10 **(B)**. The evident 5 ns structure of the time of arrival shows the suitability of this approach. The spread in the corrected arrival time is, again, caused by the long rising edge.

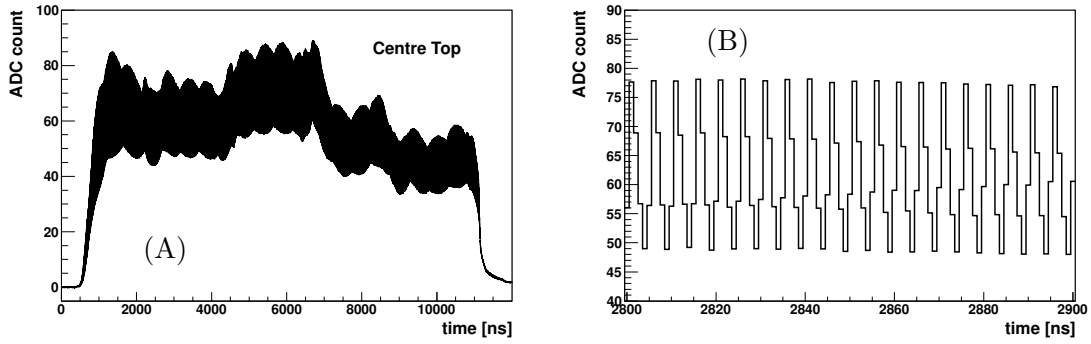

Figure 6.11.: An Overview **(A)** and a zoom **(B)** of the averaged signal for CT is shown.

6.6.4. Data Treatment

Averaging

In order to make a statement about the CNGS timing at CERN, the 119 non-empty signals are combined to form an average signal. This averaging makes the analysis robust against fluctuations in the single extractions. In order to average the signals correctly, the phase φ_i is used. The timeline of every single extraction is shifted by $-\varphi_i$ in order to ensure an aligned phase. For simplicity the baseline was shifted to zero. The average pulse values $y_{\text{avg}}(t) = \sum_i y_i(t)/119 - b$, with the baseline b from Tab. 6.3. The average signal for CT is shown in Fig. 6.11.

The difference in average shift $\Delta\overline{\varphi} = \overline{\varphi}_{\text{DD}} - \overline{\varphi}_{\text{BCT}}$ is determined for each DD with respect to the BCTF40. These average shift differences are much smaller than the errors resulting from other uncertainties, and can hence be omitted.

Note that the signal amplitude of the average pulse varies about 30 ADC on top of the DC part, about as much as for the single pulse, compare Fig. 6.10 **(A)** and Fig. 6.11 **(B)**. This is to be expected if the phase-finding algorithm is working, and hence the phases are not smeared out, and if the extractions are sufficiently alike.

Filtering and Normalisation

The averaged signal is now filtered in order to remove its 5 ns SPS beam structure facilitating the subsequent timing analyses. The applied filter method is a raised-cosine filter of width w, which belongs to the class of Finite Impulse Response filters. The applied equation for filtering is:

$$y_{\text{avg,filterd}}(t; w) = \sum_{j=-w/2}^{w/2} y_{\text{avg}}(t+j) \cdot \left(1 + \cos\left(2\pi \frac{j}{w}\right)\right), \tag{6.9}$$

and the averaged, filtered signals with $w = 15$ ns for CT, CB, L, and BCTF40 are shown in Fig. 6.12. Additionally to the filtering, each DD signal is normalised to its average amplitude between 6650 ns and 6750 ns, the section of highest signal amplitude featuring a sharp peak. The same is done for the BCTF40, but with the average amplitude taken between 6510 ns and 6610 ns. The windows for the calculation of the average amplitude do not overlap for the DDs and the BCTF40. A difference of 140 ns was chosen due to obvious indications of an offset between the starting point of the read-out windows, that is e.g. the

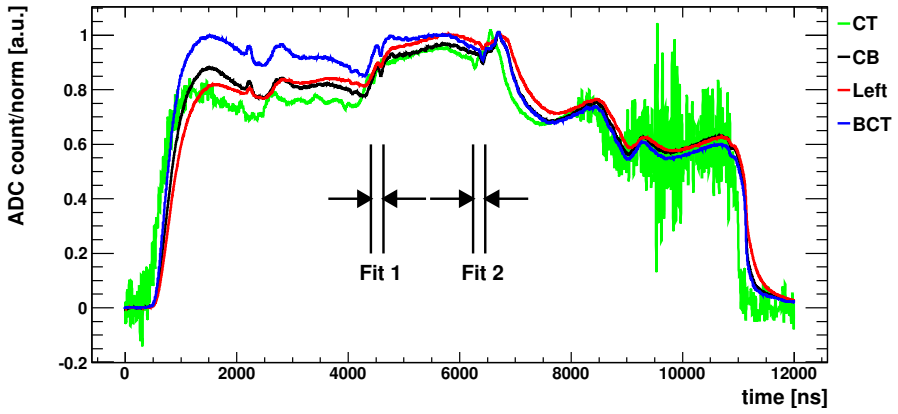

Figure 6.12.: The averaged, filtered, and normalised detector responses are displayed for the three DDs and the BCTF40.

sharp peak appearing 140 ns earlier in the BCTF40 data than in the DDs data as well as the position of the rising/falling edge at the start/end of the extractions.

6.6.5. Calculation of δ_{offset}

Figure 6.8 explains the timeline offset δ_{offset} between the signals within their read-out windows. The averaged and filtered pulses are used to determine δ_{offset} in two different ways. The "fitting method" uses the topology of the signal at two different positions applying a fit to the detector responses over a sample section of 80 ns width. The chosen sections feature a trough and are indicated in Fig. 6.12 with "Fit 1" and "Fit 2". This method is referred to as *local*. A method that uses a much wider section, is the cross-correlation method. This calculates the cross-correlations between two signals over a number of microseconds. Therefore, this method is referred to as *global*.

The Local Method

The fitting method exploits a rather simple approach of fitting a second order polynomial to an apparent trough in the detector responses,

$$y_{\text{fit}}(t) = a(t - t_0)^2 + c, \tag{6.10}$$

within a section of 80 ns width. The t_0 defines the lowest point of the trough and is readily determined for all four detector signals. The method is applied in two regions: from 4550 ns to 4630 ns (Fit 1), shown in Fig. 6.13, and from 6380 ns to 6460 ns (Fit 2) for the DDs, but 140 ns earlier for both fits for the BCTF40. By eye it is visible as well that a steep trough is apparent in all four detector signals alike, but about 140 ns earlier in time for the BCTF40. Each fit then yields a t_0. The values are collected in Tab. 6.4 **(top)**. The difference between the t_0 for the DDs and the BCTF40 form δ_{offset}, $\delta_{\text{offset}} = t_0^{\text{DD}} - t_0^{\text{BCT}}$, see Tab. 6.4 **(bottom)**. Note that pile-up adds to c, but does not affect t_0. Hence, this approach is robust against pile-up. As the result of this method, the weighted mean and error of the six δ_{offset} values are quoted:

$$\delta_{\text{offset}}^{\text{fit}} = (140.0 \pm 2.5)\,\text{ns}. \tag{6.11}$$

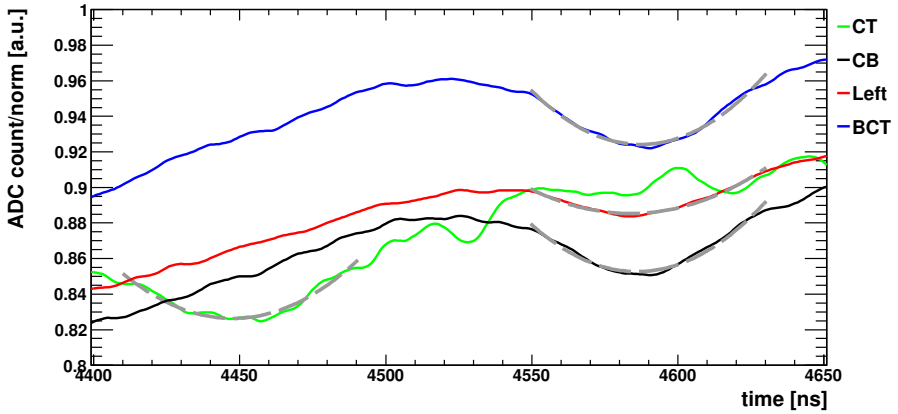

Figure 6.13.: The averaged, filtered detector response (solid lines) around a trough and the corresponding parabolic fits (dashed) are shown for one fit region.

Table 6.4.: The fit results for t_0 and the resulting δ_{offset} are listed. The top table gives the absolute position of the trough minimum. The lower table states δ_{offset}.

		BCT	CT	CB	L
trough 1	t_0/ns	4446.9 ± 0.5	4586.1 ± 0.5	4586.4 ± 0.5	4582.6 ± 1.1
trough 2	t_0/ns	6272.8 ± 0.8	6413.1 ± 0.8	6415.6 ± 0.8	6420.5 ± 1.4
			CT-BCT	CB-BCT	L-BCT
trough 1	δ_{offset}/ns		139.2 ± 0.7	139.5 ± 0.7	135.7 ± 1.2
trough 2	δ_{offset}/ns		140.3 ± 1.1	142.8 ± 1.1	147.7 ± 1.6

The Global Method

This method employs a one-parameter likelihood function (LF) between two signals to form a likelihood estimator $\hat{\Theta}$, e.g. between CT and BCTF40:

$$\hat{\Theta}(\tau; \text{CT}, \text{BCT}) = \text{LF}(f_{\text{CT}}(t), f_{\text{BCT}}(t+\tau)), \tag{6.12}$$

in order to find a possible offset between them. If a signal coming from either a DD or from the BCTF40 is correlated with itself, it is called an auto-estimator ($\hat{\Theta}_a$). A cross-estimator ($\hat{\Theta}_x$) is the result of a correlation of two signals stemming from different detectors. In order to find the δ_{offset}, the correlation is calculated as a function of a parameter τ which describes a time shift between the time arguments of the correlated functions, hence $\hat{\Theta}_x(\tau; f_1, f_2) = \text{LF}(f_1(t), f_2(t+\tau))$, and $\hat{\Theta}_a(\tau; f_1) = \text{LF}(f_1(t), f_1(t+\tau))$. The auto-estimator is used to check that the used method yields reasonable results in terms of topology and amplitude. The expected result for the $\hat{\Theta}_a$s is a minimum at $\tau = 0$. Furthermore, the depth of the minimum for the $\hat{\Theta}_a$ can be compared to that of the $\hat{\Theta}_x$; the latter is expected to be shallower than the former. The absolute value at the minimum of $\hat{\Theta}_a(\tau)$ should be zero for all auto-estimators.

The chosen likelihood function uses the **absolute difference in first derivative** at a given point in time for the two signals under test, hence $|f_1'(t) - f_2'(t+\tau)|$. This difference is calculated for every point in time t in a specified range, i.e. from t_{start} to t_{end}. The

absolute values are being summed; the sum forming the cross-estimator value $\hat{\Theta}_x(\tau)$ in case different functions are correlated, or the auto-estimator value $\hat{\Theta}_a(\tau)$ in case a function was correlated with itself. This procedure is then repeated for every τ ranging from -500 ns to +500 ns in steps of 1 ns. The **position of the minimum** of $\hat{\Theta}_x(\tau;\text{DD,BCT})$ is the offset between the recording windows. One minimum is found for every DD-BCTF40-pair. The full formula is:

$$\hat{\Theta}_x(\tau; f_1, f_2) = \sum_{t=t_{\text{start}}}^{t_{\text{end}}} \left| f_1'(t) - f_2'(t+\tau) \right|, \tau = -500\,\text{ns}, ..., 500\,\text{ns} \tag{6.13}$$

and equivalently for $\hat{\Theta}_a(\tau)$. The local derivative for a progression – the recorded signal is a progression with finite time steps rather than a continuous function – is the difference of two neighbouring points: $f' = \frac{f(t)-f(t+1\,\text{ns})}{\Delta t}$. Here $\Delta t = 1\,\text{ns}$. It is stressed that the "standard" cross-correlation function $(f * g)(\tau) = \sum f_1(t) f_2(t+\tau)$ has not been chosen as the LF. The cross-correlation is not independent of the absolute values of the tested correlated signals, hence global maxima might appear due to changes in amplitude values, and not due to a better match. Therefore, in the presented analysis the difference rather than the product of two functions is chosen for the LF in order to avoid this dependence. Then, the first derivative is chosen as the function ought to be correlated. This has the advantage that the minimum of the likelihood estimator is more pronounced, as can easily be shown. Additionally, differentiation attenuates the low frequency spectrum where most of the spectral differences between detectors are located, e.g. possible skin effect on the cables, different detector capacitances, pile-up and possible offset on the signals. Both auto- and cross-estimators have been calculated in the range from $t_{\text{start}} = 4000\,\text{ns}$ to $t_{\text{end}} = 8000\,\text{ns}$.

The calculated auto-estimators are shown in Fig. 6.14 **(top left)** for a filter width of $w = 15\,\text{ns}$. The minima of the $\hat{\Theta}_a$s are more pronounced then the minima of the $\hat{\Theta}_x$s, as expected, and their position are at 0 ns as expected from an auto-correlation. Also, their position are at $\tau = 0$ independent of w (not shown). Furthermore, the absolute value at $\tau = 0$ is exactly zero, but the functions in Fig. 6.14 **(top left)** are drawn with an offset for better visibility.

The cross-estimators of the BCTF40 signal with each DD signal separately are shown in Fig. 6.14 **(top right, bottom)** as a function of τ for three different filter widths. In order to avoid an overlay of the different cross-correlation graphs, arbitrary offsets have been added to the $\hat{\Theta}_x$s. The position of the minima for $\hat{\Theta}_x$(CT,BCT), $\hat{\Theta}_x$(CB,BCT), and $\hat{\Theta}_x$(L,BCT), i.e. the calculated δ_{offset}s, are listed in Tab. 6.5. Their mean and error are (138.1±1.2) ns. It is evident from the lower right picture of Fig. 6.14, that a raised cosine filter of 5 ns width is not sufficient to filter out the SPS bunch structure from the detector response. This results in a large variation in the cross-estimator $\hat{\Theta}_x$ value over 5 ns due to the matching (or non-matching) bunch structure depending on $\tau \mod 5$. The amplitude of the variation due to the overall extraction structure is roughly a factor 4 smaller. Additionally, the $\hat{\Theta}_x$s between different DDs have been checked. The positions of the minima are also located at $\tau = 0$, which further proves the reliability of this method. As the result of the likelihood estimator method, the mean and standard deviation of the nine δ_{offset} values are quoted:

$$\delta_{\text{offset}}^{\hat{\Theta}_x} = (138.1 \pm 1.2)\,\text{ns}. \tag{6.14}$$

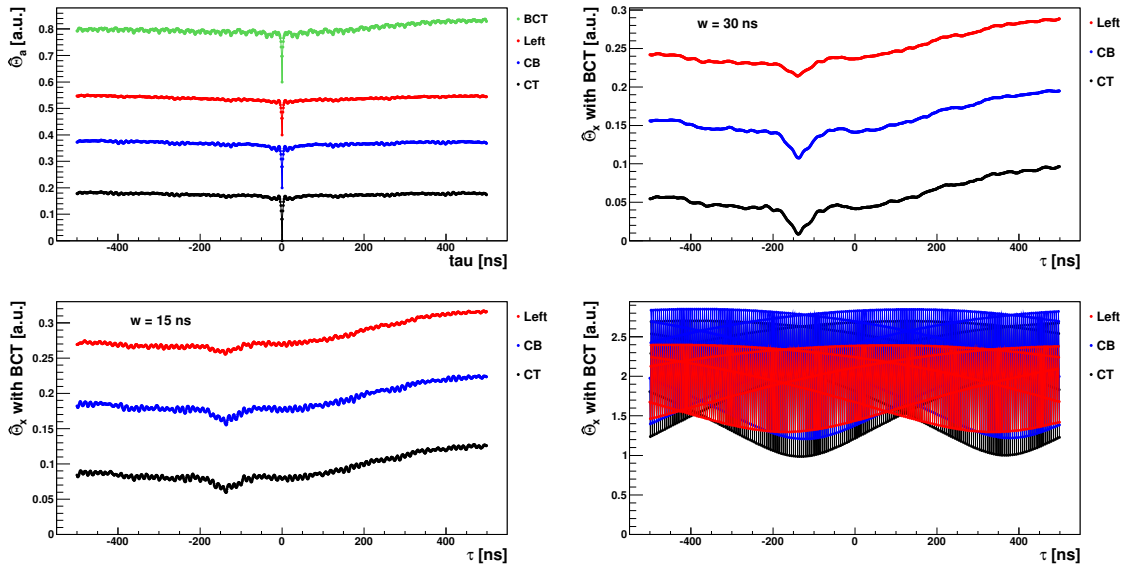

Figure 6.14.: The likelihood auto-estimators $\hat{\Theta}_a(\tau)$ are shown for $w = 15$ for the four detectors separately, with all their minima at 0 ns **(top left)**. The likelihood cross-estimators $\hat{\Theta}_x(\tau;\mathrm{DD,BCT})$ between each DD and the BCTF40 for $w = 30$ ns and $w = 15$ ns **(top right, bottom left)** have their minima around -138 ns. The likelihood cross-estimators $\hat{\Theta}_x(\tau;\mathrm{DD,BCT})$ for $w = 5$ ns **(bottom right)** shows no pronounced minimum.

6.7. Results

In order to verify the CNGS timing at CERN, the ToF for charged particles from the beam current transformer BCTF40 to the diamond detectors downstream of the CNGS target was measured and compared to its nominal value. The measured ToF uses the total delay between the start of the read-out windows δ_{delay} and the offset δ_{offset} of the timelines within the recording windows, hence $\mathrm{ToF} = \delta_{\mathrm{delay}} + \delta_{\mathrm{offset}}$. As presented in Sec. 6.5, the time difference between the start of the recording window of the BCTF40 and the recording window of the DDs is

$$\delta_{\mathrm{delay}} = (6067.1 \pm 3.4)\,\mathrm{ns}.$$

In Sec. 6.6, δ_{offset} was calculated based on two different methods to be

$$\delta^{\mathrm{fit}}_{\mathrm{offset}} = (140.0 \pm 2.5)\,\mathrm{ns} \quad \text{and} \quad \delta^{\hat{\Theta}_x}_{\mathrm{offset}} = (138.1 \pm 1.2)\,\mathrm{ns}$$

using the fitting method and the likelihood cross-estimator method, respectively. Although derived on very different parts of the signal, each method's result is consistent with the other within their precision. No additional source of a significant systematic uncertainty is known. Neither do the results suggest one. The measured ToF is hence

$$\mathrm{ToF}_{\mathrm{fit}} = (6207.1 \pm 4.2)\,\mathrm{ns} \quad \text{and} \quad \mathrm{ToF}_{\hat{\Theta}_x} = (6205.2 \pm 3.6)\,\mathrm{ns}$$

for the fitting method and for the likelihood cross-estimator method, respectively.

A cross-check of the data stemming from the second extraction was done, and no significant difference to the δ_{offset} of the first extraction is found. A full analysis of the second

Table 6.5.: The position of the minimum of the likelihood cross-estimator $\hat{\Theta}_x$(DD,BCT) between the BCTF40 and the individual DDs.

	$\min\left(\hat{\Theta}_x(\text{DD,BCT})\right)$		
	DD = CT	DD = CB	DD = L
δ_{offset}/ns for $w = 15$ ns	137	136	139
δ_{offset}/ns for $w = 20$ ns	138	137	138
δ_{offset}/ns for $w = 30$ ns	139	139	140

extraction would improve the uncertainties of $\delta^{\hat{\Theta}_x}_{\text{offset}}$ and $\delta^{\text{fit}}_{\text{offset}}$, i.e. $\sigma_{\delta^{\hat{\Theta}_x}_{\text{offset}}}$ and $\sigma_{\delta^{\text{fit}}_{\text{offset}}}$ respectively, roughly by a factor of $\sqrt{2}$. Since the uncertainty of δ_{delay} is larger than $\sigma_{\delta^{\hat{\Theta}_x}_{\text{offset}}}$ and $\sigma_{\delta^{\text{fit}}_{\text{offset}}}$ and since the ToF is the sum of δ_{delay} and δ_{offset}, the impact on σ_{ToF} caused by a possible improvement of $\sigma_{\delta^{\hat{\Theta}_x}_{\text{offset}}}$ and $\sigma_{\delta^{\text{fit}}_{\text{offset}}}$ is small: 0.4 ns and 0.1 ns for $\sigma_{\text{ToF}_{\text{fit}}}$ and $\sigma_{\text{ToF}_{\hat{\Theta}_x}}$, respectively.

The value for the nominal ToF combines the travelled distance of (1859.95±0.02) m, as measured by the CERN GEO survey, and the combined velocity v of the original proton and its production/decay products. The SPS protons have a momentum of 400 GeV/c, the pions and kaons an average momentum of 35 GeV/c, and hence the muons have an average momentum of 17 GeV/c. Under the assumption of not-completely relativistic muons, a ToF of

$$\text{ToF}_{\text{nom}} = \frac{1859.95\,\text{m}}{v} = (6205.3\pm1.7)\,\text{ns},$$

is found, where the uncertainty is dominated by the decay position of the pions/kaons within the decay tube. The 1.7 ns reflect the spread in the decay position of 68 % of the pions/kaons decaying in the decay tube, centred midway within the tube, and the resulting difference in arrival time. ToF_{nom} lies well within the errors of ToF_{fit} and $\text{ToF}_{\hat{\Theta}_x}$. Under the assumption of completely relativistic muons, $\text{ToF}_{\text{nom}} = \frac{1859.95\,\text{m}}{c} = (6204.1\pm1.7)\,\text{ns}$.

6.8. Conclusion

As a result of the neutrino time-of-flight publication of OPERA in 2011, polycrystalline CVD diamond detectors were installed in the secondary beam line downstream from the CNGS target in order to measure the time structure of the muon spill. This allows for an independent verification of the CNGS timing at CERN, which was previously only based on the measurements of the protons passing through a fast beam current transformer (BCTF40) before they hit the CNGS target. The distance between the two detector positions was carefully measured as well as all the time delays from the detection of the particles until the signal was registered. Detailed analysis of the signal shape was performed. The nominal time-of-flight of the protons and their secondary particles produced in the CNGS target travelling at almost the speed of light between the BCTF40 and the diamond detectors was compared with the measured time-of-flight of the charged particles passing through these detectors. The nominal time-of-flight lies well within the uncertainty of the measured time-of-flight. The results show that the time measurements performed at the CERN part of CNGS using the BCTF40 and the diamond detectors are consistent.

7. TIME RESOLUTION MEASUREMENTS WITH THE μ-BEAM AT CNGS

In February 2012 the diamond muon detectors in the secondary beam line of the CNGS facility were slightly modified in order to cope with the high beam intensities foreseen for the 2012 CNGS operation. Polycrystalline CVD diamond has often been tested at low fluences of minimum ionising particles, but there is a lack of data at high impact ionisation. The high intensity muon beam at CNGS is used to study the time resolution of diamond detectors at high impact ionisation. The integrated muon flux of roughly $4.7{\times}10^5\,\mathrm{cm}^{-2}$ per bunch produce a measured charge of 300 pC per bunch in the diamond sensor. A MIP creates 36 pair/µm in diamond. For a 500 µm thick sensor, the measured charge amounts to $18\,000\,\text{pairs} \cdot \mathrm{CCE}/2 \approx 7200\,e = 1.15\,\mathrm{fC}$, at a charge collection efficiency (CCE) of roughly 40 % at 1 V/µm. For a single minimum ionising particle (MIP), a time resolution of $\sigma_\mathrm{t}^\mathrm{MIP} = (687{\pm}42)\,\mathrm{ps}$ has been reported. [113] A better time resolution is expected with increasing signal charge.

7.1. The CNGS Beam in 2012

The CERN SPS accelerator delivers a fast-extracted 400 GeV/c proton beam for CNGS. One extraction per SPS super-cycle is directed towards the CNGS target lasting 7000 ns and containing on average $P = (12.5{\pm}1.4){\times}10^{12}$ p/ext (protons/extraction) for the extractions examined in this work. Each extraction consists of 64 bunches coming in 4 bunch trains containing 16 bunches each. The bunch spacing amounts to 100 ns, the train spacing is 300 ns. [114] The protons produce pions and kaons in the CNGS target, which are energy selected and steered towards Gran Sasso d'Italia. During their flight, the pions and kaons decay in a vacuum decay tube into muons and muon-neutrinos with an average muon energy of ∼17 GeV/c. The bunch profile is roughly triangular shaped with a full-width at half-maximum (FWHM) of 1.5 ns. The $12.5{\times}10^{12}$ p/ext produce a muon flux of $4.68{\times}10^5\,\mathrm{cm}^{-2}$ per bunch in the centre of the Pit 1 cavern, where the diamond detectors are placed. The muon yield per proton at the diamond detector is $\mu_p = 2.4{\times}10^{-6}\,\mathrm{cm}^{-2}$.

7.2. Experimental Set-up

The set-up used in Pit 1 is almost identical with the set-up used in 2011. All charging capacitors have been changed to be $C_1 = 11\,\mathrm{nF}$. Also the data taking and the data processing is identical with the 2011 procedure, see Chap. 6. The data used for this time resolution study was taken on April 21$^{\mathrm{st}}$, 2012 between 2 a.m. and 3 a.m.

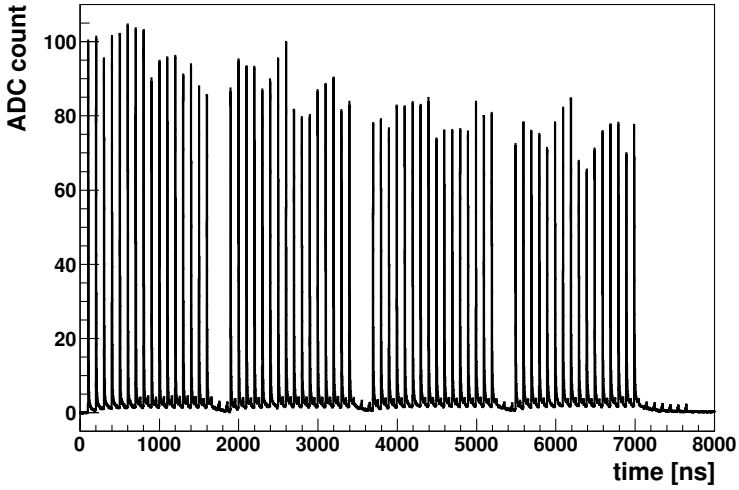

Figure 7.1.: The averaged detector response over all extraction is shown for the complete extraction.

7.3. Results and Discussion

7.3.1. The total measured charge

The average detector response over all non-empty extractions analysed in this work is shown in Fig. 7.1, and a zoom into the first bunch for a single extraction in Fig. 7.2. At first, the measured amount of charge is discussed, as it is not clear if a linear response is to be expected at this high particle flux. A first order estimate of the expected signal charge is compared to the measured signal charge. The charge created from a single MIP crossing the detector at right angle is $Q_{\mathrm{MIP}} = 18\,000\,\mathrm{pair}$, i.e. $36\,000\,e$, created over the whole thickness of the sensor. If these charges drift under the influence of an electric field, they induce a current of $i(t) = Q(t)\,v_{\mathrm{drift}}/d$. The total induced current under the assumption of infinite charge lifetime is $i(t) = Q_{\mathrm{MIP}}\,\frac{v_{\mathrm{drift}}}{d}\,\left(1 - \frac{v_{\mathrm{drift}}\,t}{d}\right)$. Hence the amount of induced charge is $Q_{\mathrm{MIP,ind}} = \int_0^{t_{\mathrm{t}}} i(t)\,dt = Q_{\mathrm{MIP}}/2$ using $d = v_{\mathrm{drift}}\,t_{\mathrm{t}}$ with the transit time t_{t}.

If a linear charge yield of the diamond detectors up to high muon fluences in combination with negligible charge trapping is assumed, the amount of expected charge for an entire extraction reads

$$Q_0 = P \cdot \mu_{\mathrm{p}} \cdot A_{\mathrm{det}} \cdot Q_{\mathrm{MIP,ind}} = 55.3\,\mathrm{nC}. \tag{7.1}$$

The *measured* amount of charge is based on the integral of the average measured signal. With the integral $I_m = 43\,470\,\mathrm{ADC/ns}$, an oscilloscope gain of $g = 15.6\,\mathrm{mV/ADC}$, and taking into account the $50\,\Omega$ read-out line and the fact that the signal was split into two signals to feed two oscilloscope channels ($-6\,\mathrm{dB}$), the measured charge is

$$Q_m = 2 \cdot I_m \cdot g/50\,\Omega = 27.1\,\mathrm{nC}, \tag{7.2}$$

which corresponds to a charge collection efficiency of $^{27.1}/_{55.3} = 49\,\%$.

As can be seen from Fig. 7.1, after a bunch crossed the sensor the signal current does not return to its baseline present prior to the first bunch. In fact, there seems to be an exponentially saturating behaviour during the bunch train, which lifts the baseline from

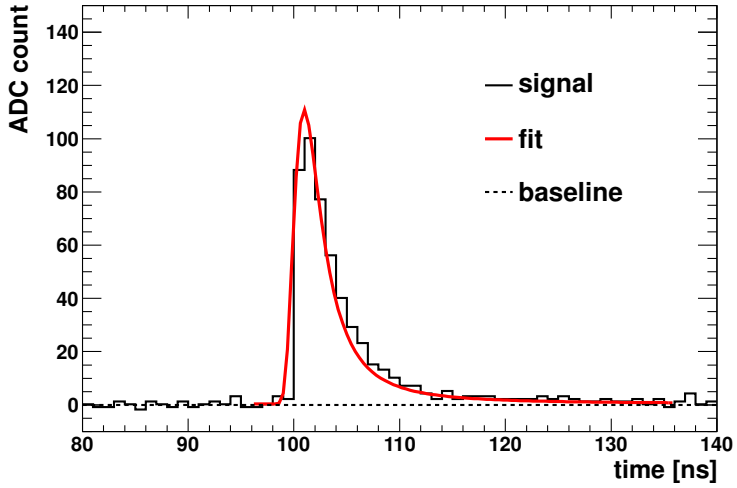

Figure 7.2.: A Landau fit to a single detector response of a first bunch is shown.

0 ADC to about 1.5 ADC. The area below this lifted baseline amounts to about 2400 ADCns per bunch train, and hence $I_{\text{base}} = 9600$ ADCns for the full extractions. If Q_m is corrected for this baseline offset,

$$Q_{\text{corr}} = Q_m - Q_{\text{base}} = 21.1\,\text{nC} \tag{7.3}$$

is found, corresponding to a charge collection efficiency of $\text{CCE}_{\text{corr}} = 38\,\%$. This is about the expected CCE for a single MIP in pCVD diamond. It may hence be concluded that the pCVD diamond has an about linear response in the fluence range from single MIP to 100 THz (300.000 particles within 3 ns). The peculiar behaviour of the baseline has been observed in other high flux experiments as well. [115] Further investigation is needed to pin down a physical explanation.

7.3.2. The time resolution

The detector response to a single traversing muon bunch as measured with the oscilloscope within a time window of 50 ns is shown in Fig. 7.2. A rise time (10%-90%) of about 1 ns is evident. For this time resolution study, the detector response to each *first bunch* from a total of 146 extractions is analysed. First, the baseline of each pulse is shifted to zero. Then, a Landau function is fitted to the detector response of the first bunch in each extraction, see Fig. 7.2 for one exemplary fit. Additionally, the baseline noise σ_{noise} of the acquisition is calculated in a time region prior to every first bunch.

The single pulse time resolution σ_{t} of a measurement system is defined as [116]

$$\sigma_{\text{t}} = \frac{\sigma_{\text{noise}}}{\max(\text{slope})}, \tag{7.4}$$

where max(slope) is the maximum slope within the rise time of the signal. In order to determine the single pulse time resolution, the maximum slope of the Landau-Fit within the rise time is calculated. Figure 7.3 **(A)** shows the noise distribution in ADC units and Fig. 7.3 **(B)** the distribution of the maximum slope in units of ADC/ns. The means and RMSs are $\overline{\sigma} = (1.23\pm0.05)$ ADC and $\overline{\max(\text{slope})} = (83.5\pm8.7)$ ADC/ns. The time resolution hence is

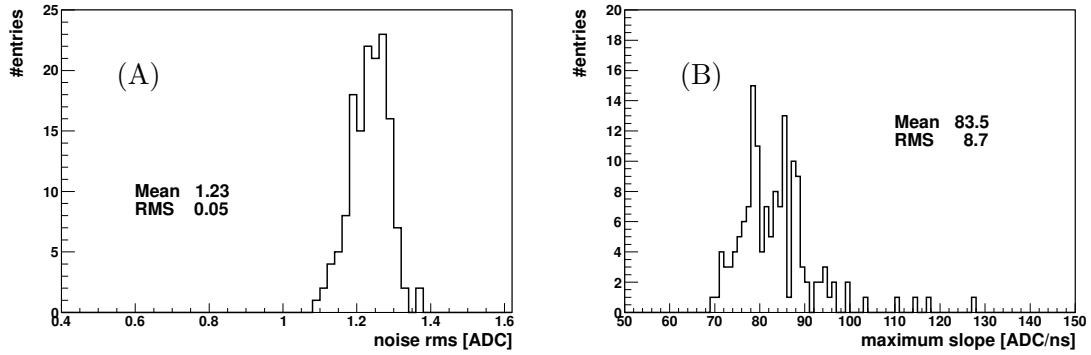

Figure 7.3.: Distribution of the rms noise of the signal prior to the extraction **(A)** and the distribution of the maximum slope of the Landau-Fits **(B)**.

$$\sigma_{\mathrm{t}} = (14.7 \pm 1.7)\,\mathrm{ps}. \tag{7.5}$$

The noise is dominated by the least-significant-bit noise of the 8-bit oscilloscope. With a 12-bit (16-bit) data acquisition system, a time resolution of $\sigma_{\mathrm{t}}^{12\mathrm{b}} \approx 1\,\mathrm{ps}$ ($\sigma_{\mathrm{t}}^{16\mathrm{b}} < 100\,\mathrm{fs}$) is feasible. The real electric noise at a gain of 5 mV/div is much smaller than 1 mV, compared to the one used for the measurement of $g \cdot \overline{\sigma} \approx 19\,\mathrm{mV}$.

7.4. Conclusion

The time resolution of polycrystalline diamond has been analysed at high impact ionisation of 300 pC per bunch with the muon beam in the secondary beam line of the CNGS facility. A single pulse time resolution of

$$\sigma_{\mathrm{t}} = (14.7 \pm 1.7)\,\mathrm{ps} \tag{7.6}$$

is found. Additionally, the linearity of the signal delivered by the diamond was estimated at first order. No significant deviation from a linear behaviour of the signal charge as a function of the flux is observed up to a muon flux per detector of 3×10^5 within 3 ns.

8. THE BEAM CONDITIONS MONITOR AT THE ATLAS EXPERIMENT

8.1. Introduction

In this chapter the characterisation of the non-collision backgrounds with the ATLAS detector is discussed, and techniques in order to identify them are presented.[1] First, the Large Hadron Collider (LHC) and the ATLAS detector are introduced, then the definitions of the sources of non-collision backgrounds are discussed. Subsequently, a brief introduction to the characteristics of the ATLAS trigger system and LHC beam structure are given, followed by characterisation of the beam induced background with the Beam Conditions Monitor (BCM) sub-detector.

8.1.1. The LHC and the ATLAS detector

The LHC [3] – the largest, man-made circular particle accelerator ever built – is managed by the European Organisation for Nuclear Research (CERN) and produced its first particle collisions in 2009. Its circumference measures 26.7 km and it resides about 100 m under ground. In its two proton storage rings, it can accelerate protons to almost the speed of light, and will be able to collide them a centre-of-mass energy of $\sqrt{s} = 14\,\text{TeV}$ at a bunch-crossing (BC) frequency of 40 MHz. Superconducting magnets, cooled to 1.9 K using superfluid helium, bend the trajectory of the protons on circular paths. The design luminosity is as high as $\mathcal{L} = 10^{34}\,\text{cm}^{-2}\text{s}^{-1}$, two order of magnitudes higher compared to the second most energetic collider: the Tevatron at Fermilab[2]. The high luminosity is made possible by filling the LHC with up to 2808 bunches with over 10^{11} protons each, adding up a total stored beam energy of 724 MJ. A combination of a photograph and a drawing of the LHC magnet is shown in Fig. 8.1.

The ATLAS detector [11] at the LHC is situated in an underground cavern at a depth of 80 m. Its basic parameters are a weight of 7000 t, a diameter of 22 m, and a width of 44 m. Proton-proton collisions occur at the centre of the experiment. In order to measure the total transverse momentum of a collision, the ATLAS detector is designed to cover a pseudo-rapidity of $|\eta| = 4.9$ around the collision point with $\eta = -\ln\big(\tan(\theta/2)\big)$. Here, θ is the polar angle with respect to the theoretical LHC beam line. An illustration of the ATLAS detector is shown in Fig. 8.2. With the x-axis pointing towards the centre of the LHC ring, ϕ defined with respect to the x-axis, and the z-axis defined along LHC beam 2, the ATLAS coordinate system is right-handed. ATLAS is divided into two sides A and C, where side A is the receiving beam 1 from the east, whereas side C receives beam 2 from the west.

The inner tracking detector of ATLAS covers a pseudo-rapidity of $|\eta| < 2.5$ and is embedded in a 2 T superconducting solenoid. High-resolution measurement of charged particle

[1] cf. [117], where the author of this thesis was a co-author
[2] ceased operations on September 30$^{\text{th}}$, 2011

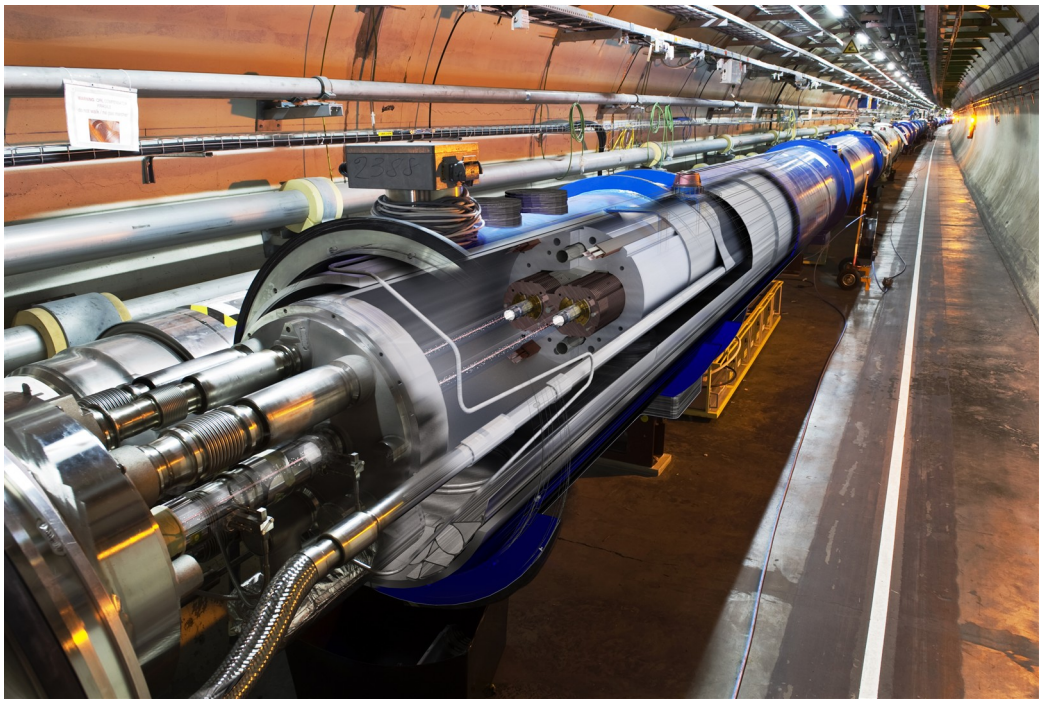

Figure 8.1.: A picture of an LHC magnet is shown. [118]

momentum and vertex position is a key feature of the inner tracking system, and is rendered possible by the combination of a pixel detector followed by a strip tracker detector. Particle identification is facilitated by a transition radiation tracker. Shell-wise, the tracker is followed by a high-granularity liquid-argon electromagnetic calorimeter and a hadronic calorimeter, which is based on scintillator-tiles for $|\eta| < 1.7$ and on liquid-argon technology for $|\eta| > 1.5$. The calorimetry is surrounded by large superconducting toroid magnets. The outermost shell is a muon spectrometer.

Another important ATLAS sub-detector, extensively used in beam-related studies is the Beam Conditions Monitor. [119] Its primary purpose is to monitor beam conditions and protect against anomalous beam-losses, that could result in detector damage. Aside from this protective function it is also used to monitor luminosity and beam-background levels. It consists of two detector stations (forward and backward) with four modules each. A module consists of two polycrystalline chemical vapour deposition diamond sensors. The sensors are about 500 µm thick and the sensor area is 10 mm × 10 mm, equipped with metal electrodes covering 8 mm × 8 mm. The diamond sensors are positioned at $z = \pm 184$ cm, corresponding to a $z/c = 6.13$ ns time-of-flight to/from the interaction point. The sensors are at a radius of 55 mm, i.e. at an $|\eta|$ of about 4.2 and arranged as a cross – two sensors on the vertical and two on the horizontal axis. They provide a precise time resolution in the sub-nanosecond regime [113], which can be used to identify beam-backgrounds, as shown in Sec. 8.3.

8.1.2. Definition of non-collision backgrounds

Signals detected in the ATLAS detector do not always origin from beam-beam collision, but also from cosmic-ray showers and so-called beam-induced background (BIB) [121]. This type of background is called *non-collision background* and the BIB part is studied herein. Cosmic-ray showers produced in proton-gas collisions in the atmosphere are another source

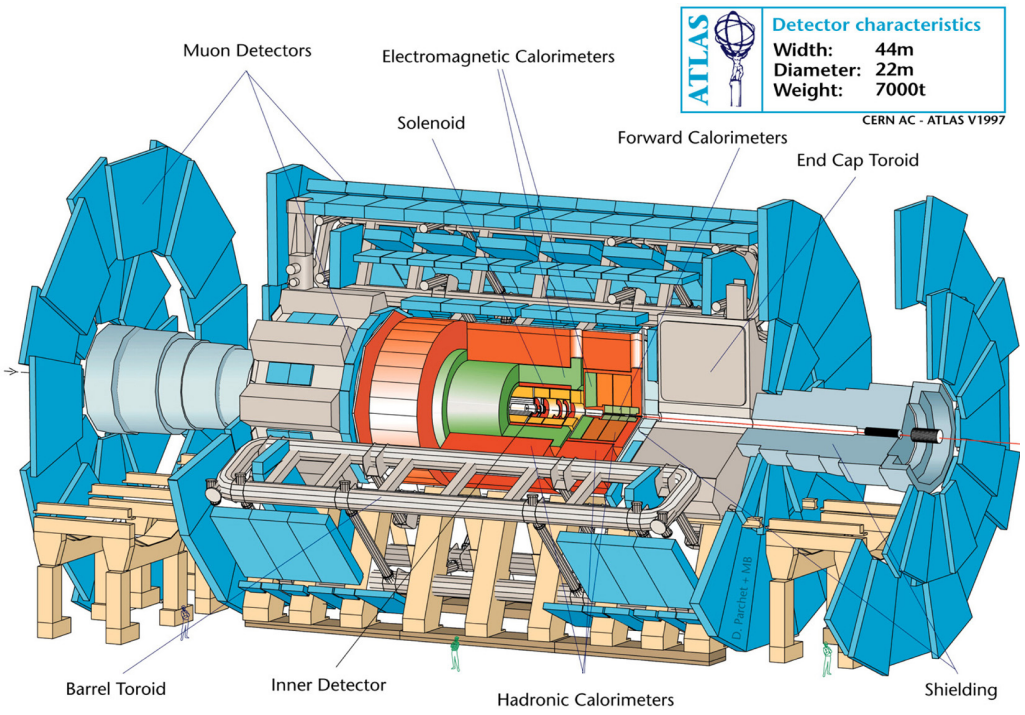

Figure 8.2.: A technical drawing of the ATLAS detector is shown. [120]

of non-collision background. [122] Out of these cosmic-rays, mostly high-energy muons reach the ATLAS cavern, whereas other contents are stopped earlier. Triggers can be fired by both the BIB or cosmic-ray muons as they deposit energy in the calorimeter, or signals from these sources can overlap with proton-proton collisions, eventually leading to false triggers.

When protons are lost upstream of the interaction point, secondary cascades are produced by hitting collimators or residual gas molecules in the LHC. These secondary particles can in general follow the LHC beam and induce background signals in the detectors, which bias the physics analyses. Different factors affect the rate of the BIB, e.g. machine optics, collimator settings, residual gas densities, and filling schemes. In general, three different types of BIBs are defined: [117]

- **Tertiary halo:** protons lost on limiting apertures near the experiment, typically the tertiary collimator (TC) situated at $z \approx \pm 150\,\mathrm{m}$ from the interaction point. These are a normal feature of the 3-stage cleaning of the LHC, where the 2-stage cleaning in dedicated sections (Interaction Region (IR) 7 for betatron and IR 3 for momentum cleaning) is complemented by a tertiary collimator.

- **Inelastic beam-gas:** produced in inelastic interactions of protons with the residual gas inside the beam-pipe. Simulation studies [123, 124] show that these give a significant contribution even from a distance larger than 550 m from the interaction point[3], i.e. from the LHC arc.

- **Elastic beam-gas:** elastic beam-gas scattering can result in small angular deflections of the protons. Usually such protons are intercepted within one turn on limiting apertures. A non-negligible fraction of them are expected to end up on the TC.

[3]The LHC long straight sections are 545 m long.

Tertiary halo and elastic beam gas events produce similar signals in the ATLAS detector as in both cases protons are lost on the TC and a collimated flux of secondaries is produced. The secondaries that reach the ATLAS detector are mostly high-energy muons. Simulation studies show that these muons cross the detector at radii typically smaller than 2 m. Also inelastic beam-gas interactions in the straight sections of the LHC produce comparable background. In contrast, inelastic beam-gas interactions from arc regions result in tangentially emitted muons crossing ATLAS at larger radii.

Additionally to the above discussed BIBs, other types of non-collision backgrounds exist. [125] The LHC operating frequency is 400 MHz, i.e. within 25 ns there are ten buckets spaced by 2.5 ns. If the crossing angle between the two LHC beams at the interaction point is zero, parasitic proton-proton collisions can occur at multiples of 37.5 cm away from the interaction point, when protons leak from their original bucket to a neighbouring bucket. Therefore, the LHC is designed to produce collisions at a nominal crossing-angle of 285 µrad, largely reducing the rate of parasitic collisions. Only if in both of the colliding bunches protons have leaked in a neighbouring bucket, so-called satellite collision can occur at the interaction point itself. These are likely to be proportional to the square of the amount of leakage in to neighbouring buckets and are therefore accordingly improbable.

Here, and to a larger extent in Ref. [117], a first qualitative characterisation of the various backgrounds is given.

8.1.3. The LHC beam structure and the ATLAS trigger system

The design bunch-crossing frequency of the LHC is 40 MHz [3], which corresponds to a 25 ns spacing between the bunches. The length of the LHC therefore offers 3564 bunch positions, which are numbered uniquely by a bunch-crossing identifier (BCID). Up to 2808 bunches can be filled in the LHC, with a maximum of 32 and a bunch spacing of 150 ns during 2010. Unfilled bunches are a consequence of the injection scheme and an abort gap is needed for a safe extraction of the beam in the event of a beam dump.

In order to group bunches of a corresponding type, the bunches are organised in bunch groups by the ATLAS Central Trigger Processor (CTP) [126]. The CTP takes the Level-1 (L1) trigger decision for every bunch based on various input signals and issues the type of trigger items that matched the signals. The trigger items requirements can be changed by software and are adapted for different filling schemes. Those items that are used for non-collision background monitoring are described in Table 8.1. With different filling schemes and on-going machine development, the definition of the bunch group needs to be programmable and is matched to the individual filling scheme for each fill. The bunch groups of interest for this study are: [117]

- **Paired:** a bunch in both LHC beams in the same BCID;
- **Unpaired isolated:** a bunch in only one LHC beam with no bunch in the other beam within 3 BCIDs
- **Unpaired non-isolated:** a bunch in only one LHC beam with a nearby (within 3 BCID) bunch in the other beam
- **Empty:** a BCID containing no proton bunch in both beams.

8.2. Beam Background Levels during 2010 Data-taking

The time measurements performed by the ATLAS sub-detectors can be used to distinguish beam backgrounds from collisions. As discussed above, particles stemming from BIB typically travel parallel to the beam direction z, enter the ATLAS detector from one side and exit on the opposite. Hence, particles from BIBs typically first produce hits on one side *before* the BC, and subsequently hits after the bunch crossing on the other. However, particles from beam collisions travel outward from the interaction point and therefore produce hits in the sub-detectors at the same point in time on both of the two ATLAS sides (A and C), with both hits on both sides occurring *after* the BC.

The hits happening before (after) the BC are called "out-of-time" ("in-time"). As a result, any sub-detector with modules at identical positions in both positive and negative z and with sufficiently high timing resolution can be used to discriminate between these processes, using the observable $\Delta t = t_2 - t_1$. For in-time hits, $\Delta t = t_2 - t_1 \approx 0$, for out-of-time hits $\Delta t = t_2 - t_1 = \Delta z/c$.

The cleanest BIB sample was provided by the BCM sub-detector with the so-called L1_BCM_AC_CA trigger, which selects beam-background-like events. For this trigger an event is selected if a hit on one side is out-of-time, i.e. early by 12.3 ns with respect to collision hits, with another hit being in-time on the other side. The width of the time window during which a hit is accepted is 6.25 ± 2.75 ns before and after the nominal collision time of any BCID. Since the time-window for accepting a L1_BCM_AC_CA trigger was rather narrow, it is a reasonably pure halo-trigger even in colliding bunch pairs. The trigger bit itself carries no information about the direction of the two beams, i.e. if the background was of type A-to-C or C-to-A. This information is available in the CTP monitoring database with less time-granularity and was not systematically used in the analysis of 2010 data.

The L1_BCM_AC_CA trigger rate normalised to the number of protons in the machine over the entire 2010 proton running period is shown in Figure 8.3. When the proton intensity was altered from low-intensity to nominal ($\sim 10^{11}$ protons/bunch) intensity at the end of June, a step in the measured background level is seen. Multi-bunch injection introduced another small step. The introduction of 150 ns bunch-trains clearly affected the background level due to electron-cloud build-up in the machine and thereby a worsening of the vacuum. It is found that the L1_BCM_AC_CA rate is correlated with the quality of the beam pipe vacuum, i.e. with the pressure inside the beam pipe. Figure 8.3 shows the average pressure per fill and the increase at the end of the year of the L1_BCM_AC_CA rate and the beam pipe pressure.

Table 8.1.: ATLAS Trigger items used during the 2010 proton runs for the monitoring and studies of non-collision backgrounds. [117]

Trigger item	Description	Usage for background monitoring/studies
L1_BCM_AC_CA_BGRP0	BCM halo-like coincidence	BIB level
L1_BCM_Wide_BGRP0	BCM collision-like coincidence	Collisions in unpaired BCIDs
L1_J5_UNPAIRED_ISO	Jet with $p_T > 5$ GeV	Fake jets due to BIB
L1_J5_UNPAIRED_NONISO	Jet with $p_T > 5$ GeV	Fake jets due to BIB
L1_TAU5_UNPAIRED_ISO	Narrow jet with $p_T > 5$ GeV	Fake jets due to BIB
L1_J10_UNPAIRED_ISO	Jet with $p_T > 10$ GeV	Fake jets due to BIB
L1_J10_UNPAIRED_NONISO	Jet with $p_T > 10$ GeV	Fake jets due to BIB

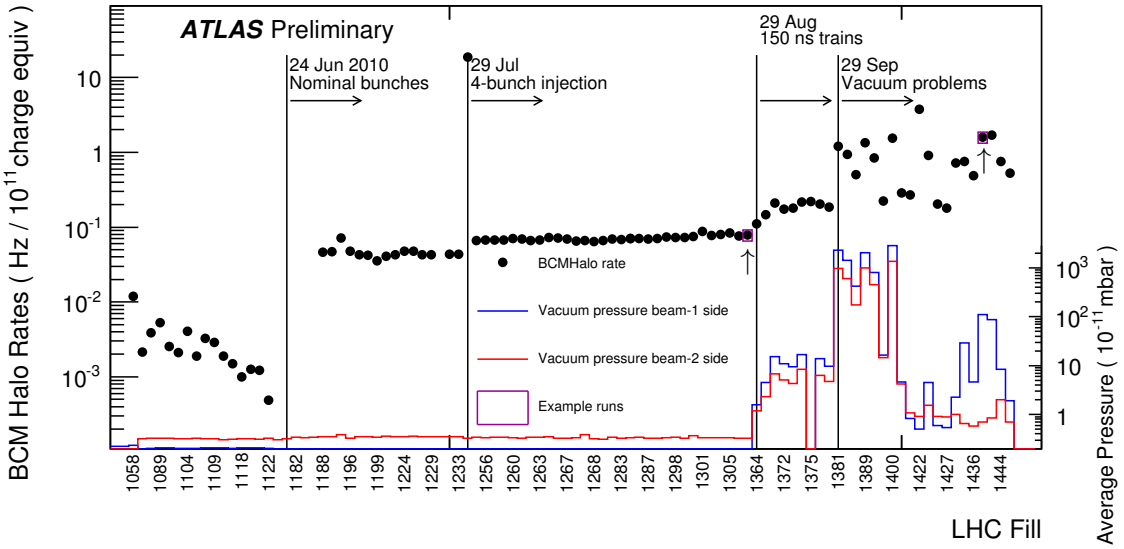

Figure 8.3.: The BCM specific BIB trigger rate is shown, with the rate normalised to 10^{11} protons, for the whole proton-proton running period of 2010. The two fills (LHC fill number 1309 and 1440) used for further studies are marked with a rectangle (original marker) and additionally with an upward arrow. The corresponding ATLAS run numbers are 162882 and 167607 with low and high BIBs, respectively. [117]

With small size diamond detectors used in the BCM, the trigger efficiency of the BCM on tertiary halo events is inherently low. Furthermore, the BCM can only detect BIB events that have particles at a certain radii from the beam pipe. BIB events triggered by the BCM can therefore be of different topology and origin compared to those e.g. seen by the calorimeter. Consequently, BIB events detected by BCM do not necessarily coincide with BIB events detected by other ATLAS subdetectors, and detectors with higher efficiency and a different coverage need to be studied, too, cf. [117].

8.3. Characterisation of BIBs with the BCM sub-detector

The properties of the BIB events can be studied using the precise time measurements of the Beam Conditions Monitor (BCM) sub-detector, described in Sec. 8.1. The different time characteristics of collisions and BIBs presented in Sec. 8.2 are used here. For events that contain at least one hit per station, the time-of-flight (Δt) can be calculated and is used to distinguish events resulting from beam losses from those occurring from proton-proton interactions. A positive Δt for the BCM sub-detector corresponds to an event containing a hit in station A with a subsequent hit in station C, and the Δt is calculated for hits occurring in the same bunch crossing as

$$\Delta t = t_{\mathrm{C}} - t_{\mathrm{A}}. \tag{8.1}$$

The data-taking sessions considered in this analysis have been chosen for their low (run 162882) and high (run 167607) beam background conditions. Events with at least one hit per station were analysed. The required CTP trigger is of type 'L1_BCM_Wide_BGRP0' or 'L1_BCM_AC_CA_BGRP0', the latter defined in Sec. 8.2. The trigger window of the

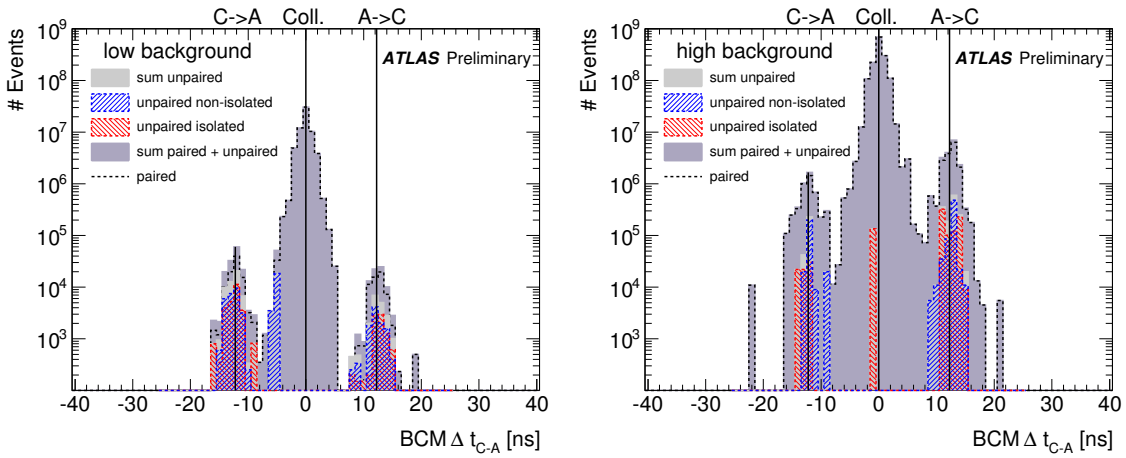

Figure 8.4.: The Δt distribution derived from BCM hits is shown for the two data-taking sessions under study, i.e. LHC run numbers 1309 **(left)** and 1440**(right)** [**117**].

'L1_BCM_Wide_BGRP0' trigger item is defined as 0.4 ns to 8.2 ns after the collision and required at least one hit on both sides.[4] The abbreviation BGRP0 is short for 'Bunch Group 0', which includes all BCIDs with the exception of the abort gap, hence it includes also paired and unpaired crossings. When multiple hits are present for an event, Δt values for all pairs are calculated and each Δt is weighted by the inverse number of pairs $w = 1/n$. Additionally, each event is corrected according to the trigger prescale in each luminosity block. A luminosity block is a certain time interval during which the luminosity, trigger, and detector conditions can be considered as constant. A change in the LHC beam, trigger, or detector conditions will cause the creation of a new luminosity block.

The Δt distributions derived from BCM hits are shown in Fig. 8.4 for the two data-taking sessions under study. Collision-like events accumulate around $\Delta t = 0$ ns and background-like events around $\Delta t = \pm 12.3$ ns, as marked with solid lines. Note the logarithmic scale on the vertical-axis. The three distinctive peaks around the three mentioned positions function as a proof of the ability of the BCM to distinguish between the two types of events under discussion here. Hence, it can be used to select a pure background sample, but it should be mentioned that due to the small area of the BCM detector, the selection has a quite low acceptance.

For the two data-taking sessions examined here, the number of collision events and the number of halo events is estimated by the area of the histograms around the three peaks, i.e. the area around $\Delta t = 0$ ns and the sum of areas around $\Delta t = \pm 12.3$ ns. For the low background run, a ratio (collision over halo) of roughly 280 is found. In contrast to that, the high background run presented with a ration of $\sim$60 as measured with the BCM. Hence, a smaller difference between the two event numbers indicates a worsening of the background conditions. The L1_BCM_Wide trigger lacks statistics to observe collision-like events in unpaired BCIDs (red hatched areas around $\Delta t = 0$ ns) as its prescale is set according to the collision hit rate with paired bunches, and is therefore heavily prescaled. In order to remedy this, dedicated BCM triggers for unpaired crossings have been introduced in the course of 2011.

The BCM Δt is plotted versus the BCID in Fig. 8.5 in order to determine whether there is any BCID dependence in the beam conditions. It can be concluded from Fig. 8.5 that

[4] The expected arrival time for particles originated in collisions is 6.13 ns.

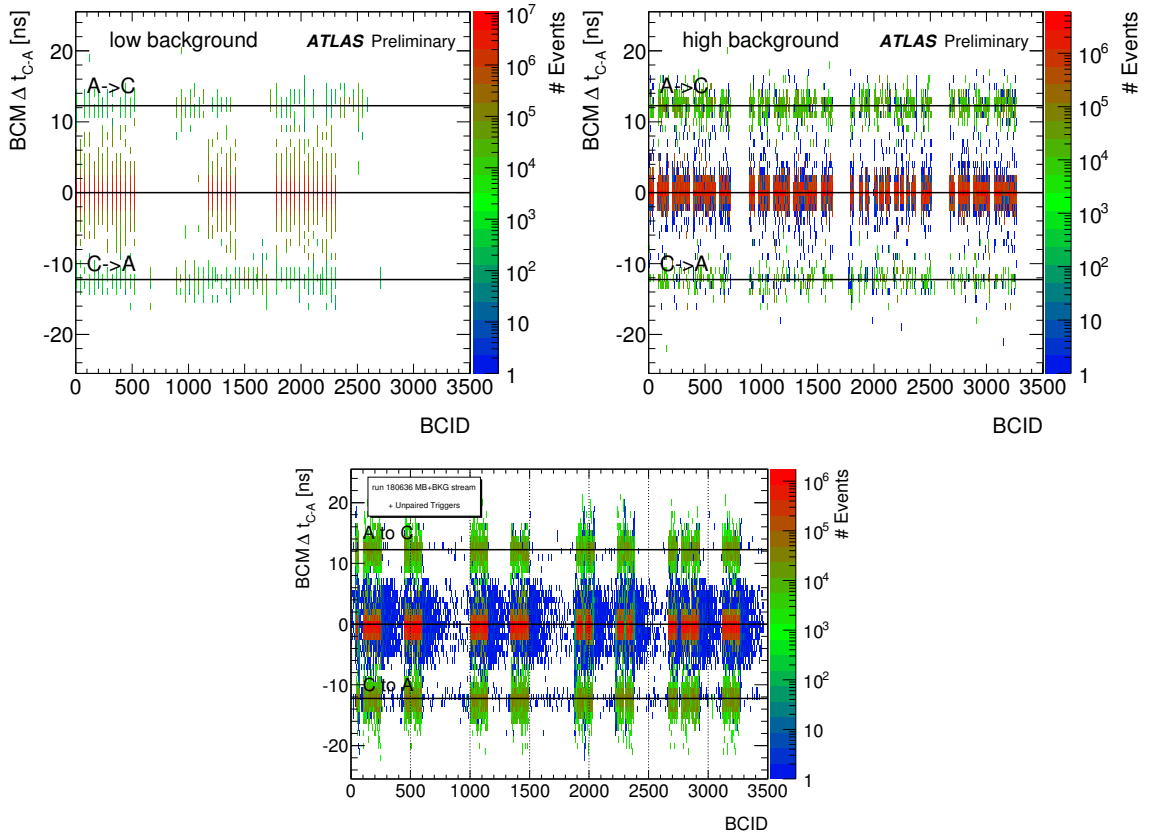

Figure 8.5.: The BCM Δt is plotted against the BCID for the two data-taking sessions under study, i.e. LHC fill numbers 1309 **(top left)** and 1440 **(top right)**. [117] Additionally, the same plot is shown for a run from end of April 2011. There, events occurring in between trains are clearly visible (mostly blue and around $\Delta t = 0$).

the conditions are comparable for all filled BCIDs. The discrimination power of the BCM is again corroborated by the fact that, visible especially in the low background run, events from unpaired crossing are readily identified in those BCIDs, that are actual unpaired bunches according to the LHC filling scheme [127]. Also, the paired BCIDs can be identified and correspond to the fill structure. Additionally, the same plot is shown for a run from end of April 2011. There, 598 bunches were arranged in 11 bunch trains, and the bunch spacing within the train was 50 ns (compared to 150 ns in run 167607). Events occurring in between trains are clearly visible (mostly blue and around $\Delta t = 0$).

8.3.1. Conclusion

The ATLAS Beam Conditions Monitor is an ATLAS sub-detector, which makes use of fast diamond sensors in order to detect charged particles. The sub-nanosecond time resolution allows for an excellent timing measurement of the passage of these particles. With station on both sides of the interaction point, the BCM is capable of distinguishing beam halo from collision events, by measuring the time difference between hits on different sides. It can therefore provide a pure halo sample. However, owing to the low acceptance of the small sensors, the BCM provides poor efficiency. With the BCM serving as a proof of principle of

the capabilities of a diamond based charged particle sensor, an upgrade project, the ATLAS Diamond Beam Monitor (DBM), is foreseen to be installed in the ATLAS experiment during the ongoing shut-down (2013/2014). Unlike the BCM, the DBM is equipped with a pixelised read-out, allowing for bunch-by-bunch collision point tracking. With other experiments, for example the CMS experiment at the LHC, installing diamond based detectors, too, diamond becomes more and more the detector material of choice for time-critical sub-detectors.

9. SUMMARY AND FUTURE WORK

Along with a broadening fundamental knowledge about diamond comes the possibility of its usage in numerous applications. Besides the examples given in the preface, this work proves the usability of diamond as a charged particle detector at liquid helium temperatures and in high-flux environments.

A temperature controlled TCT set-up has been constructed, which is a powerful tool for the characterisation of the temperature dependence of semiconductor properties. Three single-crystal CVD diamond samples, that have been studied with the transient current technique, show a very similar behaviour in all measured aspects. The measured transit time at various field strength enables the measurement of the charge carrier mobility. For holes the mobility increases with decreasing temperature due to the acoustic phonon scattering, but it saturates for ultra-cold temperatures. The low-field mobility for holes at room temperature is measured to be $\mu_0^h(295\,\mathrm{K}) = (2534{\pm}20)\,\mathrm{cm}^2/\mathrm{Vs}$ and $\mu_0^h(2\,\mathrm{K}) = (10\,740{\pm}250)\,\mathrm{cm}^2/\mathrm{Vs}$. For electrons, only a lower limit on the low-field mobility results from the pursued measurements. It is measured to be $\underline{\mu}_0^e(295\,\mathrm{K}) = (1802{\pm}14)\,\mathrm{cm}^2/\mathrm{Vs}$ and $\underline{\mu}_0^e(2\,\mathrm{K}) = (3061{\pm}55)\,\mathrm{cm}^2/\mathrm{Vs}$. These measurements, for the first time, allow for an experimental estimation of the mobility governed by the neutral impurity scattering. Holes show a NIS mobility of $\mu_{\mathrm{NIS}}^h = (11\,130{\pm}120)\,\mathrm{cm}^2/\mathrm{Vs}$, and electrons of $\underline{\mu}_{\mathrm{NIS}}^e = (3058{\pm}27)\,\mathrm{cm}^2/\mathrm{Vs}$.

The lifetime of excitons in diamond is usually studied using spectrometry in order to measure the light from radiative recombination processes. No literature about the combination of a spectroscopic measurement with an applied electric field is available. Herein, an electric measurement of currents resulting from evaporating excitons is presented. The recorded pulse shapes are modelled under the assumption of the creation and subsequent evaporation and recombination of excitons. Details of the derivation of the exciton model are given and a subsequent discussion compares the model to the data. The evaporation time at room temperature is found to be a few tens of picoseconds, a few nanoseconds at 100 K, and further exponentially increasing towards even lower temperatures. A non-radiative recombination lifetime can be estimated to be of the order of a few nanoseconds. Additional measurements undertaken with a silicon pad detector are compared to the diamond data, and a successful plausibility check of the model is performed.

Additionally, an anomalous temperature behaviour of the transit time of electrons is observed. This is thought be the result of different drift velocities present in the longitudinal and transversal valleys of the multi-valley semiconductor diamond; a future application being valleytronic devices that make use of the valley quantum number of the electron in order to encode binary information.

The secondary beam line of CNGS and the proton-proton collisions at ATLAS were taken as use cases of diamond detectors, where time resolution is critical. At CNGS, the time-of-flight of charged particles is studied, helping to solve the problem of "faster than light"-neutrinos. Additionally, the charge yield and the single-pulse time resolution at high impact ionisation is measured. The charge yield of polycrystalline CVD samples is shown to increase linearly with the impact ionisation up to a muon flux per detector of $3{\times}10^5$ within 3 ns. The measured single-pulse time resolution is $\sigma_{\mathrm{t}} = (14.7{\pm}1.7)\,\mathrm{ps}$. At ATLAS, the

diamond sensors of the BCM are used to successfully distinguish halo events from collision events.

In the future, the temperature controlled transient current technique needs to be carried out on irradiated samples. This opens the possibility of studying radiation induced defects in unprecedented accuracy, and might render the determination of the energy level of these defects possible. If it was possible to create shallow defects with radiation, an important problem of diamond as a transistor material could be overcome, as there are no shallow donors nor acceptors known in diamond. A second possibility to study radiation induced defects is the thermally stimulated current technique, which could be used at radiation levels, at which the current resulting from an α-particle is not detectable any more.

It is clear from this work and other recent studies, that diamond is a diversely applicable material, with many prospects in future devices; researches today just lifting the curtain for discoveries to come.

A. Stopping Power Values from NIST

Listed is the $\mathrm{d}E/\mathrm{d}x$ in diamond for various α-energies.

E_α [MeV]	$\mathrm{d}E/\mathrm{d}x$ [MeV/µm]	E_α [MeV]	$\mathrm{d}E/\mathrm{d}x$ [MeV/µm]	E_α [MeV]	$\mathrm{d}E/\mathrm{d}x$ [MeV/µm]
1.00×10^{-3}	3.480×10^{2}	2.75×10^{-1}	1.897×10^{3}	1.75×10^{1}	3.117×10^{2}
1.50×10^{-3}	3.730×10^{2}	3.00×10^{-1}	1.934×10^{3}	2.00×10^{1}	2.811×10^{2}
2.00×10^{-3}	3.930×10^{2}	3.50×10^{-1}	1.992×10^{3}	2.50×10^{1}	2.360×10^{2}
2.50×10^{-3}	4.104×10^{2}	4.00×10^{-1}	2.031×10^{3}	2.75×10^{1}	2.189×10^{2}
3.00×10^{-3}	4.262×10^{2}	4.50×10^{-1}	2.055×10^{3}	3.00×10^{1}	2.043×10^{2}
4.00×10^{-3}	4.547×10^{2}	5.00×10^{-1}	2.067×10^{3}	3.50×10^{1}	1.808×10^{2}
5.00×10^{-3}	4.803×10^{2}	5.50×10^{-1}	2.069×10^{3}	4.00×10^{1}	1.624×10^{2}
6.00×10^{-3}	5.039×10^{2}	6.00×10^{-1}	2.064×10^{3}	4.50×10^{1}	1.477×10^{2}
7.00×10^{-3}	5.259×10^{2}	6.50×10^{-1}	2.052×10^{3}	5.00×10^{1}	1.357×10^{2}
8.00×10^{-3}	5.467×10^{2}	7.00×10^{-1}	2.037×10^{3}	5.50×10^{1}	1.257×10^{2}
9.00×10^{-3}	5.664×10^{2}	7.50×10^{-1}	2.017×10^{3}	6.00×10^{1}	1.171×10^{2}
1.00×10^{-2}	5.853×10^{2}	8.00×10^{-1}	1.995×10^{3}	6.50×10^{1}	1.098×10^{2}
1.25×10^{-2}	6.290×10^{2}	8.50×10^{-1}	1.971×10^{3}	7.00×10^{1}	1.034×10^{2}
1.50×10^{-2}	6.690×10^{2}	9.00×10^{-1}	1.946×10^{3}	7.50×10^{1}	9.773×10^{1}
1.75×10^{-2}	7.060×10^{2}	9.50×10^{-1}	1.920×10^{3}	8.00×10^{1}	9.274×10^{1}
2.00×10^{-2}	7.406×10^{2}	1.00	1.893×10^{3}	8.50×10^{1}	8.829×10^{1}
2.25×10^{-2}	7.730×10^{2}	1.25	1.753×10^{3}	9.00×10^{1}	8.429×10^{1}
2.50×10^{-2}	8.037×10^{2}	1.50	1.621×10^{3}	9.50×10^{1}	8.067×10^{1}
2.75×10^{-2}	8.329×10^{2}	1.75	1.504×10^{3}	1.00×10^{2}	7.738×10^{1}
3.00×10^{-2}	8.607×10^{2}	2.00	1.401×10^{3}	1.25×10^{2}	6.459×10^{1}
3.50×10^{-2}	9.128×10^{2}	2.25	1.311×10^{3}	1.50×10^{2}	5.576×10^{1}
4.00×10^{-2}	9.609×10^{2}	2.50	1.232×10^{3}	1.75×10^{2}	4.928×10^{1}
4.50×10^{-2}	1.006×10^{3}	2.75	1.162×10^{3}	2.00×10^{2}	4.431×10^{1}
5.00×10^{-2}	1.048×10^{3}	3.00	1.100×10^{3}	2.25×10^{2}	4.037×10^{1}
5.50×10^{-2}	1.087×10^{3}	3.50	9.950×10^{2}	2.50×10^{2}	3.716×10^{1}
6.00×10^{-2}	1.125×10^{3}	4.00	9.097×10^{2}	2.75×10^{2}	3.451×10^{1}
6.50×10^{-2}	1.160×10^{3}	4.50	8.398×10^{2}	3.00×10^{2}	3.226×10^{1}
7.00×10^{-2}	1.194×10^{3}	5.00	7.812×10^{2}	3.50×10^{2}	2.868×10^{1}
7.50×10^{-2}	1.226×10^{3}	5.50	7.313×10^{2}	4.00×10^{2}	2.595×10^{1}
8.00×10^{-2}	1.257×10^{3}	6.00	6.881×10^{2}	4.50×10^{2}	2.379×10^{1}
8.50×10^{-2}	1.287×10^{3}	6.50	6.502×10^{2}	5.00×10^{2}	2.204×10^{1}
9.00×10^{-2}	1.315×10^{3}	7.00	6.168×10^{2}	5.50×10^{2}	2.060×10^{1}
9.50×10^{-2}	1.342×10^{3}	7.50	5.870×10^{2}	6.00×10^{2}	1.938×10^{1}
1.00×10^{-1}	1.368×10^{3}	8.00	5.602×10^{2}	6.50×10^{2}	1.834×10^{1}
1.25×10^{-1}	1.485×10^{3}	8.50	5.360×10^{2}	7.00×10^{2}	1.745×10^{1}
1.50×10^{-1}	1.584×10^{3}	9.00	5.141×10^{2}	7.50×10^{2}	1.667×10^{1}
1.75×10^{-1}	1.668×10^{3}	9.50	4.941×10^{2}	8.00×10^{2}	1.598×10^{1}
2.00×10^{-1}	1.739×10^{3}	1.00×10^{1}	4.758×10^{2}	8.50×10^{2}	1.538×10^{1}
2.25×10^{-1}	1.800×10^{3}	1.25×10^{1}	4.029×10^{2}	9.00×10^{2}	1.483×10^{1}
2.50×10^{-1}	1.852×10^{3}	1.50×10^{1}	3.509×10^{2}	9.50×10^{2}	1.435×10^{1}
[continued]		[continued]		1.000×10^{3}	1.391×10^{1}

Zusammenfassung

Diamant, ein Halbleiter mit großer Bandlücke und außergewöhnlichen elektrischen Eigenschaften, wird in verschiedensten Anwendungen verwendet. Diese reichen von der Benutzung als Sensormaterial in Strahlverlustmonitoren (engl.: Beam Loss Monitor, BLM) an Teilchenbeschleunigern, über Laserfenster, bis hin zu UV-Licht-Sensoren in der Raumfahrt, z.B. für Weltraumwettervorhersagen. Auch ist Diamant ein interessanter Kandidat für hitzetolerante, strahlenharte, sehr schnelle, verlustarme Transistoren. Seine große Bandlücke (5.47 eV) hat eine hohe Durchbruchspannung von über $1\times10^3\,\mathrm{V/\mu m}$ zur Folge. Einkristall-Diamant besticht außerdem mit einem äußerst niedrigen Leckstrom von der Ordnung pA für Feldstärken $E \leq 1\,\mathrm{V/\mu m}$, welches die sehr genau Messung eines Signalstroms ermöglicht.

Diamant wird oft bei Raumtemperatur verwendet, jedoch ist wenig über den Ladungstransport bei Flüssig-Helium Temperaturen bekannt. Jedoch ist ein besseres Verständnis der Transportmechanismen ausschlaggebend für den Betrieb eines kryogenen BLMs, der zum Beispiel in der Kaltmasse eines LHC-Magneten eingesetzt werden soll. Darüber hinaus sind für die Raumfahrt Transistormaterialien von Nöten, die verlässlich funktionieren und über einen großen Temperaturbereich gut verstanden sind. In dieser Arbeit wird die Methode der transienten Strommessung (engl.: transient current technique) unter der Benutzung von α-Strahlung in einem Bereich von 2 K bis 295 K eingesetzt. Die elektrische Feldstärke wird um einen Faktor 30 variiert. Dies ermöglicht die Messung der Temperaturabhängigkeit und der Feldstärkenabhängigkeit der Pulsform, der Ladungstransitzeit, sowie der Driftgeschwindigkeit, der Saturationsgeschwindigkeit, und der Niederfeldbeweglichkeit in Einkristall-Diamant von Detektor-Qualität. Modelle werden vorgestellt, die konsistent die Daten einerseits mittels Ladungserzeugung und Fundamentalanregungen in Halbleitern und Transportmechanismen wie akustische Phononstreuung andererseits beschrieben.

Drei Diamantproben wurden studiert; alle zeigen ein sehr ähnliches Verhalten. Die Messung der Transitzeit bei verschiedenen Feldstärken ermöglicht die Berechnung der Beweglichkeit. Für Löcher steigt die Beweglichkeit mit fallenden Temperaturen aufgrund der akustischen Phononstreuung, und saturiert gen ultra-kalte Temperaturen. Die Niederfeldbeweglichkeit für Löcher beträgt $\mu_0^h(295\,\mathrm{K}) = (2534\pm20)\,\mathrm{cm^2/Vs}$ bei Raumtemperatur und saturiert gegen $\mu_0^h(\to 2\,\mathrm{K}) = (11\,130\pm120)\,\mathrm{cm^2/Vs}$. Für Elektronen kann nur eine untere Grenze der Niederfeldbeweglichkeit angegeben werden. Diese wurde zu $\underline{\mu}_0^e(295\,\mathrm{K}) = (1802\pm14)\,\mathrm{cm^2/Vs}$ gemessen und saturiert gegen $\underline{\mu}_0^e(\to 2\,\mathrm{K}) = (3058\pm27)\,\mathrm{cm^2/Vs}$. Die Elektrontransitzeit bei niedrigen Feldstärken zeigt ein anderes Verhalten als die der Löcher, und folgt nicht dem erwarteten Verlauf. Es wird vermutet, dass dies durch einen, durch Verunreinigungen ermöglichten, Repopulations-Effekt verursacht wird. Die gemessenen Pulsformen werden unter der Annahme der Erzeugung und der anschließenden Verdampfung oder der Rekombination von Exitonen modelliert. Details der Herleitung des Exitonenmodells werden diskutiert, gefolgt von einem Vergleich von Daten und Modell. Zusätzlich werden Messungen an einem Silizium-Pad-Detektor mit denen von Diamant verglichen, und die Modellvorhersagen für Silizium überprüft.

Schließlich wird die Einsetzbarkeit von Diamant in zeitkritischen Anwendungen demonstriert, und die wichtigsten Ergebnisse dargestellt. Die Flugzeitmessung von Muonen im Sekundärstrahl des CERN Neutrino to Gran Sasso-Experiments (CNGS) wurden benutzt um die Korrektheit und Genauigkeit des CNGS Zeitmesssystems zu bestätigen. Dies war entscheidend bei der Suche nach dem fehlerhaften System, welches zu einer Neutrino-Geschwindigkeitsmessungen oberhalb der Lichtgeschwindigkeit führte, dessen Veröffentlichung durch die OPERA Kollaboration später zurückgezogen wurde.

Zusätzlich wurde die Zeitauflösung von Diamantdetektoren in einem Hochflussexperiement zu $\sigma_t = (14.7 \pm 1.7)\,\mathrm{ps}$ gemessen. Abschließend wurde Daten der Diamantdetektoren des ATLAS Beam Conditions Monitor (BCM) ausgewertet, welcher viele Informationen über den Protonstrahl am LHC, z.B. über die Lumnositaet und die Menge an Strahlverlusten, liefert. Hier wird der Fokus auf nicht-kollisions Untergründe gerichtet.

Bibliography

[1] J. R. Weber, et al., Quantum computing with defects, Proceedings of the National Academy of Sciences 107 (19) (2010) 8513–8518. doi:10.1073/pnas.1003052107.

[2] S. Reardon, Nanodiamonds Could Be a Cancer Patient's Best Friend, `http://news.sciencemag.org/sciencenow/2011/03/nanodiamonds-could-be-a-cancer-p.html` (2011).

[3] L. Evans, P. Bryant, The LHC Machine, J. Inst. 3 (08) (2008) S08001.

[4] B. Dehning, et al., Diamond Detectors as Beam Monitors, Tech. Rep. CERN-BE-2011-001, CERN, Geneva, `http://cds.cern.ch/record/1338040` (May 2010).

[5] C. Kurfürst, et al., Investigation of the use of Silicon, Diamond and liquid Helium detectors for Beam Loss Measurements at 2 K, Tech. Rep. CERN-ATS-2012-094, CERN, Geneva, `http://cds.cern.ch/record/1459186` (May 2012).

[6] O. A. Williams, M. Nesladek, J. J. Mares, P. Hubik, Growth and Properties of Nanocrystalline Diamond Films, Wiley-VCH Verlag GmbH & Co. KGaA, Weinheim, 2008.

[7] Y. Kawano, S. Chiba, A. Inoue, Application of diamond window for infra-red laser diagnostics in a tokamak device, Review of Scientific Instruments 75 (1) (2004) 279 –280. doi:10.1063/1.1633990.

[8] A. T. Collins, Detectors for UV and Far UV Radiation, John Wiley & Sons, Ltd, 2009, pp. 163–183. doi:10.1002/9780470740392.ch7.

[9] T. Adam, et al., Measurement of the neutrino velocity with the OPERA detector in the CNGS beam, arXiv:1109.4897.

[10] M. Güler, et al., An appearance experiment to search for $\nu_\mu \rightarrow \nu_\tau$ oscillations in the CNGS beam: experimental proposal, Tech. Rep. CERN-SPSC-2000-028, CERN, Geneva, `http://cds.cern.ch/record/456523` (Jul 2000).

[11] The ATLAS Collaboration, The ATLAS Experiment at the CERN Large Hadron Collider, J. Inst 3 (08) (2008) S08003.

[12] R. Sauer, Halbleiterphysik: Lehrbuch für Physiker und Ingenieure, Oldenbourg Wissenschaftsverlag, 2009.

[13] S. Sze, K. N. Kwok, Physics of Semiconductor Devices; 3rd ed., Wiley, Hoboken, NJ, 2007.

[14] L. S. Pan, D. R. Kania, Diamond: electronic properties and applications, Kluwer Academic Publ., Boston, MA, 1995.

[15] Hazmat2, http://commons.wikimedia.org/wiki/File:Wigner%E2%80%93Seitz_cell.svg.

[16] Prof. C. Röhr, http://ruby.chemie.uni-freiburg.de/Vorlesung/SVG/E_in_fk/fcc_punkte_b.svg.

[17] R. Gross, A. Marx, Festkörperphysik, Oldenbourg Wissenschaftsverlag, 2012.

[18] Matthias M., http://commons.wikimedia.org/wiki/File:Lattice_face_centered_cubic.svg.

[19] Magasjukur2, http://commons.wikimedia.org/wiki/File:Diamonds_gitter.svg.

[20] C. D. Clark, P. J. Dean, P. V. Harris, Intrinsic Edge Absorption in Diamond, Proceedings of the Royal Society of London. Series A. Mathematical and Physical Sciences 277 (1370) (1964) 312–329. doi:10.1098/rspa.1964.0025.

[21] Nepomo, http://commons.wikimedia.org/wiki/File:StructureNVcenter.jpg.

[22] G. Glover, The C-V characteristics of Schottky barriers on laboratory grown semiconducting diamonds, Solid-State Electronics 16 (9) (1973) 973 – 978. doi:http://dx.doi.org/10.1016/0038-1101(73)90196-2.

[23] L. A. Vermeulen, R. J. Farrer, Diamond Research, Vol. 18, 1975.

[24] K. Okano, H. Kiyota, T. Iwasaki, T. Kurosu, M. Ida, T. Nakamura, in: Proc. Second Int. Conf. on the New Diamond Science and Technology, Washington D.C., 1990, pp. 917–922.

[25] N. Bar-Gill, L. Pham, A. Jarmola, D. Budker, R. Walsworth, Solid-state electronic spin coherence time approaching one second, Nature Communications 4 (2013) 1743. doi:10.1038/ncomms2771.

[26] W. Kohn, Shallow impurity states in silicon and germanium, Vol. 5 of Solid State Physics, Academic Press, 1957, pp. 257 – 320. doi:http://dx.doi.org/10.1016/S0081-1947(08)60104-6.
URL http://www.sciencedirect.com/science/article/pii/S0081194708601046

[27] B. G. Streetman, S. Banerjee, Solid state electronic devices / Ben G. Streetman and Sanjay Banerjee, 5th Edition, Upper Saddle River, N.J. : Prentice Hall, 2000.

[28] P. Drude, Zur Elektronentheorie der Metalle, Annalen der Physik 306 (1900) 566–613.

[29] H. Pernegger, et al., Charge-carrier properties in synthetic single-crystal diamond measured with the transient-current technique, J. Appl. Phys. 97 (7) (2005) 073704. doi:10.1063/1.1863417.

[30] M. Nesladek, et al., Charge transport in high mobility single crystal diamond, in: Proceedings of Diamond 2007, the 18th European Conference on Diamond, Diamond-Like Materials, Carbon Nanotubes, Nitrides and Silicon Carbide, Vol. 17, 2008, pp. 1235 – 1240.

[31] J. Isberg, A. Lindblom, A. Tajani, D. Twitchen, Temperature dependence of hole drift mobility in high-purity single-crystal CVD diamond, Physica status solidi (a) 202 (11) (2005) 2194.

[32] A. Matthiessen, On the Electrical Conductivity of Alloys, Ann. Physik. Chem. 110 (1860) 190.

[33] A. Matthiessen, C. Vogt, Über die elektrische Leitfahigkeit der Metalle, Ann. Physik. Chem. 122 (1864) 19.

[34] J. Bardeen, W. Shockley, Deformation Potentials and Mobilities in Non-Polar Crystals, Phys. Rev. 80 (1950) 72–80. doi:10.1103/PhysRev.80.72.

[35] E. Conwell, V. F. Weisskopf, Theory of Impurity Scattering in Semiconductors, Phys. Rev. 77 (1950) 388–390. doi:10.1103/PhysRev.77.388.

[36] C. Erginsoy, Neutral Impurity Scattering in Semiconductors, Phys. Rev. 79 (1950) 1013–1014.

[37] N. Sclar, Neutral Impurity Scattering in Semiconductors, Phys. Rev. 104 (1956) 1559–1561.

[38] A. I. Ansel'm, J. Exptl. Theoret. Phys. (U.S.S.R.) 24 (1953) 85.

[39] M. Prunnila, P. Kivinen, A. Savin, P. Törmä, J. Ahopelto, Intervalley-scattering-induced electron-phonon energy relaxation in many-valley semiconductors at low temperatures, Phys. Rev. Lett. 95 (2005) 206602. doi:10.1103/PhysRevLett.95.206602. URL http://link.aps.org/doi/10.1103/PhysRevLett.95.206602

[40] J. L. Moll, Physics of Semiconductors, Wiley, New York, Chapter 10.

[41] R. S. Sussmann, CVD diamond for electronic devices and sensors, John Wiley & Sons, Chichester, 2009.

[42] D. K. Ferry, High-field transport in wide-band-gap semiconductors, Phys. Rev. B 12 (1975) 2361–2369. doi:10.1103/PhysRevB.12.2361.

[43] M. Osman, M. Imam, N. Nintunze, Diffusion coefficient of electrons in diamond, Applications of Diamond Films and Related Materials (1991) 611–614Y. Tzeng, M. Yoshikawa, editors.

[44] Z. Li, H. Kraner, Modeling and simulation of charge collection properties for neutron irradiated silicon detectors, Nuclear Physics B - Proceedings Supplements 32 (1993) 398 – 409.

[45] J. Frenkel, On the Transformation of light into Heat in Solids. I, Phys. Rev. 37 (1931) 17–44. doi:10.1103/PhysRev.37.17.

[46] G. G. Macfarlane, T. P. McLean, J. E. Quarrington, V. Roberts, Fine Structure in the Absorption-Edge Spectrum of Si, Phys. Rev. 111 (1958) 1245–1254. doi:10.1103/PhysRev.111.1245.

[47] P. J. Dean, E. C. Lightowlers, D. R. Wight, Intrinsic and Extrinsic Recombination Radiation from Natural and Synthetic Aluminum-Doped Diamond, Phys. Rev. 140 (1965) A352–A368. doi:10.1103/PhysRev.140.A352.

[48] R. Sauer, N. Teofilov, K. Thonke, Exciton condensation in diamond, Diamond and Related Materials 13 (48) (2004) 691 – 699, 14th European Conference on Diamond, Diamond-Like Materials, Carbon Nanotubes, Nitrides and Silicon Carbide. doi:http://dx.doi.org/10.1016/j.diamond.2003.10.005.
URL http://www.sciencedirect.com/science/article/pii/S0925963503003509

[49] K. Takiyama, M. Abd-Elrahman, T. Fujita, T. Oda, Photoluminescence and decay kinetics of indirect free excitons in diamonds under the near-resonant laser excitation, Solid State Communications 99 (11) (1996) 793 – 797. doi:http://dx.doi.org/10.1016/0038-1098(96)00309-2.

[50] N. Naka, J. Omachi, H. Sumiya, K. Tamasaku, T. Ishikawa, M. Kuwata-Gonokami, Density-dependent exciton kinetics in synthetic diamond crystals, Phys. Rev. B 80 (2009) 035201. doi:10.1103/PhysRevB.80.035201.

[51] R. Sauer, private communications.

[52] A. YARNELL, The many facets of man-made diamonds, Chemical & Engineering News Archive 82 (5) (2004) 26–31. doi:10.1021/cen-v082n005.p026.

[53] L. S. Pan, D. R. Kania, Diamond: electronic properties and applications, Kluwer Academic Publ., Boston, MA, 1995, chapter 3.4.

[54] Diamond Materials, http://www.diamond-materials.com/DE/company/deposition.htm.

[55] M. Sunkara, J. C. Angus, C. C. Hayman, F. A. Buck, Nucleation of diamond crystals, Carbon 28 (6) (1990) 745 – 746. doi:http://dx.doi.org/10.1016/0008-6223(90)90265-Z.

[56] J. Dodson, private communications.

[57] L. S. G. Plano, Structure and chemistry in diamond-producing dc plasmas, Ph.D. thesis, Leland Stanford Jr. University, 1991.

[58] S. Mehandru, A. B. Anderson, Adsorption of H, CH_3, CH_2 and C_2H_2 on 2 1 restructured diamond (100): Theoretical study of structures, bonding, and migration, Surface Science 248 (3) (1991) 369 – 381. doi:http://dx.doi.org/10.1016/0039-6028(91)91183-X.

[59] H. Bethe, Zur Theorie des Durchgangs schneller Korpuskularstrahlen durch Materie, Annalen der Physik 397 (3) (1930) 325–400. doi:10.1002/andp.19303970303.

[60] H. Andersen, J. Ziegler, Hydrogen stopping powers and ranges in all elements, Stopping and ranges of ions in matter, Pergamon Press, 1977.

[61] J. Lindhard, Kgl. Danske Videnskab. Selskab, Mat.-Fys. Medd. 28 (8).

[62] J. Beringer, et al., Review of particle physics, Phys. Rev. D 86.

[63] See http://www.nist.gov/pml/data/star/index.cfm for stopping power values.

[64] M. Gabrysch, Charge Transport in Single-crystalline CVD Diamond, Ph.D. thesis, Uppsala University, Electricity (2010).

[65] C. Weiss, A CVD Diamond Detector for (n,α) Cross-Section Measurements, Ph.D. thesis, Vienna University of Technology, Vienna, Austria, (in preparation) (2013).

[66] F. Nava, et al., Transport Properties of Natural Diamond Used as Nuclear Particle Detector for a Wide Temperature Range, Nuclear Science, IEEE Transactions on 26 (1) (1979) 308 –315. doi:10.1109/TNS.1979.4329650.

[67] S. Uehara, H. Nikjoo, Monte Carlo Track Structure Code for Low-Energy Alpha-Particles in Water, J. of Phys. Chemistry B 106 (42) (2002) 11051–11063. doi:10.1021/jp014004h.

[68] G. Laczk, Investigation of the Radial Ionization Distribution of Heavy Ions with an Optical Particle Track Chamber and Monte-Carlo Simulations, Ph.D. thesis, GSI, Darmstadt (2006).

[69] S. Zhao, Characterization of the electrical properties of polycrystalline diamond films, Ph.D. thesis, Ohio State University (1994).

[70] H. Kagan, private communications.

[71] S. Friedland, J. Mayer, J. S. Wiggins, The Solid-State Ionization Chamber, Nuclear Science, IRE Transactions on 7 (2-3) (1960) 181–185. doi:10.1109/TNS2.1960.4315761.

[72] S. Ramo, Currents Induced by Electron Motion, Proceedings of the IRE 27 (9) (1939) 584 – 585.

[73] R. C. Alig, S. Bloom, C. W. Struck, Scattering by ionization and phonon emission in semiconductors, Phys. Rev. B 22 (1980) 5565–5582. doi:10.1103/PhysRevB.22.5565.

[74] M. Lampert, P. Mark, Current Injection in Solids, Academic Press, New York, 1970.

[75] V. Eremin, N. Strokan, E. Verbitskaya, Z. Li, Development of transient current and charge techniques for the measurement of effective net concentration of ionized charges (Neff) in the space charge region of p-n junction detectors, Nucl. Instrum. Methods Phys. Rev. A 372 (3) (1996) 388 – 398. doi:10.1016/0168-9002(95)01295-8.

[76] M. Pomorski, et al., Characterisation of single crystal cvd diamond particle detectors for hadron physics experiments, Phys. Status Solidi A 202 (11) (2005) 2199–2205. doi:10.1002/pssa.200561929.

[77] J. Fink, P. Lodomez, H. Krüger, H. Pernegger, P. Weilhammer, N. Wermes, TCT characterization of different semiconductor materials for particle detection, in: Proceedings of the International Workshop on Semiconductor Pixel Detectors for Particles and Imaging PIXEL 2005, Vol. 565, 2006, pp. 227 – 233. doi:10.1016/j.nima.2006.05.003.

[78] Element Six Ltd, Kings Ride Park, Ascot, Berkshire, SL5 8BP, UK, `http://www.e6.com/`.

[79] Diamond Detectors Ltd, 16 Fleetsbridge Business Centre, Upton Road, Poole, Dorset, BH17 7AF, UK, `www.diamonddetectors.com`.

[80] MINCO, France, zone Industrielle, 09310 Aston, France.

[81] CIVIDEC Instrumentation GmbH, Schottengasse 3A/1/41, A - 1010 Vienna, Austria, http://www.cividec.at/.

[82] H. Jansen, et al., Temperature Dependence of Charge Carrier Properties in Single Crystal CVD Diamond Detectors, in: Proceedings of the 2nd International Conference on Technology and Instrumentation in Particle Physics (TIPP 2011), Vol. 37, 2012, pp. 2005 – 2014. doi:10.1016/j.phpro.2012.02.527.

[83] H. Jansen, D. Dobos, T. Eisel, H. Pernegger, V. Eremin, N. Wermes, Temperature dependence of charge carrier mobility in single-crystal chemical vapour deposition diamond, J. Appl. Phys. 113 (17) (2013) 173706. doi:10.1063/1.4802679.

[84] F. Nava, et al., Electron effective masses and lattice scattering in natural diamond, Solid State Communications 33 (4) (1980) 475 – 477. doi:10.1016/0038-1098(80)90447-0.

[85] L. Reggiani, S. Bosi, C. Canali, F. Nava, S. F. Kozlov, Hole-drift velocity in natural diamond, Phys. Rev. B 23 (1981) 3050–3057. doi:10.1103/PhysRevB.23.3050.

[86] M. Gabrysch, S. Majdi, D. J. Twitchen, J. Isberg, Electron and hole drift velocity in chemical vapour deposition diamond, Journal of Applied Physics 109 (6) (2011) 063719. doi:10.1063/1.3554721.

[87] C. Jacoboni, C. Canali, G. Ottaviani, A. A. Quaranta, A review of some charge transport properties of silicon, Solid-State Electronics 20 (2) (1977) 77 – 89. doi:10.1016/0038-1101(77)90054-5.

[88] J. Isberg, M. Gabrysch, S. Majdi, D. J. Twitchen, Negative electron mobility in diamond, Applied Physics Letters 100 (17) (2012) 172103. doi:10.1063/1.4705434.

[89] S. Gkoumas, A. Lohstroh, P. Sellin, Low temperature time of flight mobility measurements on synthetic single crystal diamond, Diamond and Related Materials 18 (11) (2009) 1338 – 1342.

[90] C. J. Rauch, in: Proc. of Int. Conf. on the Physics of Semiconductors, Exeter, The Inst. of Phys. an the Physical Soc., London, UK, 1962, p. 276.

[91] L. Reggiani, et al., On the lattice scattering and effective mass of holes in natural diamond, Solid State Communications 30 (6) (1979) 333 – 335. doi:10.1016/0038-1098(79)90645-8.

[92] C. Kurfürst, Cryogenic Beam Loss Monitoring for the LHC, Ph.D. thesis, Vienna University of Technology, Vienna, Austria, (in preparation) (2013).

[93] R. Sauer, private communications, Letter from 22.08.2012 to the author.

[94] R. Sauer, private communications, Letter from 11.01.2013 to the author.

[95] E. Segre, Nuclei and particles: an introduction to nuclear and subnuclear physics; 1st ed., Benjamin, New York, NY, 1964.

[96] J. Isberg, M. Gabrysch, J. Hammersberg, S. Majdi, K. K. Kovi, D. J. Twitchen, Generation, transport and detection of valley-polarized electrons in diamond, Nature Materials 12. doi:10.1038/nmat3694.

[97] H. Lofas, A. Grigoriev, J. Isberg, R. Ahuja, Effective masses and electronic structure of diamond including electron correlation effects in first principles calculations using the GW-approximation, AIP Advances 1 (3) (2011) 032139. doi:10.1063/1.3630932.

[98] H. Jansen, et al., Verification of the CNGS timing system using fast diamond detectors, J. Inst. 8 (01) (2013) P01017.

[99] K. Elsener (Editor), The CERN neutrino beam to Gran Sasso (CNGS): conceptual technical design, CERN 98-02, INFN/AE-98/05, Geneva, Frascati, 1998.

[100] G. Alimonti, et al., The Borexino detector at the Laboratori Nazionali del Gran Sasso, Nucl. Instrum. Methods Phys. Rev. A 600 (3) (2009) 568 – 593. doi:10.1016/j.nima.2008.11.076.

[101] The ICARUS Collaboration, ICARUS: a proposal for the Gran Sasso Laboratory, INFN/AE-85/7, Frascati, 1985.

[102] The LVD Collaboration, The Large Volume Detector (LVD) of the Gran Sasso Laboratory, Nuovo Cim., 9C, 1986.

[103] H. Jakob, J. J. Savioz, R. Jones, L. Jensen, A 40 MHz Bunch by Bunch Intensity Measurement for the CERN SPS and LHC, Tech. Rep. CERN-AB-2003-056-BDI, http://cds.cern.ch/record/624188 (Jun 2003).

[104] B. Dehning, E. Effinger, H. Pernegger, D. Dobos, H. Frais-Kolbl, E. Griesmayer, Test of a Diamond Detector Using Unbunched Beam Halo Particles, Tech. Rep. CERN-ATS-2010-027, CERN, Geneva, http://cds.cern.ch/record/1258407 (Feb 2010).

[105] Draka Communications, http://communications.draka.com/.

[106] A. Ferrari, P. R. Sala, A. Fass, J. Ranft, FLUKA: A multi-particle transport code (program version 2005), CERN, Geneva, 2005.

[107] A. Ferrari, A. M. Guglielmi, M. Lorenzo-Sentis, S. Roesler, P. R. Sala, L. Sarchiapone, An updated Monte Carlo calculation of the CNGS neutrino beam, Tech. Rep. CERN-AB-Note-2006-038, CERN, Geneva, http://cds.cern.ch/record/979037 (Aug 2007).

[108] D. Autiero, et al., The CNGS neutrino beam: status, Nuclear Physics B - Proceedings Supplements 188 (0) (2009) 188 – 190. doi:10.1016/j.nuclphysbps.2009.02.047.

[109] P. Alvarez, J. Serrano, Time transfer techniques for the synchronisation between CERN and LNGS, Tech. Rep. to be published, CERN, Geneva, http://www.ohwr.org/documents/112.

[110] P. Alvarez, Calibration of the reference CTRIs in CCR and HCA442 for CNGS time transfer, Tech. Rep. to be published, CERN, Geneva, http://www.ohwr.org/documents/116.

[111] TIMBER, http://lhc-logging.web.cern.ch/lhc-logging/.

[112] R. Brun, F. Rademakers, Root an object oriented data analysis framework, Nuclear Instruments and Methods in Physics Research Section A: Accelerators, Spectrometers, Detectors and Associated Equipment 389 (12) (1997) 81 – 86. doi:10.1016/S0168-9002(97)00048-X.

[113] D. Dobos, H. Pernegger, Diamond Pixel Modules and the ATLAS Beam Conditions Monitor, Tech. Rep. ATL-INDET-PROC-2010-007, CERN, Geneva, http://cds.cern.ch/record/1248212 (Mar 2010).

[114] M. Antonello, et al., Precision measurement of the neutrino velocity with the ICARUS detector in the CNGS beam, Journal of High Energy Physics 2012 (11) (2012) 1–21. doi:10.1007/JHEP11(2012)049.

[115] E.g. at the HighRadMat experiment, private communications with E. Griesmayer.

[116] H. Spieler, Semiconductor detector systems, Semiconductor Science and Technology, Oxford Univ. Press, Oxford, 2005.

[117] The ATLAS Collaboration, Non-collision backgrounds as measured by the atlas detector during the 2010 proton-proton run, Tech. Rep. ATLAS-CONF-2011-137, CERN, Geneva, http://cds.cern.ch/record/1383840 (Sep 2011).

[118] CERN and Deutsche Elektronen-Synchrotron DESY, http://www.weltmaschine.de/sites/site_weltmaschine/content/e5/e105102/e105104/2010-12-16_0911188_01-A4-at-144-dpi.jpg.

[119] V. Cindro, et al., The ATLAS Beam Conditions Monitor, J. Inst. 3 (02) (2008) P02004.

[120] University of California Santa Cruz, http://scipp.ucsc.edu/personnel/atlas.html.

[121] G. Corti, V. Talanov, Aspects of Machine Induced Background in the LHC Experiments, Tech. rep., https://cds.cern.ch/record/974592 (2006).

[122] K. Nakamura, P. D. Group, Review of Particle Physics, Journal of Physics G: Nuclear and Particle Physics 37 (7A) (2010) 075021.

[123] N. V. Mokhov, T. Weiler, Machine-Induced Backgrounds: their Origin and Loads on ATLAS/CMS, Tech. rep., http://cds.cern.ch/record/1184447 (2009).

[124] A. I. Drozhdin, N. V. Mokhov, S. I. Striganov, Beam Losses and Background Loads on Collider Detectors Due to Beam-Gas Interactions in the LHC, Tech. Rep. FERMILAB-CONF-09-172-APC, http://cds.cern.ch/record/1370157 (2010).

[125] The ATLAS Collaboration, Measurement of the Rate of Collisions from Satellite Bunches for the April-May 2010 LHC Luminosity Calibration, Tech. Rep. ATLAS-CONF-2010-102, CERN, Geneva, http://cds.cern.ch/record/1317334 (Dec 2010).

[126] S. Ask, et al., The ATLAS central level-1 trigger logic and TTC system, J. Inst. 3 (08) (2008) P08002.

[127] ATLAS, http://atlas-runquery.cern.ch/query.py?q=find+run+162882%2C167607%2C180636+%2F+show+all+and+lhc.

List of Figures

List of Tables

Acknowledgements

The support of this work by CIVIDEC Instrumentation GmbH is gratefully acknowledged.

At first, I would like to express my gratitude to Heinz Pernegger and Daniel Dobos for welcoming me at CERN and in the ATLAS BCM group, for many, many discussions, hints, introductions, critic and encouragement, paper readings, and so on and so forth. To Norbert Wermes I am equally indebted.

My sincerest thanks go to Erich Griesmayer for many electronics lessons, introduction to amplifiers, borrowing of fine equipment, invitations to the annual CIVIDEC dinner party, discussions about CVD diamond, etc.

I would like to thank Vladimir Eremin for many discussions about semiconductors and the 'how-to' of setting up a TCT experiments. Also, thanks go to Jaakko Härkönen and RD 39, for lending me their set-up giving rise to my first results on cryogenic TCT measurements. I am indebted to Thomas Eisel and the CryoLab group for the introduction to cryogenics, vacuum engineering, and the 'how-to' of building a cryogenic experiment.

Special and earnest thanks go to Prof. Sauer for innumerable hours of discussions on semiconductor physics, for giving me an understanding of excitons and charge carrier properties in semiconductors, and, particularly, for contributing the basic ideas as to modelling the pulse shapes and the measured total charge with its temperature dependence plus the impurity-assisted repopulation effects.

Furthermore, I owe thanks to Edda Gschwendtner, the CNGS group, and the CERN service groups for their support before, during, and after the 2011 and 2012 CNGS data taking. Sincere thanks are given also to the entire ATLAS group.

Additionally, I would like to thank Nicoletta Garelli, Harris Kagan, William Trischuk, and RD 42, Michal Pomorski, Eleni Berdermann, Christina Weiss, Christoph Kurfürst, Riccardo Mori and Mara Bruzzi, Bernd Dehning and the Beam Instrumentation group, and, last but not least, my family and friends.